Convective and Atmospheric Boundaries of Asymptotic Giant Branch Stars

Graham Wagstaff

München 2017

Convective and Atmospheric Boundaries of Asymptotic Giant Branch Stars

Graham Wagstaff

Dissertation
an der Fakultät für Physik
der Ludwig–Maximilians–Universität
München

vorgelegt von
Graham Wagstaff
aus Falkirk, Scotland

München, den 19.12.2017

Erstgutachter: Prof. Dr. Achim Weiss
Zweitgutachter: Prof. Dr. Adalbert Pauldrach
Datum der Abgabe: 19.12.2017
Datum der mündlichen Prüfung: 20.2.2018

Contents

List of Figures

List of Tables

Zusammenfassung

Thermisch pulsierende Sterne auf dem asymptotischen Riesenast (Thermally Pulsing Asymptotic Giant Branch (TP-AGB) stars) haben einen signifikanten Einfluss auf ihre Umgebung und sind sehr wichtig für die chemische Entwicklung von Galaxien. Gleichzeitig sind diese Sterne überaus komplex aufgrund der miteinander verflochtenen Prozesse, die ihre Entwicklung steuern. Der AGB ist die evolutionäre Endphase für Sterne mit Massen zwischen etwa 0.8-8$M_{\odot}$, wobei die TP-AGB Phase durch eine Änderung der chemischen Zusammensetzung an der Oberfläche und hohen Massenverlustraten gekennzeichnet ist, wodurch das Material in das interstellare Medium zurückgeführt wird, was die ideale Voraussetzung für die Bildung von Staub schafft.

In dieser Arbeit werden mehrere Randerscheinungen im Bezug auf die Entwicklung von TP-AGB Sternen untersucht, von denen eine direkte Beeinflussung sowohl auf den sog. dritten dredge-up als auch auf die Massenverlustraten erwartet wird. Die Untersuchung der atmosphärischen Behandlung im Sternenentwicklungscode betrachtet die Annahmen näher, die für die häufig genutzten plan-parallelen Atmosphären mit grauen Opazitäten getätigt werden. Hierbei werden die Geometrie und die Opazitäten geändert und ein Gitter von Modellen für den Strahlungstransport in der Atmosphäre implementiert. Auch wenn dies eine Änderung der Effektivtemperatur der Modelle zur Folge hat, bleibt das Sterninnere weitestgehend unbeeinflusst und es gibt keine signifikanten Änderungen der beobachtbaren Größen, die verwendet werden um TP-AGB Modelle einzuschränken. Jedoch wurde im Laufe der Untersuchung ein bislang nicht beschriebenes Verhalten der TP-AGB Modelle beobachtet und genauer untersucht, was zeigte, dass die thermischen Pulse zeitweise unterdrückt werden, wodurch weiterhin stabiles Brennen in zwei Schalen stattfinden kann.

Mischung an konvektiven Grenzen (Convective boundary mixing, CBM) bleibt weiterhin eine signifikante Unsicherheit bei der Modellierung des TP-AGB. Die Indizien deuten darauf hin, dass die Grenzen verschiedener Konvektionsbereiche unterschiedlich behandelt werden müssen. Mit einer Reihe von numerischen Experimenten und vollständigen Berechnungen der Entwicklung wurde die Mischung an jeder Grenze separat behandelt um die individuelle Bedeutung zu untersuchen. Diese Arbeit hebt hervor, dass es aufgrund von Beobachtungsdaten und dem Einfluss auf den TP-AGB wichtig ist die CBM in konvektiven Kernen miteinzubeziehen. Beobachtungen weisen auch darauf hin, dass die CBM am unteren Rand sowohl der konvektiven Hülle als auch der pulsgetriebenen Konvektionszone notwendig ist. Das Ausmaß der CBM konnte in dieser Arbeit teilweise eingegrenzt werden.

In dieser Arbeit wurden zwei wichtige Ursachen von Unsicherheiten, die durch fehlerhafte Grundannahmen oder abweichende Beobachtungsdaten bedingt werden, beim Modellieren von TP-AGB gründlich untersucht. Diese Arbeit kann als Referenz für zukünftige Berechnungen dieser Entwicklungsphase herangezogen werden, da die in diesem Zusammenhang wichtigen Aspekte hervorgehoben wurden.

Abstract

Thermally Pulsing Asymptotic Giant Branch (TP-AGB) stars have a significant impact on their surrounding environment and are very important for the chemical evolution of galaxies, while at the same time being incredibly complex due to the intertwined processes which govern their evolution. The AGB is the final evolutionary phase for stars with masses between approximately 0.8-8$M_{\odot}$, with the TP-AGB characterised by the change in chemical composition at the surface and high mass loss rates, returning this material to the surrounding interstellar medium and providing an excellent environment for dust production.

This thesis aims to investigate several boundaries relating to the evolution of TP-AGB stars, which are expected to directly impact on both the third dredge-up and mass loss rates. The investigation of the atmospheric treatment in the stellar evolution code examines the assumptions taken for the widely used plane-parallel, grey opacity, atmosphere. This is done by changing the geometry and the opacities, and implementing a grid of radiative transfer stellar atmosphere models. Although this results in a change to the effective temperature of the models, the interior is largely unaffected and there is no significant difference in the observables used to constrain TP-AGB models. However, during the course of this investigation, previously unseen behaviour of TP-AGB models was observed, and investigated further, whereby the thermal pulses are temporarily suppressed and stable double shell burning resumes.

Convective boundary mixing (CBM) remains a significant uncertainty when modelling the TP-AGB, with the evidence suggesting that different treatments are required at the boundaries of the various convective regions. Mixing was treated separately at each boundary in order to investigate their individual importance through a series of numerical experiments and full evolutionary calculations. This work emphasises the importance of including CBM in convective cores, due to the observational constraints and the impact on the TP-AGB. Observations also seem to suggest that CBM is required at the base of both the convective envelope and pulse-driven convection zone, the extent of which has been partially constrained by this thesis.

The investigations pursued within this thesis have thoroughly examined two significant sources of uncertainties in TP-AGB modelling, whether due to the flawed underlying assumptions or tension with observations. This should provide a good reference point for any future calculations of this evolutionary phase, outlining the important aspects which must be taken into consideration when doing so.

Chapter 1

Introduction

The Thermally Pulsing Asymptotic Giant Branch (TP-AGB) is both a highly complicated and hugely important phase in stellar evolution, not just for the stars themselves but for the surrounding environment and galactic chemical evolution. This is the final nuclear burning evolutionary phase of moderate mass stars, within the approximate range 0.8-8$M_{\odot}$. This stage in a star's lifetime is defined by the hydrogen and helium burning shells, surrounding the inert carbon-oxygen core. Many characteristics of this phase are governed by this unstable, double shell burning which results in the thermal pulses that give the TP-AGB its name. These thermal pulses are responsible for many aspects such as the third dredge-up, the mechanism responsible for the formation of carbon stars and which results in the unique conditions which define this as one of the most interesting and productive times in a stars life-cycle.

The nuclear processes which occur in the interior of TP-AGB stars extend beyond simple burning of hydrogen and helium, as it is thought this is the main site for s-process nucleosynthesis, the source of half of the elements heavier than iron (Arlandini et al., 1999). Combined with the high mass loss rates, as high as $\dot{M}_{\rm AGB} \sim -10^{-a} M_{\odot} {\rm yr}^{-1}$ where $a \sim 4...6$ (Wood et al., 1992), these stars are clearly important for galactic chemical evolution (Kobayashi et al., 2011). Furthermore, they determine the transition between which stars form planetary nebulae, and which go onto forming electron capture supernovae (Doherty et al., 2015) while also providing commonly accepted explanations for the multiple populations in Globular Clusters (for a review, see Gratton et al., 2012) and the abundance pattern in CEMP-s stars (Abate et al., 2016).

Unfortunately, many uncertainties remain within the theoretical models of such stars. The aim of this thesis is to investigate the current treatment in two such

cases, where either the fundamental assumptions are questionable, or the evidence suggests there is a tension between theory and observations. This chapter outlines the evolution of moderate mass stars in Sec. 1.1 followed by a discussion of the basic principles of stellar evolution codes in Sec. 1.2 and finally some relevant observational data in Sec. 1.3.

1.1 The Life of Moderate Mass Stars

The beginning for all stars is believed to be when a chemically homogeneous cloud of interstellar gas collapses into a protostar (Kippenhahn et al., 2012, Ch. 27), with the future evolution almost entirely decided by the mass at this stage and, to some degree, composition (excluding external influences, e.g. binary interactions). At the lower limit, below approximately $0.08M_{\odot}$, the gravitational collapse will be halted by electron degeneracy pressure before temperatures are reached which allow for the onset of hydrogen burning, and the protostar will instead radiate the gravitational energy, becoming a brown dwarf.

At the opposite end of the mass spectrum, above $\sim 8M_{\odot}$[1], stars not only ignite hydrogen in their core but proceed through the burning of successively heavier elements until an iron core is produced, prior to becoming a core-collapse supernova.

Although the remaining stars between these limits ignite hydrogen in their cores and do not proceed to the burning of elements heavier than helium, there is an additional boundary. Only stars above a mass of $0.8M_{\odot}$[2] but below $8M_{\odot}$ will end their nuclear burning life on the AGB, before evolving through the planetary nebulae stage and ending their life as a white dwarf. These are the stars which are of importance for this thesis and, as such, more detail concerning their evolution follows within this section, discussing first the evolution up until the AGB (§1.1.1), followed by particular details relating to the AGB itself (§1.1.2) and finally the final fates of these curious stars (§1.1.3).

However, to begin with, an initial outline of how each phase relates to one another. Fig. 1.1 shows the evolutionary tracks in the Hertzsprung-Russell (HR) diagram, for 2, 3 and $5M_{\odot}$ stars. Each begins on the main sequence (black) where the stars

[1]This limit may be closer to $10M_{\odot}$ or higher and varies with metallicity, see Fig. 1.3 taken from Doherty et al. (2015).

[2]The lower limit could, in fact, be closer to $0.5M_{\odot}$, required by the need for a core which is sufficiently massive that it could ignite helium under degenerate burning conditions. However, due to the main sequence lifetimes of such stars being longer than the age of the universe, the limit is usually placed at $0.8M_{\odot}$ or $1M_{\odot}$ as these masses may actually contribute to the AGB stars in the universe.

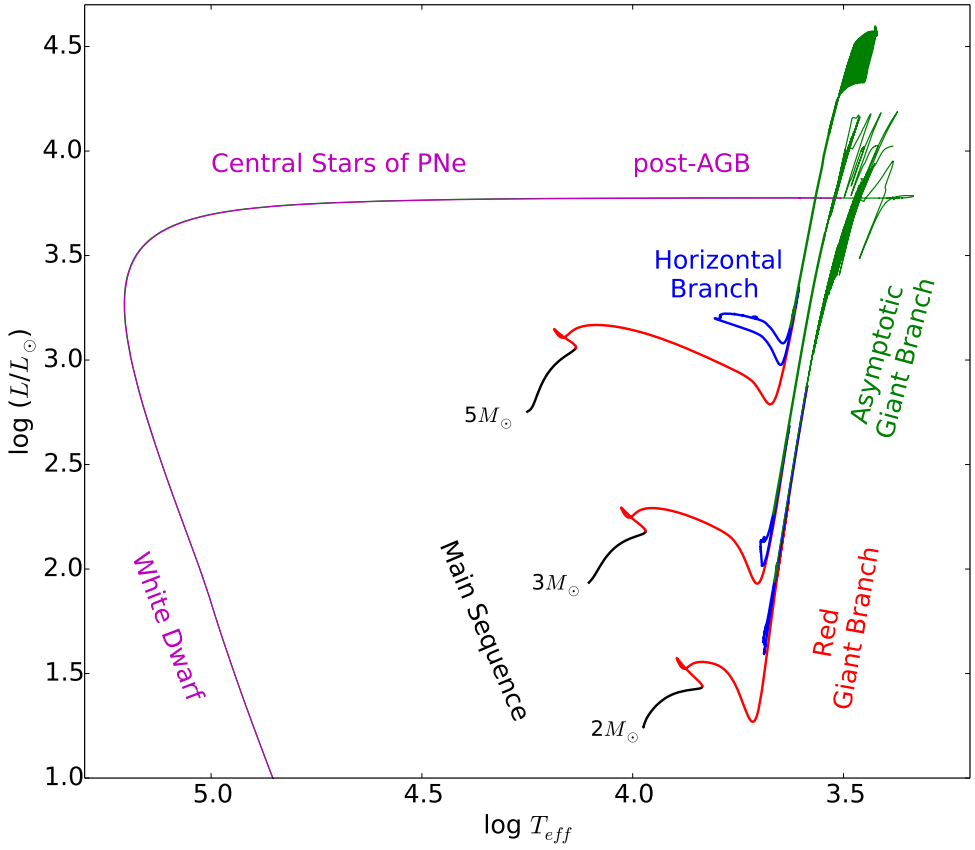

Figure 1.1: HR-diagram showing the evolutionary tracks of 2, 3 and 5$M_\odot$ stars for solar metallicity. Colour coded with labels showing different evolutionary phases, only the 2$M_\odot$ post-AGB evolution is included. Evolutionary tracks taken for models calculated for the thesis of Kitsikis (2008).

are burning hydrogen in their core, with each initial mass beginning the zero-age main sequence (ZAMS) at a progressively higher temperature and higher luminosity location for increasing initial mass. This can be understood by considering the simple homology relations (as derived in Ch. 20 of Kippenhahn et al., 2012, for example) for the case of an ideal gas with constant opacity. These suggest that, on the main sequence, the luminosity is strongly dependent on the mass and even more dependent on the chemical composition, such that $L \propto M^3\mu^4$, where μ is the mean molecular

weight. The exponents given here are for the simple case described so should only be taken as a rough guide but they give an idea of how the luminosity on the ZAMS is increasing with mass and also that there is a distinct ZAMS for each chemical composition.

After the main sequence, the tracks become red to signify the ascent of the red giant branch, as the hydrogen in the core becomes exhausted and the burning region begins to move outwards from the core and instead burns in a shell around an inert helium core. As the inert helium core grows, the temperature increases as the core contracts and for higher mass stars the helium begins burning in the centre, causing the star to descend in the HR-diagram onto the horizontal branch (blue). For lower mass stars (up to approximately $\sim 2M_{\odot}$), helium is ignited under degenerate conditions meaning all low mass star cores reached the same critical mass, which causes the helium flash, where the helium is violently ignited (although, not at the centre). Core helium burning ends analogously to core hydrogen burning, as the helium in the core becomes exhausted and the helium burning instead moves to a shell, below the hydrogen burning shell and above the inert carbon-oxygen core left behind by helium burning. Thus begins the ascent of the asymptotic giant branch, or AGB (green).

As the star loses its envelope as a result of strong winds during the TP-AGB, the star again moves to hotter temperatures beginning the post-AGB phase, as indicated by the magenta line for the $2M_{\odot}$ model only. The ejected envelope becomes the diffuse circumstellar envelope (CSE) and may evolve into a planetary nebula (PN), which is lit by the central star, or what was the core of the AGB star (Herwig, 2005). Until this PN phase, the central star can still be burning hydrogen just below the surface of the star, but when it is no longer possible for this to continue, the star begins the descent of the white dwarf cooling track, which it will follow until all excess energy is radiated away and thermal equilibrium with the star's surroundings is achieved.

1.1.1 Prior to the AGB

Following the commencement of core hydrogen burning, a star is considered to be on the main sequence (MS). It is known as such because it is where stars spend the majority of their nuclear burning lives and hence where the largest number of stars are observed. When the position of stars at the onset of nuclear burning is taken for stars at all masses, this forms the zero-age main sequence (ZAMS). During this phase, the star is a very good approximation of hydrostatic equilibrium, with changes occurring on very long timescales and remaining observationally static.

At the end of core-hydrogen burning, the depletion of hydrogen in the centre of the star results in the burning region moving outwards in the search for new fuel. However, this means that the equilibrium that existed previously, where the energy generation supports the structure of the star against gravitational contraction, no longer exists. As the now inert helium core proceeds to contract, the envelope of the star compensates, expanding outwards and increasing the stellar radii to ~ 50 times larger than on the MS. This transformation is the beginning of the RGB phase, characterised by the small inert core, surrounded by the increasingly loosely bound, radially large envelope which has become convective due to the increased opacities as it expands and cools. This move in the HR-diagram is towards the locus which defines the solutions for a fully convective star (for a given set of parameters) called the Hayashi line (Hayashi, 1961). The high luminosities and the more loosely bound surface of these stars also result in appreciable mass loss taking place, something which was largely negligible on the MS.

Another feature of this phase is the convective envelope moving inwards in mass coordinates as the star ascends the RGB, which can result in regions which have undergone partial hydrogen burning being incorporated into this convective region and changing the surface abundances of the star. This is the First Dredge-Up (FDU) event of a stars life (Karakas, 2003). This affects low-intermediate mass stars and primarily results in a decrease in the surface ^{12}C abundance and an increase in those of ^{14}N and ^{13}C as a result of the CNO-cycle path which is the primary method for converting hydrogen to helium stars $\gtrsim 1M_{\odot}$. The discontinuity left behind at the deepest extent of convection results in a blip in the ascent of the RGB (Thomas, 1967; Iben, 1968). As the hydrogen burning shell moves outward it encounters the drop in mean molecular weight, increasing the opacity in the shell, such that the luminosity briefly decreases (Refsdal & Weigert, 1970) causing a slight excess of stars at a particular luminosity of the RGB, called the red bump.

The end of the RGB can be marked in two different ways, with the transition due to initial mass varying based on initial parameters and treatment of convective boundary mixing but it is typically found at M$\sim 2M_{\odot}$. This boundary distinguishes those stars which begin fusing helium under non-degenerate conditions and begins in the centre relatively slowly or those which undergo the helium flash, where ignition takes place far more violently under degenerate conditions. During the flash, the helium luminosity can peak at $\log L/L_{\odot} \gtrsim 10$ and even modern calculations are restricted to the peak of the flash for only part of the core (Mocák et al., 2008, 2009) due to the short time-scales and high-resolution necessary.

For stars which undergo degenerate helium ignition, the core mass at the end of the RGB is essentially the same (approximately $\sim 0.45M_{\odot}$), irrespective of to-

tal mass, as in all cases the conditions for helium ignition are determined by the degeneracy pressure. This also means a common peak luminosity for the RGB is observed, called the tip of the RGB, above which an RGB star will not exist, as stars that undergo non-degenerate helium ignition begin burning before reaching this peak luminosity.

As a consequence of core helium ignition, the entire star contracts, descending in the HR-diagram to the Horizontal Branch (HB). Low mass stars which ignite helium under degenerate conditions will remain at the cool end of the HB close to the RGB, and form what is observationally known as the red clump (Cannon, 1970). For higher mass stars, the HB can incorporate a blue loop, where the star moves to higher temperatures, before ascending the AGB.

1.1.2 Evolution on the AGB

The ascent of the AGB happens in a manner which is in many ways analogous to the RGB, also explaining the observationally similar behaviour. As the helium in the core is exhausted, the burning region moves to a spherical shell around an inert carbon-oxygen core, which contracts as the convective envelope expands. In a similar manner to the FDU, the convective envelope of more massive stars (M $\gtrsim 4M_{\odot}$) extends into regions which have previously undergone hydrogen burning, resulting in the Second Dredge-Up (SDU). In the stars for which this occurs, the envelope actually extends deeper than for the FDU, resulting in a large increase in ^{4}He at the surface, also for ^{14}N and an increase in the ^{14}N/^{15}N ratio.

Analogously to the bump in the RGB, it was predicted (Caputo et al., 1978) that a similar feature would appear in the AGB shortly after a star leaves the horizontal branch and was first observed by Gallart (1998). This AGB bump occurs after the helium core contraction leads to the expansion of the convective envelope, cooling the hydrogen burning shell until the expansion stops due to the cooling and contracts causing a temporary dip in luminosity.

This phase where the two nuclear burning shells are progressing harmoniously is the Early AGB (E-AGB) and is the stable time in the life of an AGB star, prior to the beginning of the thermally pulsing or TP-AGB. A star typically only spends of the order 1% of its nuclear burning lifetime on the E-AGB, and perhaps only 10% of that on the TP-AGB, so it would be easy to dismiss TP-AGB stars as irrelevant. This would, of course, be a mistake, as this a phase of evolution during which dramatic events occur (such as the third dredge-up and strong mass loss), contributing to their surrounding environment and the integrated luminosity of stellar systems.

What is more, the processed nuclear material is not only brought to the surface

during this phase but also ejected into the surrounding environment due to the high stellar winds. This can also result in these stars being obscured to observations due to the ejected material surrounding the star in a circumstellar envelope (CSE). As the TP-AGB is such a crucial aspect of this thesis, some of the key points are examined individually in more detail. This includes the mechanism behind the thermal pulse itself, the third dredge-up, hot-bottom burning, mass loss and the nucleosynthesis.

Thermal Pulse

During this double shell burning phase, unstable burning in the thin He-burning shell causes thermal pulses, which dramatically impact on the star. A contributing factor to this instability is the high temperature dependence of the triple-α reaction which dominates helium burning, proportional to the temperature to a power of $\sim$40. However, this condition is not sufficient to take sole responsibility for the thermal pulses, as if it weren't for the second, the star would adjust accordingly to limit the burning.

Although remarkable that it is sufficient to result in such drastic behaviour in a star, the second necessary condition is the thin shell (see Kippenhahn et al., 2012, Ch. 34.2 for detailed discussion). As the helium burning shell moves outwards in the star during the ascent of the AGB, it becomes thinner until it reaches approximately $m/M \sim 0.16$. The importance of the thin shell condition is the negligible change in pressure that any expansion of the shell causes, leaving the shell vulnerable to an increase in temperature. For example, a significant increase in the thickness of the shell, to expel the additional energy generated, will lead to a correspondingly decreased density. However, even though the relative thickness of the shell has increased significantly, as it is thin, this results in a tiny change in the radial position of the boundary of the shell. If the boundary of the shell does not move significantly, the layers above remain almost stationary and there is no change in the pressure necessary for hydrostatic equilibrium.

The simple case of an ideal gas ($P \propto \rho T$) illustrates that this lack of a change in the pressure, coupled with the decrease in density in the shell, leaves a necessary increase in the temperature, as opposed to the decrease and quenching of any additional burning, as may have been expected. The high temperature dependence of the triple-α reaction only exacerbates this problem, causing the shell to expand further leading to a thermal runaway which is responsible for such drastic changes in the star. This thermal runaway is only halted a few years after it begins, as the shell expands sufficiently, when the pressure finally decreases, that it again becomes stable.

The thermal runaway leads to peak helium luminosities of $\log(L_{\rm He}/L_\odot) \sim 6-8$, with the thermal pulse lasting tens or hundreds of years, followed by an interpulse phase on the order of thousands or tens of thousands of years before the next thermal pulse. However, most of the additional energy is used in expanding layers above, and coupled with the quenching of the hydrogen burning shell means that although the surface luminosity changes significantly (up to ∼0.5 dex in $\log L_*/L_\odot$), it does not reflect the dramatic variations of the interior.

Third-Dredge-Up

The third dredge-up occurs after a thermal pulse, when the convective envelope briefly extends into regions which have previously undergone nuclear burning below the largely extinguished hydrogen burning shell, changing the chemical composition at the surface. This mechanism is responsible for several effects which give AGB stars added significance in a wider context, particularly when coupled with the high mass-loss rates which occur during this period. For instance, this is the process by which carbon stars are produced.

An overview of this effect can be seen in Fig. 1.2 showing the interior of a star during two thermal pulses, on different time-scales to the panel in between showing the interpulse phase, taken from Herwig (2005). After the thermal pulse, the base of the convective envelope dips into what was previously the hydrogen free core, mixing additional hydrogen down from the surface and nuclear-processed material to the surface. This results in a reduction of the H-free core size, which then increases again between thermal pulses. The third dredge-up efficiency, λ, is measured as the ratio between the decrease in core size, and the core growth since the previous thermal pulse, i.e.

$$\lambda = \frac{M_{\rm DU}}{M_{\rm growth}}. \tag{1.1}$$

Another outcome of this mechanism, is the creation of the ^{13}C pocket, as the convective envelope mixes additional hydrogen into the hydrogen burning shell. This is the source of the s-process nucleosynthesis, discussed in more detail in section 1.1.2

Hot-Bottom Burning

Additionally, higher mass AGB stars, M$\gtrsim 4M_\odot$, can undergo a process known as hot bottom burning (HBB), during which the base of the convective envelope extends further into the hydrogen burning shell than for low mass stars, meaning the base of the convective envelope reaches higher temperatures. These higher temperatures lead to the carbon, which is being dredged-up from the H-free core, being efficiently

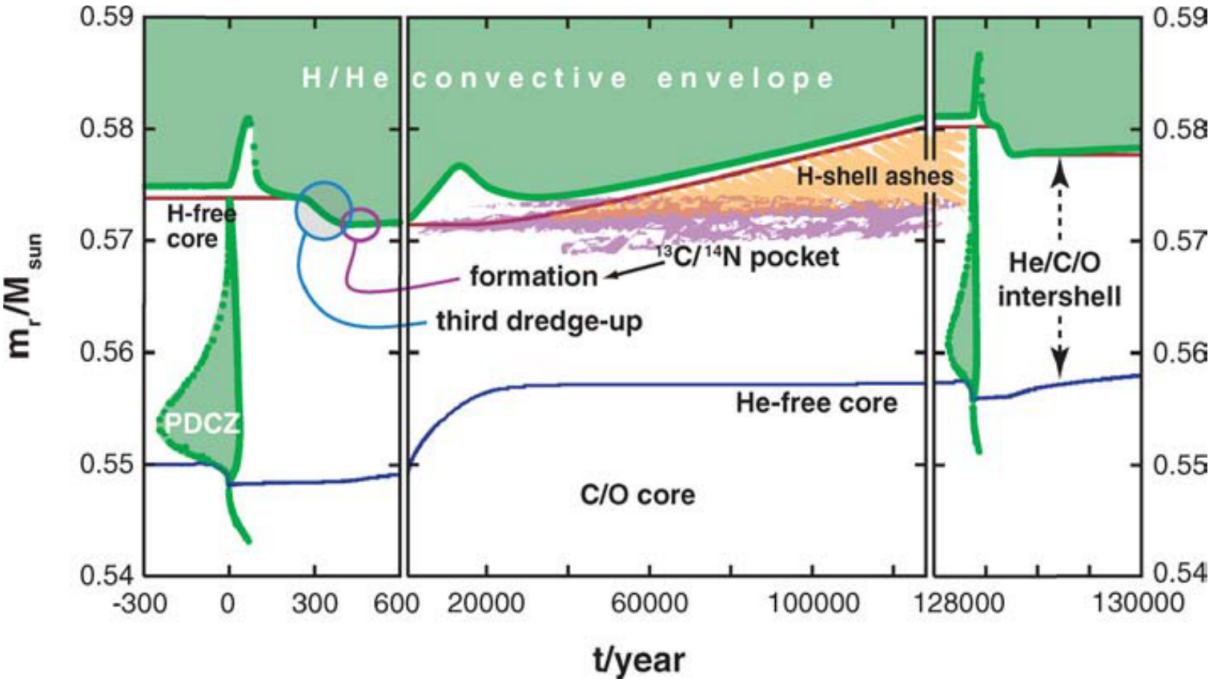

Figure 1.2: A depiction of the stellar interior during two thermal pulses and the interpulse phase in between, where each panel has a different time-scale, taken from Herwig (2005).

transformed into nitrogen. This gives characteristic chemical changes, which indicate HBB has taken place in a star, such that a reduced C/O ratio is observed, along with high N and He abundances and a reduction in the $^{12}C/^{13}C$ ratio.

These chemical changes mean that HBB can prevent or delay the formation of carbon stars (where the surface C/O>1), and can even cause a star which had previously become carbon rich to return to a state where C/O<1. Another effect is the increased luminosity caused by HBB, such that these stars can diverge from the core mass-luminosity relation which is used by synthetic evolution codes.

Mass Loss

To evolve into the central stars of planetary nebulae, AGB stars must expel the majority of their convective envelope, which is done during the TP-AGB phase with significantly increased mass loss, reaching rates as high as $\dot{M}_{\rm AGB} \sim -10^{-a} M_{\odot} {\rm yr}^{-1}$ where $a \sim 4...6$ (Wood et al., 1992). Since early attempts at incorporating so-called super-

wind prescriptions into evolutionary modelling (Vassiliadis & Wood, 1993; Bloecker, 1995), both theoretical models (Wachter et al., 2002) and observations (van Loon et al., 2005; Goldman et al., 2017) have tried to improve on the description and understand the differences between O- and C-rich stars. This is a hugely important aspect of TP-AGB modelling, as this determines when the phase ends, and the composition of material ejected into the interstellar medium. Without significant mass loss, these stars would instead undergo thousands of thermal pulses before exiting this phase of evolution.

The mechanism driving such strong mass loss is believed to be dust-driven winds (see Höfner, 2015, for a summary), which are helped by the stellar pulsations periodically raising material to lower surface gravities. The pulsation cycle mentioned here refers to general stellar pulsations, not thermal pulses, which occur on a much longer timescale. The mechanism behind these pulsations is believed to be the κ-mechanism, whereby ionisation is the source of the instability leading to pulsations (Cox, 1967). In a layer close to an ionisation temperature (in AGB stars, primarily believed to be hydrogen), if a non-ionised layer moves inwards, the temperature increases then the opacity also increases rather than decreasing as might otherwise be the case. Therefore, rather than allowing the excess heat to escape, the pressure builds as the layer moves inwards until the pressure is sufficient to raise the layer, lowering the temperature, beginning the pulsation cycle anew. In TP-AGB stars, these pulsation cycles are typically on the order of a few hundred days.

During the pulsation cycle, the star expands and contracts periodically, with the loosely bound atmosphere being elevated to a lower surface gravity and ejected some distance from the star. In many cases, this material will then fall back onto the surface of the star. However, due to the already low temperatures at the surface of AGB stars, material that is expelled to the condensation radius, R_{C}, is able to form dust. The formation of molecules and latterly dust is due to the low temperatures, though it must also be remembered that these stars are very luminous which helps to drive the higher opacity dust away from the star.

Dust-driven winds are believed to be the mechanism which results in such substantial mass loss on the TP-AGB, and also explains the high sensitivity of the mass loss prescriptions to the effective temperature. The densities and temperatures in these winds also provide an excellent site for the production of seed particles which help to form dust in the universe.

Nucleosynthesis

Related to the third dredge-up, is the formation of the ^{13}C pocket below the hydrogen burning shell, as a result of the mixing of additional hydrogen into the ^{12}C rich region by the convective envelope. This enables the ^{12}C(p,γ)^{13}N(β^+)^{13}C reaction, supplying the ^{13}C which is the main source of neutrons in AGB stars via the ^{13}C(α,n)^{16}O reaction. The other source of neutrons, the ^{22}Ne(α,n)^{25}Mg reaction is found at the bottom of the Pulse-Driven Convection Zone (PDCZ) during the thermal pulse, and produces a higher neutron density ($\log N_n \sim 9...11$ cm^{-3}) for a shorter time, on the scale of years (Herwig, 2005). This compares to the ^{13}C pocket, which sustains neutron densities of $\log N_n \sim 7$ cm^{-3} for a period of thousands of years.

Neutrons are required for the s-process, or slow neutron capture process, which is believed to be the source of almost all elements heavier than iron (Arlandini et al., 1999). Low-mass AGB stars are the location for the production of s-process elements within the range $90 < A < 204$, with other elements being produced in massive stars, by another mechanism.

1.1.3 Beyond the AGB

The inevitable result of the strong mass loss experienced by AGB stars is the reduction of mass in the envelope until it reaches the point where it can no longer sustain the current structure. There is now insufficient mass in the envelope to support a large and diffuse convective region, and therefore the envelope contracts. The two burning shells continue to be productive below the reduced envelope, such that the luminosity remains constant. Therefore, the reduction in size corresponds to an increase in temperature as the star shifts in the HR-diagram, while the ejected material surrounding this star begins to cool. This material can continue to be lit by the central star, creating a planetary nebula, and continues until nuclear burning can no longer be supported. This end of the nuclear burning lifetime of the star signifies the beginning of the white dwarf cooling track.

There are exceptions to this basic outlook for the end of an AGB star, for instance it is believed that a quarter of all post-AGB stars experience a very late thermal pulse (Herwig, 2005), where despite having moved to much higher temperature regions of the HR-diagram, the helium shell is still capable of another thermal pulse, moving the star briefly (∼200yr) back to the giant branch solutions. In this scenario, it is also believed that any hydrogen remaining above this shell may be consumed, leaving a severely hydrogen-depleted object.

Another question facing the end of the AGB life-cycle is the final fate of these objects, particularly around the boundary to massive stars. Fig. 1.3, taken from

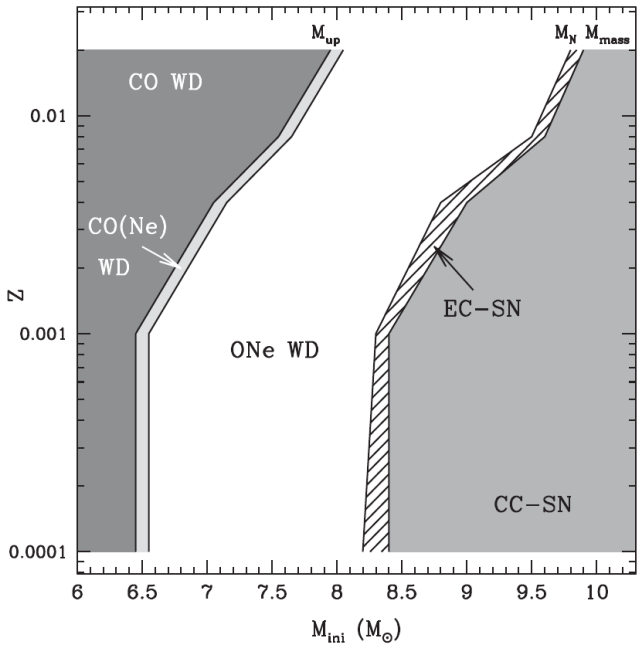

Figure 1.3: The final fates of super AGB stars, taken from Doherty et al. (2015).

Doherty et al. (2015), shows the outcomes for super-AGB calculations, indicating for different masses and metallicities which stars become carbon-oxygen white dwarfs (CO-WD), oxygen-neon white dwarfs (ONe-WD) and which would carry on to become core-collapse supernovae (CC-SN). Additional boundary cases, for potential candidates for electron capture supernovae (EC-SN), are also shown. The possibility that stars may also ignite carbon before carrying on to become ONe-WDs at this boundary has been suggested, although this is still an active field of study, as is also the case for the EC-SN, and it may be that neither is a true reflection of the boundary between AGB stars and CC-SN, but is included here to give some perspective on how it is theorised to look.

1.2 Modelling Stellar Evolution

Although modern computers allow for hydrodynamic simulations which can probe certain physical processes in ways which simply aren't possible in one-dimension, it simply isn't feasible to follow the evolution of a star in such a manner. To do so requires a stellar evolution code.

The stellar evolution code GARSTEC, as described in Weiss & Schlattl (2008) with AGB specific alterations outlined in Weiss & Ferguson (2009), was used for all calculations within this thesis. Calculations presented here are consistent with the physics described in the above papers, and all details of the applied physics can be found therein. However, it is nonetheless pertinent to review the fundamental aspects of stellar evolution codes generally and, in particular, those which are relevant to this work.

1.2.1 General

Following the general principles of stellar evolution codes, GARSTEC solves the one-dimensional equations of stellar structure in hydrostatic equilibrium. These equations are solved using the Heyney scheme (Henyey et al., 1964, 1965) which has been updated, along with many aspects of the original code created at the Max-Planck-Institut für Astrophysik in Garching by Kippenhahn et al. (1967), over the years to produce the modern code.

The equations of stellar structure, for a spherically symmetric star in hydrostatic equilibrium are as follows:

$$\text{Mass Conservation :} \qquad \frac{\partial r}{\partial m} = \frac{1}{4\pi r^2 \rho} \,, \tag{1.2}$$

$$\text{Hydrostatic Equilibrium :} \qquad \frac{\partial P}{\partial m} = -\frac{Gm}{4\pi r^4} \,, \tag{1.3}$$

$$\text{Energy Conservation :} \qquad \frac{\partial l}{\partial m} = \epsilon_n - \epsilon_\nu + \epsilon_g \,, \tag{1.4}$$

$$\text{Energy Transport :} \qquad \frac{\partial T}{\partial m} = -\frac{GmT}{4\pi r^4 P}\nabla \,. \tag{1.5}$$

These equations relate the radius, r; temperature, T; pressure, P; density, ρ and mass within a given spherical shell, m at all grid points. The equation for energy conservation, 1.4 relates the luminosity with the nuclear energy generation rate, ϵ_n; the gravothermal energy, ϵ_g and the energy lost through neutrinos, ϵ_ν. The expression for ∇ in the equation for energy transport, 1.5, is dependent on whether a region is convective or radiative with the former requiring some description of convection, and the latter being the radiative gradient(as discussed Kippenhahn et al., 2012, Ch. 5.2).

Taking the relative mass coordinate, $m \equiv M_r/M_*$, as the Lagrangian coordinate, a solution to the above equations is found using the aforementioned Heyney scheme

at each evolutionary timestep, for a grid typically numbering 1500-2000 mass shells, although this can significantly increase to several times that during particular phases such as a thermal pulse or the core He-flash. The evolutionary timestep is controlled through limits to the changes of the main structural variables ($P,\ T,\ r,\ L$) while the grid resolution can be also be changed depending on the variation of these variables. Additionally, the timestep can be limited by the accuracy of the solutions for the differential equations (Wagenhuber & Weiss, 1994).

Supplementing these structural equations are the set of equations denoted by

$$\frac{\partial X_i}{\partial t} = \frac{m_i}{\rho}\left(\sum_j r_{ji} - \sum_k r_{ik}\right) \ , \ i = 1, ...I, \tag{1.6}$$

which govern the chemical evolution. An equation is formed for the I isotopes considered, each with their own mass fraction X_i at a given grid point and mass m_i. Here r refers to reaction rates for an isotope i, with the equation taking into account those which produce an element (r_{ji}) and those which destroy it (r_{ik}). This time-dependent description for the nuclear burning is accounted for explicitly by integrating between two structure models given at different evolutionary timesteps, and are usually split into 10-20 separate nuclear timesteps, with the exact number determined by limits on the variations in mass fractions for any given step.

There are two separate nuclear networks in GARSTEC, which can be treated simultaneously when necessary, but otherwise the hydrogen burning network explicitly tracks the nuclei p, ^{3}He, ^{4}He, ^{12}C, ^{13}C, ^{14}N, ^{15}N, ^{16}O and ^{17}O while the helium burning network tracks p, n, ^{4}He, ^{12}C, ^{16}O, ^{20}Ne, ^{24}Mg, ^{28}Si and ^{56}Ni. Detailed information about the sources of specific nuclear reaction rates can be found within papers previously mentioned (Weiss & Schlattl, 2008; Weiss & Ferguson, 2009) and are not discussed further here. However, it should be noted that the ^{14}N(α,p)^{17}O reaction is not included and the nitrogen abundances in the code are therefore overestimated during helium burning.

Although different options are available within GARSTEC for the equation of state (EOS), this work uses the Irwin EOS[3] (Cassisi et al., 2003) based on that of Eggleton et al. (1973), calibrated to the OPAL EOS (Rogers et al., 1996). The Rosseland mean opacities are the same as outlined in Weiss & Ferguson (2009), where high-temperature OPAL96 tables (Iglesias & Rogers, 1996) are combined with low-temperature tables from Ferguson et al. (2005), and where a variable C/O value has been implemented for use on the TP-AGB. Additionally, for the purposes of this

[3] http://freeeos.sourceforge.net/

thesis, Plank mean opacities are now also included and discussed in further detail in Ch. 2.

The usual boundary conditions are applied at the centre of the star ($m = 0$, $r = 0$, $l = 0$), and the outer boundary condition is not discussed further here as it forms the basis of the investigation in chapter 2 and is discussed there in detail.

1.2.2 Mass Loss

Although not altered for this work, it is worth drawing attention to the mass loss prescriptions implemented on the TP-AGB, given their significant influence on the evolution and calculation results. These were updated for the thesis of Kitsikis (2008), as the more common prescriptions for including mass loss on the AGB previously (Vassiliadis & Wood, 1993; Bloecker, 1995) relied on the pulsation period of the star, with no dependence on the effective temperature which is expected to strongly influence the dust formation driving these large mass loss rates. For the case of O-rich stars, the prescription of van Loon et al. (2005)

$$\begin{aligned} \log \dot{M} = & - 5.65 + 1.05 \cdot \log \left(10^{-4} \frac{L}{L_{\odot}} \right) \\ & - 6.3 \cdot \log \left(\frac{T_{\rm eff}}{3500K} \right) \end{aligned} \tag{1.7}$$

and of Wachter et al. (2002) for C-rich stars

$$\begin{aligned} \log \dot{M} = & - 4.52 + 2.47 \cdot \log \left(10^{-4} \frac{L}{L_{\odot}} \right) \\ & - 6.81 \cdot \log \left(\frac{T_{\rm eff}}{2600K} \right) - 1.95 \cdot \log \left(\frac{M}{M_{\odot}} \right) \end{aligned} \tag{1.8}$$

is taken for the TP-AGB mass loss.

It is worth noting that although large uncertainties remain in mass loss prescriptions, or the $T_{\rm eff}$ which they refer to, a consistent picture emerges amongst all relations of this high $T_{\rm eff}$ dependence, typically $\dot{M} \propto T_{\rm eff}^{a}$, where $a = 6...7$. This has the potential to be significantly influenced by the outer boundary condition, which is itself closely connected to the $T_{\rm eff}$.

As implemented for this work, these relations only come into effect once a period of 400 days, determined according to Ostlie & Cox (1986).

$$\log(P_0/d) = -1.92 - 0.73 \log M + 1.86 \log R \tag{1.9}$$

When $P < 400$d, the mass loss reverts to a Reimers rate (Reimers, 1975) given by

$$\dot{M}_R = 4 \times 10^{-13} \frac{(L/L_\odot)(R/R_\odot)}{M/M_\odot} \eta_R \tag{1.10}$$

where the parameter η_R was introduced by Bloecker (1995) and takes a value of $\eta_R = 1$ for the moderate mass star considered in this thesis.

The cutoff period implemented is in fact intended for the O-rich case only, as the relation used there is derived from observations of such stars, however, it is also applied in the case of the C-stars.

1.2.3 Convection

It has already been mentioned that the equation of energy transport, 1.5, takes a different value depending on whether the region is radiative or convective. Within the convective regions, the standard mixing length theory (MLT) describes the behaviour, based on the formulation of Kippenhahn & Weigert (1990) with the free parameter, $\alpha_{\rm MLT}$, taking a value of $\alpha_{\rm MLT} = 1.75$ for models calculated here. This value of $\alpha_{\rm MLT}$ is taken from solar calibration and applied to all stages of evolution. Convective regions are defined by the Schwarzschild criterion (Schwarzschild, 1906) such that if the radiative gradient is less than the adiabatic gradient, i.e. $\nabla_{\rm rad} < \nabla_{\rm ad}$, for any grid point, then it is stable against convection. An alternative which can be used is to add an additional term to the adiabatic gradient to account for any compositional change, which typically makes the region more stable against convection and is known as the Ledoux criterion (Ledoux, 1958).

The treatment of convective boundaries is of particular interest for this thesis, and as such is discussed in more detail in Ch. 4, nonetheless a brief description is appropriate here; Traditionally referred to as overshooting, Convective Boundary Mixing (CBM) has become a more commonly used term to account for the uncertainty about the mechanism responsible for such mixing and to acknowledge that it may not, in all cases, be momentum-based overshooting. In GARSTEC, CBM is treated diffusively, according to the description of Freytag et al. (1996), where the diffusion constant at a distance z from the convective boundary is given by

$$D(z) = D_0 \exp\left(\frac{-2z}{f_{\rm CBM} H_{\rm P}}\right) \tag{1.11}$$

where D_0 is the value of the diffusion constant at the last convective grid point (given by the properties of MLT, such that $D_0 = v_{\rm MLT}\alpha_{\rm MLT}H_{\rm P}$), $H_{\rm P}$ the pressure scale height at the last convective grid point and $f_{\rm CBM}$ a free parameter, with a value $f_{\rm CBM}$

= 0.016, calibrated to match main sequence observations, taken unless otherwise stated. A cutoff value is taken such that when the calculated diffusion constant $D(z) < 10^{-20} D_0$ it is no longer applied. This is discussed further in Appendix B.3.1.

It should be noted that the subscript of this efficiency parameter is, at times, used interchangeably with more specific subscripts to denote the particular boundary at which it is applied. If not otherwise stated, $f_{\rm CBM}$ refers to all boundaries but may be replaced by $f_{\rm CE}$ for instance, to refer to CBM from the convective envelope only. The subscripts which may be used are defined in Appendix A.

1.2.4 Abundances

The composition clearly plays a significant role in stellar evolution as seen in the homology relations (as derived in Ch. 20 of Kippenhahn et al., 2012, for example) for the case of an ideal gas with constant opacity. This results in a main sequence luminosity which is strongly dependent on the chemical composition, such that $L \propto M^3 \mu^4$, where μ is the mean molecular weight. Additionally, there is the effect on the opacity which must be considered.

There are two methods for determining the solar-system element abundance distribution, by performing mass spectroscopy on meteorites (Lodders et al., 2009) or through photospheric abundance determinations of the sun (Asplund et al., 2009). Even the most pristine meteorites, which are believed to best represent the original composition of the solar system, are not representative of the most volatile elements, including the six most abundant and hence significant for stellar evolution (H, He, C, N, O, Ne). While photospheric determinations cannot achieve the same accuracy, not including the $\sim$10% change arising from diffusion and gravitational settling (Asplund et al., 2009), it is the only way of inferring the abundance of these important elements.

Focusing on the more recent solar-abundance determinations, which are to varying degrees used in stellar evolution models, there has been a general decline in the solar metal mass fraction, as derived from the solar models based on the measured Z/X. Beginning with the canonical value Z=0.02 (Anders & Grevesse, 1989) there was a gradual decrease to Z=0.018 (Grevesse & Noels, 1993) and then Z=0.017 (Grevesse & Sauval, 1998), all of which relied on line determinations from 1D model atmospheres. This trend became even stronger with the inclusion of NLTE (non local thermodynamic equilibrium) calculations and 3D hydrodynamic model atmospheres resulting in Z=0.012 (Asplund et al., 2005; Grevesse et al., 2007).

This created a new problem, namely that the sound speed and depth of the convective zone inferred from helioseismology were in good agreement with the older

solar abundances of Grevesse & Sauval (1998) but this was not the case when the new lower value from Asplund et al. (2005) was included (Basu & Antia, 2008). This could be compensated for by increased opacities but would require revisions up to 15% (Serenelli et al., 2009).

The tension has been at least partially alleviated by a reversal in the trend for a decreasing solar metallicity, with Asplund et al. (2009) suggesting a value of Z=0.014 and other calculations with different 3D model atmospheres also suggesting values lower than the more canonical value (Caffau et al., 2011, Z=0.015) but higher than Asplund et al. (2005). There certainly seems to be the suggestion to forget about the older values and rely instead on those of Asplund et al. (2009) as is discussed in Grevesse et al. (2013), however that is not to say that all stellar models do so and there is often a desire to choose a composition for other purposes.

In Part I of this thesis, the solar abundance distribution of Grevesse et al. (2007) was taken to match that of the MARCS grid, giving a metal mass fraction of Z=0.012 and Y=0.245, which is on the low side of solar metallicities. In Part II models were calculated with abundances from Grevesse & Noels (1993) at Z=0.02 and Y=0.28, as a more typical solar case and at Z=0.008 and Y=0.245 to be more representative of the LMC.

1.2.5 Synthetic Codes

The section has so far outlined the way in which stellar evolution codes are organised, with the ingredients necessary for following the evolution of a star up to the TP-AGB and beyond. Of course, this was done with a particular focus on GARSTEC, but the basic principles are the same for most stellar evolution codes, even if there are slight differences.

An alternative method for calculating such models is a synthetic code, where relations are derived from full evolutionary calculations to, for instance, parameterize the third dredge-up. These codes have a massive advantage in terms of speed, which allows for large grids to be computed quickly, also making calibration with observations more simple. There are, of course, disadvantages, such as only being able to probe parameter spaces where evolutionary calculations have already been performed, and sometimes struggle to capture all variations in the models.

Such codes have been specifically created for the TP-AGB (Izzard et al., 2004), or for binary star evolution (Izzard et al., 2006) while hybrid codes have been developed (Marigo et al., 1998, 2013), where the stellar structure equations are integrated for the envelope in order to better reproduce certain physical processes, but there are still certain fitting relations used. The hybrid nature allows for some shortcomings

of the previous codes to be addressed, such as the divergence of hot-bottom burning stars from a simple core-luminosity relation, while also being able to incorporate more physics that is included in stellar evolution models (such as on the fly equation of state and opacity calculations (Marigo et al., 2013)), while remaining orders of magnitude faster. Nevertheless, this all relies upon there being up-to-date, full evolutionary calculations.

The ability of synthetic and full stellar evolution codes to tackle the uncertainties in TP-AGB evolutionary calculations from a different perspective is an example of multiple approaches complimenting one another and is useful in gaining insights not possible in considering only one such method. However, it should not be forgotten that synthetic models rely on the relations derived from full evolutionary models and often implement relations which may have been derived from older evolution models (such as those of Wagenhuber & Groenewegen, 1998) even in the more modern synthetic codes (Marigo et al., 2013).

1.3 Observational Constraints

Producing models of TP-AGB stars is interesting in and of itself, however, the investigations carried out for the purpose of this thesis require some method of testing whether the results are reasonable or not. A few of the key observables as far as TP-AGB stars are concerned are briefly outlined here, in order to understand their benefits and their limitations.

However, first, a few general characteristics of AGB stars should be noted, in particular how they are distinguished and classified. Identifying an AGB star is not necessarily straightforward, given they can occupy a similar region of the HR-diagram as supergiants (which are rare, so can usually be discounted) or more generally RGB stars. Although, a common method for distinguishing TP-AGB stars is by excluding stars with a luminosity lower than the tip of the RGB, on the E-AGB it can be very difficult from traditional colour-magnitude diagrams (CMD), as can be seen in Fig. 1.4, and is only becoming reliable with the advent of asteroseismology. Indeed, Fig. 1.4 gives a good overview of the evolutionary phases up till the AGB, showing the stars in the globular cluster M3, and labeling the respective evolutionary phases, although with the difference that the RGB is labeled the FGB, or first giant branch given this is a star's first ascent into this region of the diagram.

As the stars in a cluster are believed to form at the same time, there is a place where the main sequence ends, which is known as the main sequence turnoff. This point can usually be well determined, given the large number of stars on the main sequence, and 1.4 is an excellent example of being able to see the point in the CMD

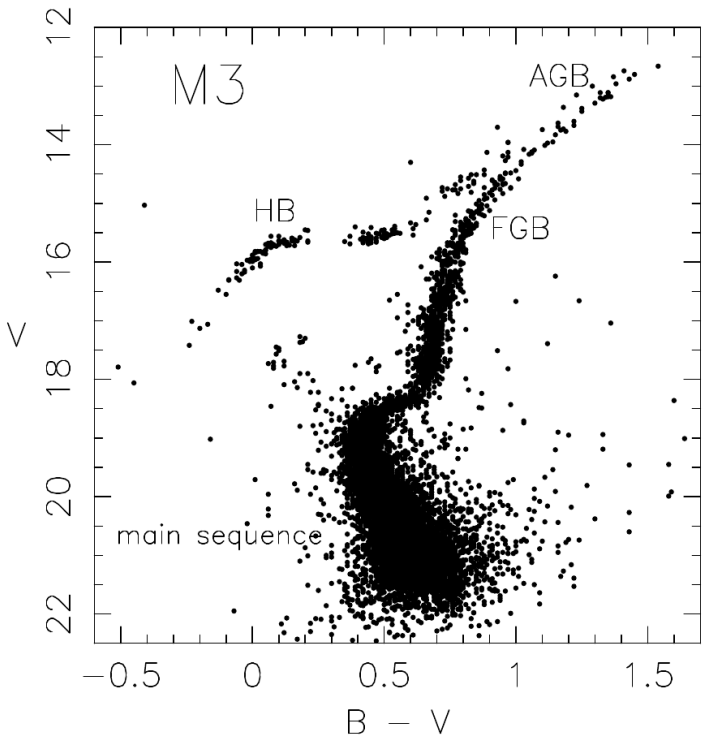

Figure 1.4: Colour-magnitude diagram of the globular cluster M3, taken from Karakas (2003), which in turn is based on data from Buonanno et al. (1994).

where the maximum magnitude of the main sequence is. By fitting stellar evolution isochrones, lines which connect the points at the same age for evolutionary tracks of different masses, it is possible to determine the age and distance of a cluster, based on the stars with the maximum mass which are still on the main sequence. Additional determinations of the distance help to reduce the degeneracy in those parameters, as alone this method would result in large uncertainties.

Changes in the surface abundances, due to the third dredge-up, is a fairly concrete way of identifying AGB stars. It is also believed that anomalous abundance patterns in non-AGB stars can be due to binary interactions with an AGB star, for instance, Carbon-Enhanced Metal-Poor (CEMP) stars, where an increase in s-process elements is observed. However, in general, when a star in the high luminosity, low-temperature region of the HR-diagram is observed to have a higher than expected carbon abundance, or indications of s-process enhancement, it is likely to be a TP-AGB star.

There are many historical classifications of giants which tend to depend on the carbon to oxygen ratio, where a value of C/O less than unity indicates a star is oxygen-rich and greater than one is carbon-rich. This is given as a ratio of the number abundances rather than mass fractions as the critical value of unity is related to the formation of the CO molecule, with almost all atoms of the less abundant element locked into this molecule in the atmosphere of cool stars.

The most basic distinction classifies oxygen-rich stars as M-stars, named after Mira variable star, or C-stars for carbon-rich stars. There is a general progression in classification from M $\rightarrow$ MS $\rightarrow$ S $\rightarrow$ SC $\rightarrow$ C with increasing C/O value, where S-stars have a value close to unity (Abia et al., 2003). More historical classifications which are less used include N and R type stars (Knapp et al., 2001), where the N-type stars are essentially the same as C-stars and R-stars aren't on the AGB at all but are rather core helium burning stars.

1.3.1 Initial-Final Mass Relation

The Initial-Final Mass Relation (IFMR) is a semi-empirically derived relation, which attempts to connect the final mass of a star to its ZAMS mass. This is done through the observations of white dwarfs, typically within open clusters and connecting their mass to isochrone fits of the open cluster to determine the initial mass of the star. This is combined with the cooling time of the white dwarf, to account for the time since it has ended its nuclear burning life and its mass as determined spectroscopically.

There are, of course, drawbacks of this method, with stellar models also required as an input in determining the relation which it is hoped will constrain the models themselves. However, it is primarily the TP-AGB phase of stellar models this relation is used to constrain, which should not significantly influence the derived relation. The reason it is so useful in constraining the TP-AGB evolution is that the white dwarf is the remainder of the stellar core and so directly connects to the potential core growth and the loss of the envelope during the TP-AGB phase.

1.3.2 Post-AGB Stars

After the star has left the TP-AGB, it is expected to have lost most, if not all, of its outer envelope. This exposes what was previously the interior of the star, and in particular what is believed to be the remains of the intershell region which existed between the hydrogen and helium burning shells. In particular, it is believed that two classes of observed objects can, therefore, provide unique insight into the

composition of the intershell region at the final thermal pulse, namely central stars of planetary nebulae and PG 1159 stars. This insight into the composition of the intershell region in turn gives a particular constraint on any additional mixing from the PDCZ, as is discussed in Herwig (2000).

There are some observations of the central stars of planetary nebulae (Koesterke & Hamann, 1997), which suggest that the surface abundances comprise approximately 30% carbon and 15% oxygen. Furthermore, there is the class of objects known as PG 1159 stars, which are believed to be in the phase between being the central stars of planetary nebulae and on the way to becoming white dwarfs. Such objects also show high surface values of carbon and oxygen (Dreizler & Heber, 1998), with ratios suggested to be C/He $\sim$ 0.1-0.3 and O/He $\sim$ 0.01-0.3 with the list of such objects increasing, this trend appears to continue with Werner & Herwig (2006) showing most objects to have ratios in the range C/He $\sim$ 0.15-1.5 and O/He $\sim$ 0.1-0.5.

These notably high abundances, particularly of oxygen, cannot be reproduced for the intershell region by stellar models which contain no additional mixing beyond the formal convective boundary at the base of the PDCZ. As such, these observations provide a useful constraint for this boundary, as it does not appear possible to create a scenario by which they can be explained through other means.

1.3.3 Magellanic Clouds

Trying to find populations for the testing of TP-AGB models can prove difficult, and the obvious choice tends to be the Magellanic Clouds or, more specifically, open clusters contained within them. The distances and metallicities are reasonably well constrained and there are appreciable numbers of both oxygen and carbon-rich AGB stars. Drawing on previous observations (Frogel et al., 1990), Girardi & Marigo (2007) set about compiling this information for clusters in both the Large and Small Magellanic Clouds (LMC and SMC). The number counts of such stars, when combined with the turnoff masses associated with each cluster provides perhaps one of the best laboratories available for the study of TP-AGB stars. Girardi & Marigo (2007) used this information to derive the C-star and M-star lifetimes by combining the number counts with the integrated V-band Luminosity, L_V, but this also makes use of isochrones for the TP-AGB in deriving the lifetimes.

In Girardi & Marigo (2007), the data for the clusters were binned according to the turnoff mass M_{TO}, as it was considered the statistics from single clusters were too insignificant to be dealt with alone. This still results in quite low numbers within many of the bins, as can be seen in their Table 2, however, this still represents a good sample of such stars.

1.4 Structure of the Thesis

This thesis concentrates on understanding and improving the treatment of TP-AGB stars by stellar evolution codes and is split into two primary investigations. The first of these is an investigation of the outer boundary condition in stellar evolution codes in Part I, while Part II explores the influence of additional mixing beyond the various convective boundaries, prior to and during the TP-AGB.

The motivation behind the investigation carried out in Part I of this thesis was the lack of justification on the TP-AGB for the assumptions typically used in determining the outer boundary condition. The first of these being the plane-parallel nature of the atmosphere, which may be considered valid on the main sequence but is clearly not justified when considering the large diffuse atmospheres of AGB stars. The second being the mean opacity treatment, with the Rosseland mean opacities not being strictly valid in the outermost layers of a star, due to the requirement for the diffusion approximation to be satisfied in the derivation.

Chapter 2 focuses on exploring the importance of these conditions and tries to understand their significance for TP-AGB models. While Ch. 3 investigates a new phenomenon in TP-AGB models which was discovered during the investigation of the outer boundary condition. The anomalous behaviour observed is the suppression and resumption of the thermal pulses due to a low core mass, which can lead to drastically different observable quantities.

Part II focuses on the treatment of mixing at convective boundaries, with an additional introduction to the topic presented in Ch. 4. This was in part motivated by the anomalous behaviour observed in Part I and comparing the results of the investigation with the IFMR, suggesting that the CBM implemented was too strong resulting in decreasing core masses when they are expected to grow on the TP-AGB (Kalirai et al., 2014). Additionally, there appeared to be a good argument that perhaps the mixing at different convective boundaries should not be the same in all cases and as such it was implemented in GARSTEC that these could be treated separately.

There were multiple approaches taken to investigating the mixing at different boundaries, with Ch. 5 focusing on the more technical investigations, such as estimating the maximum distance for momentum-based overshooting and what could be called numerical experiments where the mixing parameter is varied for a single thermal pulse. There was also a desire to probe the effect of CBM during earlier evolutionary phases, as not all TP-AGB models produced include mixing at the boundary of the convective core (Karakas & Lattanzio, 2007; Cristallo et al., 2009). Therefore, full evolutionary models were calculated to probe the influence CBM dur-

ing core burning, along with some initial testing of the boundaries during the TP-AGB. This was done to determine the effect on two main processes of the TP-AGB evolution, namely the third dredge-up and hot-bottom burning and whether CBM during pre-AGB phases alter the masses at which they become important with the results presented in Ch. 6. Finally, Ch. 7 tries to constrain the mixing at the base of the PDCZ and convective envelope by comparing full evolutionary calculations with observational data.

Furthermore, some additional material has been included as appendices, with Appendix A listing some acronyms and model labels used throughout the thesis. Appendix B focuses on several technical aspects related to the stellar evolution code or other things discussed in the thesis. While Appendix C provides some additional physical information about the models, including tables which give an overview of the properties of every evolutionary model calculated for this thesis.

Part I

Atmospheric Boundary Condition

Chapter 2

Atmospheric Boundary Condition

This chapter focuses on the outer boundary condition, or atmosphere, required for stellar evolution codes and its influence on the TP-AGB. The separate atmospheric treatment is a necessity arising from the different physics which governs the outer layers of the star compared to the interior part of the code (as discussed in Ch. 1) and may have particular importance for the TP-AGB evolution, given the close connection to the effective temperature and, hence, the mass loss.

The work presented within this chapter, along with the following chapter, has been submitted in paper form on the 3^{rd} of November 2017 to the journal Monthly Notices of the Royal Astronomical Society and is largely consistent with that work. There are of course certain changes which have been made for this chapter, particularly the inclusion of some additional figures (Fig. 2.1, 2.2, 2.3, Fig. 2.5 and Fig. 2.10), which help to further explain some technical details.

To begin with, the following section, Sec. 2.1, introduces the background and motivation behind the work within this chapter, followed by Sec 2.2 which outlines the theoretical framework of the atmospheric calculation with respect to the stellar evolution code. Sec. 2.3 discusses the calculations performed during the investigation, and the reasoning behind any choices made. The primary results are then considered in Sec. 2.4 before being discussed more broadly along with future work in Sec. 2.5.

2.1 Background

The outer boundary condition in stellar evolution codes is a necessity arising from the numerical and physical difficulties which one would encounter if trying to integrate directly from a naive $P = 0$ point outside of the star, right through to the centre.

Current implementations of the stellar atmosphere typically derive boundary conditions for the interior model from either grey plane-parallel atmospheres or scaled solar atmospheres, neither of which can be considered to have appropriate underlying assumptions for the TP-AGB. The complex interaction of processes, such as the third dredge up and mass loss, governing the TP-AGB can be affected by varying the treatment of this boundary condition. Work has been done to investigate the effect of changing this treatment (VandenBerg et al., 2008) however, this typically concentrates on earlier evolutionary phases, such as the main sequence or possibly the red giant branch.

AGB models have been produced for a variety of reasons, all with the common goal of understanding this crucial phase of stellar evolution. Some tend to focus on the nucleosynthesis (Karakas & Lattanzio, 2007; Cristallo et al., 2009, 2011) while synthetic codes avoid full model calculations and are more suitable for population synthesis (e.g. Marigo et al., 2013). All calculations tend to rely on similar methods of treating the outer boundary, although the TP-AGB is a phase in which the typical underlying assumptions are likely to break down. This could potentially play a role in the evolution which is not as readily expected to manifest itself during the main sequence evolution.

Indeed, it is possible to show through approximate analytic solutions (see Kippenhahn et al., 2012, Ch. 11.3.3) that for stars with a radiative envelope, the interior solution rapidly converges to the same solution almost independent of the boundary condition provided. However, based on the same simplifying assumptions, it can be shown that for stars with a convective envelope, changes in the outer boundary influence the interior solution to a larger extent, in particular for very super-adiabatic convective envelopes.

In order to determine whether this is the case, this work investigates the effect of altering the treatment of the stellar atmosphere and aims to tackle the underlying assumptions in turn. The first of these is the geometry of the atmosphere, where the typical analytic relation for a plane-parallel geometry (Eddington, 1959, p320) is replaced by an analogous relation for a spherically symmetric atmosphere (Lucy, 1976).

Another assumption is the mean opacity treatment, where Rosseland mean opacities are taken in the atmospheric calculation as well as for the interior. However, the Rosseland mean opacity is derived under the diffusion approximation, which is not strictly valid in the diffuse outer layers. This assumption is tested through the use of Planck mean opacities.

Finally, interpolation in grids of MARCS (Gustafsson et al., 2008) or COMARCS (Aringer et al., 2009) model atmospheres allows for an exploration of a far more

physically motivated atmospheric boundary condition and also allows the depth at which the atmosphere is attached to be tested, as it is also questionable whether the diffusion approximation is satisfied at $\tau = 2/3$ where the interior model typically begins.

2.2 Atmospheric Treatments

2.2.1 Grey Plane Parallel Atmosphere

The use of plane-parallel grey atmospheres in Local Thermodynamic Equilibrium (LTE), as first outlined by Eddington (1959, p320), is widespread in the stellar evolution community. It allows for a quick and reliable method of generating a boundary condition unique to a star's position within the HR diagram, based on particular simplifications.

The geometric simplification involves considering certain parameters (radius, luminosity, interior mass) to be constant throughout the atmosphere, which allows the equation of hydrostatic equilibrium to be combined with the definition of optical depth ($d\tau/dr = \kappa\rho$) to obtain

$$\frac{d\tau}{dP} = g\kappa(T, P) \tag{2.1}$$

with the surface gravity $g = GM/R^2$ for constant stellar mass, M, and radius, R.

The temperature stratification is then taken from the derivation by Eddington under the assumptions of a plane-parallel, grey atmosphere such that

$$T^4 = \frac{3}{4}T_{\rm eff}^4\left[\tau + \frac{2}{3}\right] \tag{2.2}$$

in the range $\tau = [0, 2/3]$. However, this can be generalised by replacing the factor $2/3$ in the brackets with the Hopf function $q(\tau)$, which allows scaled solar relations to be implemented such as that of Krishna Swamy (1966).

Equation 2.1 is integrated from $\tau = 0$, with $P(\tau = 0) = 0$, to $\tau = 2/3$ using a Adams-Bashford/Adams-Moulton predictor/corrector method to obtain the pressure at the outermost point of the interior model, along with the derivatives of the pressure with respect to the luminosity and effective temperature. In conjunction with the Stefan-Boltzmann law ($L = 4\pi R^2\sigma T_{\rm eff}^4$), this provides the outer boundary conditions for the stellar evolution code.

2.2.2 Spherical Geometry

The assumption that the stellar atmosphere can be approximated as plane-parallel may be valid on the Main Sequence, it is, however, hard to justify on the RGB and AGB where the atmospheric extent is expected to be a significant proportion of the stellar radius. In order to investigate this assumption a spherical grey atmosphere, as outlined in Lucy (1976), was implemented.

Within this framework, the effective temperature is taken analogously with the Eddington solution, i.e. $T_{\rm eff} = T_*$ at $\tau = 2/3$, where T_* is referred to as the photospheric temperature to acknowledge the lack of a unique definition of $T_{\rm eff}$ in an extended atmosphere. This approach has the advantage of reducing to the Eddington plane-parallel atmosphere already implemented within GARSTEC when the geometric extent of the atmosphere is negligible. This results in a consistent definition and implementation of $T_{\rm eff}$, allowing the influence due to geometry to be isolated.

The temperature stratification is given by

$$T^4 = \frac{1}{2}T_*^4[2W + \frac{2}{3}\tau] \tag{2.3}$$

where W is the geometric dilution factor $W = \frac{1}{2}\{1 - \sqrt{[1-(R/r)^2]}\}$ and the optical depth is defined by

$$\frac{d\tau}{dr} = -\kappa r \left(\frac{R}{r}\right)^2 \tag{2.4}$$

In order to implement the spherical approximation, equation 2.4 is integrated along with the equation of hydrostatic equilibrium and making use of the equation of state. This is done using the same method as in the plane parallel case. This is outlined in Fig. 2.1, which illustrates the way in which the module for calculating the spherically symmetric grey atmospheres interacts with the interior part of the stellar evolution code, as well as giving an overview of the method by which the atmosphere is obtained.

Estimated values for T and L are provided by the interior code at the outermost grid point, corresponding to $\tau = 2/3$, which are combined with the Stefan-Boltzmann law to calculate a radius. As the sphericity is accounted for in the atmospheric calculation, an outer radius R_0, defined at $\tau = 0$, is required. This is not known prior to the integration of the atmospheric equations, therefore it is necessary to take an initial estimate for the outer radius (based on testing for the first model, and on the previous outer radius for all subsequent evolutionary models). The atmospheric integration is performed (using EOS and opacity information, along with the temperature stratification given by Eq. 2.3), stopping when the expected radius at the

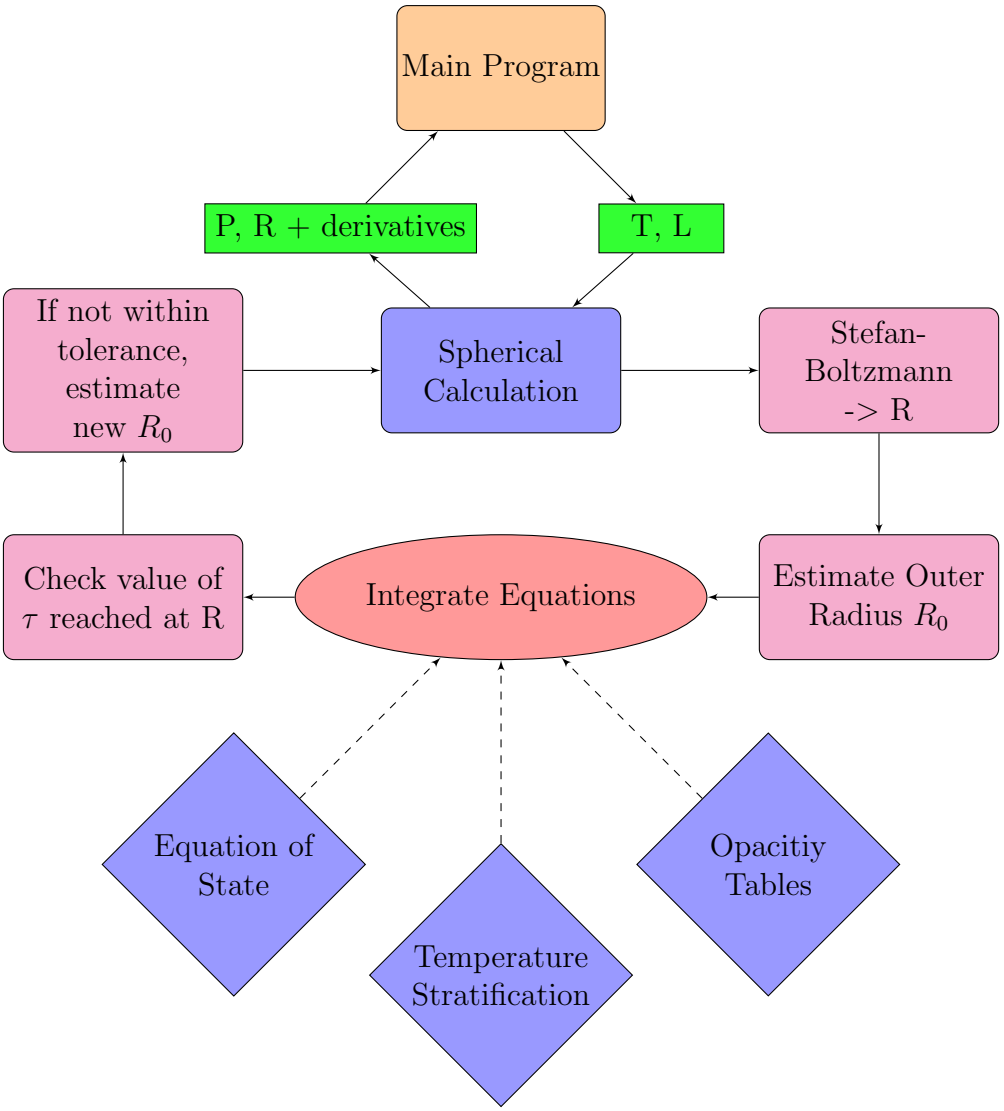

Figure 2.1: A diagram illustrating the process by which the spherically symmetric, grey atmospheres provide an outer boundary condiiton for the interior evolution code.

base of the atmosphere is reached. Here, the optical depth reached at the end of the integration is checked to see whether $\tau = 2/3$ as it should. If this is not the case, a new estimate of R_0 is produced and the procedure is repeated.

2.2.3 Opacities

To avoid time consuming and complicated radiative transfer calculations some definition of a frequency independent, or grey, opacity is required. Under the assumption of Local Thermodynamic Equilibrium (LTE) and the Diffusion Approximation (DA), which are strictly valid only in the stellar interior, it is possible to derive the Rosseland Mean (RM) opacity (Rosseland, 1924), denoted by κ_{R} and related to the Planck function B_ν by the equation

$$\frac{1}{\kappa_{\mathrm{R}}(\rho,T)} = \frac{\int_0^\infty \frac{1}{\kappa(\nu)}\frac{\partial B_\nu}{\partial r}d\nu}{\int_0^\infty \frac{\partial B_\nu}{\partial T}d\nu} \tag{2.5}$$

at a particular density, ρ, and temperature, T, for a given chemical composition which results in the frequency dependent opacity $\kappa(\nu)$. This is the standard treatment for opacities in the atmospheric calculations in stellar evolution codes.

The typical optical depth taken to be the surface of a star, $\tau = 2/3$, corresponds to the depth from which photons experience on average less than a single scattering before escaping the star. This would, therefore, be the first point at which it could, with at least some justification, be claimed that the local conditions satisfy the DA, although in reality, it is likely to be even deeper, perhaps at $\tau = 10$ although it is difficult to say exactly.

As such, in the outer layers of a star, the DA, which is a necessary condition for the RM opacity, breaks down as the mean free path is no longer much smaller than the depth. Therefore, an alternative is desirable. Unfortunately, there is no analytically derived mean opacity for the optically thin stellar atmosphere, though one possibility is to use a straight average, or the Planck mean (PM) as outlined in Eddington (1922), such that

$$\kappa_{\mathrm{P}}(\rho,T) = \frac{\int_0^\infty \kappa(\nu)B_\nu d\nu}{\int_0^\infty B_\nu d\nu} \tag{2.6}$$

which may better represent the high line opacities in a diffuse region.

Tables of the PM molecular opacities at low temperatures were produced (Ferguson 2014, priv. comm.) with the program described in Ferguson et al. (2005) and are equivalent to those produced in the same manner as for the RM opacities. These tables are combined with OPAL-tables (Iglesias & Rogers, 1996) for high-temperature opacities in the same way as has previously been done for the RM, low-temperature tables as described in Weiss & Ferguson (2009).

The RM tends to favour opacity intervals in the spectrum, which allow the majority of the radiation flux to pass through at frequencies of least resistance. This is

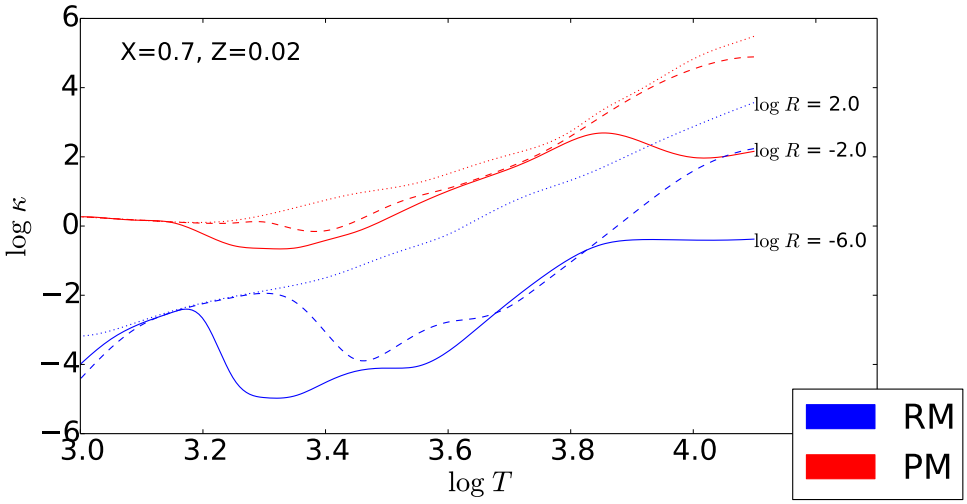

Figure 2.2: Rosseland Mean (blue) and Planck Mean (red) opacities as a function of temperature for a hydrogen mass fraction of X=0.7, and metal mass fraction Z=0.02. Each linestyle represents a different value of log R (for definition, see text), as indicated for the RM cases.

likely to result in a systematic undersampling of the actual mean opacity in a stellar atmosphere. On the other hand, as the PM opacities are a straight average, the high (but spectrally narrow) line and molecular opacities which become particularly important in the outer layers of AGB stars can be expected to artificially raise the average opacity.

Given the expectation that one treatment undersamples the opacity, while the other oversamples it, the two should result in an upper and lower bound for what is possible in the context of a grey atmospheric treatment.

Fig. 2.2 shows the Rosseland Mean (blue) and Planck Mean (red) opacities as a function of temperature for a hydrogen mass fraction of X=0.7, and metal mass fraction Z=0.02, to illustrate the differences between the two sets used within this chapter. Each linestyle represents a different value of log R, as indicated in the figure for the RM cases, where the solid line is log R=-6, the dashed line log R=-2 and the dotted line log R=2. The usual meaning of R in the context of opacities is taken, such that

$$R = \frac{\rho}{T_6^3} \tag{2.7}$$

with the density, ρ, having units $[g\ cm^{-3}]$ and the temperature $T_6 \equiv T/[10^6]$ and

units [K].

It is notable that in all cases, the Rosseland mean values are much lower than the Planck mean, but also that there appears to be much less variation in the Planck mean across different temperatures and log R. The exception being the Rosseland mean case for log R=2, where it more closely resembles the form of the Planck mean cases and is also closer in absolute value. This seems to suggest that the Planck mean is far less sensitive to local conditions than the Rosseland mean is.

As for implementation, it is well-accepted (Hubeny & Mihalas, 2014, p376) that the RM opacity is suitable for stellar evolution models within the interior, where the diffusion approximation holds. If we also take this to be true, at least predominantly, at $\tau = \frac{2}{3}$, then it is desirable to recover the limit of the RM at the lower boundary of the atmospheric calculation.

Conversely, at $\tau = 0$, the justification for using the RM is at its weakest, lines are expected to have a greater influence on the opacities and as such this is where the PM is, if not reasonable, at least worth considering as an extreme case to determine if the use of RM opacities in unjustified regions is having a substantial influence on the atmospheric treatments, and subsequently the stellar evolution models.

Given this reasoning, the following method for the opacity treatment within both the plane-parallel and spherically-symmetric atmospheric calculations was implemented in GARSTEC. A transition for the opacity as a function of the optical depth in the range $\tau = [0, 2/3]$ is applied as follows

$$\ln(\kappa(\tau)) = \ln(\kappa_{\mathrm{P}}(\tau)) + (\ln(\kappa_{\mathrm{R}}(\tau)) - \ln(\kappa_{\mathrm{P}}(\tau))) * \left(\frac{\tau}{2/3}\right) \tag{2.8}$$

This function allows for the smooth change between the two mean opacity treatments and is implemented as it provides the desired treatment of PM at $\tau = 0$ and RM at $\tau = 2/3$ while providing at least a reasonable agreement with the models calculated using the COMARCS radiative transfer atmospheres, as is discussed further in Sec. 2.4.1.

Suffice it to say, however, that a grey atmosphere, with any mean opacity, will not be able to reproduce the detail of full radiative transfer calculations, although changing the mean opacity which is used should allow for something to be said about the range of results which are obtainable when using the typical grey atmospheric methods.

C/O ratio

The C/O ratio is known to be hugely important in contributing to the opacities in the low-temperature regimes experienced in the outer layers of AGB stars (Marigo,

2002; Marigo & Aringer, 2009). There can be drastic changes due to the molecular lines which can form, with the underlying O-rich or C-rich abundance entirely dominating given the CO molecule has a high binding energy and freezes out, leaving the respective excess to govern additional molecule formation.

The dependence on the C/O ratio is investigated here, based on the implementation discussed in Weiss & Ferguson (2009). The RM opacities are taken from interpolation within the usual values at different C/O values, with an additional interpolation performed to reach the desired C/O value. This is done for all regions above the H-burning shell, including the atmospheric calculation, for the following values of C/O: 0.48 (solar), 0.9, 1.0, 1.1, 3.0 and 20. The PM opacities are implemented in a similar manner and are equivalent to the low temperature RM tables as described in Weiss & Ferguson (2009).

Fig. 2.3 shows a comparison of both the RM (blue) and PM (red) opacities for different C/O ratios, with each panel showing a different log R and metallicity combination. Although it is clearly seen in the case of the RM opacities that there is a significant variation with the changing C/O value, the PM case is far more consistent in all cases. This is likely to signify that the lines dominating the generated PM values are coming from line opacities which are not governed by the molecular opacities changing with the varying C/O at low temperatures and as such only the solar value PM case is considered further.

2.2.4 Radiative Transfer

The previously mentioned cases are intended as a step to determine if the exterior boundary condition of stellar models influences the evolution of AGB stars, and which also allow particular assumptions to be investigated. However, in the case that this outer boundary condition alters the evolutionary behaviour it is clear that a numerical solution to the equations of radiative transfer would be preferable as a way of providing a better description of the underlying physics, as the above assumptions become redundant.

In order to investigate the effect of using full radiative transfer models, a grid of atmospheres was implemented. The atmospheric models used are the MARCS grid (Gustafsson et al., 2008) and for the low surface gravity regions, the COMARCS grid (Aringer et al., 2009, 2016). The grids are generally labelled by the parameters ($T_{\rm eff}$, log g, [Fe/H]) with an additional mass parameter in the spherical models. All COMARCS models are spherical, while for MARCS plane parallel models are used when log g>3 and spherical otherwise. The COMARCS models also include C/O as a parameter (in the range C/O=[0.275,10]), however only models with a solar value

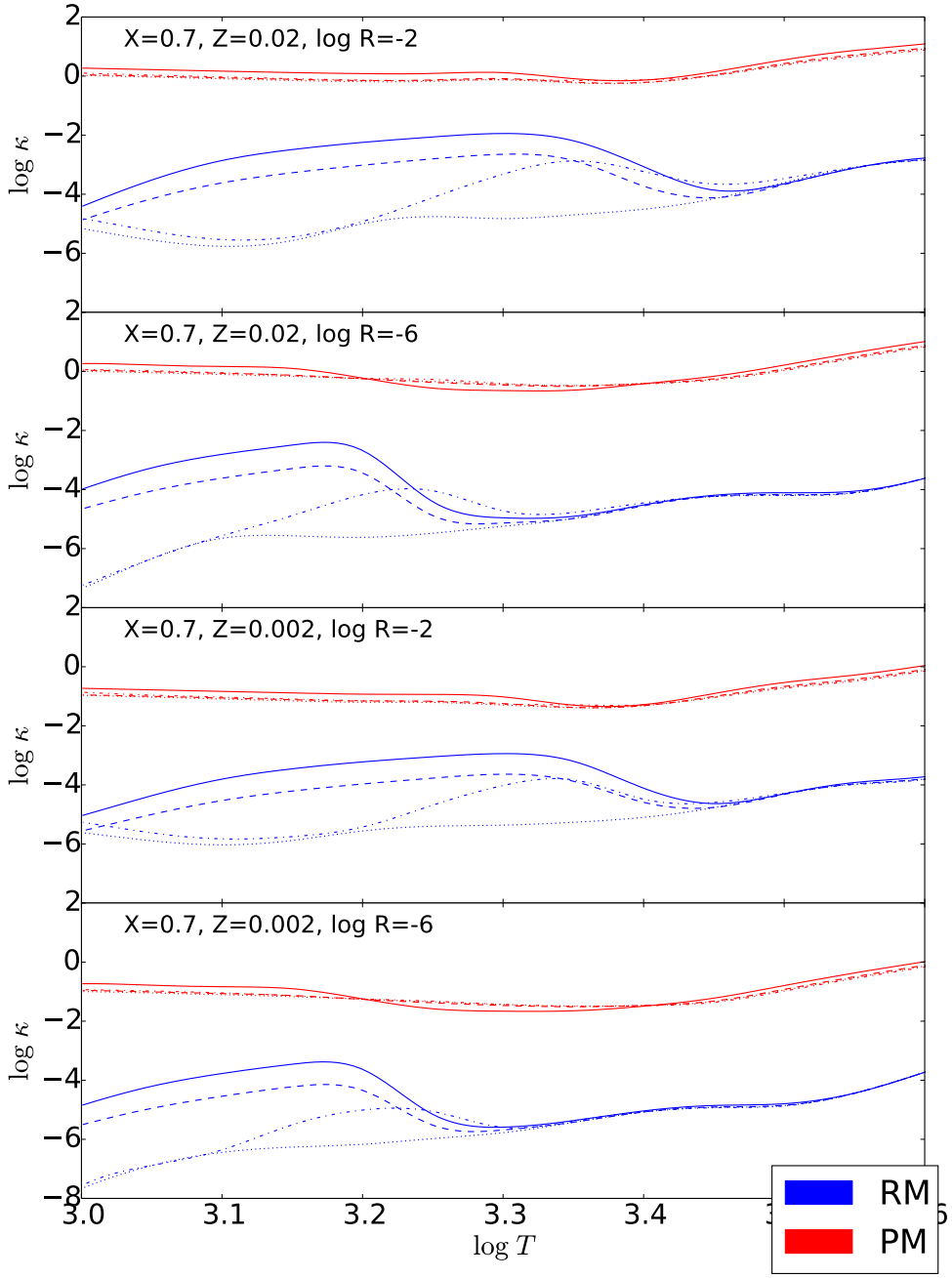

Figure 2.3: Rosseland Mean (blue) and Planck Mean (red) opacities as a function of temperature for a hydrogen mass fraction of X=0.7, and metal mass fraction Z=0.02 and log R=-2. Each linestyle represents a different value of C/O, with C/O=0.48, solid line; C/O=0.9, dashed line; C/O=1, dotted line and C/O=1.1, dot-dashed line.

of the ratio (C/O = 0.55) were used in evolutionary calculations due to a limited grid being available at other C/O values, with a reduced density in both $T_{\rm eff}$ and log g. As such, the COMARCS grid is analogous to the MARCS models in terms of parameter labels ($T_{\rm eff}$, log g, [Fe/H]).

For lower surface gravities, spherically-symmetric models are produced instead of plane-parallel models, for both MARCS and COMARCS grids, as the geometric extent of the more diffuse atmospheres becomes relevant. This results in an additional mass parameter, the dependence on which was investigated. However, the effect on the structural atmospheric quantities is minimal based on changes in the mass, whether plane-parallel models or spherical models with masses ranging from $0.5 - 5M_{\odot}$, with the dependency on log g being far more important. To illustrate this, Fig. 2.4 shows the percentage change in the gas pressure at $\tau = 1$ (where the atomspheres are attached to the interior model), compared to the value for a $1M_{\odot}$ model for different MARCS atmospheres. Each panel represents the respective difference between the models at a given log g (log g=[0,1,2,3,3.5]), across a range of temperatures. The blue line represents models with a mass of $2M_{\odot}$, the green models with $0.5M_{\odot}$ while the red shows the plane-parallel models. As the plane-parallel models are only available at the higher log g values (3, 3.5) they are only shown in the lower two panels, while there are no models for $0.5M_{\odot}$ or $2M_{\odot}$ at log g=3.5.

Clearly, in all cases, differences are limited to below 1%, so it appears that the structural effect from the mass is not particularly significant. What differences do exist, are larger for the plane-parallel models than the differences which arise from changing the mass, at least at comparable stellar parameters. It should, of course, be noted that this is at the highest log g value (log g=3) available for the non-solar mass models, which is when any effect arising from mass is expected to be a minimum, and the model should be close to the plane-parallel case. Of more relevance for this work, is the noticeable increase in the disparity for models in the low log g, low $T_{\rm eff}$ region, as can be seen in the top two panels of Fig. 2.4. Furthermore, the fact that the change from the $1M_{\odot}$ model to the 0.5 and $2M_{\odot}$ models appear to always be in the opposite direction, would suggest that in principle it should be possible to interpolate the atmospheric properties within an additional mass parameter. However, as the grids of atmospheric models are, in both the MARCS and COMARCS cases, too sparse for any mass other than $1M_{\odot}$, the boundary conditions provided by integration in the $1M_{\odot}$ grid are used for all stellar models, with no explicit mass dependency (although this of course still enters into the log g parameter).

The boundary condition is implemented by interpolation of the required structural values (pressure and temperature) within the grid parameters. This is typically only done at the optical depth required for fitting to the interior model, however,

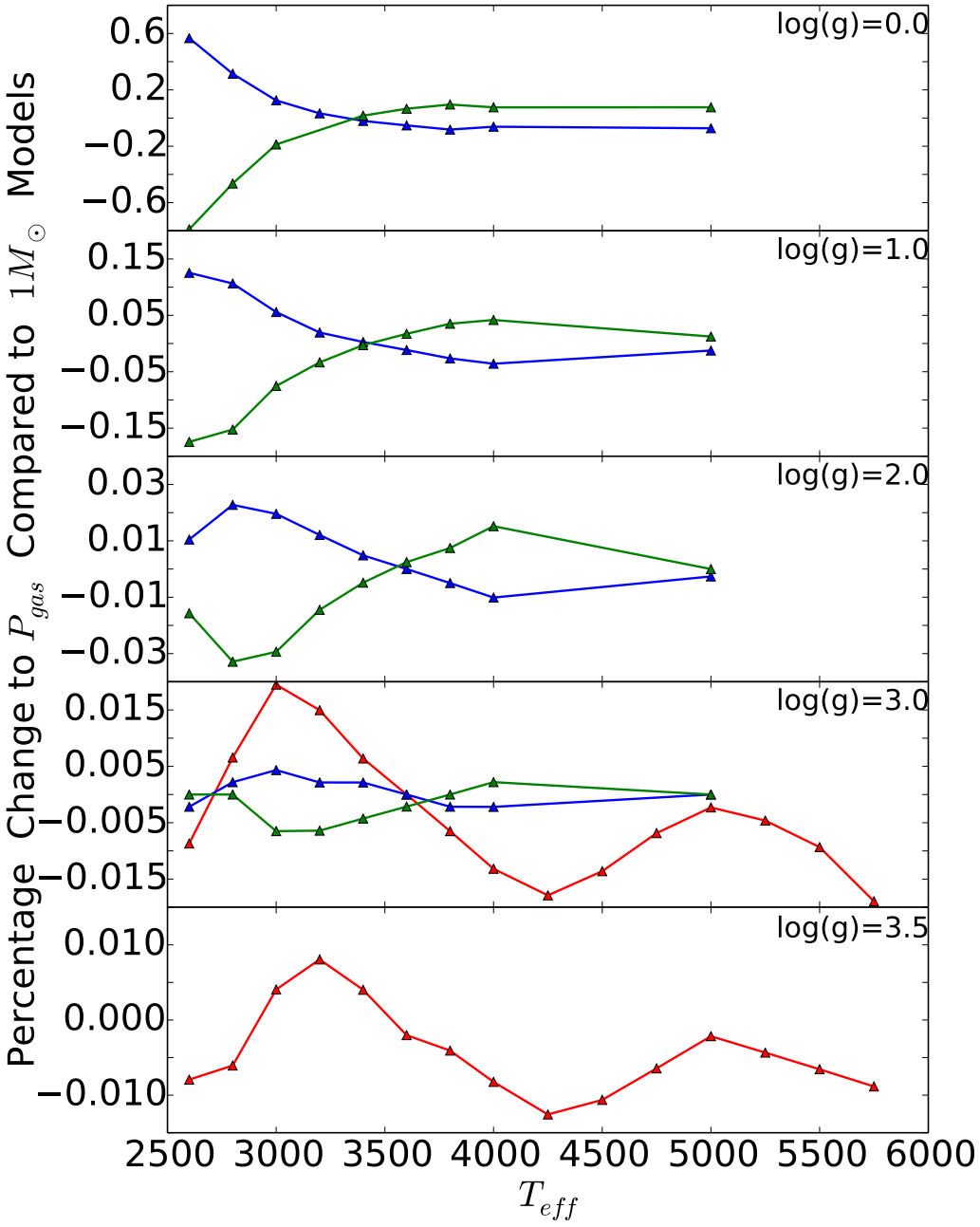

Figure 2.4: MARCS atmospheric models, percentage change in gas pressure at $\tau = 1$ relative to a $1M_\odot$ model for red: plane-parallel, blue: $2M_\odot$ and green: $0.5M_\odot$ models across a range of $T_{\rm eff}$. The panels from top to bottom represent log g=[0,1,2,3,3.5], all models are solar metallicity.

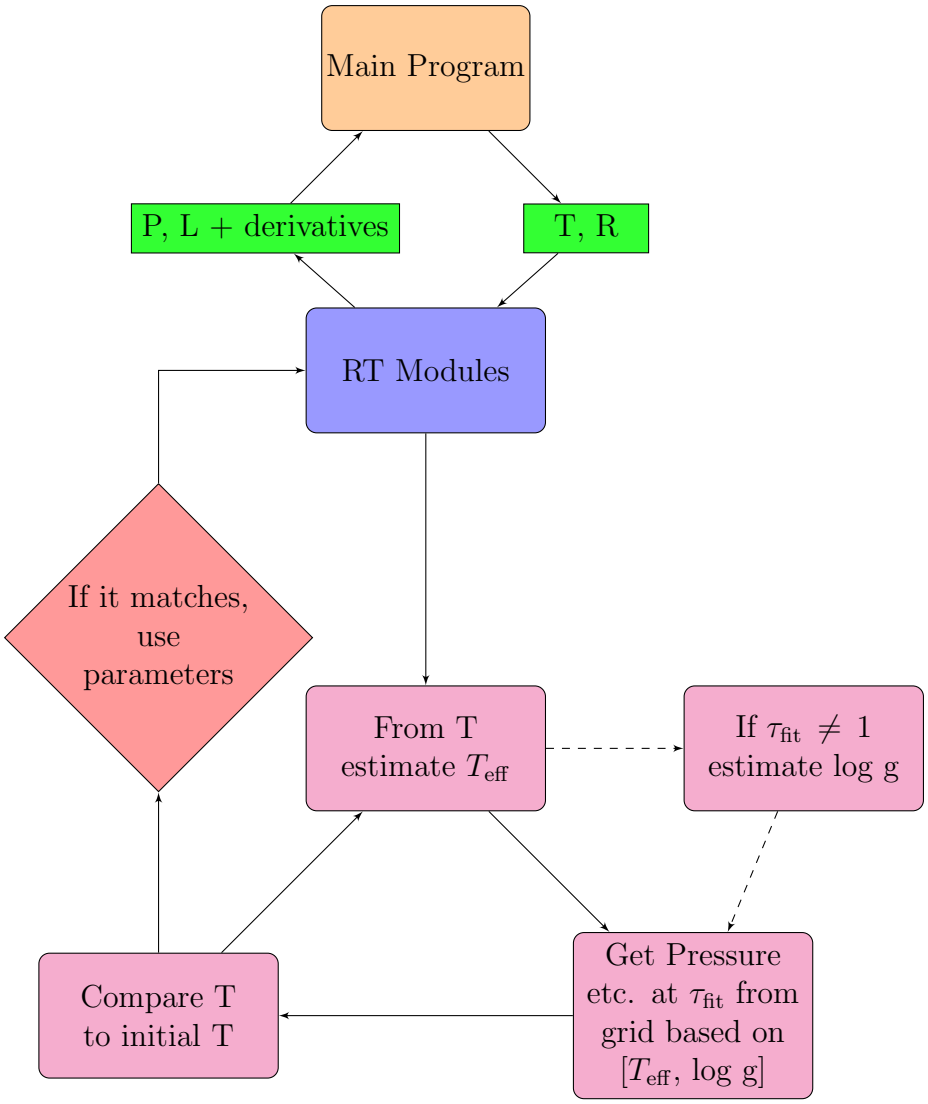

Figure 2.5: A diagram illustrating the process by which the grid of radiative transfer models provide the outer boundary condition for the interior evolution model.

this can be done for all optical depth points in order to attach the full atmospheric structure (e.g. when a comparison is required). The interpolation is done in a piecewise manner, first interpolating in one of the grid parameters, then another and so on, using a 4th order polynomial fit.

An outline of how this boundary condition is obtained, and how it relates to the interior evolution model, is shown in Fig. 2.5. In this case, the temperature and

radius are taken from the outermost grid point of the interior model, such that a log g value can be calculated, and the pressure and luminosity are returned. This is done differently to the case for both the plane-parallel and spherical analytic relations (as shown in Fig. 2.1) as the radius is required to calculate the surface gravity, and the Stefan-Boltzmann law can only be applied after the effective temperature has been determined, as it does not correspond to the temperature at the outermost grid point in the interior model.

Additionally, the temperature at the fitting depth (usually $\tau = 1$) for the radiative transfer model also does not correspond to the effective temperature, which means that an iterative procedure is required. This is done such that the effective temperature is estimated based on the structural temperature given by the interior model, this effective temperature is used along with the log g value to extract a structural pressure and temperature from the grid of radiative transfer models. If the structural temperature from the atmospheric model matches that given by the interior model, a solution has been found. If not, a new effective temperature is estimated. Once a solution has been found, the Stefan-Boltzmann law can be used to calculate the luminosity based on the effective temperature and radius.

This procedure is further complicated if the atmospheric model is not attached at an optical depth of $\tau = 1$. In this case, the additional radius (which exists in the spherical models only) between $\tau = 1$ and τ_{fit} is added to the radius from the interior model to get the surface gravity. However, in order to do this, a similar iterative procedure has to be applied as was done in the case of the effective temperature. This means that both an effective temperature and surface gravity are estimated from the values of T and R taken from the interior code, these are then used to get the structural temperature and atmospheric radius from the grid of radiative transfer models, and this is iterated until the values match within a given tolerance.

2.3 Calculations

As the primary focus of this work is to study the influence of the outer boundary on the TP-AGB evolution, models were separated into their evolution prior to the first thermal pulse, and the TP-AGB itself. This allows for a more consistent analysis of the models, as any change in the core mass at the onset of the first thermal pulse can itself become an influence, and in addition some of the assumptions being challenged by the investigation, such as the use of different opacities, may only be justifiable during this phase of a star's lifetime.

For completeness, models are also produced for the full evolution using different atmospheric treatments, and discussed in section 2.4, although this primarily illus-

trates that any influence is more pronounced on the TP-AGB. In this case it is stated the models are calculated from the main sequence using the stated boundary, otherwise, models using the plane-parallel atmosphere with Rosseland mean opacities up until the first TP are used.

The models presented here are calculated with the solar abundance distribution of Grevesse et al. (2007) to match the MARCS grid, giving a solar metallicity of Z=0.012, lower than typically taken for stellar modelling. On the other hand, the COMARCS atmospheres take the abundances from Anders & Grevesse (1989) for all values other than C, N and O which are taken from Grevesse & Sauval (1994). Although the metallicity taken in this work is lower than generally taken for solar composition models, the main purpose of this work is for comparison between atmospheric treatments, so it is not particularly significant. The difference in abundances assumed by the two radiative transfer grids, along with them being computationally different is another reason for separating the pre- and TP-AGB evolution, as there is a clear difference in the evolutionary models if a direct transition is attempted.

Models are labelled according to their geometry (plane-parallel-'pp', spherically symmetric-'ss') and opacity treatment (Rosseland Mean-'RM', Planck Mean-'PM', including C/O interpolation -'CO'). Additionally, 'RT' signifies Radiative Transfer models used as an outer boundary condition and 'ms' that the model was calculated from the main sequence with an atmosphere other than RM-pp. A full list is given in Appendix A for reference.

Models implementing a RT grid would be the clear, physically motivated, preference for these calculations, however, due to the lack of atmospheric models at the low surface gravities reached during the TP-AGB evolution, there was a limit to how far such evolutionary models could be continued. As such, an alternative for modelling the outcome which could be reasonably expected from such a treatment was investigated and is discussed in more detail in Sect. 2.4.1.

2.3.1 C/O in COMARCS Atmospheres

It is already known that the opacities at a given metallicity vary as a function of changing C/O (Marigo, 2002, also seen in the previous section) and has been shown to influence the TP-AGB evolution (Cristallo et al., 2007; Weiss & Ferguson, 2009) including at low metallicities (Constantino et al., 2014). It is nonetheless worth taking a moment to look directly at the COMARCS models which have at specific locations in the log g, $T_{\rm eff}$ grid a large number of detailed radiative transfer calculations with varying C/O. This results in a change in the atmospheric structure, producing a resulting change to the photospheric boundary condition taken for the

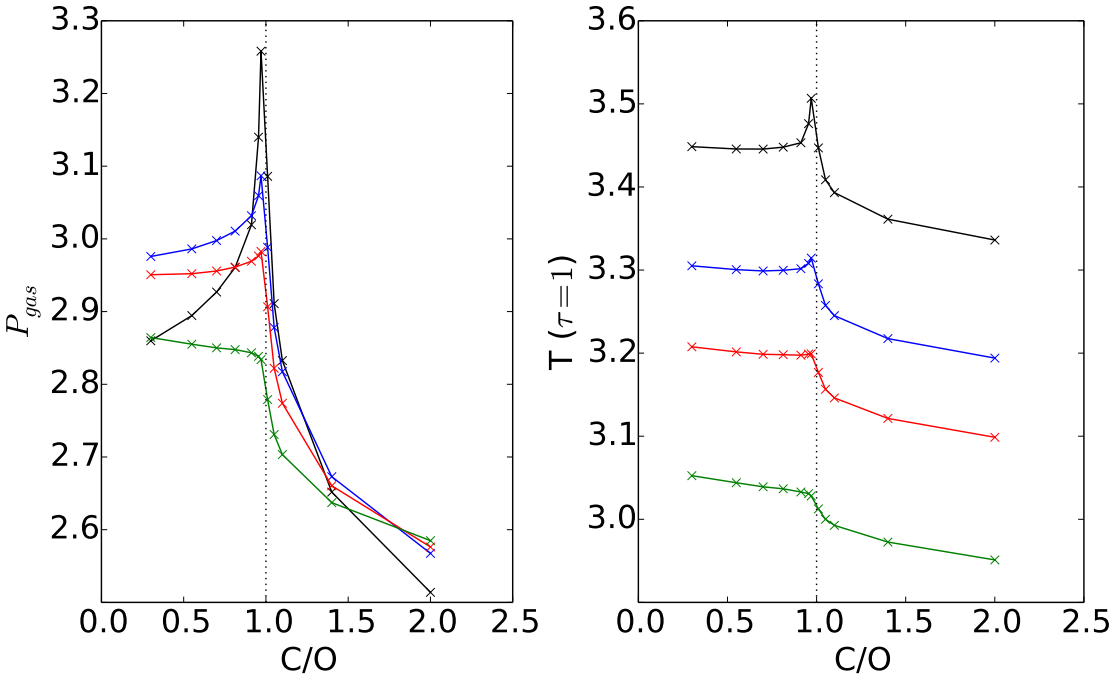

Figure 2.6: COMARCS atmospheric parameters ($P_{\rm gas}$, $T_{\rm gas}$) at $\tau = 1$ for atmosphere at $\log g = 0$, [Fe/H] = 0, $M = 1 M_{\odot}$ and $T_{\rm eff}$ = [2700K: black, 3000K: blue, 3200K: red, 3500K: green] for a varying carbon to oxygen ratio (C/O).

stellar evolution code.

Fig. 2.6 shows the gas pressure and temperature at $\tau = 1$ for models with a different $T_{\rm eff}$ but the same log g and metallicity. The difference in these values, as a function of the C/O value, can be seen to vary quite drastically in the transition region between O-rich and C-rich, particularly at lower temperatures where molecules become increasingly important.

The increase in both pressure and temperature as C/O approaches 1, and subsequent decrease as the models become further carbon enhanced is a result of the CO molecule having such an overwhelming influence on the resulting molecular chemistry and the lack of it as all the C and O is bound up within the CO molecule. Unfortunately, the extent of this grid is insufficient to interpolate in the C/O value during the evolutionary calculations and would require very careful consideration if done in the future, given the discontinuity in the slope at unity within the C/O value.

2.3.2 Obtaining the Analysis

There are inherent difficulties in analysing the often complex evolution during the TP-AGB, which regularly requires certain decisions to be taken about how a result is defined. As the objective during this work is to proceed in a manner which allows for direct comparison between two models which differ only in their treatment of the outer boundary, how this is done can become fairly crucial, and as such taking a moment to outline how this is done is considered pertinent.

Of particular significance can be the method for obtaining final results during the evolution, with it often being the case that models cannot proceed through the end of the TP-AGB evolution, directly to the post-AGB phase due to issues of convergence. While it is possible to follow this evolution to the end of the star's nuclear burning lifetime, it usually requires some alteration of numerical parameters and tends to be required on an individual model basis. In this investigation, this is not desirable. It is considered for the purposes outlined previously, better to use common methods of analysis of the models, rather than to force the evolution to complete the evolution.

Convergence has been known for many years to be a problem towards the end of TP-AGB evolution (Wood & Faulkner, 1986), encountered by various groups since its discovery (Karakas & Lattanzio, 2007; Weiss & Ferguson, 2009), with the primary cause, a dominance of radiation pressure at the base of the convective envelope, more thoroughly investigated by Lau et al. (2012). In general, it is easier to follow low to intermediate mass stars up until the last TP, although even then it is often the case that convergence becomes an issue as the star loses the remainder of its convective envelope, forming the central stars of planetary nebulae (Miller Bertolami, 2016). Unfortunately, the exact moment during the final TP cycle where calculations stop is not always consistent, influencing the final core mass obtained due to the cycle of core growth from burning and reduction due to the 3DU. The definition of final core mass is thus taken to be the extent of the hydrogen-free core at the TP prior to the final TP.

A similar approach is taken in producing the yields for the models, removing the remainder of the envelope at the second to last TP, giving the overall material ejected by the star. Beyond this inclusion of the final envelope mass in the yields, no further extrapolation is used in any of the results presented here. As such any final values which are given for the more massive stars and which typically encounter convergence issues with multiple TP cycles remaining incomplete, should not be taken as definitive.

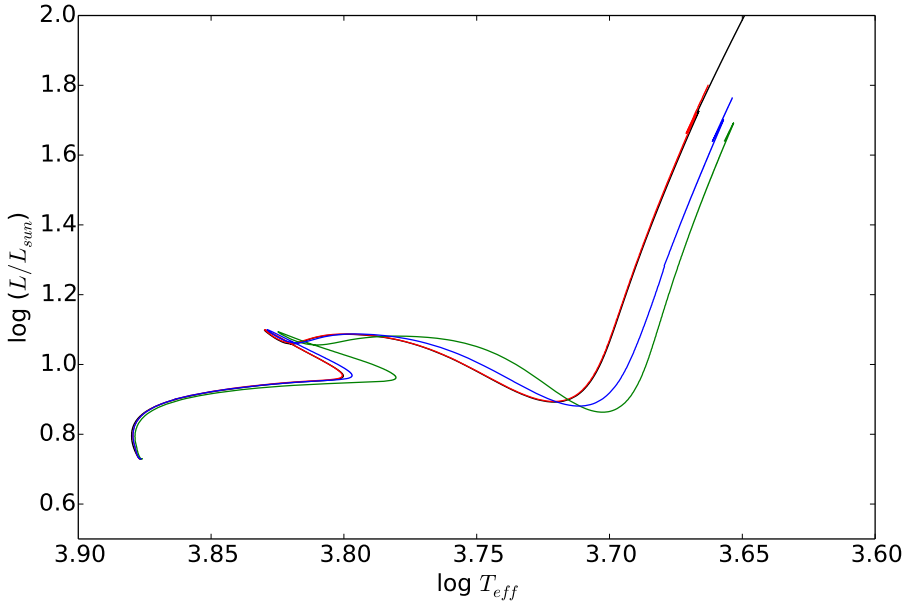

Figure 2.7: HR-diagram for $1.5M_{\odot}$ models with outer boundary denoted by colour. Black: RM-pp, red: RM-sph, blue: RT (MARCS), green: PM-pp

2.4 Results

2.4.1 Planck Mean as a Proxy

Although it is not possible to use radiative transfer models to cover the entire TP-AGB evolution, it is still desirable to be able to consider what the overall influence may be, if such a possibility were available.

When viewing the different evolutionary tracks, the first thing which became apparent is the influence on the effective temperature of the models. Of particular relevance is that in both the cases of using RT models and the PM opacities, the effect is to move the models to a lower temperature. However, this only occurs as the models move away from the main sequence evolution. Fig. 2.7 demonstrates this, showing the evolution of a $1.5M_{\odot}$ model with different atmospheric treatments. The evolutionary tracks overlap on the MS until the development of a convective core, only fully separating as the stars begin to ascend the RGB.

Although justification for using the PM opacities during the earlier evolution is perhaps even less than on the TP-AGB, Fig. 2.7 gives a clear indication that stellar

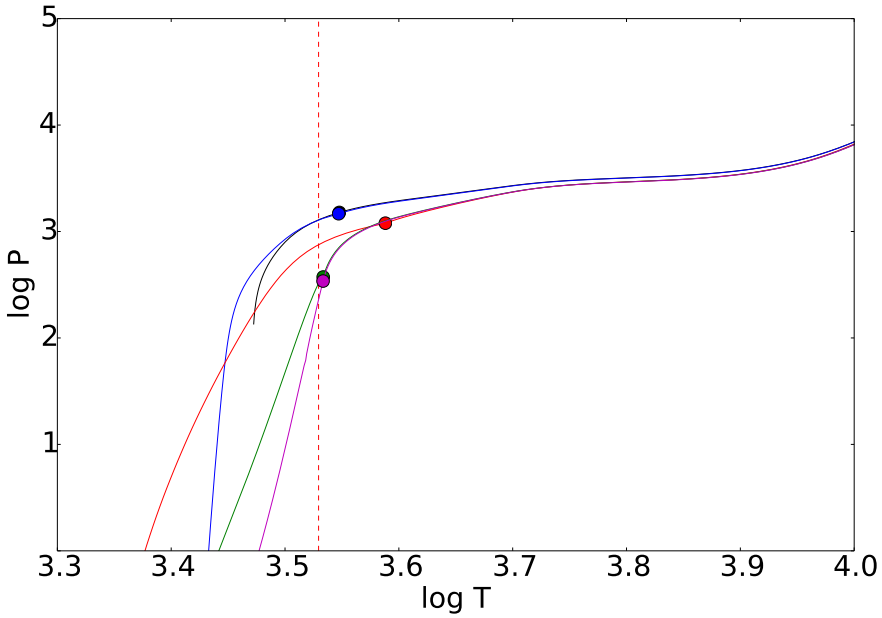

Figure 2.8: The pressure-temperature structure for the outer layers of the stellar model and atmosphere. Marker denotes position of boundary, dashed line $T_{\rm eff}$ of COMARCS model. Black: pp-RM, blue: ss-RM, purple: pp-PM, green: ss-PM, red: COMARCS

evolution models are predominantly independent of the outer boundary condition during MS evolution, at the masses considered here. Concurrently, it shows that as the star expands, traversing the HR diagram into the red giant region, the effective temperature of the model is altered.

Additionally, the tracks suggest that the RT models are indeed bound by the two opacity treatments and that on the RGB, more closely follow the PM models. A similar behaviour is observed on the TP-AGB for models using the COMARCS atmospheres, rather than the MARCS models used in this example. This leads to the interesting question of whether the PM could in some way be used to allow for the study of the stellar evolution models throughout the low log g environment, which was the intended subject of this study, but where it is computationally difficult to produce sufficient RT models to allow for a direct investigation.

To address this question, Fig. 2.8 shows $\log T$ vs $\log P$ for several atmospheric treatments, and the continuation into the interior stellar evolution model for a $3M_{\odot}$ model at the beginning of the TP-AGB phase with $L = 3.66 - 3.72L_{\odot}$ and $T_{\rm eff} =$

$3.53 - 3.55K$. The range in $L, T_{\rm eff}$ arises from all treatments being applied to the same interior model, without evolving the model, to understand the influence of the outer boundary condition. In the case of the analytic treatments, pp/ss, the point at which the outer boundary condition is implemented corresponds to the effective temperature and is marked by a correspondingly coloured marker in each case. However, for the RT model, the effective temperature is defined separately and is marked by the vertical dashed line.

In all cases, the interior model converges to a similar solution, not far into the stellar interior. Although it is notable that the form of the RT model is not reproduced by the analytic models, $T_{\rm eff}$ is matched fairly closely for the PM opacities, as expected from the evolutionary tracks. Furthermore, the PM models follow the interior solution of the RT models from a shallower depth than the RM opacity models.

Fig. 2.9 shows the effective temperature (top panel) and pressure at the fitting depth (lower panel) as a function of age for the same models as shown in Fig. 2.7. This shows that physically, the PM opacities result in a significantly lower fitting pressure, and emphasises both the inability of the analytic approximations to replicate the physical properties of the RT models, and also to indicate how even this extreme change in the value of the pressure at the outer boundary has such a negligible influence on the MS evolution. This is not to say that using the PM treatment is meaningless, as it has already been shown in Fig. 2.8 that the interior model quickly forgets the outer boundary condition, and that the PM appears to best approximate the overall influence of the RT treatment.

Of course, it cannot be claimed that this is a fully justified physical description of the outer layers of the star, nevertheless, it does suggest that the initial belief that the opacity is likely to lie between the RM and PM is reasonably good. More importantly, this provides a reasonable method for pursuing the full influence of this change to the outer boundary condition, which in some way mimics the behaviour of the RT models. Given this result, the PM-pp models were used to calculate a denser grid of models for additional study and can be considered in some ways as a proxy for how the models may be changed by the inclusion of a full radiative transfer calculation for the atmosphere. The choice to continue using the pp models rather than ss model, coupled with the PM opacity, was taken as the opacity change appears to have a more significant influence than the geometry, which has little impact on the evolutionary models in the analytical framework investigated here.

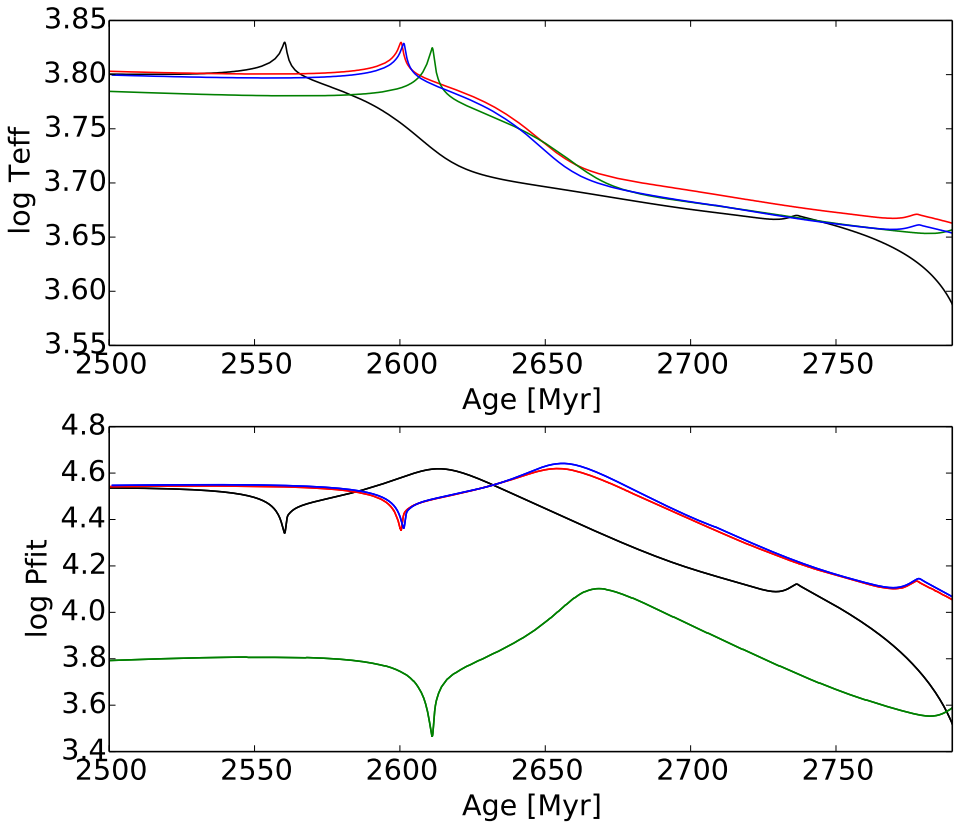

Figure 2.9: Effective temperature (top panel) and the pressure at fitting between interior and atmospheric model (lower panel) for the pre-AGB evolution of a $1.5 M_{\odot}$ model with boundary conditions represent denoted by Black: RM-pp, red: RM-sph, blue: RT (MARCS), green: PM-pp.

2.4.2 Depth

As has been previously mentioned, the equations of stellar structure, which are implemented in the interior of the stellar evolution code, require that the diffusion approximation holds. Although this is commonly taken to be at a depth of $\tau = 1$, this is not necessarily the case. As such it is worth considering the effect of attaching the grid of radiative transfer models at a greater depth.

To illustrate how the interior model compares to the radiative transfer atmospheric models, Fig. 2.10 show the pressure-temperature diagram for a $1 M_{\odot}$ model,

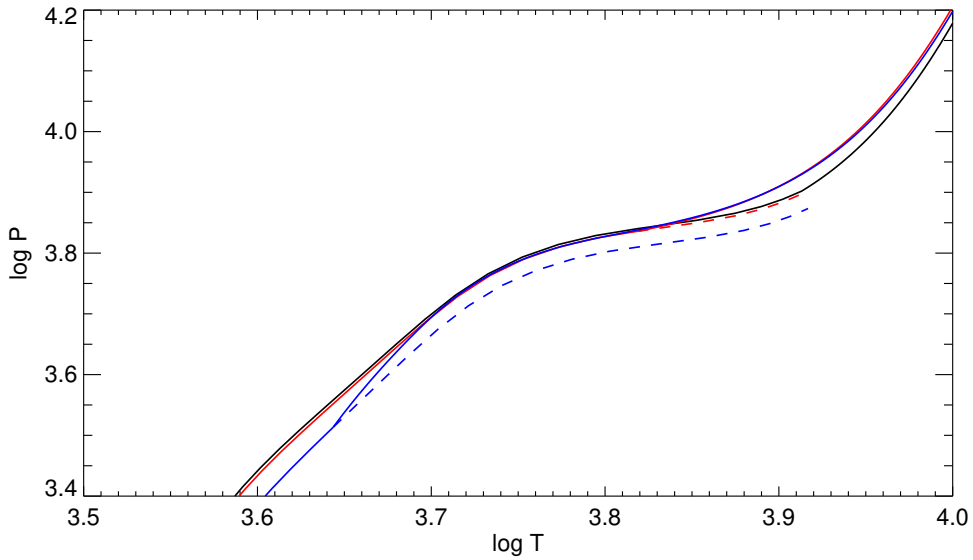

Figure 2.10: The pressure-temperature diagram for a $1M_{\odot}$ model, during the RGB (at $\log g \simeq 1.25$) with an interpolated MARCS atmosphere attached to the interior model at $\tau = 1$ (blue), $\tau = 10$ (red) and $\tau = 100$ (black). Dashed lines show the remainder of the MARCS model beyond the fitting depth for comparison to the interior model.

during the RGB (at $\log g \simeq 1.25$) with an interpolated MARCS atmosphere attached to the interior model at optical depths of $\tau = 1, 10, 100$. The additional extent of the atmospheric model, which always extends to a depth of $\tau = 100$, is included in all cases and illustrates how the interior model attached at $\tau = 1, 10$ diverges from the remainder of the atmospheric model. It also shows that the interior model already begins to converge to a similar solution in all cases, even within this limited plot of the pressure and temperature, however it should be noted that the models attached at $\tau = 1$ and $\tau = 10$ converge to the same interior solution far quicker than the model attached at $\tau = 100$, suggesting in this case at least that it could be an indication that the diffusion approximation is also not valid at $\tau = 10$, or that some other difference exists to distinguish the exterior and interior models.

Taking an evolutionary calculation for a $1.5M_{\odot}$ solar metallicity model, with a fitting depth of $\tau_{\rm fit} = 1$, a separate RGB evolution with a fitting depth of $\tau_{\rm fit} = 100$ was also calculated. The separate evolution for the $\tau_{\rm fit} = 100$ model was only calculated once the star had begun the ascent of the RGB, so as to avoid the use of

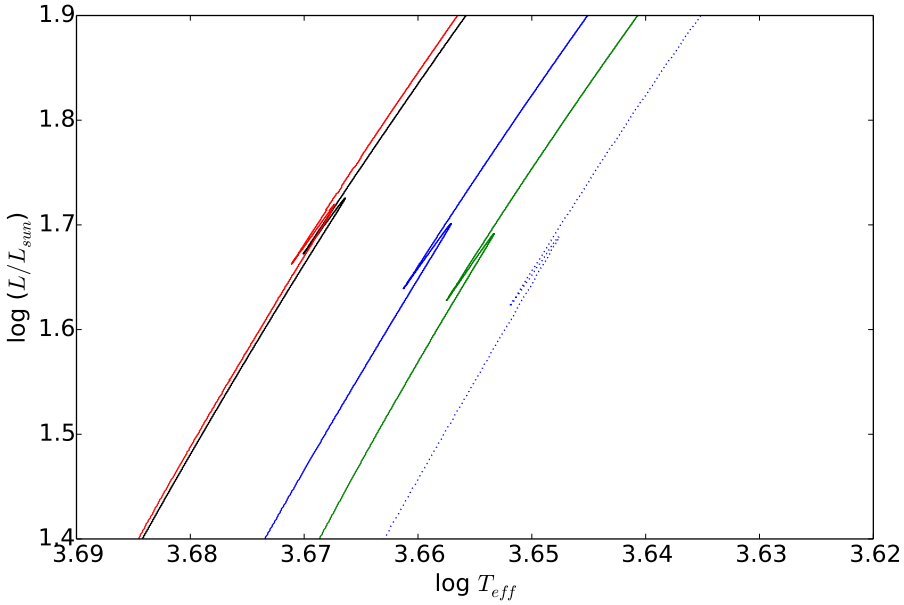

Figure 2.11: HR-diagram of the red bump for $1.5M_{\odot}$ models using the MARCS atmospheres, attached at $\tau_{\rm fit} = 1$ (blue) and $\tau_{\rm fit} = 100$ (blue-dotted). Other atmospheres also shown are black: RM-pp, red: RM-ss, green PM-pp.

the plane-parallel models at higher log g, with the full evolution of the $\tau_{\rm fit} = 1$ model using the MARCS grid of atmospheres. This was done for the sake of consistency as it is, at least in principle, necessary to account for the additional radial extent of the atmosphere between $\tau_{\rm fit} = 1$ and $\tau_{\rm fit} = 100$ in determining the outer boundary condition.

The resulting evolutionary tracks around the red bump on the RGB are shown in Fig. 2.11 where the solid-blue line indicates the case where the MARCS atmospheres were attached at a depth of $\tau_{\rm fit} = 1$ while the dotted-blue line shows a model where the fitting depth was shifted to $\tau_{\rm fit} = 100$. Primarily, there is a clear shift in $T_{\rm eff}$, to lower temperatures, when attaching the model at greater depth.

Shown alongside these tracks are the same models which appear in Fig. 2.7, where the black line is RM-pp, red is RM-ss and green is the PM-pp model. This shows that actually, attaching the MARCS atmospheres at a greater optical depth results in an effective temperature even lower than that given by the PM-pp models. Additionally, it can be seen that with the shift to lower temperatures, there is also a slight decrease in the luminosity of the red bump, which was discussed in Ch. 1.

Accounting for Atmospheric Radius

Typically, when attaching a model atmosphere to the interior stellar evolution code, the radius at the outermost point of the interior model is required in the calculation of log g, which is used for finding a corresponding solution from the atmospheric grid. In the case of the spherical models, there is a radial extent within the atmospheric model ($\Delta R = R(\tau = 1) - R(\tau_{\rm fit})$) when the optical depth is not $\tau_{\rm fit} = 1$. In principle, this radius must also be taken into account when determining the log g which allows a boundary condition to be obtained from the grid of radiative transfer models for $\tau_{\rm fit} \neq 1$, however, it is worth taking a moment to consider whether this is necessary.

Attaching the atmosphere without accounting for this radial extent would correspond to assuming the stellar radius is $R_* = R_* - \Delta R$ and, assuming a constant luminosity, would result in an increased effective temperature. As an estimate of the difference this change in radius might make to the outcome, if neglected, it is possible to begin with the Stefan-Boltzmann law, $L = 4\pi R^2 \sigma_B T_{\rm eff}^4$. If it is assumed that the luminosity remains constant, then it can be said that a given radius corresponds to a particular effective temperature and that given two models with different radii, R_1 and R_2, with the same luminosity and respective effective temperatures, $T_{\rm eff,1}$ and $T_{\rm eff,2}$, then the quantities in question can be related by $R_1^2 T_{\rm eff,1}^4 = R_2^2 T_{\rm eff,2}^4$, which means that based only on a change in the radius of a particular model, the simple relation

$$T_{\rm eff,2}^4 = \frac{R_1^2}{R_2^2} T_{\rm eff,1}^4 \tag{2.9}$$

allows a new effective temperature to be determined.

Fig. 2.12 shows the difference, as calculated in this way, for the change in the effective temperature for $1 M_\odot$ MARCS atmospheric models, across a range of temperatures, with each line indicating a different log g (black: 0, blue: 1, red: 2, green: 3). It is not possible to calculate such a value for the plane-parallel models, given they have no atmospheric extent, however, the fact that the difference for the higher log g values in the spherical models is so small is already an indication that the models are close to the plane-parallel approximation. On the other hand, for the low log g values, particularly towards the low-temperature regime, this is not the case. Indeed, it could be argued that in this regime, which concerns the TP-AGB, the extent of the atmosphere should also be included if $\tau_{\rm fit} \neq 1$.

This presents an additional problem, in that such depths are dependent on the mass of the model. Therefore, although it has been argued in Sec. 2.2.4 that it is justifiable to use only the $1 M_\odot$ grid, due to the small structural differences between the different masses, this would be another reason for it to be preferable to use

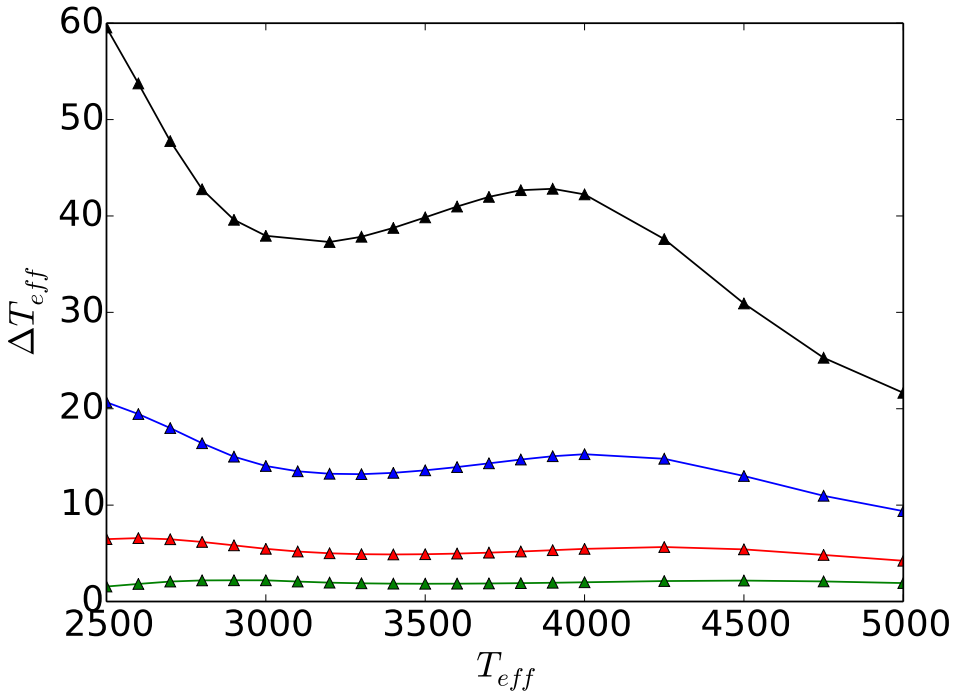

Figure 2.12: The resultant change in $T_{\rm eff}$ when radial extent of atmosphere is accounted for, when attaching a model at $\tau = 100$. Shown as a function of $T_{\rm eff}$ for log g = 0 (black), 1 (blue), 2 (red), 3 (green) for a $1M_{\odot}$, solar metallicity MARCS atmosphere.

additional mass grids for consistency when considering fitting depths greater than $\tau = 1$. For the further purposes of this work, a fitting depth of $\tau_{\rm fit} = 1$ is always taken, although it should not be forgotten that the effective temperature would be lowered by fitting at a greater optical depth.

2.4.3 Initial Impression

On first viewing, the differences between atmospheric treatments are relatively minor, and with the numerical and physical uncertainties which are already known to influence the TP-AGB evolution (mass loss, mixing processes and nucleosynthesis to name a few. See Herwig (2005) for more details), it would be rather straightforward to dismiss such differences.

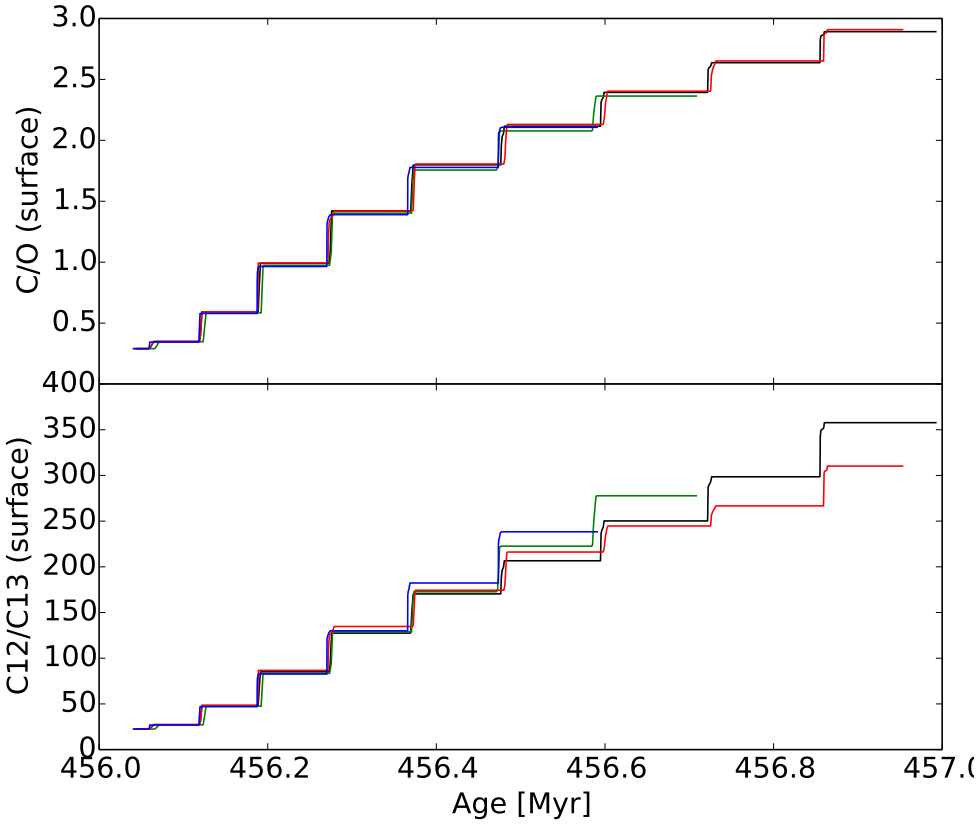

Figure 2.13: Surface C/O (upper panel) and $^{12}C/^{13}C$ (lower panel) for the TP-AGB evolution of a $3M_{\odot}$ star. Outer boundary condition altered such that black: RM-pp, red: RM-pp with C/O-interpolation, green: PM-pp, blue: RT (COMARCS)

The third dredge-up is a defining feature of the TP-AGB, so any change in the behaviour would be of great interest. Looking at the top panel in Fig. 2.13, the changing C/O as a result of third dredge-up in a $3M_{\odot}$ can be seen. Although the overlap between models is not absolute, it would be difficult to justify any claim that the outer BC is playing any significant role on the third dredge-up and TP cycle based on looking at a single mass model. There is perhaps a slight change in the interpulse period, and a small difference in the C/O value, although nothing compared to the changes which are induced by variation of the overshoot parameter.

The lower panel of Fig. 2.13 shows the corresponding ^{12}C/^{13}C value. In this

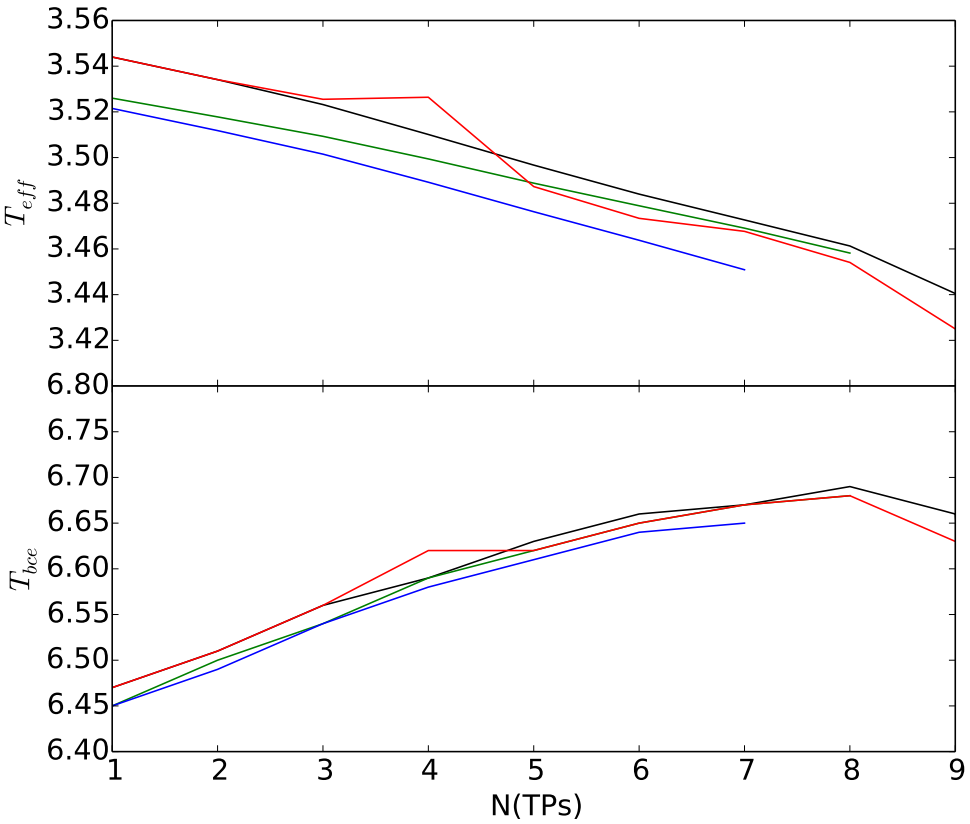

Figure 2.14: $T_{\rm eff}$ and T_{bce} as a function of TP number for a $3M_{\odot}$ star. Outer boundary altered such that black: RM-pp, red: RM-pp with C/O-interpolation, green: PM-pp, blue: RT (COMARCS)

instance, the difference is more pronounced although the overall values are still of a comparable magnitude and nothing which could be distinguished in itself.

Fig. 2.14 allows for a closer look at whether there is a resulting change in the interior of the stellar model. $T_{\rm eff}$ is shown in the top panel, while the temperature at the base of the convective envelope $T_{\rm bce}$ is shown in the lower panel, both as a function of thermal pulse number, where the temperature is taken at the minimum helium luminosity of the interpulse phase following a thermal pulse. This is done for clarity, and to hopefully allow for a more consistent representation of the differences since plotting the values as a function of time results in large variations over short

timescales during the TP cycle.

As has already been seen in the previous section, the effective temperature of the PM and RT models are consistently lower than for the RM models. This does, however, change in the case of the RM-CO (red) model, where the variation of the opacity as a function of C/O results in an initially higher temperature with respect to the standard RM case until it reaches the critical value of C/O=1. After this time, $T_{\rm eff}$ quickly begins to decrease to a value lower than the standard case, as is expected from other works (Marigo, 2002; Weiss & Ferguson, 2009).

The lower panel demonstrates that the change in the temperature at the surface is mirrored at least partially in the interior and the depth to which the convective envelope descends. Taken in conjunction with the change in $^{12}C/^{13}C$ which is seen in the lower panel of Fig. 2.13, it can be said that the outer boundary is having at least some influence on the interior physics and as a consequence the third dredge-up is modified, again illustrating the coupled nature of the processes within these stars.

2.4.4 Influence on Mass Loss

A more direct result of altering the atmospheric boundary is the resulting mass loss history, which can be heavily dependent on $T_{\rm eff}$. Due to the lower effective temperatures, the PM and RT models start losing more mass earlier, so while the evolution can look fairly similar when considering the C/O value as a function of time, as in Fig. 2.13, it can be viewed somewhat differently when considered as a function of mass.

Fig. 2.15 shows the evolution of $2, 3, 4, 5$ and $6 M_{\odot}$ mass models in the mass vs C/O plane, with the colours each representing a different boundary condition. Especially in the case of the higher mass stars, a clear distinction can be seen between the various treatments, with RT and PM models having a substantially lower mass for the same abundance ratio. The evolution as a function of mass can also be considered an evolutionary indicator, given they are always losing mass.

In principle this would indicate a difference between models, however, it is only of a theoretical interest as it would not be possible to constrain masses and C/O values for these dust-enshrouded stars to a point such features could be distinguished. If that were the case, the mass loss history would be so tightly constrained as to provide empirical yield measurements and place far more observational constraints on the evolutionary models. However, for a given mass loss description, the outer boundary plays an important role, also influencing the yields. Along with being generally important for the chemical evolution of the galaxy, this is relevant for initial mass and thus timescale of second generation globular cluster stars, given the alternate

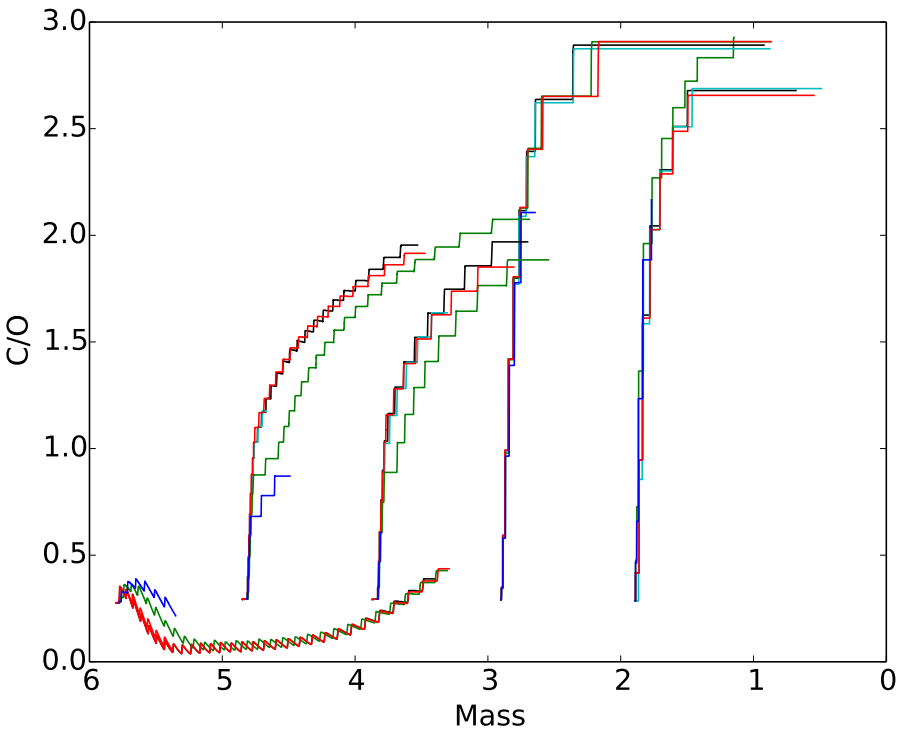

Figure 2.15: Carbon-to-Oxygen ratio as a function of mass during the TP-AGB evolution of models with ZAMS masses M=[2,3,4,5,6]. The colours denote different atmospheric boundary conditions given by Black: pp-RM, red: pp-RM-CO , green: pp-PM, blue: RT, cyan: ss-RM

composition and quantity of material expelled by the TP-AGB stars.

2.4.5 Observable Quantities

The results presented here focus on the PM-pp and RM-pp models, as this should allow for the extent of the influence of the outer boundary condition to be investigated. The higher mass models ($\gtrsim 3M_{\odot}$) tend not to reach the final TP, while all of the models in the mass range $1.6 - 2.8M_{\odot}$ have reached what is considered likely to be the final TP, i.e. it would be expected that if the calculation had continued to the post-AGB phase, it would not have required more TPs in order to lose any remaining envelope mass. In the case a model does not reach the final TP, no extrapolation has

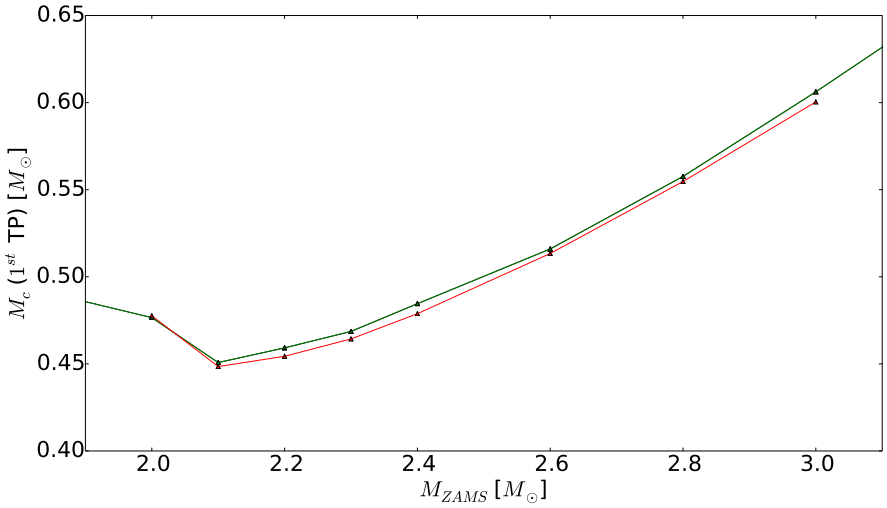

Figure 2.16: Core mass at the onset of the first TP for sets of models as denoted by black: RM-pp, green: PM-pp, red: PM-pp-ms

been carried out (for instance, as is done in Karakas & Lattanzio, 2007), as trying to determine when the final TP where significant mass loss occurs is fraught with danger and, as such, these models are not discussed in as much detail.

Additionally, models in the mass range $2.1 - 2.3 M_\odot$ experienced what can only be described as anomalous behaviour, where the thermally pulsing phase was interrupted by a brief return to stable double shell burning, before the resumption of thermal pulses. After the re-ignition of the thermal pulses, no third dredge-up was present in the models and the cores began to grow and, as such, the models in this mass range have substantially larger final masses and C-star lifetimes than the general trend would have suggested. This phenomenon is discussed in further detail in the following chapter.

IFMR

The initial-final mass relation (IFMR) tests the integrated mass-loss of a star and is one of the most concrete methods for testing TP-AGB stellar models, making it an obvious choice for investigating if the outer boundary is having any systematic effect across a range of masses. This is particularly important given the sometimes chaotic nature of the TP-AGB evolution.

The solid lines in Fig. 2.17 indicate the IFMR for the RM-pp (black), PM-pp

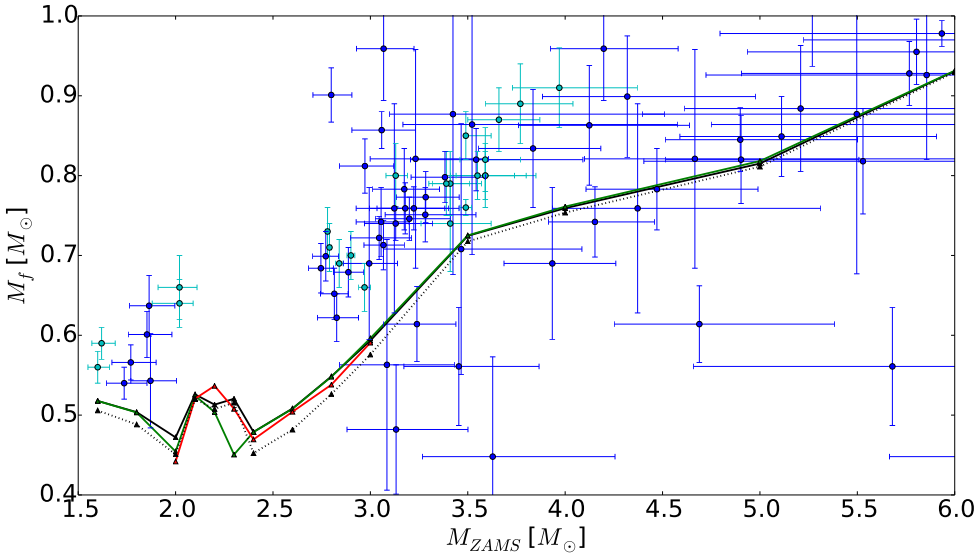

Figure 2.17: IFMR. Final massed denoted by solid line, black: RM-pp, green: PM-pp, red: PM-pp-ms. Black dotted line shows the RM-pp relation if minimum core mass taken. Observational data represented by blue makers (Salaris et al., 2009) and cyan markers (Kalirai et al., 2014).

(green) and PM-pp-ms (red) treatments, with corresponding markers at the location of a model. Fig. 2.16 shows the initial mass vs core mass at the 1^{st} thermal pulse for the same models, where the RM-pp and PM-pp lines overlap due to starting from the same initial model prior to the 1^{st} thermal pulse. The data included in Fig. 2.17 are observational constraints from open cluster white dwarfs, taken from Table 1 in Kalirai et al. (2014) and from the results of Salaris et al. (2009) where overshooting was included in the derivation. Additionally, the black dotted line shows the IFMR for the RM-pp models if the final mass is taken as the minimum value from the last thermal pulse rather than the maximum value.

It is already known (Andrews et al., 2015) that there is some tension between the final masses of the models presented here and observations, however, a comparison is shown nonetheless, as it is still beneficial to have some context when judging the changes to the models by changing the atmospheric treatment. The general trend seen in Fig. 2.17 for the lower final mass of the models is due to the treatment of overshooting, which is likely to be overly efficient during third dredge-up, resulting in a lower core mass. This can be seen from the fact that rather than experiencing

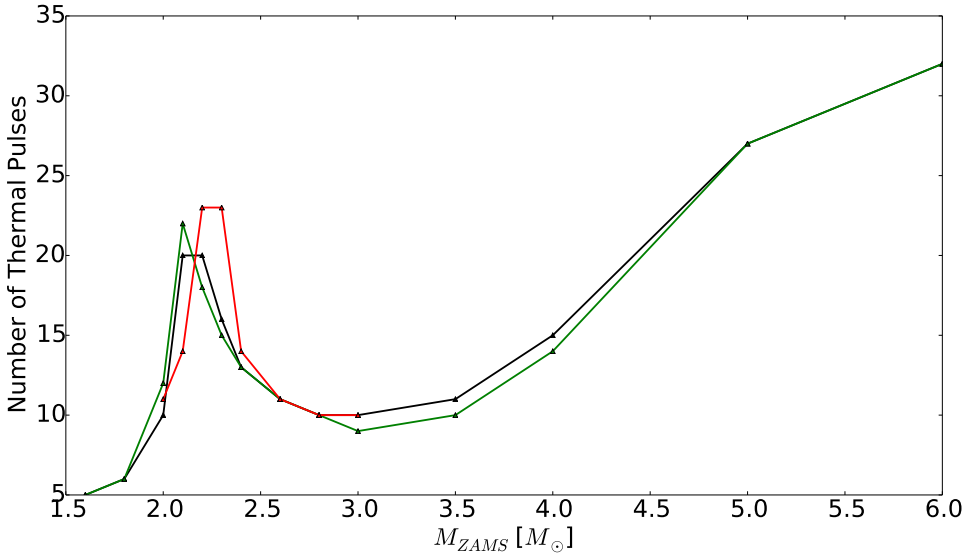

Figure 2.18: number of thermal pulses undergone, as a function of ZAMS mass for models. Black: RM-pp, green: PM-pp, red: PM-pp-ms

overall core mass growth during the TP-AGB, as would be expected (Kalirai et al., 2014), the models presented here can, in fact, see the core mass decrease due to the strength of the third dredge-up. This forms a significant part of the motivation for the work which follows in Part II of this thesis.

The first point to take from this plot is the minor influence of the outer boundary on the evolution of the star prior to the TP-AGB phase, there is a minor difference in the core mass, which is consistent across the models which have been evolved from the MS with a different treatment at the outer boundary, however it is not in itself noticeably significant.

Additionally, excluding the mass range $2.1 - 2.3 M_\odot$ where the anomalous behaviour was observed, there is essentially no influence of the atmospheric boundary condition on the final core mass of the star. This seems to suggest that although the outer boundary may allow for the models to be distinguishable during the evolution, as was seen in Fig. 2.15, the final outcome which might be observed is unchanged. This appears to be due to the fact that, although changing the outer boundary condition alters the mass loss during the evolution, it does not noticeably alter the dredge-up mechanism and therefore the final mass is more dependent on the number of thermal pulses. As the number of thermal pulses experienced by the models, as

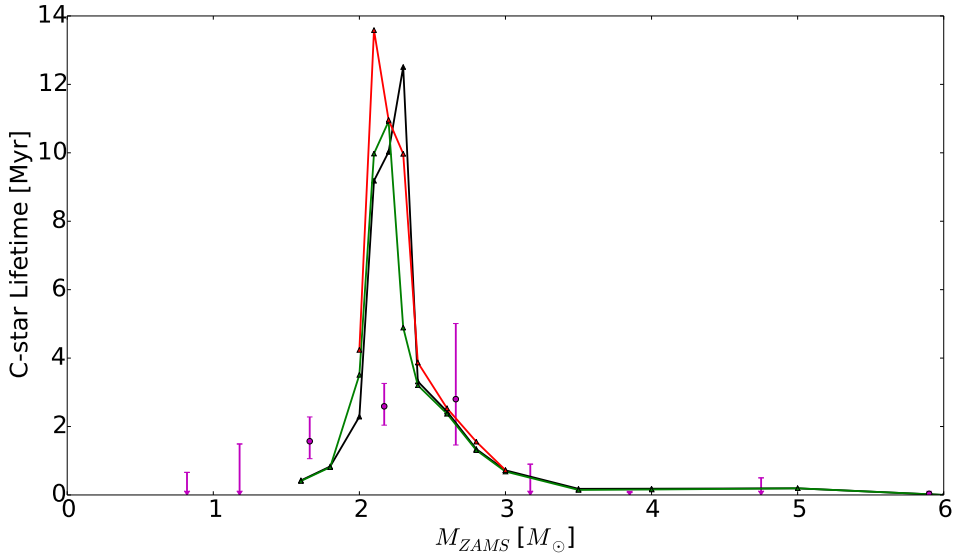

Figure 2.19: Carbon-star lifetime for models denoted by black: RM-pp, green: PM-pp, red: PM-pp-ms. Magenta observational markers taken from LMC data (Girardi & Marigo, 2007), placed at the expected cluster turn-off mass (binned data).

seen in Fig. 2.18, is largely consistent, the final masses are also consistent.

However, the line showing the IFMR for the RM-pp models based on the minimum core mass shows that the difference in the relation can vary noticeably depending on the phase of the thermal pulse cycle at which the core mass is taken. This is not something which is usually stated when providing such a comparison and there would be a more noticeable difference in the atmospheric treatments if the final masses of the models were taken as the last calculated, although the difference would not be consistent at different masses, as it is purely down to when each individual model ends.

C-star Lifetime

The proportion of TP-AGB stars which are carbon-rich (C/O>1) allows for a useful diagnostic tool for this evolutionary phase. Fig. 2.19 shows the time spent as carbon stars for the RM-pp, PM-pp and PM-pp-ms models, along with the data taken for the LMC from Girardi & Marigo (2007). Although this data is for the LMC, this is commonly taken to be a metal fraction of Z=0.008, while the current work relies on solar metallicity models but with a value of Z=0.012, and is thus still a useful

reference point.

It must again be taken into consideration, that the unexpected behaviour in the mass range $2.1 - 2.3 M_{\odot}$ has a significant impact on the calculated quantities, and in this case, the peak of the C-star lifetimes coincides with this region of initial masses. However, it is an explanation as to why the lifetimes presented here are a factor of 3 higher than might be expected. Of course, as the observational data is binned into mass ranges based on cluster turn-off masses, it is also possible that any sudden peaks are smoothed out of the observational data. Although, it must be said the anomalous behaviour seen in this mass range would likely not happen if the overshooting parameter is reduced as this behaviour requires a specific set of conditions, as is discussed in Ch. 3.

It can, however, be seen that the values outside of this limited range are in line with expectation, and the values from the RM-pp models are again consistent with both cases which use the PM opacities.

2.4.6 Yields

For the wider astronomical community, TP-AGB models are of interest for their predictive power, and their contribution to the chemical evolution of host galaxies in particular. As such the C, N and O yields for the same models as in the previous section are presented as a function of ZAMS mass in Fig. 2.20. s-process production elements would be highly interesting as a further test/exploration in this instance, given the connection to the base of the convective envelope which has been shown to be at least partially influenced by the outer boundary, however, it is not considered here and must instead be left for future work but which has been considered in conjunction with GARSTEC previously (Cruz et al., 2013).

For masses $2.1 - 2.3 M_{\odot}$, it is difficult to say anything significant about the resulting yields due to the odd behaviour in the evolution. There does appear to be a consistent change across the masses suggesting that both the PM-pp and PM-pp-ms models eject more of carbon, oxygen and nitrogen. The difference is not hugely significant but is nonetheless an indication that some change is arising due to the atmospheric boundary.

2.5 Discussion/Future Work

The results presented in the previous section summarize the effects of implementing different atmospheric treatments in conjunction with a stellar evolution code. An initial point to note is that although the geometry has a minor influence on the

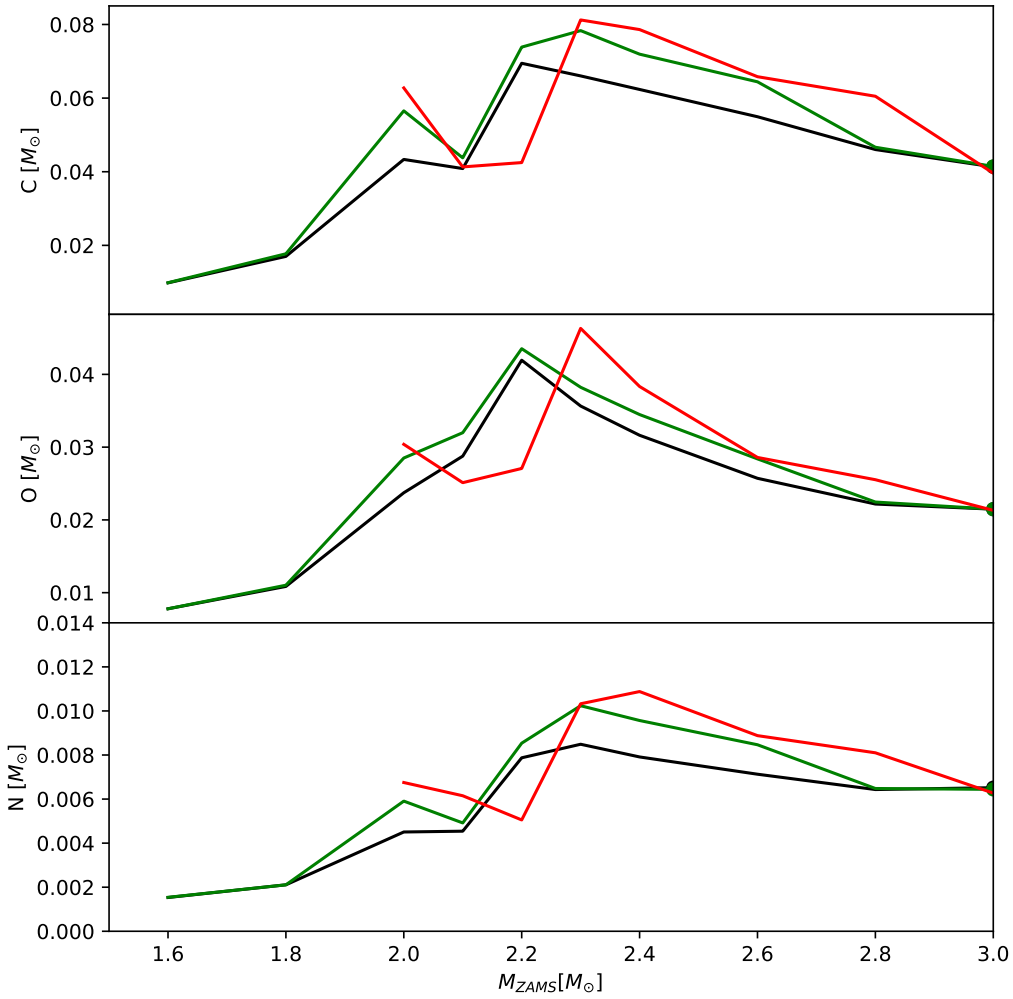

Figure 2.20: Chemical yields of Carbon, Oxygen and Nitrogen as a function of ZAMS mass for models with atmospheric boundary conditions denoted by Black: RM-pp, green: PM-pp, red: PM-pp-ms

problem when comparing the plane-parallel and spherical analytic relations, it is not significant. In particular, changes resulting from this alteration are negligible in comparison to changing the mean opacity treatment used, whether in conjunction with the plane-parallel or spherical analytic method.

Indeed, changing the mean opacity used within the analytic frameworks appears to provide a method for anticipating the effect that using RT models for the full TP-

AGB evolution would have since it is not currently possible to do this directly. Section 2.4.1 outlines that using PM opacities in the outer layers of the atmosphere in some way mimics the behaviour of using the RT models to provide the outer boundary condition. Although not ideal, this provides a platform to consider the implications for stellar evolution models based on current assumptions used in defining the stellar atmosphere.

Furthermore, it has been shown that attaching such models at greater optical depth moves the evolutionary tracks, at least on the RGB, to even lower effective temperatures than the use of the Planck mean opacity in the outermost layers. There is also a slight decrease in the luminosity of the red bump on the RGB in conjunction with this shift to lower effective temperatures.

The influence on the TP-AGB evolutionary models is at first glance not very significant. However, when considered in a wider context, and seeing the same behaviour across several mass models it becomes apparent that the outer boundary should not be dismissed so easily. That is not to say that it is causing drastic changes to the models, at least not in a way which can be separated from the outcome of using a different mass-loss prescription.

There are indications that the outer boundary can at least potentially influence the third dredge-up mechanism, as evidenced by the $^{12}C/^{13}C$ ratio and the temperature at the base of the convective envelope. The variation of the yields, although small, are also indicative of changes due to the atmosphere, although any observational differences are negligible for both the IFMR and C-star lifetimes, at least outside the mass range exhibiting anomalous behaviour. The only notable effect is the change in effective temperature, which could also be brought about by changing the mixing length parameter and whose influence could also be reproduced by a change in mass-loss prescription

The comparison of models calculated from the MS with different atmospheric treatments, alongside those calculated from the same stellar model at the start of the thermally pulsing phase, suggests that the atmosphere is also not playing a significant role in the earlier phases of evolution. Additionally, an odd behaviour in models with a mass $2.1 - 2.3 M_{\odot}$ was observed and which is discussed in more detail in the next chapter.

This work has predominantly focused on test cases and trying to understand what, if any, influence the outer boundary has on the evolutionary models. For the investigation to carry on further would require detailed RT models to be produced at very low log g values, in order to cover the entire evolutionary cycle of these models. In addition, it would be desirable to do so for a fine grid of C/O values in the abundances, as it is clear this can rapidly change the outer boundary in the

region around C/O=1. More immediately it would be possible to further investigate whether the effects become stronger at different metallicities. However, given the lack of any significant changes arising from the outer boundary condition in comparison to other areas of uncertainty, such as mass loss and convective boundaries, there is no urgent need to update the treatment of the atmosphere in stellar evolution codes.

2.6 Conclusion

This work has considered the influence of the outer boundary condition on the evolution of TP-AGB stars and presented the effects of changing standard treatments. The geometry and mean opacity treatment were investigated, along with a grid of radiative transfer models of stellar atmospheres.

Given the complexities involved in TP-AGB evolutionary calculations, drawing definitive conclusions is far from straightforward. However, this work has shown that although not significantly changing the interior evolution of the stellar models or observational constraints, the outer boundary condition does have some minor influence on the results obtained, for instance in terms of the predictive powers of the models.

In particular, it appears that whether through the implementation of radiative transfer models, or the use of some form of equivalent opacity treatment the result is to reduce the effective temperature of the models. This is also the case if a larger optical depth is taken for fitting the atmospheric model to the stellar interior. This change in effective temperature could largely be down to the lower value of the mixing parameter ($\alpha_{\rm MLT} = 1.5$) taken in the radiative transfer models, effectively reducing the value used in the outer layers of the star lowering the temperature. It is in some way possible to consider the effects of altering the outer boundary condition to be equivalent to changing the mass-loss prescription implemented, but that does not negate the meaning of the results presented here, but instead only highlights the complex nature of these stars and the many uncertainties which still exist.

There is, of course, a significant degeneracy with the mass loss prescription on the results of the model, and given the lack of an immediately realisable, physically realistic alternative for the atmospheric treatment in stellar evolution models, it is not currently necessary to consider the matter further. However, in principle, a physically realistic treatment would require full radiative transfer models covering the entire TP-AGB evolution, also covering both the C/O and mass parameter space, but most importantly extending to sufficiently low surface gravities to follow the full evolution.

Chapter 3

Anomalous Behaviour

During the course of the investigation into the atmospheric boundary condition in Ch. 2, an unexpected behaviour was observed which is not believed to have been previously observed in TP-AGB evolutionary models. Within a specific mass range ($2.1 - 2.3 M_{\odot}$), the regular thermally pulsing behaviour was seen to terminate before the star had lost a significant proportion of its outer envelope, instead returning to a more stable double shell burning configuration. This was followed by a resumption of the thermally pulsing phase, albeit with a substantially altered behaviour where the interpulse period is reduced and the amplitude of the maximum helium luminosity has decreased. This also resulted in significantly changed observable properties arising in the models which experience this phenomenon, in comparison to those which don't, with significantly increased carbon-star lifetimes ($\gtrsim$10Myr) and final core masses $\sim 0.1 M_{\odot}$ larger than might otherwise have been expected. These changes in the properties of the models could, in fact, help to alleviate tension with the observed IFMR and C-star lifetimes, as can be seen in both Ch. 2 and Ch. 7.

Further investigations were considered to be prudent, in an attempt to ascertain whether this behaviour is indeed physical rather than a numerical artefact and to determine the cause of this behaviour. This chapter focuses on this anomaly and begins in Sec. 3.1 by introducing the behaviour which was observed in the calculations discussed in the previous chapter. Following this, Sec. 3.2 presents further investigations which try to understand the physical reasons for the observed behaviour.

3.1 Models from Atmospheric Calculations

Of particular note from models calculated in Ch. 2 is the odd behaviour which was encountered in the models at a mass of $2.2 M_{\odot}$, as was seen in Fig. 2.17, which

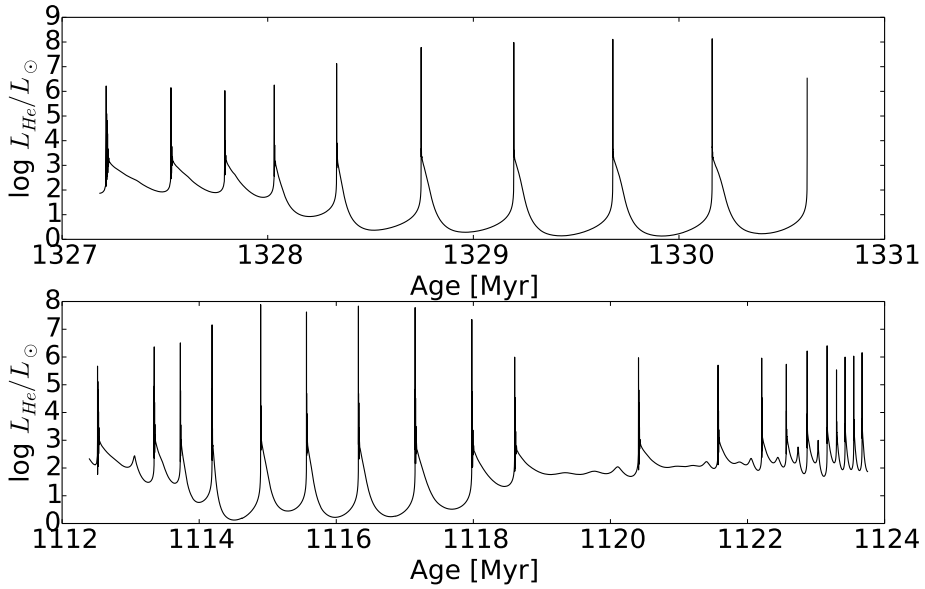

Figure 3.1: Helium luminosity for a $2M_\odot$ (top panel) and a $2.2M_\odot$ (bottom panel) TP-AGB model.

resulted in additional models being calculated at $2.1M_\odot$ and $2.3M_\odot$. Rather than an anomaly, a similar outcome was found with the addition of these masses, whereby the TP-AGB evolution is, in one particular way, quite different to what is observed at other masses. The top panel in Fig. 3.1 shows a typical helium luminosity for a $2M_\odot$ star progressing through the TP-AGB, where there is a fairly regular interpulse period and a gradual increase and then decrease in the peak luminosity at each thermal pulse. In contrast to this, the bottom panel in Fig. 3.1 shows the same thing for a $2.2M_\odot$ star, where something quite different is observed. In addition to the occasional irregular feature, the model progresses through a similar pattern of regular thermal pulses, before experiencing a quiescent phase ($\sim$ 2Myr) and then resuming thermally pulsing behaviour, but with a drastically reduced interpulse period and more erratic peak helium luminosity. During this second phase, third dredge-up does not occur as the star is not thermally pulsing, which leads to a continuing core growth, and hence the noticeably increased final masses in Fig. 2.17. Additionally, as the models have already become carbon-rich prior to the quenching and re-ignition of the thermal pulses, the C-star lifetimes were drastically increased to above $\sim$10Myr, as was also seen in Fig. 2.19.

Given this behaviour is seen in three separate mass models, with different atmo-

spheric treatments, gives the initial impression that this effect is physical rather than numerical. Additionally, that this occurs in the models which have the lowest core masses at the onset of the TP-AGB suggests that this is more than a coincidence and is, in fact, more likely connected in some way to this physical phenomenon. The overall effect may also be due to the overly-efficient third dredge-up implemented here (see Weiss & Ferguson, 2009; Andrews et al., 2015, for evidence of tension with observations), as running the same model without overshooting avoids this behaviour altogether. The physics of this phenomena is further explored in the next section.

3.2 Understanding the Physical Behaviour

To begin with, it is worth taking a moment to define what is meant by quiescent phase. This is distinct from a prolonged interpulse period where the helium luminosity drops lower prior to the next thermal pulse but is rather where the star returns to a state of double shell burning without the occurrence of thermal pulses. This can also be seen in the more moderate and consistent, if a little erratic, helium luminosity which is clearly distinguishable from the more typical decrease and increase seen in the normal thermal pulse cycle.

3.2.1 Varying the CBM Efficiency

The core mass and helium luminosity for four models, evolved with different CBM efficiency through the TP-AGB taken from the same model prior to the first thermal pulse of a $2.2M_{\odot}$ star with Z=0.012 and evolved up till the first thermal pulse with CBM mixing parameter f_{CBM} =0.016. The first column of 3.2a shows the same model which was shown in the previous section, demonstrating that the quiescent phase begins when the model has reached its lowest core mass. This gives an indication that the idea the core mass is in some way important, as was indicated by the mass range in which the behaviour was observed, may be correct. This also demonstrates that the treatment of the convective boundaries is also likely playing a role, given the decreasing core mass prior to the quiescent phase, when the core mass is expected to grow during the TP-AGB (Kalirai et al., 2014).

The second column in 3.2a shows a model where no CBM has been applied during the TP-AGB, with the absence of any such odd behaviour quickly becoming apparent. However, it also clearly shows that the core mass is growing throughout the TP-AGB, which could again indicate the anomalous behaviour is an artefact of the low core masses reached through the combination of the low core mass at the first thermal pulse and the decreasing core mass due to overly efficient third

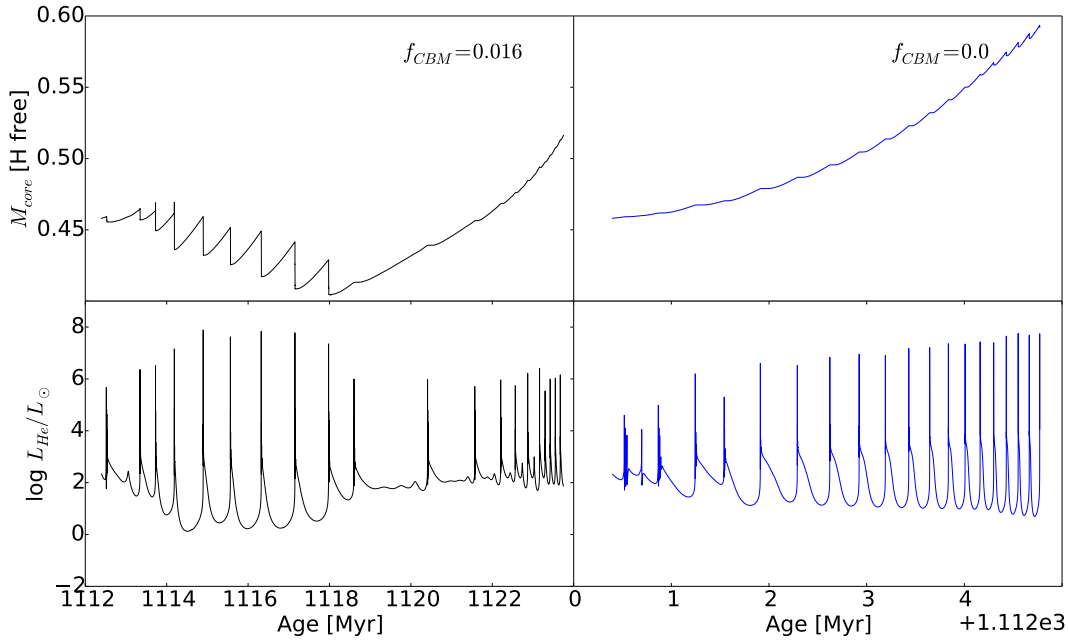

(a)

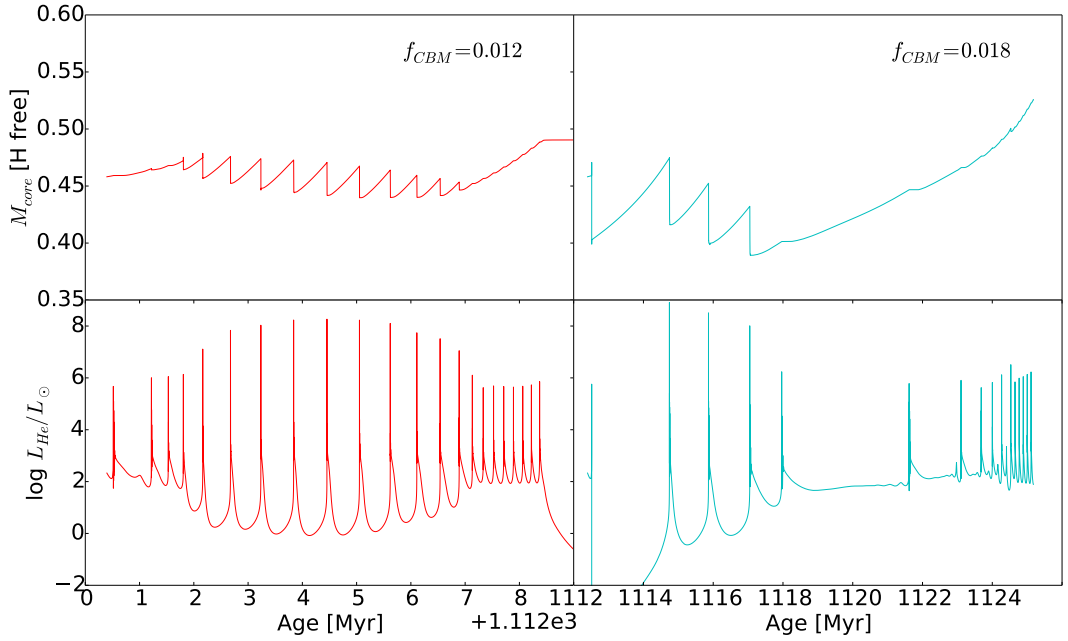

(b)

Figure 3.2: The hydrogen-free core masses (top panels) and helium luminosities (bottom panels) for 4 different $2.2M_\odot$ models, taken from the same pre-AGB evolution with $f_{\rm CBM}$ =0.016 and then evolved separately through the TP-AGB with the value indicated ($f_{\rm CBM}$ =0.016, 0.0, 0.012, 0.018).

dredge-up. Another point to note is the gradually reducing interpulse period as the evolution progresses, something which is already known to be related to to the core mass (Paczynski, 1975) and which will be discussed further in the following section.

The first column of 3.2b shows a model where $f_{\rm CBM}$ =0.012 has been applied during the TP-AGB and which does not experience the quiescent burning phase, but does have a decreasing core mass initially and then a quenching of the third dredge-up followed by a rapid decrease in the interpulse period as the core begins to grow uninhibited by the third dredge-up mechanism.

The second column of 3.2b shows a model where $f_{\rm CBM}$ =0.018 has been applied during the TP-AGB and which does experience a quiescent phase. This occurs, perhaps expectedly, earlier than for the model with $f_{\rm CBM}$ =0.016 but is preceded by an extremely strong third dredge-up event after the first thermal pulse. However, it is notable that although this leads to a significant drop in the core mass and leads to a prolonged interpulse period, it differs from the quiescent phase which occurs later and which is the focus of this chapter. Although odd in comparison to the other thermal pulses observed, the characteristic behaviour is still the same with the dip and gradual increase of the helium luminosity and is only quantitatively different from the other thermal pulse cycles. This contrasts with the quiescent phase where a fairly constant helium luminosity of $L_{\rm He} \sim 2L_{\odot}$ is observed between thermal pulses.

Additionally, models were calculated with $f_{\rm CBM} = 0.014$ and $f_{\rm CBM} = 0.02$ with the first also experiencing a similar behaviour to that seen in the $f_{\rm CBM}$ =0.016 case and the final one struggling with convergence problems early on, perhaps experiencing an even stronger dredge-up event than is seen in the case of $f_{\rm CBM}$ =0.018. This may be a result of the sudden change to the value of CBM applied, given all sequences begin from a model taken prior to the first thermal pulse which had until that point had $f_{\rm CBM}$ =0.016 applied at all boundaries.

Although this behaviour can thus only be observed in a limited range, where the core mass is decreasing from an already low core mass at the first thermal pulse but before the dredge-up is too strong to prevent convergence, it progresses in such a way as to suggest it is indeed physical.

3.2.2 Core Mass-Interpulse Period Relation

A core mass-interpulse period relation (Paczynski, 1975) has previously been empirically derived which helps to understand the reduction in the interpulse period after the quiescent phase, when the core begins to grow. For each thermal pulse of the models calculated, the core mass and subsequent interpulse period are shown in Fig. 3.3 with the top panel showing the maximum core mass prior to the interpulse

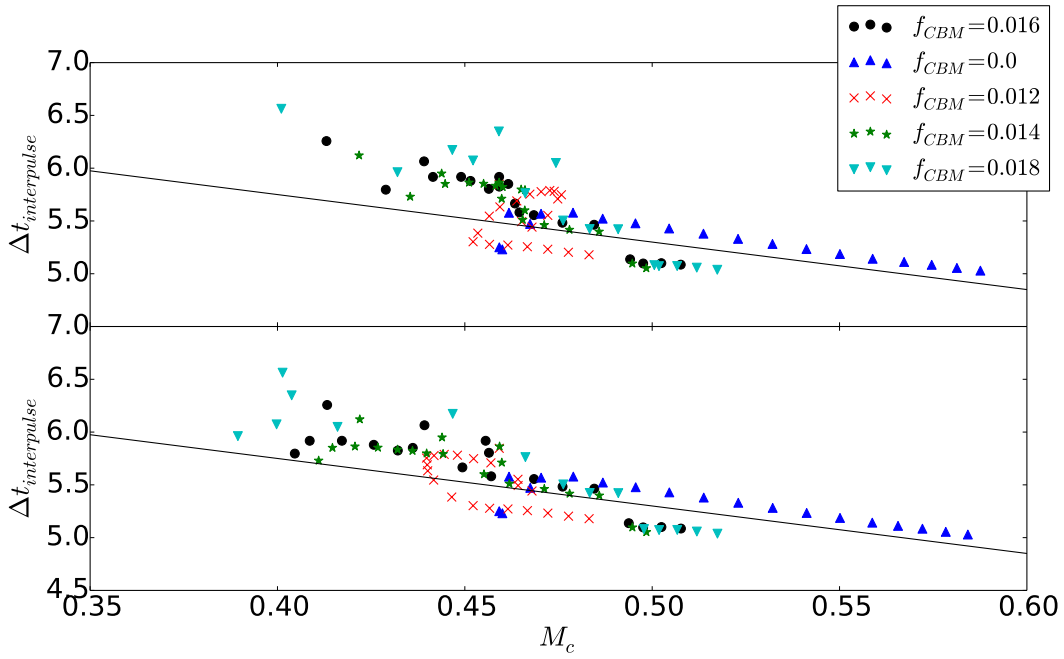

Figure 3.3: The core mass plotted vs the interpulse period for each thermal pulse, with different markers for each evolutionary model. The top panel takes the core mass at the maximum before the thermal pulse, the lower panel the minimum immediately after the thermal pulse and the solid black line is the relation between core mass and interpulse period taken from Paczynski (1975).

period, the lower panel the minimum core mass. For the moment, only the lower panel is considered as the expectation would be this is what is directly related to the interpulse period, although the relation appears to hold in both cases. The solid line is the relation determined by Paczynski (1975) and can be seen to be largely consistent with the models calculated here.

Beginning with the simplest case, where $f_{\rm CBM}$ =0, it can be seen that after the first couple of thermal pulses, the increasing core mass and decreasing interpulse period agrees very well with the slope of the relation taken from Paczynski (1975), albeit shifted slightly above the line. A smooth behaviour is also seen in the case where $f_{\rm CBM}$ =0.012, except that, to begin with, the markers move in the opposite direction due to the decreasing core mass, but similarly above the relation of Paczynski (1975). This model then proceeds to turn around as the third dredge-up is quenched and the core begins to grow, now running parallel to the relation but slightly below.

Interestingly, this is also what is observed in the other cases, with an initial agreement with the slope of the relation taken from Paczynski (1975) as the core mass is decreasing, before later following it in the opposite direction shifted slightly downwards. Of course, in the cases of $f_{\rm CBM}$ =0.014 and 0.016, the effect is not quite as obvious, as there is a break (corresponding to the quiescent phase) where the core mass begins growing but no thermal pulses occur, as opposed to the $f_{\rm CBM}$ =0.012 case where there is a smooth transition from a decreasing core size to core growth. The $f_{\rm CBM}$ =0.018 case also follows this trend, although the pulses prior to core growth beginning are more erratic due to the substantial third dredge-up experienced in this model.

Furthermore, a more complex core mass-interpulse period relation was considered, that of Wagenhuber & Groenewegen (1998), which gives a specific relation for each core mass at the first thermal pulse. This reproduced the shape of the model with $f_{\rm CBM}$ =0, where there is initially a curve before the linear behaviour begins, however, this is not able to reproduce the behaviour of the decreasing core masses and is therefore not considered further.

All of this seems to explain the drastic change in interpulse period before and after the quiescent phase, however, it does not do anything to explain the onset of the quiescent phase itself. This leads to the inclusion of the top panel in Fig. 3.3, as there seems to be a more significant cutoff in the core mass at the onset of the thermal pulse $\sim 0.43 M_{\odot}$ below which there is one point for each of the models which experience the quiescent phase and where this point corresponds to the thermal pulse preceding the first (and longest) quiescent phase. The minimum core mass in the lower panel seems to be less clear-cut, which is believed to be due to the effects of strong dredge-up episodes, but which are distinct from the odd behaviour leading to this investigation.

The core mass-interpulse period relation is again shown in Fig. 3.4, this time for $2 M_{\odot}$ models calculated at Z=0.008. The models were again evolved up to just prior to the first thermal pulse with $f_{\rm CBM}$ =0.016 and then evolved with different values during the TP-AGB. It was again the case that for each of the models with $f_{\rm CBM}$ =0.014, or higher, the quiescent phase was observed, while for $f_{\rm CBM}$ =0.012 it was not. However, in each case, there was a very strong dredge-up episode after the first thermal pulse, similar to that seen in the $f_{\rm CBM}$ =0.018 case previously. This perhaps explains why the behaviour for these models is also more erratic than for the previous set of models. What can be seen, however, is again a more distinct cutoff for the peak core mass-interpulse period in the top panel. There is one point for each of the three models which experience the quiescent phase below $\sim 0.43 M_{\odot}$ corresponding to the thermal pulse prior to the onset of the quiescent phase.

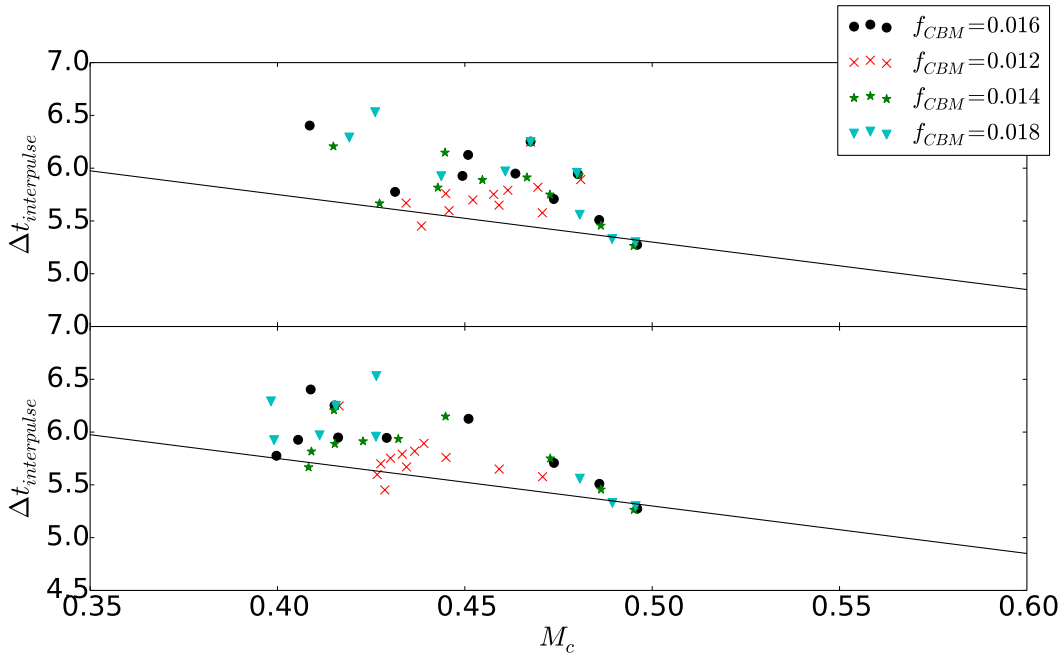

Figure 3.4: The core mass plotted vs the interpulse period for each thermal pulse, with different markers for each evolutionary model calculated at Z=0.008. The top panel takes the core mass at the maximum before the thermal pulse, the lower panel the minimum immediately after the thermal pulse and the solid black line is the relation between core mass and interpulse period taken from Paczynski (1975).

The strong CBM is clearly necessary to decrease the core mass to this level, yet the low core mass at the onset of the first thermal pulse also seems to be required. Although not identified as such, this behaviour is also present in a $2M_{\odot}$ model at Z=0.008 previously calculated with GARSTEC (Kitsikis, 2008; Weiss & Ferguson, 2009). However, a comparison of core masses at the first thermal pulse (see Fig. 6.4 in Kitsikis, 2008), with models from Karakas (2003), shows that this may be difficult to reproduce with other codes. The sharp dip in core mass at the transition between degenerate/non-degenerate core helium ignition seen in the models here (as seen in Fig. 6.1) is not present in the models of Karakas (2003). This could also indicate an importance of the pre-AGB treatment, as initial $2M_{\odot}$ models at Z=0.008 calculated with the MONASH and MESA codes result in the core mass at the first thermal pulse being $\sim 0.55M_{\odot}$ and $\sim 0.5M_{\odot}$ respectively (Simon Campbell, private communication). This compares with $\sim 0.47M_{\odot}$ for the equivalent model discussed

here. It also shows the importance of the initial mass, if trying to reproduce this behaviour, as the dip seen in the function of initial core masses in 6.1 shows the minimum core mass depends on pre-AGB treatment and that the difference in core mass from a $1.9M_{\odot}$ model to a $2M_{\odot}$ model is in that case almost $0.03M_{\odot}$.

3.2.3 Shell Thickness

Although it appears to be related to the small core masses, there is still the question of why it is different, what is causing the quiescent phase of burning and leading to the suppression of the thermal pulses. To understand this, the geometric argument, outlined in Ch. 1.1.2, necessary for the thermal runaway in the helium burning shell is considered. This requires that the thin shell condition is satisfied, with the full argument in Kippenhahn et al. (2012) requiring that the ratio between the shell thickness and the distance from the centre of the star should not exceed $D/r = 1/4$ for the case of an ideal monatomic gas.

This is, of course, a simplified argument, however, the thin shell condition is known to be a necessary component of the thermal pulse. Therefore, the ratio of the shell thickness, D, to the radius at the base of the shell, r, is shown in the top panel of Fig. 3.5, with the helium luminosity again shown in the lower panel, for the $2.2M_{\odot}$ model calculated with the standard RM-pp atmosphere and $f_{\rm CBM}$ =0.016 at all times. The shell thickness and radius are only calculated when the full evolutionary model is stored, hence it is not as smooth a function as for the helium burning luminosity which is saved for every evolutionary time-step.

Although it does not correspond to a value of 1/4, it must be said that the thickness of the helium burning shell during the quiescent phase is a much larger fraction of the radius than during the preceding interpulse phases, and again decreases during the subsequent interpulse phases.

Although not absolute, this may also explain why there is a more obvious transition in the core mass at the onset of the thermal pulse, rather than this occurring in the $f_{\rm CBM}$ =0.018 case after significant dredge-up events. It is not only the core size, which can be reduced by strong dredge-up but the more general conditions which appear if the core size decreases to $\lesssim 0.43M_{\odot}$ at the beginning of the thermal pulse.

3.2.4 Conclusion

Overall, the evidence seems to be very much in favour of this behaviour being physical, as opposed to numerical, albeit something which is only possible under very specific conditions. However, it is seen across a range of masses with varying CBM

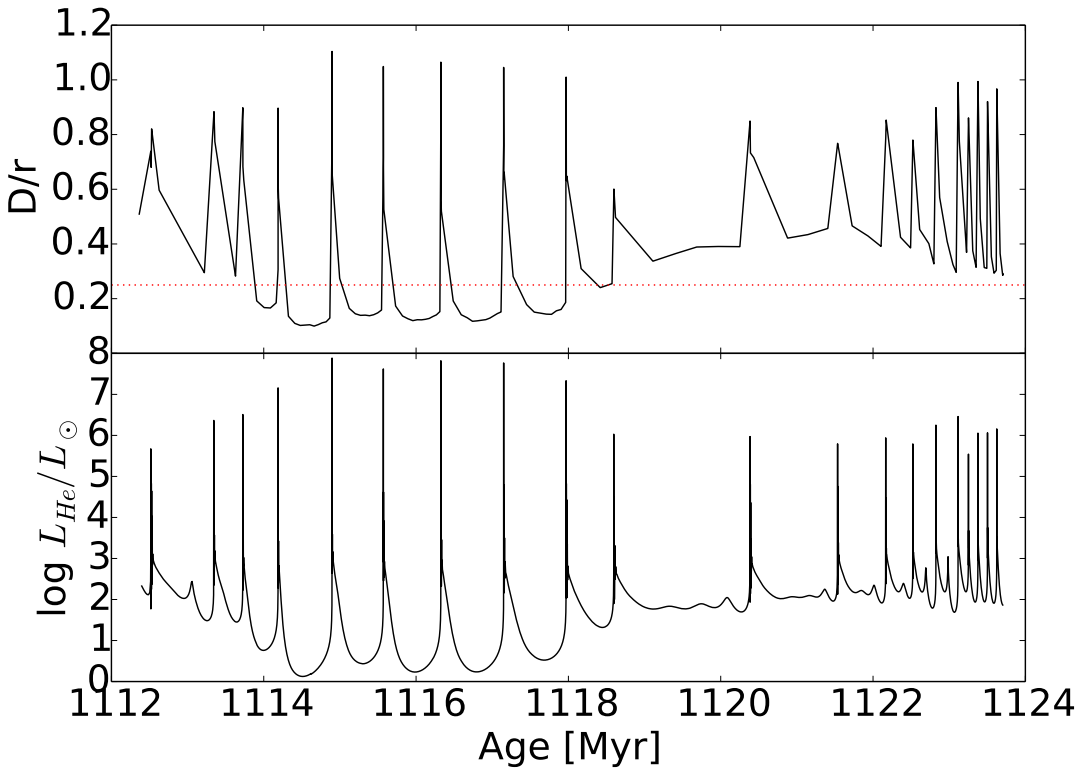

Figure 3.5: The ratio between the thickness of the helium burning shell and the radius at the base of the shell (top panel) and the helium burning luminosity (lower panel) for a $2.2M_{\odot}$ model. Horizontal red dotted line indicates D/r=0.25.

during the TP-AGB and at different metallicities. It may only occur when a combination of factors culminate in the reduction in core size, from an already low value, where the models can also converge, yet it does appear to be physical. From the models considered here, a core mass below $\sim 0.43M_{\odot}$ at the start of a thermal pulse is required to instigate this phenomenon.

Each step of the observed behaviour has an explanation in line with the expectations of the physical arguments. Initially, the strong CBM causes the core mass to decrease, due to efficient third dredge-up, until the thin shell condition, requiring small D/r, is no longer fulfilled, quenching the thermal pulses. The lack of thermal pulses prevents the third dredge-up, allowing the core to grow until D/r is sufficiently small and the thermal pulses resume. As the core mass is now larger, the interpulse

period is noticeably shorter than prior to the quiescent phase, in line with expectations from previously seen core mass-interpulse period relations (Paczynski, 1975; Wagenhuber & Groenewegen, 1998).

None of this is intended to suggest that it is present in stars, but rather that it is in principle possible. This could be especially true if the mechanism behind convective boundary mixing is, in fact, something more object specific, such as rotation, meaning that only a limited number of stars could experience such a quiescent phase during the TP-AGB.

Part II

Convective Boundaries

Chapter 4

Introduction

This chapter presents background information about additional mixing beyond the sharply defined Schwarzschild boundary of convective zones, which is the focus of this part of the thesis. The investigation into CBM in the following chapters outlines the importance and influence arising from such mixing with regards to TP-AGB stars, including the treatment of convective boundaries during prior stages of stellar evolution, and tries to constrain additional mixing on the TP-AGB. This is set out through several subsequent chapters and is done by distinguishing which convective region is being considered, by performing a series of numerical experiments and through the calculation of a large number of evolutionary models.

After an introduction to the background material, and motivation for this work in this chapter, there follows in Ch. 5 a series of technical investigations and numerical experiments, with a focus here on a thorough, theoretical investigation, understanding to what extent the treatment of the various interfaces between convective and radiative regions plays a role in the ongoing TP-AGB evolution. Following this, Ch. 6 investigates the influence of CBM during pre-AGB phases, along with a basic investigation of the TP-AGB, with an emphasis on the effect this has on the masses which undergo third dredge-up and hot-bottom burning. Subsequently, the final chapter accounts for the limits placed by the theoretical considerations discussed within the other chapters, and proceeds to combine this with observational data to constrain, as far as possible, the way in which such stars are modelled.

This chapter, beginning in section 4.1, outlines the current status and hence motivation behind the work presented here with the method of implementing the desired functionality outlined in section 4.2 and a review of the current evidence for mixing at these boundaries in section 4.2.2.

4.1 Background and Motivation

Stellar evolution codes have been remarkably successful since their inception, however, an area which remains problematic when working within their 1-dimensional description of 3-dimensional stars is convection (Arnett et al., 2015). In particular, the boundary between convective and radiative zones presents a challenge which, even with the advent of 3D hydrodynamical simulations (Hurlburt et al., 1994; Freytag et al., 1996; Herwig et al., 2007; Baraffe et al., 2017), has proven to be a persistent source of uncertainties in the evolutionary models which are produced.

This is a fact which can become especially relevant when considering the evolution during the TP-AGB, where boundaries at the edge of convective zones are known to play an important part in governing many important properties and observables of these stars (Herwig et al., 1997; Herwig, 2005), such as 3^{rd} dredge-up and the initial-final mass relation, which were outlined earlier in Ch 1.1.2.

Initial thoughts on the subject, were based on a simple physical justification that it seems improbable that the convective boundary in a physical star could be as absolute as was typically found in a stellar evolution code (Viallet et al., 2015), where one grid point is convective and the next radiative (as determined principally by the Schwarzschild (Schwarzschild, 1906) or alternatively the Ledoux criterion (Ledoux, 1958) for stability, given in Ch. 1.2). The premise was that an eddy within the convective zone itself would have some finite velocity as it reached the boundary, and the momentum would carry the eddy some distance beyond the strict boundary into the radiative zone.

Based upon this initial physical argument, the phenomenon was commonly referred to as convective overshooting, although this has since been replaced in many instances by convective boundary mixing (CBM) or sometimes convective penetration. Further references to the process of additional mixing beyond the strictly defined convective boundary shall use the term CBM. This is to account for the fact that, although the same descriptions which were typically derived for the case of convective overshooting, they are often also taken to account sufficiently for other forms of additional mixing at convective boundaries, and the more general term masks current uncertainties on the subject of which form of mixing is taking place in stellar interiors.

Certainly, it has been seen in hydrodynamic simulations (Freytag et al., 1996; Herwig et al., 2007; Meakin & Arnett, 2007; Mocák et al., 2009; Baraffe et al., 2017; Pratt et al., 2017) that the strict Schwarzschild boundary, as implemented in 1D stellar evolution codes, simply doesn't appear in the form of a composition discontinuity in a spherically symmetric manner when it comes to multi-dimensional

models.

The principle way in which mixing beyond the formal convective boundary is included in stellar evolution codes follows the same implementation as Herwig et al. (1997) who was the first to incorporate results of hydrodynamic simulations performed by Freytag et al. (1996) and discussed in more detail in Ch. 1.2. The method used throughout this work, at least in principle, follows this description, and as such the mixing efficiency parameter, $f_{\rm CBM}$, has comparable meaning to others who also use it. There are of course always slight differences when it comes to code implementation, and as has been highlighted (e.g. by Miller Bertolami, 2016) the cutoff value is one such area where differences can arise. This is discussed in later sections, and the effect of changing the cutoff value, in particular, is investigated in Appendix B.3.

There are alternative ways of including some form of additional mixing, for instance, Karakas & Lattanzio (2007) follows the method outlined in Lattanzio (1986) where no explicit mixing is applied, but instead, a point between the last convective grid point and the first radiative grid point is found, which is determined to be neutral. This is not overshooting in the traditional sense but does allow for certain aspects of CBM to be reproduced, such as increased third dredge-up efficiency (Frost & Lattanzio, 1996). Alternatively, Cristallo et al. (2009) also implements an exponential decay, but working with the velocity rather than calculating a diffusion coefficient as outlined by Herwig et al. (1997). More importantly, a significant difference with this approach is that it is only ever applied to lower boundaries, meaning that their models do not include additional mixing from convective cores.

For the purposes of this work, it is taken to be the case that the Herwig et al. (1997) description of CBM is sufficient to represent the various forms of mixing, beyond the momentum based variety it was originally intended to reproduce. This may not be the case, as it does not account for any time-dependence which may exist from other sources of mixing, whereby different mechanisms could become dominant during the thermal pulse cycle, altering the outcome. However, this is too poorly understood at this time, to extend beyond the current investigation.

Of the other mechanisms which may be responsible for additional mixing at convective boundaries, rotation and gravity waves have been at least partially investigated. It is questionable whether the 1D models which have been used to explore the effect of rotation on AGB stars (Langer et al., 1999; Herwig et al., 2003; Piersanti et al., 2013) is representative of the physics at play. From the models available, it seems that not only is rotation insufficient to create the ^{13}C on its own (Langer et al., 1999), it in fact hinders s-process nucleosynthesis (Herwig et al., 2003). Having said that, the picture is not entirely clear as although Piersanti et al. (2013) agrees that

s-process abundances decrease with increased rotation velocity, they suggest that rotation can induce additional mixing and higher abundances at velocities above 60 km s^{-1}, and particularly for lower metallicities. Rotation is also used to explain the spread in observed abundance patterns (Piersanti et al., 2013). As for gravity waves, much also remains unclear, although it has been suggested (Denissenkov & Tout, 2003) that they could provide an additional source of mixing, although Herwig et al. (2007) emphasises the need to study this in greater detail.

In many instances previously, the extent to which additional mixing occurs has been calibrated based on one particular phase of evolution and then been applied in all cases. This is an approach which is founded in a necessity due to a lack of better information and has gradually been replaced by an acknowledgement that different treatments of convective boundaries are required during various stages of evolution. Although fraught with the danger of essentially increasing the number of free parameters in a stellar evolution code, this approach is a necessary requirement in trying to understand the physical processes and which has foundations in observational evidence and hydrodynamical simulations. A more detailed discussion of the different boundaries and available evidence for additional mixing is presented in section 4.2.2.

Trying to untangle the justifications for the various treatments chosen is not the aim of the following chapters, rather to outline the different arguments for, and against, additional mixing at a given boundary. Additionally, it is desired to obtain a deeper understanding of the overall possible influences on the theoretical models of any given parameter choice, and to test the sensitivity of what can often be to some extent arbitrary choices of CMB treatments as determined by what a particular group is interested in studying.

For instance, although it is quite well established (Maeder & Meynet, 1991; Stothers & Chin, 1992; Schroder et al., 1997; Ekström et al., 2012) that some additional mixing is required from convective cores on the upper main sequence, it is not always the case that models produced for the TP-AGB (such as for yields or evolutionary tracks) include significant, or any, CMB from convective cores (Cristallo et al., 2009; Karakas & Lattanzio, 2007). Part of Ch. 6 focuses on this pre-AGB treatment of CBM, to ascertain whether this is having a significant knock-on effect on the models which are then produced. This is of relevance given the output from these grids of models are utilized by the wider astrophysics community, and if there is a significant influence from the treatment of convective boundaries during the main-sequence phase of the evolution on the later AGB phase, then it is something which is of relevance for the community as a whole.

Furthermore, the application of the value taken for additional mixing, as calibrated from core hydrogen burning stars, can lead to results which are in tension

with observations when applied to all boundaries during the TP-AGB evolution. This has been shown to be the case for the stellar evolution code used here (Weiss & Ferguson, 2009; Andrews et al., 2015), and provides an additional motivation for examining the influence of additional mixing at the various convective boundaries.

4.2 Method

Within GARSTEC a grid point is considered to be convective if the Schwarzschild criterion[1] for dynamical stability is not satisfied, i.e. if the radiative gradient is larger than the adiabatic gradient. Successive convective grid points are then grouped together and considered to be a single convective zone. This then requires the addition of some further prescription within the code, to allow for the implementation of convective boundary mixing. In this case, the method as described in Ch. 1.2 is then applied at the outermost grid point of a convective zone, and a description of convective boundary mixing is thus incorporated into the stellar evolution code.

Although it is, to some extent, possible to investigate the effect of mixing at different convective boundaries by carefully changing the efficiency parameter f_{CBM} for different stages of the evolution, this can be time-consuming and open to variations between comparative models. Furthermore, despite the ability to say which is the main convective boundary that is influencing the evolution at a given stage, it is not necessarily certain. For example in Herwig (2000), a numerical experiment was performed to investigate the influence of the different boundaries on the third dredge-up efficiency over the course of a thermal pulse cycle. The same $3M_{\odot}$ model was run from when the PDCZ disappears after the 8th thermal pulse, for multiple values of f_{CBM}. Therefore the dredge-up during this phase probes the influence of f_{CBM} at the convective envelope, and following the models through the next thermal pulse shows how also including this value for f_{CBM} at the PDCZ changes the third dredge-up efficiency.

In any case, for an in depth study and for future ease of use, it is desirable to have flexibility in choosing values for f_{CBM} at different convective boundaries. This presents its own challenges, however, the procedure implemented here seems to work reliably for GARSTEC, for all the models which have been investigated in the course of this work. The convective zones are identified through a combination of their location within the star, the position and type of nuclear burning, and how the positions of convective and nuclear burning regions relate to each other. This is outlined in more detail in Appendix B.1.1, however a brief summary is as follows.

[1] The Ledoux criterion can also be taken, however, the Schwarzschild criterion is used as standard.

If the lower boundary of the convective zone is at the centre of the star, the type of nuclear burning identifies which convective core burning phase is taking place. If the upper boundary of the convective zone is the surface of the star then it is the convective envelope. If the convective region falls between the two nuclear burning shells, then it is the pulse-driven convection zone.

When defining such criteria as those which are given in Sec. B.1.1, it is impossible to claim they are always, and will always be, correct in their assignments. It is, however, possible to say that basic physical knowledge of the subject of study and the code being used informs the classification of the convective zones, while some minor tweaks after testing are to be expected. For the masses and evolutionary phases considered, the methodology has been carefully reviewed such that convective zones can be assigned consistently and correctly. Furthermore, the results from this work have been compared with prior tests which have been run for certain cases (see section 5.2), and it is not an entirely unknown subject area. As such it can be said with a reasonable degree of confidence that the assignment of convective zones functions as desired, and that if there are cases where this becomes an inherent problem, it is likely outside of the scope of this investigation.

4.2.1 Calculations and Analysis

How the calculations were carried out is specified in more detail in each relevant chapter, with some covering the full evolution and others a single thermal pulse, however, it can generally be said that they follow the same basic physics as outlined in Ch. 1.2. The models here are distinct from the previous chapter in that all include a standard plane-parallel grey atmospheric treatment, but also include interpolation in the C/O value for the Rosseland mean opacities. A further difference is that the models here, with the exception of the single thermal pulse models presented in section 5.2, follow the full evolution from the zero-age main sequence through to the end of the TP-AGB (where convergence allows).

Differences between models amongst groups do not only arise from the calculations, but also from the analysis so it is worth making a quick note of some of the ways certain things have been defined with respect to the results presented in this part of the thesis.

Extrapolation

Convergence remains an issue with TP-AGB models (see Lau et al., 2012, for a detailed overview), which leaves a decision to be made regarding extrapolation when presenting the results. It is again the case within this chapter that this is not done,

and final values are those taken at the final completed thermal pulse of the models. It would be possible to simply take the final core mass as the final mass, but as this varies during a thermal pulse cycle it was deemed more consistent to take the core mass at the same point relative to the helium luminosity in the sequence for each of the models. This does not equate to the final values for comparative models being taken at the same age or thermal pulse number.

Intershell Abundances

Within GARSTEC, the intershell abundances are not, as a matter of course, calculated and written as output after every thermal pulse, as would, in hindsight, be desirable. Instead, the values presented within this thesis are only calculated for times at which the full structure of the model is written. For these calculations, this was typically done every 2500 evolutionary models and is sufficient given the relatively small changes in the abundances after the early thermal pulses (this can be seen in Fig. B.2).

The time at which the values are most interesting is just after the PDCZ disappears, having mixed the region and setting the composition until the next thermal pulse. This is what is believed to be observed in the hydrogen deficient PG 1159 stars (Herwig, 2005). In hindsight, it would, therefore, have been preferable to store the values at the top of the intershell shortly after each thermal pulse, as this would be the relevant quantity for the study of post-AGB stars.

As this was not done, values are taken to be those at the mass shell halfway between the mass shells of maximum hydrogen and helium burning. However, certain additional requirements were also used to exclude individual models which were just prior to or during the thermal pulse, where the abundances obtained are either entirely Helium (which has built up below the hydrogen burning shell) or during the quiescent phase in hydrogen burning. Further discussion of this can be found in Appendix B.1.2.

Definitions: Third Dredge-Up and Hot-Bottom Burning

Part of the motivation of this project was to ascertain how the position between initial masses at which the transition, for models which undergo third dredge-up and hot-bottom burning, change due to the variation in the convective boundary treatment. It, therefore, becomes pertinent to point out how this has been done and importantly to introduce what is referred to within subsequent chapters as mild hot-bottom burning and also how the other quantities are determined numerically, which is not always trivial.

Primarily, all such assertions are based upon identifying the positions of the maximum and minimum helium luminosity and taking relevant quantities from the models at those positions. An exception would be the core mass, which is taken at the maximum value prior to the maximum in the helium luminosity, and the minimum is taken as the minimum value afterwards, before the core again begins to grow. The abundances are taken from the time of the minimum helium luminosity, as, at this point, they have had a chance to adjust since any third dredge up occurred.

This is demonstrated in Fig. 4.1 showing the surface C/O value, hydrogen free core mass and helium luminosity for two thermal pulses, with the blue vertical line indicating the maximum helium luminosity of one thermal pulse and the red line indicating the subsequent minimum helium luminosity. The top panel, showing the C/O value, demonstrates how the surface composition changes at the thermal pulse, although upon close examination also shows that there is a slight curve before it reaches its final interpulse value. This shows why taking the surface composition values at the time of the minimum helium luminosity is a good idea. Equally, the middle panel shows why the minimum helium luminosity would be a bad choice for taking the minimum core mass, as it has grown since the preceding thermal pulse. Instead, the core mass is taken either side of the maximum helium luminosity, finding the maximum/minimum core mass before/after the thermal pulse.

The identification of third dredge-up is then defined such that the core mass has decreased during the thermal pulse, and additionally that either the surface C/O value has increased by $\Delta\mathrm{C/O} > 0.005$ or the surface nitrogen abundance has increased by $\Delta\mathrm{N} > 0.00001$.

Hot-bottom burning is classified purely based on the surface abundances, and a model is said to have undergone hot-bottom burning during a thermal pulse cycle if the C/O value has decreased by $|\Delta\mathrm{C/O}|/ > 0.005$ or the C/N value has decreased by $|\Delta\mathrm{C/N}| > 0.03$.

This classification of hot-bottom burning appeared sufficient in terms of representing the observed phenomenon which is typically kept in mind, in particular the prevention of high mass carbon stars forming. However, during the course of the investigation, it was felt this did not necessarily represent the full picture, which can of course be a very difficult thing to do when trying to summarise the overall effect on a set of models. In any case, it was decided to introduce a further term for this purpose, referring to mild hot-bottom burning. This can be used to refer to the fact that although the temperature has not reached the values necessary to alter the CNO abundances, the depth to which the convective envelope penetrates is still having a notable influence on the star.

As such, mild hot-bottom burning is defined such that the criteria for standard

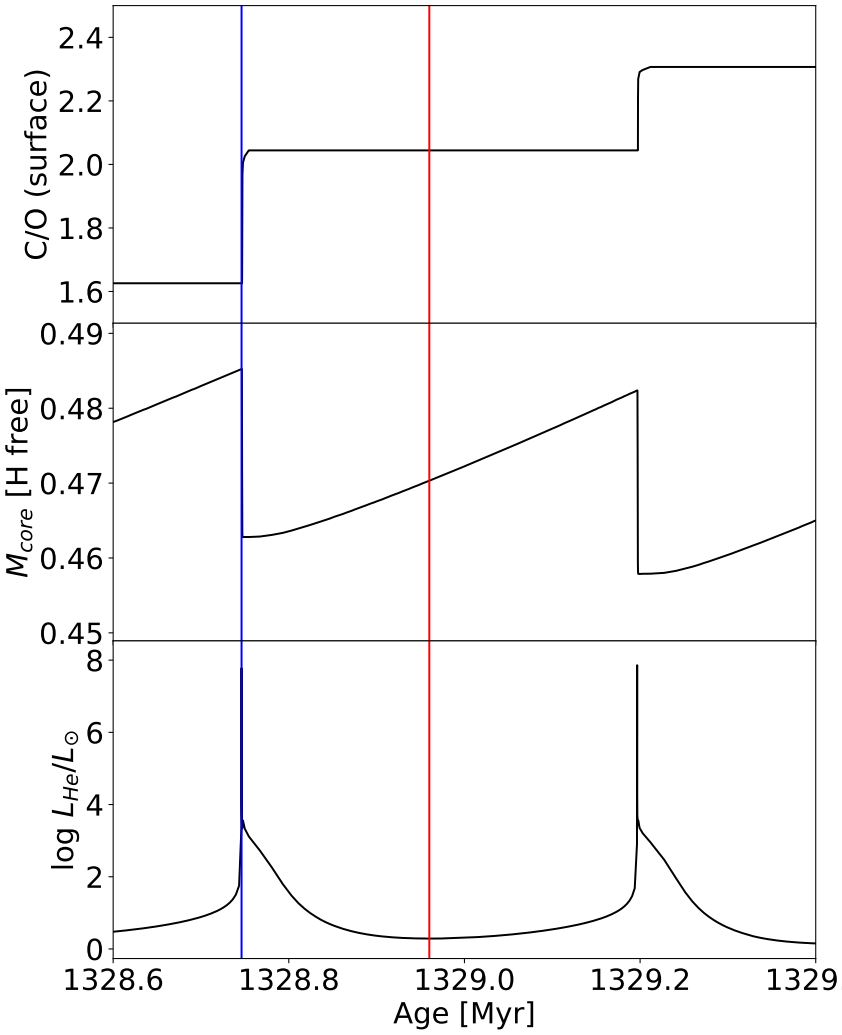

Figure 4.1: The surface C/O value (top panel), the mass of the hydrogen free core (middle panel) and the helium luminosity (bottom panel) for a $2M_{\odot}$ model for two thermal pulses. The blue vertical line indicates the maximum helium luminosity and the red the minimum helium luminosity during the subsequent interpulse phase.

hot-bottom burning are not met, but that there is a decrease in the carbon isotopic ratio, $^{12}C/^{13}C$.

4.2.2 Possible Extent of Additional Mixing

It is very difficult to determine how much additional mixing is likely needed in stellar evolution models at different convective boundaries and as such a variety of methods are used for current TP-AGB evolutionary models. This ranges from nucleosynthesis arguments for the extent of CMB necessary to reproduce the ^{13}C pocket below the convective envelope to hydrodynamical simulations or post-AGB observations to determine the additional mixing required from the PDCZ. These arguments are reviewed for the individual boundaries in this section.

Core Hydrogen Burning

There is considerable evidence for additional mixing, with a consensus of up to roughly 20% of the local pressure scale height (Herwig et al., 1997; Weiss & Ferguson, 2009; Miller Bertolami, 2016), for core Hydrogen burning stars on the upper main sequence. This is seen by the ability to reproduce the observations of the main sequence stars in open clusters (Maeder & Meynet, 1991; Stothers & Chin, 1992; Schroder et al., 1997) and eclipsing binaries (Claret, 2007; Stancliffe et al., 2015; Higl & Weiss, 2017).

For the thesis of Kitsikis (2008), a limit was manually included in GARSTEC for low mass stars (see also Weiss & Ferguson, 2009) following previous works on the topic (Ventura et al., 1998) whereby the value for $f_{\rm CBM}$ is gradually increased from $f_{\rm CBM}$ =0 at a lower mass ($1M_{\odot}$) to the chosen value for $f_{\rm CBM}$ at a slightly higher value ($1.5M_{\odot}$). The range across which this mass dependence of $f_{\rm CBM}$ is varied is sometimes taken to change with metallicity Miller Bertolami (2016), however, as models presented within this work are all above $1.5M_{\odot}$, this is not something which has been considered further.

Core Helium Burning

Although it can be physically motivated (Castellani et al., 1985), and there is some logic in thinking that one convective core should act in a similar manner to another, reliable constraints on mixing beyond the helium burning core do not exist in the same way as for core hydrogen burning stars.

A series of papers which try to constrain additional mixing at convective boundaries in core helium burning, red clump stars, begins with asteroseismic constraints

(Constantino et al., 2015) which support CBM. The evidence from star counts (Constantino et al., 2016) also seems to suggest that additional mixing is required beyond the Schwarzschild boundary in core helium burning stars. The most recent paper in the series, actually implements a physically motivated limit for additional mixing (as outlined in Spruit, 2015), with the result also supporting CBM, although with the constraint helping to suppress core breathing pulses [2], something which is not as much of an issue in the mass ranges considered in this chapter.

As such, it is not uncommon to take the same value for the core hydrogen burning phase (which may have been specifically calibrated for a given code) and applying this to the core helium burning as well (e.g. Weiss & Ferguson, 2009; Miller Bertolami, 2016; Jones et al., 2016; Ritter et al., 2017), given the lack of a convincing argument against it and a natural inclination to thinking it reasonable that it be similar to the core hydrogen burning phase.

Convective Envelope & Pulse-Driven Convective Zone

The boundaries of these convection zones are best considered together, given the inevitable connection between the two when considering the TP-AGB. It is already known that stellar evolution codes tend to require some form of additional mixing on the TP-AGB in order to achieve sufficient dredge-up to reproduce statistics from carbon star counts (e.g. from Girardi & Marigo (2007), at the necessary mass and metallicity (Herwig et al., 1997; Weiss & Ferguson, 2009; Miller Bertolami, 2016). However, it has also been shown that the inclusion of the value for $f_{\rm CBM}$ as calibrated by upper main sequence stars at all convective boundaries (e.g. in Weiss & Ferguson, 2009) results in such efficient third dredge-up that core growth is suppressed during the TP-AGB, leading to an IFMR that is in tension with observations (Salaris et al., 2009; Andrews et al., 2015, see also Ch. 2 and Ch. 7).

From the perspective of nucleosynthesis, the partial mixing zone, below the convective envelope, requires much higher values of $f_{\rm CE}$ compared with the values calibrated for core hydrogen burning or values typically taken for evolutionary models which can be non-existent, with $f_{\rm CE}$ =0 (Miller Bertolami, 2016), or when explored for super-AGB stars in Jones et al. (2016), the range considered covers $f_{\rm CE}$ =0.0035-0.022. These values are far lower than what is necessary to reproduce s-process abundances, which results in a value of $f_{\rm CE}$ =0.126 (Miller Bertolami, 2016; Ritter et al., 2017) when converted from the necessary mass within the partial mixing zone given in Lugaro et al. (2003) and Herwig et al. (2003). In a similar investigation, it is

[2] A core breathing pulse occurs when the convective helium core rapidly expands, ingesting additional helium and prolonging this evolutionary phase.

suggested in Lugaro et al. (2003) that applying this additional mixing at all boundaries results in abundances which are the result of a too high neutron flux, and a preliminary suggestion of $f_{\rm PDCZ}$ =0.008 is tested and confirmed as more suitable, as this limits the activation of the ^{22}Ne neutron source, although no further testing beyond this is mentioned. It should be noted that, in both cases, these values are predicated upon a single evolutionary model, with the investigations then focusing on reproducing nucleosynthesis objectives.

Beyond early hydrodynamic work of Freytag et al. (1996), which forms the basis of the most commonly used algorithm for additional mixing in stellar evolution as first implemented in Herwig et al. (1997), a combined 2D/3D study by Herwig et al. (2007) tried to focus specifically on the TP-AGB boundaries. The result of which suggested that the boundary at the base of the PDCZ could be approximated by two exponential decays, the first beginning inside the convective region with a value $f_{\rm CBM}$ =0.01, and a second outside the convective zone by a value $f_{\rm CBM}$ =0.14. The top boundary was more simply modelled by a single decay, with a value of $f_{\rm CBM}$ =0.1, but which for reasons discussed in section 5.2 and 6.2 is not thought to be relevant. Confusingly, later works which produced grids of evolutionary models, such as Ritter et al. (2017), suggest that a value of $f_{\rm PDCZ}$ =0.008 is motivated by simulations of Herwig et al. (2007), so it can only be assumed that further, unpublished, analysis of the simulations exists.

At least some additional mixing appears to be required from the observations of post-AGB stars (specifically those referred to as PG1159 stars) which are believed to indicate the final intershell abundances of TP-AGB stars Herwig et al. (1999). A constraint of $f_{\rm PDCZ}$ =0.01-0.03 was suggested from a preliminary investigation carried out by Herwig (2000). Although these results were extrapolated from a few thermal pulses of a single evolutionary model, it has been shown that some additional mixing across a range of masses may indeed be necessary Miller Bertolami (2016).

The reliance on investigations limited to a single mass model, or even a single thermal pulse, is an entirely understandable circumstance to be in, particularly when it comes to hydrodynamic explorations. It is something which it is hoped can be countered within this investigation, but is again highlighted by a study of super-AGB stars (Jones et al., 2016) where the standard values taken are 36 and 4 times smaller (for $f_{\rm CE}$ and $f_{\rm PDCZ}$ respectively) than usually taken at lower masses by the same group (e.g. Pignatari et al., 2016; Ritter et al., 2017). Although some exploration of the values is performed in Jones et al. (2016), it is difficult to draw any conclusions other than the claim that $f_{\rm CE}$ >0.014 prevents core growth.

This Work

Some of the methods for constraining mixing beyond the formal convective boundary have been discussed above, and it becomes clear that there is no straightforward method for defining a 'best fit' model. This is, of course, part of the motivation for this work, to try to understand the sensitivities of these choices. An initial basis was taken to be the work outlined in Miller Bertolami (2016), where it is claimed that the choices of parameters taken there allow certain observational constraints to be met (but by no means suggests these to be the values which should always be taken). This means choices of f_{CHB} =0.0174, f_{CHeB} =0.0174, f_{CE} =0.0 and f_{PDCZ} =0.0075, with an important difference to note being the different choice of a cutoff value within the code, the effect of which is discussed further in section B.3.

Following the work of Miller Bertolami (2016), it is not suggested here that these values are correct or even reproduce all observables when included in GARSTEC, only that it is a starting point in the investigation with the intention to explore the influence of the reasonably well constrained core CBM on the TP-AGB, and to first do so with a consistent and realistic treatment of CBM on the TP-AGB. It has of course already been mentioned that $f_{\mathrm{CE}} > 0$ is required in order to reproduce the ^{13}C pocket, and this will be taken into account further into the investigation.

Chapter 5

Technical Investigations

It is necessary to produce a grid of full evolutionary calculations to observe the overall influence of changing the convective boundary treatments and, of course, for comparing to observable quantities or for calculating the contribution of the stars to the chemical enrichment of the galaxy. However, in particular instances, much can be learned from a far more limited approach, which can allow for the parameter space to be more thoroughly explored or allow for a particular case to be considered in far more detail than is typically the case when performing full model simulations. Within this chapter, several such cases are presented, which can be considered to be numerical experiments of a sort.

To begin with, section 5.1 considers a physical argument, related to the original interpretation of overshooting. This is primarily a study of an argument previously presented in Lattanzio et al. (2017) that there should be no momentum-based overshooting from the base of the PDCZ, although this has been expanded here to also consider the convective envelope.

This is then followed by two sections, each dedicated to a separate, but related, investigation of a single mass, where the focus is on exploring the parameter space. In this instance, by concentrating on a single thermal pulse, where models are repeatedly run through a single pulse with only the treatment at the convective boundaries changing. The first of those, for a $3M_{\odot}$ model, presented in section 5.2 focuses on the influence of additional mixing from the PDCZ and convective envelope, and the effect this has on the efficiency of the third dredge-up. After this, a similar investigation, which also considers the effect on hot-bottom burning, is performed for a $6M_{\odot}$ model in 5.3.

5.1 Maximum Extent of Overshooting

The exact nature of any additional mixing is not fully understood, and it is not necessarily the same process at each boundary. However, overshooting as it was originally formulated, in terms of material with some velocity penetrating a finite distance beyond the formal boundary, can nonetheless be studied in and of itself. There have been attempts at quantifying the maximum distance which this momentum based overshooting extends (Roxburgh, 1978, 1989), however, these works focused on convective cores, and must still be parameterised in order to match observations (VandenBerg et al., 2006).

This section explores an analytic argument against any physical overshooting from the base of the PDCZ, calculating the maximum distance which it could penetrate and putting this in context in terms of what this corresponds to for the convective boundary mixing efficiency parameter f_{CBM} .

5.1.1 Physical Argument

During a thermal pulse, the high luminosity generated in the Helium burning shell induces extreme conditions within the star, including a PDCZ along with a temperature inversion below (this can be seen later in Fig. 5.2). The thermal runaway in the helium-burning shell, which causes the thermal pulse, rapidly raises the temperature locally and creates this temperature inversion below, while also creating the PDCZ.

An argument has been made (Lattanzio et al., 2017) that this temperature inversion would act so strongly against any convective eddy which may emerge from the bottom of the convective zone, that it would be impossible for any physical overshooting of this nature to extend any appreciable distance, and would not even reach the next grid point in a typical stellar evolution model. This is motivated by the radiative temperature gradient in this region is negative and should, therefore, remain unconditionally stable against convective motions.

A basic physical argument is outlined in Lattanzio et al. (2017), based on the buoyancy acting against any convective cells which may extend beyond the convective boundary. By considering a convective eddy, with a density $\rho_e(r)$ at the base of the PDCZ, moving adiabatically downwards and assuming this eddy will then have a buoyancy force acting against it, they derive the relation

$$\int_{v_0}^{v_1} d\left(\frac{1}{2}v^2\right) = \frac{1}{2}v_0^2 = \int_{r_0}^{r_1} g(r)\left[\frac{\rho(r)-\rho_e(r)}{\rho_e(r)}\right] dr \tag{5.1}$$

where the bottom of the convective zone is defined at r_0 with a velocity v_0 and integrating beyond the convective zone until the point r_1 where the velocity is v_1.

As it is desired to find the maximum distance this eddy will travel, $v_1 = 0$ is taken for this final point and the RHS of equation 5.1 is then integrated downwards from the convective boundary until a position r_1 is found which results in the RHS of the equation being equal to $\frac{1}{2}v_0^2$. This distance r_1 can then be considered to be the furthest possible position that the convective eddy could reach when extending from the PDCZ.

As is done in Lattanzio et al. (2017), the velocity which has been used in the calculation, in order to calculate the maximum distance, is taken such that v_0 is equal to the maximum convective velocity within the convective zone, rather than that at the edge. This is done to try and calculate the maximum possible distance that a physical overshooting process could extend.

The argument presented here is, of course, a simplification, from which it can not be definitively claimed that this is truly the maximum distance such a physical overshooting could penetrate. Indeed, although it is claimed in Lattanzio et al. (2017) that this represents an upper limit due to the assumptions made, such as in taking the maximum velocity within the entire convective zone to be the velocity with which the eddy crosses the convective boundary. Within the framework this assumption gives the maximum possible value, but does not account for the fact that this maximum velocity is derived from the 1-dimensional analytic mixing length theory, which may not be representative of the high velocity eddies which are, in fact, expected to penetrate the furthest and therefore be responsible for any additional mixing. This has also been seen in hydrodynamic simulations (Pratt et al., 2017), where it has been shown that mixing beyond the convective boundary is largely due to the stochastic nature of the velocities which enter the radiative zone.

Coming from another perspective, there are also multiple arguments as to why this could, in fact, be overestimating the maximum distance allowed, given the assumptions taken. There is an inherent upper limit placed by such an argument, where the eddy extends into the radiative zone adiabatically. Clearly, it is unknown the level to which the eddy would simply dissipate, possibly losing all of its momentum immediately upon entering the radiative region. Furthermore, this argument is only probing the density profile of the star, which may be influenced by the temperature inversion but does not directly probe the inversion itself, which was the original motivation for the stability of the region.

Suffice it to say, there are many uncertainties within this particular argument, though it is nonetheless instructive to consider what scales this maximum distance would fall under to try to gauge how likely such physically motivated, momentum-based overshooting is at a particular boundary, or if it really seems far more probable that some other mechanism is responsible for any additional mixing, which would be

required for the models to match observational constraints.

5.1.2 Results

As an initial comparison, the maximum distance from the convective boundary for which overshooting is allowed, as calculated in the above manner, is presented in Fig. 5.1a as a blue line. Additionally, the distance from the base of the PDCZ to the position of the temperature inversion is shown in the same panel as a red line, while the dashed lines indicate the distance to the three next nearest grid points below the boundary. This is shown here for a $3M_{\odot}$ star, during the 3^{rd} thermal pulse and covers the range where the convective region between burning shells is present (outside of this time range, no convective boundary exists for which these quantities can be considered).

It should be noted that the values presented here for the maximum distance are perhaps 1-2 orders of magnitude larger than those given in Lattanzio et al. (2017), in which their Table 1 gives the calculated maximum distance at three times during a thermal pulse resulting in 1m, 6m and 200m at the start middle and peak of the thermal pulse. Although, it is generally still less than the distance to the next grid point, this is not the case during the peak of the thermal pulse, when this maximum distance even extends right until the temperature inversion. The distance to the next grid point is, of course, no measure of this maximum distance, however, it is indicative of whether mixing to this calculated maximum distance can be included in the code and also shows that the integration to estimate this distance is generally restricted to interpolation between only two grid points.

An attempt was made to increase the resolution of grid points below this boundary, by decreasing the linearisation tolerance in the region below convective boundaries. This was done by decreasing the order δ up to which the differential equations must be satisfied i.e. that

$$\left| f(x_0 + \epsilon) - \left(f(x_0) + \frac{df(x)}{dx}|_{x_0} \xi \right) \right| < \delta \tag{5.2}$$

as described in Wagenhuber & Weiss (1994). This factor δ was decreased by 2 orders of magnitude in the region below the convective boundary with respect to the standard calculations (from $\delta = 0.1$ to $\delta = 0.001$). The result is presented in Fig. 5.1b as a direct comparison to Fig. 5.1a. Before considering the implications for the physics, it is worth noting that the distances between grid points in the respective figures are clearly smoother in the case of the increased resolution, and it should be noted that the evolution through the TP ran quicker and with fewer models during

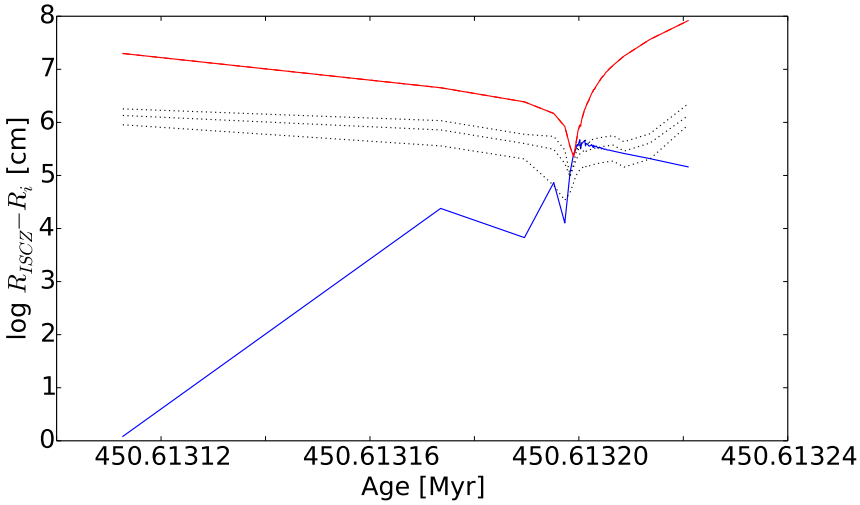

(a)

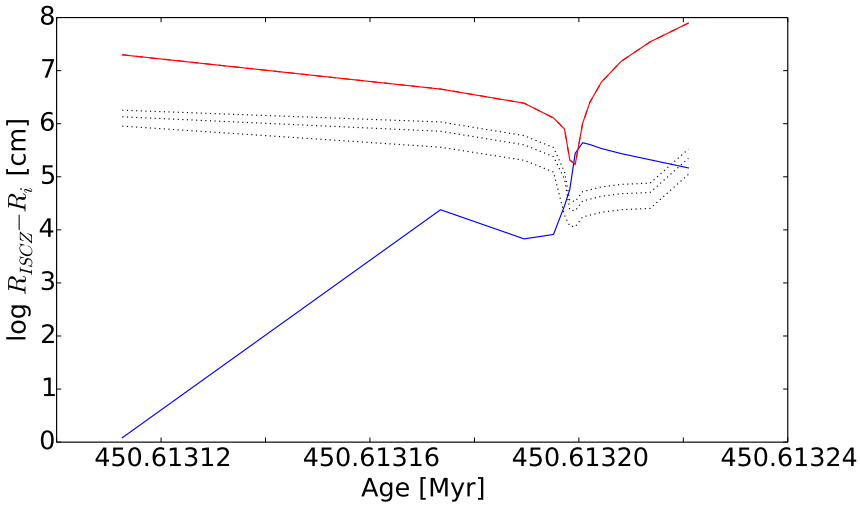

(b)

Figure 5.1: The distance from the base of the PDCZ as a function of age during a thermal pulse, for a lower resolution model (top panel) and a higher resolution model (lower panel). Each line represents the distance to a different feature, with blue indicating the maximum possible distance of convective overshooting, red the distance to the temperature inversion, and the dashed lines the distance to the next three grid points below the convective region.

Panel	Age [Myr]	Distance$_{max}$ [cm]	Distance$_{Tinversion}$ [cm]
Top	450613198.26	5.8×10^4	2.1×10^5
Middle	450613199.3	2.8×10^5	1.7×10^5
Bottom	450613200.72	4.3×10^5	1.0×10^6

Table 5.1: Information about the evolutoinary models shown in the three panels of Fig. 5.2.

the PDCZ phase than in the original case. Unfortunately, when treated this way for a full evolutionary model, this did not solve the usual convergence problems which can be met when trying to reach the end of the TP-AGB evolution and are due to other conditions (see Ch. 2.3.2 for a discussion).

This increased resolution results in a number of grid points falling within the range of this maximum distance during the peak of the thermal pulse, which is reassuring in terms of the calculation. It is also not the case that this increased resolution significantly changes the distance calculated and in fact this maximum distance even briefly extends slightly beyond the temperature inversion.

Fig. 5.2 shows the model structure (temperature, density and mass fractions) for 3 evolutionary models from the high resolution case, when the base of the PDCZ is closest to the temperature inversion, with the age, maximum calculated distance and distance to the temperature inversion for the model in each panel given in Table 5.1. Also shown is the location of the convective boundary at the base of the PDCZ (vertical red line) which is close to/overlaps with the line indicating the temperature inversion (black, dashed). The fact the vertical lines are so close together shows the scales which are being probed by this buoyancy argument (as, in this context, the maximum allowed distance is essentially at the marked temperature inversion). The location of the temperature inversion marked indicates the first point at which the temperature begins to decrease, but is really only the beginning of the much larger region which forms the overall temperature inversion.

The sudden drop in the density at the convective boundary, seen particularly in the top panel but visible in all, is as far as this maximum allowed distance allows for. The middle panel shows the model where the maximum allowed distance can technically extend beyond the temperature inversion as the two are still close together but have moved slightly away from the location, still visible in the density, signifying the maximum extent of the PDCZ. The final panel demonstrates that even once the boundary has visibly moved away from this drop in the density, the maximum calculated distance for momentum-based overshooting does not significantly increase and the relatively small increase in density covered by this small distance provides

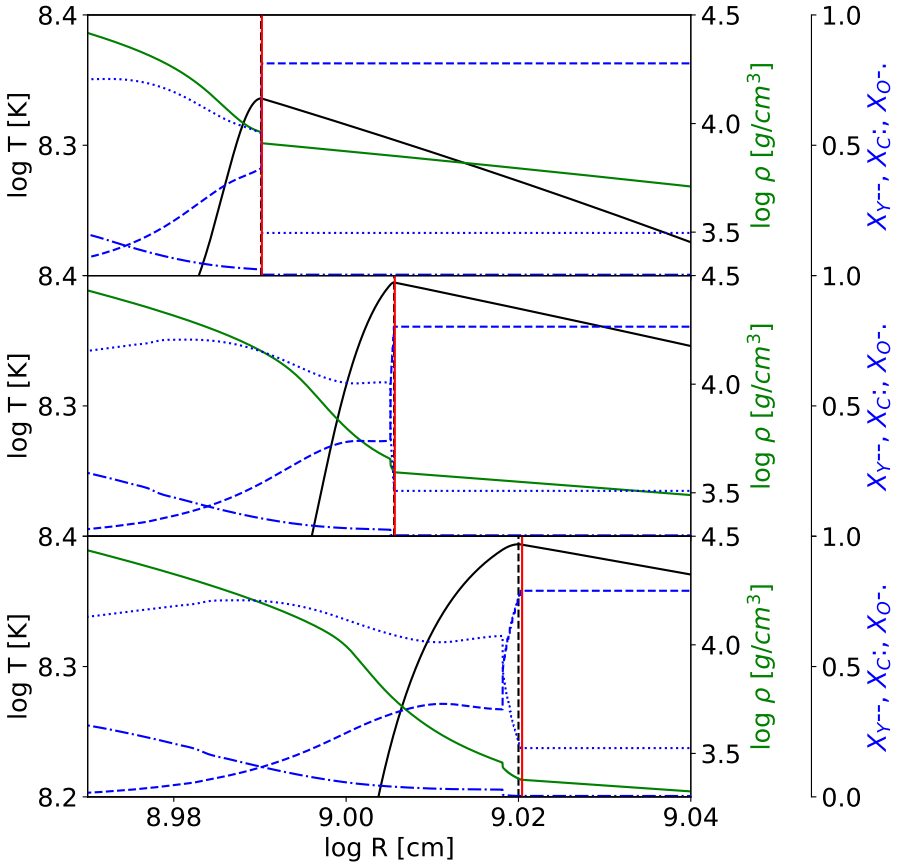

Figure 5.2: The internal structure of the high resolution, $3M_{\odot}$ model during the third TP at 3 evolutionary timesteps with ages given in Table 5.1. Each panel shows the temperature (black), density (green) and mass fractions (blue) for helium (dashed), carbon (dotted) and oxygen (dashed, dotted). A vertical red line marks the convective boundary at the base of the PDCZ, and a vertical black dashed line marks the temperature inversion (always close to the red line).

sufficient buoyancy to stop the convective eddy.

Therefore, it must be said that the temperature inversion does not appear to be the limiting factor in determining this maximum distance, but rather the density profile left by the maximum extension of the PDCZ. However, the temperature inver-

sion is responsible for determining the maximum extent of the formal Schwarzschild convective region, which determines the location of the density profile. It can really be seen from the maximum distances calculated, that even the smoother density profile beyond the convective boundary in the bottom panel results in a maximum distance which does not even reach the sudden drop in density left by the PDCZ. Overall, it can be seen that the physical buoyancy argument does not probe the large variations beyond the first point of the temperature inversion.

The argument presented by Lattanzio et al. (2017) was motivated by the belief that the temperature inversion below the PDCZ would act so strongly on any momentum-based overshooting, that it would not be possible for this physical process to account for any additional mixing which may be required. Although this physical argument does suggest a severely limited distance to which momentum-based overshooting could extend, it seems to be limited by even a modest increase in the density. Furthermore, the basic physical description that is given relying on an active restoring force due to buoyancy can also be applied to the convective envelope, another important feature in the TP-AGB evolution.

To investigate whether this is also relevant, this maximum overshooting distance has also been calculated for the convective envelope of both the low and high resolution models, and are shown in figures 5.3a and 5.3b respectively. In this case, the figures cover a larger time range, as it is not restricted to the phase during which the PDCZ is present. Clearly, the distances allowed are several orders of magnitude higher than in the case of the PDCZ models. In the lower resolution case, it is clear that this maximum allowed overshooting distance typically extends only as far the next grid point at most, as was the case for the PDCZ. The increase in the resolution again brings multiple grid points within this allowed range.

This application to the convective envelope clearly shows an increase in the allowed distance for which the overshooting could penetrate given this description of buoyancy. This does not take into account that overshooting is not typically implemented as a distance, but instead as a function of the pressure scale height, H_P. Given the standard method of implementing additional mixing at the convective boundary, by calculating an effective diffusion co-efficient for overshoot, D_{CBM}, as a function of the diffusion co-efficient, D_0, as calculated from MLT at the last convective grid point ($D_0 = v_{\mathrm{MLT}}\alpha_{\mathrm{MLT}}H_{\mathrm{P}}$), related by

$$D_{\mathrm{CBM}} = D_0 \exp\left[\frac{-2z}{f_{\mathrm{CBM}}H_P(0)}\right] \tag{5.3}$$

where $H_P(0)$ is the pressure scale height at the convective boundary, f_{CBM} is the overshooting efficiency parameter and z the distance from the convective boundary.

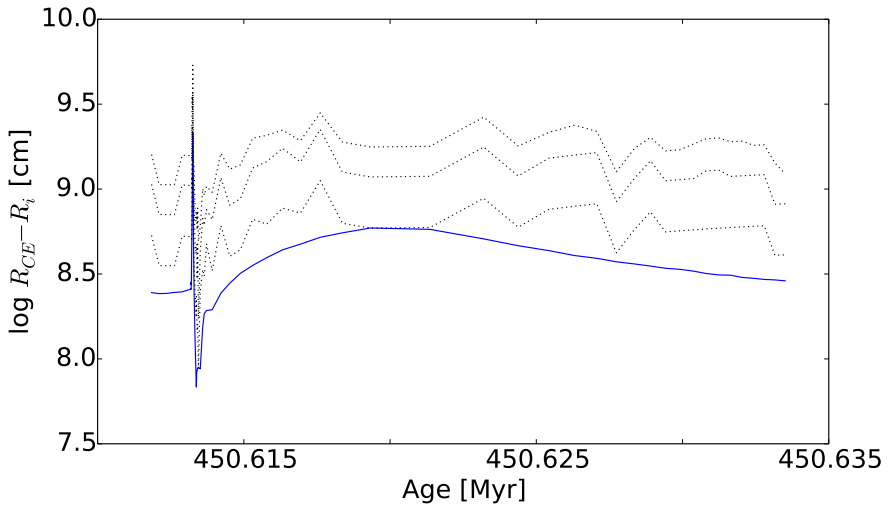

(a)

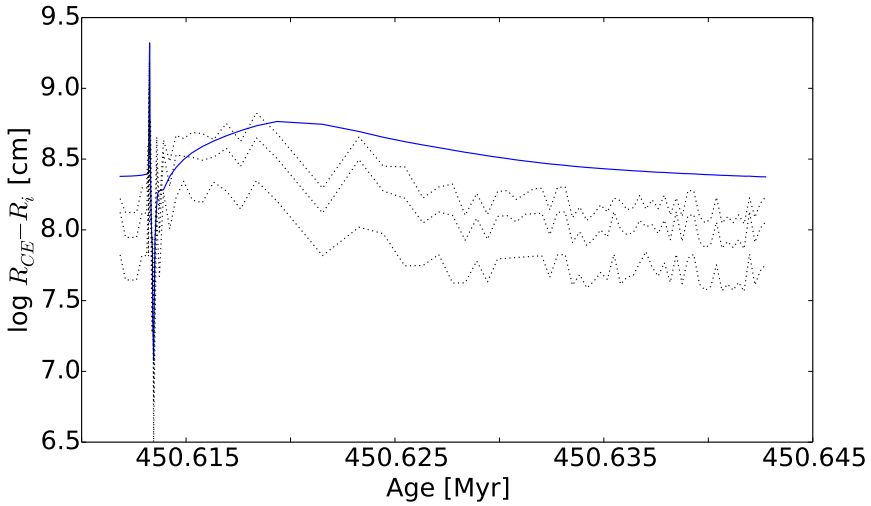

(b)

Figure 5.3: The distance from the base of the convective envelope as a function of age during a thermal pulse, for a lower resolution model (top panel) and a higher resolution model (lower panel). Each line represents the distance to a different feature, with blue indicating the maximum possible distance of convective overshooting and the dashed lines the distance to the next three grid points below the convective region.

Model	Max f_{CBM}	Mean f_{CBM}
	PDCZ	
Low Res	1.63×10^{-4}	9.47×10^{-5}
High Res	1.47×10^{-4}	5.7×10^{-5}
	CE	
Low Res	3.21×10^{-3}	1.8×10^{-3}
High Res	3.18×10^{-3}	1.75×10^{-3}

Table 5.2: Maximum value for the CBM efficiency parameter from the base of the PDCZ and convective envelope based on the buoyancy argument.

By taking the maximum extent this overshooting reaches to be when D_{CBM} reaches some fractional cut-off value of D_0, for instance if $D_{\mathrm{CBM}} = D_{\mathrm{cutoff}} D_0$, then it is possible to calculate what the corresponding f_{CBM} value would be given the calculated maximum allowed distance, and the known pressure scale height at the convective boundary. As such, taking the maximum allowed distance for convective overshoot, and rearranging Eq. 5.3 with the assumption $D_{\mathrm{CBM}} = D_{\mathrm{cutoff}} D_0$ at z_{max} then

$$f_{\mathrm{CBM}} = \frac{-2 z_{\mathrm{max}}}{H_P(0)} \ln(D_{\mathrm{cutoff}}) \tag{5.4}$$

allows for the calculation of the corresponding CBM efficiency parameter.

Table 5.2 shows the maximum and mean values for f_{CBM} for both the convective envelope and PDCZ, for both low and high resolution models based on the assumption of $D_{\mathrm{cutoff}} = 10^{-10}$.

It is clear that the value for f_{CBM} is over an order of magnitude smaller for the PDCZ, approximately a factor of 20. However, it should be noted that overshooting from the convective envelope appears to only become influential at values for f_{CBM} which are perhaps an order of magnitude higher than for those at the PDCZ lower boundary as overshooting from the convective envelope only really becomes relevant at $f_{\mathrm{CBM}} \simeq 0.012$, while for the PDCZ there is already a comparable influence on the 3DU efficiency at $f_{\mathrm{CBM}} \simeq 0.001$ (see section 5.2 for more details).

5.1.3 Discussion

Given the number of assumptions which have gone into the calculation of the maximum overshooting distance, even if those attempt to allow for the upper limit,

it is not the case that the values are so far off to completely rule out momentum based overshooting downwards from the PDCZ or convective envelope. However, it is a valid point that it is possible any additional mixing which takes place at these boundaries may not arise from physical overshooting, as there are also indications that such downwards overshooting is severely limited (Herwig et al., 2007). What can be said is that if physical overshooting really is negligible at the lower boundary of the PDCZ, then it is also likely to be the case for the convective envelope, at least in terms of the influence on TP-AGB evolution. It may well be the case that this buoyancy argument is correct, that momentum driven overshooting is not a possible source of additional mixing at either of these boundaries, however, it does appear that this is not solely due to the temperature inversion but rather a more general result of the conditions at the boundary.

This argument only probes the density structure of the star, not taking into account the radiative gradient which becomes negative due to the temperature inversion and which motivated the investigation in the first place. The limitations placed on momentum-based overshooting are influenced by the temperature inversion, although only due to this defining the extent of the PDCZ which laterally leaves a density profile which severely limits the mixing based on the buoyancy argument. The buoyancy places such strong restrictions that the region of the temperature inversion, beyond the first point the temperature begins to decrease, isn't probed.

Overall it seems the buoyancy presents a feasible argument that momentum based overshooting should not extend significantly beyond the base of the PDCZ, although it is not due to the temperature inversion directly, if at all. Indeed, the same argument applied to the convective envelope would also suggest a severe limitation to the physical overshooting allowed and in that respect the buoyancy argument is valid.

5.2 $3M_{\odot}$ Investigation: Third Dredge-Up

Given the number of boundaries, it is difficult to test each comprehensively while also varying the strength of the additional mixing parameter, f_{CBM}, applied. In order to investigate this in more detail, an initial step is to focus on a single thermal pulse, and calculate a range of models which can at least begin to provide insight into the possible outcomes.

A similar approach has previously been taken by Herwig (2000) and is, therefore, a good place to begin. The numerical experiment, which is considered in that case, involves the computation of a single thermal pulse cycle with various values for f_{CBM}, but which is investigated in a manual manner. There, models are calculated until after the PDCZ disappears, at which point f_{CBM} is altered to measure the resulting

variation on 3DU efficiency λ, before being continued to the next TP to see how λ then changes as the additional mixing is also applied to the PDCZ.

Although models include mixing at convective boundaries in different ways, as discussed in Ch 1.2, the implementation in GARSTEC is at least in principle the same as in Herwig (2000) so the general behaviour and parameter ranges should be related, even if numerical differences will always arise between codes. These results should thus still be comparable to those calculated here, where a single starting model prior to the formation of the PDCZ is taken, and evolved through the thermal pulse using the specific f_{CBM} for each boundary, which have been implemented as separate quantities in GARSTEC for the purpose of this thesis.

The model taken for this investigation is from a $3M_{\odot}$ evolutionary sequence just prior to the 11th thermal pulse where additional mixing from both the hydrogen and helium burning core was included, but no CBM treatment during the TP-AGB was applied prior to the thermal pulse. Given the separation of the boundaries within the PDCZ, into upwards (U) and downwards (D), it is first worth determining if both are influential. Fig. 5.4 shows the third dredge-up efficiency λ[1] for sets of models calculated independently of one another, with values for the parameter f_{CBM} =[0.002, 0.016, 0.064] for combinations of convective boundaries at the CE, PDCZ-U and PDCZ-D. In each case, it can be seen that mixing upwards from the PDCZ has almost no effect, apart from in the cases with high f_{CBM} values in conjunction with mixing from the CE where it alters the outcome to a small degree. This is the boundary which is not expected to have any influence on the evolution, and as this appears to be the case in initial testing, it is from this point on ignored.

The mixing at the base of the PDCZ influences the dredge-up through an increase in the helium burning luminosity, a result of mixing additional fuel from the intershell region into the helium burning shell. This, in turn, has a greater effect on the layers above, and of relevance, includes those layers in the region at the base of the convective envelope. This additional expansion, and therefore cooling of these layers, creates more favourable conditions for third dredge-up due to how it relates to the radiative gradient, with $\nabla_{\mathrm{rad}} \propto T^{-4}$ (Herwig, 2000).

A combination of the PDCZ-D and CE boundaries were then calculated for f_{CBM} = [0.002, 0.004, 0.008, 0.016, 0.032, 0.064] with the resulting third dredge-up efficiencies presented as λ in Fig. 5.5. The red line in this figure represents models which have f_{CBM} applied only to the CE, the blue for PDCZ-D and the black for the combined CE-PDCZ-D. Additional points were calculated at f_{CBM} =[0.012, 0.014,

[1]The third dredge-up efficiency is defined as the ratio between the mass of material dredged-up from the core to the mass by which the core grew during the preceding interpulse phase, given by $\lambda = \frac{M_{\mathrm{DU}}}{M_{\mathrm{growth}}}$.

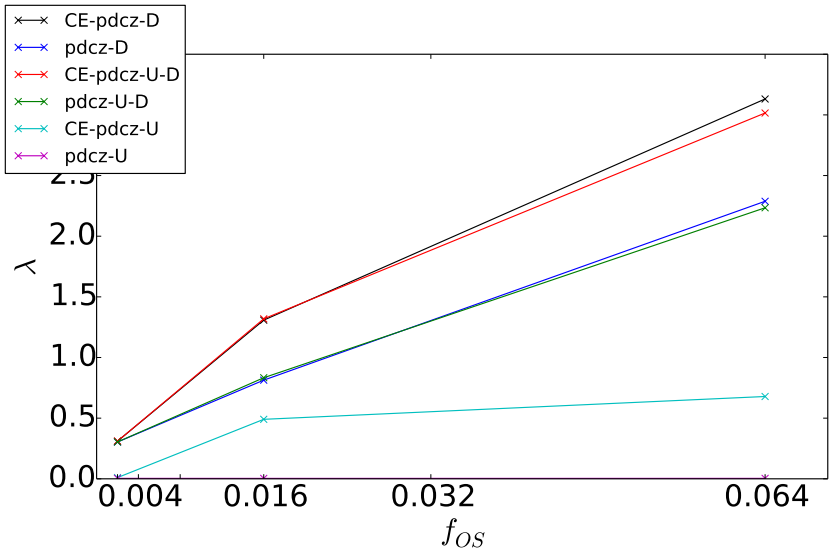

Figure 5.4: Dredge-up efficiency, λ as a function of convective boundary mixing efficiency $f_{\rm CBM}$, for a single thermal pulse of a $3M_{\odot}$ model. Each line represents the inclusion of CBM at the different boundaries indicated.

0.020] for the models where only the CE boundary is active, as it was desired that the step-like function, which is otherwise observed, be resolved. Furthermore, the green line is also for models with only CE, but where the resolution below the convective boundary has been resolved more accurately, something which is discussed further in section 5.1 but which is not relevant here given the agreement with the red markers. It also serves to illustrate why further values of $f_{\rm CBM}$ at the CE boundary were required.

As has already been alluded to, the CE models as a function of $f_{\rm CBM}$ exhibit an almost step like function in the third dredge-up efficiency λ, although this becomes more continuous with increased resolution in the models here. This is something which is also observed in Herwig (2000) but with a value of $f_{\rm CBM}$ =0.004 already having what could be described as the maximum dredge-up efficiency for the thermal pulse in question, where only CE boundary mixing is applied. The models presented there exhibit a far more defined step function, and for a lower overshoot efficiency, however, $f_{\rm CBM}$ =0.004 is the lowest value calculated where additional mixing is included, so it may also be the smoother function is simply not resolved.

In any case, it can be seen that the qualitative observation of a limiting value

for λ is observed in both sets of models for mixing from the convective envelope and that here, if not quite the on-off switch observed previously, there certainly appears to be a limited range of $f_{\rm CBM}$ where the CE is relevant other than to say it is present or not. Additionally, the approximate limiting value of $\lambda \simeq 0.7$ is quantitatively comparable, although this could be as much coincidental as anything else, given the differing initial models, methodology and operating codes.

Focusing instead on the blue line, representing the models with only PDCZ-D, it can be seen that the base of the PDCZ already begins to have an influence on the third dredge-up at the lower values of $f_{\rm CBM}$ and, from $f_{\rm CBM}$ =0.004 onwards, has a linearly increasing effect on λ to a fairly reasonable approximation. This behaviour is also observed in the models calculated by Herwig (2000), and has fairly strict observational limits (discussed further in Ch. 7) making it unnecessary to consider higher $f_{\rm CBM}$ values to discover if the observed trend would continue indefinitely.

At the lower end of the $f_{\rm CBM}$ range, additional models were run for the PDCZ-D case, at values of $f_{\rm CBM}$ =[0.0005, 0.001]. This was considered worthwhile as, although the dredge-up efficiency appears to increase linearly with $f_{\rm CBM}$ for the PDCZ-D models, at lower values it appeared to begin decreasing more quickly. This was proven to be the case, with a very rapid drop-off in the dredge-up efficiency such that none is observed in the case of $f_{\rm CBM}$ =0.0005.

It is also interesting to note that the behaviour of the two convective boundaries do not appear to be coupled, at least in the case of their effect on the dredge-up efficiency. The black line in Fig. 5.5 shows the combined CE-PDCZ-D models, which clearly represent the sum of the two individual mechanisms. At the lower values of the CBM parameter, the trend follows that of the PDCZ-D models, as there is no significant influence from the CE boundary, while there is the almost step like increase in the CE-PDCZ-D models at the $f_{\rm CBM}$ =0.016 model, to move away from the PDCZ-D set of models before continuing with the linear increase in λ as the PDCZ-D boundary again entirely dominates the outcome.

To check the results obtained through the single thermal pulse investigation, full TP-AGB models were also calculated for a single star, beginning from the same initial model taken prior to the first thermal pulse, as a consistency test to check the validity of the previous results. The initial model taken was again a $3M_{\odot}$ star, with convective core CBM during both hydrogen and helium core burning for the pre-AGB evolution, and was then evolved for different boundary mixing parameters applied to the base of the convective envelope only.

Fig. 5.6 shows the outcome of this run of models, with the dredge-up efficiency λ plotted as a function of thermal pulse number as a separate line for each value of $f_{\rm CE}$. As is expected, there is little or no 3DU for the models with smaller values of

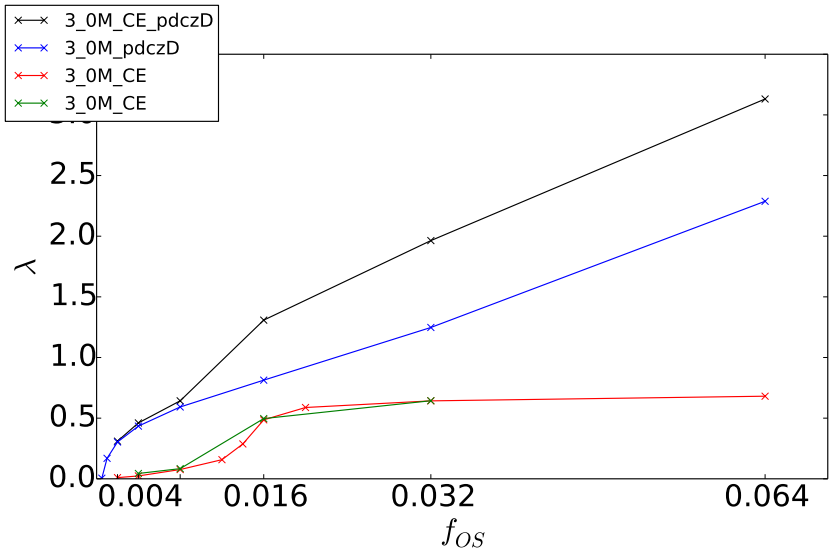

Figure 5.5: Dredge-up efficiency, λ as a function of convective boundary mixing efficiency $f_{\rm CBM}$, for a single thermal pulse of a $3M_{\odot}$ model. Each line represents the inclusion of CBM at the different boundaries indicated.

$f_{\rm CE}$ while in the models which for the single thermal pulse analysis were approaching the observed upper limit of dredge-up efficiency, the typical evolution of λ is seen. A steadily increasing amount of third dredge-up with increasing thermal pulse number as the core mass increases during the TP-AGB evolution, before the decrease as the model approaches the end of the evolutionary phase.

Moreover, the step-like behaviour exhibited in the single thermal pulse study also appears to be present to some degree in the full TP-AGB evolution calculations. With the lines representing the $f_{\rm CE}$ =[0.002, 0.004] clustering towards $\lambda = 0$, while the lines representing $f_{\rm CE}$ = [0.032, 0.064] show comparatively small differences amongst themselves. This leaves the lines $f_{\rm CE}$ = [0.008, 0.016] somewhere in between, in a manner which again suggests the presence of a transition region in the value of $f_{\rm CE}$, which is if anything larger than in the case of the single thermal pulse models. This can be seen by the peak λ value of the $f_{\rm CE}$ =0.016 model reaching perhaps 0.25 less than the $f_{\rm CE}$ =0.064 model. It is also worth noting that this peak also occurs one TP later.

Overall this suggests that the single thermal pulse analysis is qualitatively correct, although the cumulative effect of the third dredge-up events accentuates the

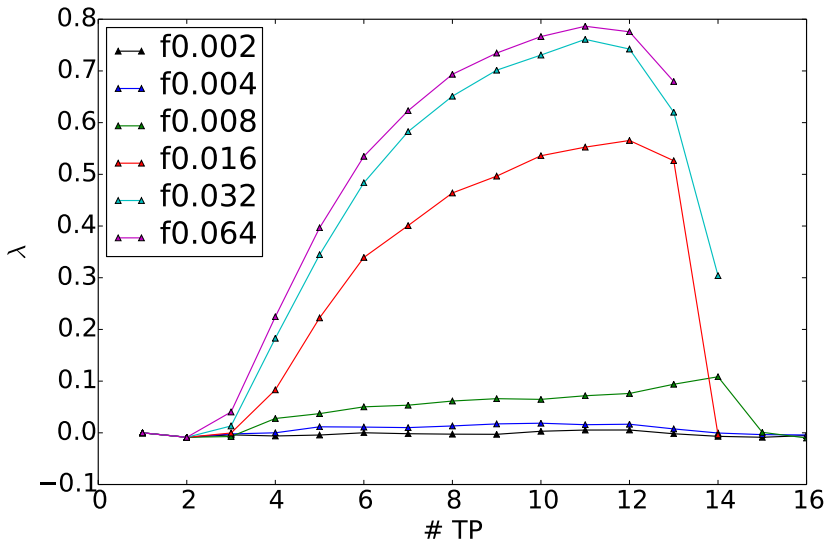

Figure 5.6: Dredge-up efficiency, λ as a function of thermal pulse number, for full TP-evolutions starting from the same $3M_{\odot}$ model taken before the first thermal pulse. Each line represents a different value of $f_{\rm CE}$, with not mixing from the boundaries of the PDCZ.

differences over the course of the TP-AGB evolution. It also appears as though there is indeed a maximum dredge-up efficiency which can be achieved when applying additional mixing to the convective envelope only, which in this case is around $\lambda \simeq 0.8$

In both the case of single thermal pulse analysis and the full TP-AGB calculations, it should be stressed that this is not a claim this is always the maximum dredge-up efficiency, or that a maximum value would always be observed, only that the evidence in this case of modelling a $3M_{\odot}$ star, the evidence is rather convincing.

5.3 $6M_{\odot}$ Investigation: Hot Bottom Burning

Although not a complete view of the effect of changing the overshooting efficiency, $f_{\rm CBM}$, this method of focusing on a single thermal pulse has allowed for a more thorough investigation of the parameter space and the resulting change to the third dredge-up efficiency than would otherwise be realisable. However, the third dredge-

up is not the only physical process which significantly alters the overall TP-AGB evolution, and this lead to the question of whether it would be feasible to perform a similar investigation of the influence on hot-bottom burning.

Following this line of thinking, comparable calculations were performed as in the previous section, but this time for a $6M_{\odot}$ model during the 6^{th} thermal pulse, taken from a sequence which had previously been evolved with the standard CBM parameters for this investigation, i.e. core CBM was included during both the hydrogen and helium core-burning phases with a value of $f_{\rm CBM}$ =0.0174 and also for the pulse-driven convective zone, with a value $f_{\rm CBM}$ =0.0075. This model was chosen as, when left to evolve further under this treatment, it undergoes mild hot-bottom burning and at the following thermal pulse transitions to full hot-bottom burning. Therefore it was believed that this initial model would allow for some variability in the level of additional nucleosynthesis during a single thermal pulse investigation.

This is, of course, not the entire story, with the onset of hot-bottom burning also being dependent on the core mass (as is discussed later in section 6.1). It is nonetheless informative to see the outcome, as is shown in Fig. 5.7. The top panel again shows λ, the dredge-up efficiency parameter, as a function of the CBM parameter. The middle and lower panels, on the other hand, show the change in the carbon to oxygen and carbon to nitrogen ratios respectively. This provides some insight into the behaviour of the hot-bottom burning, and therefore indicates how it has been influenced by the treatment of the convective boundaries. The lines again represent black for convective envelope overshooting, red for overshooting from the lower boundary of the pulse-driven convective zone, while blue has the two combined.

There is a lack of a model for $f_{\rm CBM}$ =0.064 for the combined case with additional mixing from both the CE and PDCZ-D boundaries, which was down to a problem of convergence. This problem also affected the model at $f_{\rm CBM}$ =0.032, however, in this case, was overcome by increasing the resolution as discussed in section 5.1. Unfortunately, this approach did not allow the $f_{\rm CBM}$ =0.064 model to fully evolve through the thermal pulse, and as such has been excluded from the remainder of the analysis.

Initially, it is striking just how high the value of λ reaches in the case of increased mixing and both convective boundaries being active, with values significantly exceeding unity. This also likely explains the problems which were encountered in terms of convergence, with a noticeably steep incline in the amount of material dredged up in the case with $f_{\rm CBM}$ =0.032 applied at both convective boundaries. It must be noted, that this may also be in part down to the way λ is defined, with the core growth since the previous thermal pulse taken into account. for a $6M_{\odot}$ model, with a shorter interpulse phase, this core growth is not as large as for other models. This means

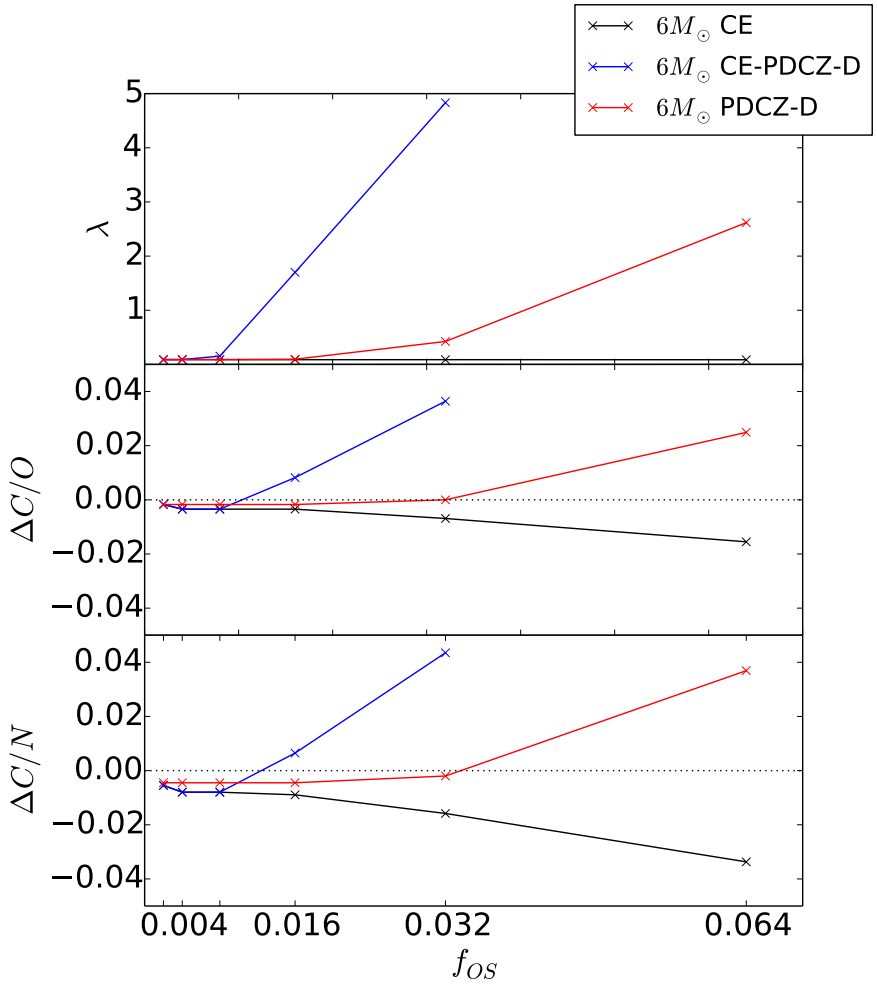

Figure 5.7: From top to bottom; The dredge-up efficiency parameter, λ, the change with respect to the initial C/O value and the change to the initial C/N value, all as a function of the CBM efficiency parameter f_{CBM} , with each line representing its application to different convective boundaries.

that once dredge-up begins to be influenced, any changes become significantly more pronounced in this method of analysis. Nonetheless, over the course of the TP-AGB, this would suggest a significant reduction in the core mass if such additional mixing was applied for the entire evolution.

What appears to be very different in terms of behaviour, in comparison to the

$3M_{\odot}$ case examined previously, is the cumulative influence of the boundaries. In section 5.2 it was shown that the influence on third dredge-up from the base of the PDCZ and convective envelope, really became a summation of the two when they were both applied at the same time. This is in contrast to what is observed here, where the effect of applying both is clearly more than the sum of the constituent boundaries when acting on their own.

The reasoning given for the influence of the PDCZ on the dredge-up, also likely explains it acting to hinder the hot-bottom burning; Namely, the increase in the helium luminosity results in extra expansion and therefore cooling of layers above. This not only allows for more efficient dredge-up due to the resulting increase in the radiative gradient, but also explains the suppression of hot-bottom burning due to lower temperatures.

When acting alone, the convective envelope clearly has an increasing influence on the hot-bottom burning taking place when stronger mixing is included, while simultaneously experiencing no dredge-up whatsoever. Indeed, there is already a small decrease in the C/N value at $f_{\rm CBM}$ =0.04 due to the convective envelope, which is also seen in the models with both boundaries active. However, in the CE-PDCZ-D models, this increase in the hot-bottom burning is quickly overcome by the strong effect of the combined boundaries on the dredge-up. An alternative would be that the changing of the conditions at the base of the convective envelope, due to the higher helium luminosities generated by mixing at the base of the PDCZ, combines with the mixing at the convective envelope to suppress hot-bottom burning entirely.

5.4 Discussion

To begin with, it was highlighted in section 5.1 that, based on the basic physical argument outlined in Lattanzio et al. (2017), momentum-based overshooting would be quite severely limited for the case considered. However, the limitations are not explicitly due to the temperature inversion below the PDCZ as expected but rather the density profile creating a strong buoyancy force. This would limit the efficiency parameter describing additional mixing at the base of the PDCZ to a value of $f_{\rm PDCZ-D}$ $\simeq$0.00015, an order of magnitude lower than the value for which this boundary was shown to become relevant during the investigation of a single thermal pulse of a $3M_{\odot}$ in section 5.2.

However, this same physical argument, when applied to the convective envelope, resulted in a similar restriction to be placed on the momentum based overshoot which could be reasonably expected from the base of the convective envelope. In this case, the limiting value of $f_{\rm CE}$ $\simeq$0.0032 was obtained, which is still 3-5 times lower than

the investigation in section 5.2 suggested was necessary for the convective envelope to influence a $3M_{\odot}$ star.

At first glance, these results may be taken to conclusively rule out such momentum based overshooting being responsible for additional mixing below the base of the PDCZ. However, given the uncertainties and assumptions which go into the analysis, and the relatively limited mixing required for this boundary to become relevant to the TP-AGB evolution, it would be difficult to suggest that it plays no role, especially given the stochastic nature of convection (Pratt et al., 2017). Furthermore, if such a mechanism can be ruled out as a source of additional mixing from the base of the PDCZ, it surely also has to be taken to be the case for the base of the convective envelope as well. Whether the basic assumptions are valid or not, the buoyancy argument invoked results in restrictions for both boundaries which are closer to each other in magnitude than they are to values which could explain observations.

Whether or not the traditional momentum-based overshooting is responsible for additional mixing, there is clearly still a good argument for the inclusion of some form of CBM. As such, section 5.2 aimed to investigate the sensitivity of the mixing efficiency parameter at the different convective boundaries during the TP-AGB.

For the $3M_{\odot}$ case investigated, the results obtained largely confirmed those of a similar numerical experiment performed by Herwig (2000). Although not quite the on/off switch described in those results, it was observed that the convective envelope has only a limited range of f_{CE} where the dredge-up efficiency can be varied, in this case the range f_{CE} = 0.008 - 0.016. Above this range, the efficiency plateaus and below it is negligible, results which were also confirmed by full TP-AGB evolutionary sequences calculated for a $3M_{\odot}$ model. The base of the PDCZ, on the other hand, was shown to increase the dredge-up efficiency almost linearly from a value of $f_{\mathrm{PDCZ-D}}$ =0.004 upwards, tailing off below that to no dredge-up at a value of $f_{\mathrm{PDCZ-D}}$ =0.0005. The upper boundary of the PDCZ was shown to have negligible effect on dredge-up, also when used in conjunction with the other convective boundaries. Interestingly, the effect of the base of the PDCZ and the base of the convective envelope appear to have a cumulative effect on the dredge-up efficiency.

A similar approach was taken for a $6M_{\odot}$ model, albeit with more mixed results. Nothing significant can be said about the effect on dredge-up, and hence core growth, in this case, showing the limitations of analysing a single thermal pulse in this manner. However, it did provide important insight into the connection to hot-bottom burning. For this particular model, the convective envelope already begins to increase hot-bottom burning at a lower mixing value of f_{CE} =0.004, and above f_{CE} =0.016 the increase in hot-bottom burning only becomes stronger. Meanwhile, the base of the PDCZ has no influence at lower values, but at values of $f_{\mathrm{PDCZ-D}}$ =0.032

begins to suppress hot-bottom burning, and strongly does so at $f_{\mathrm{PDCZ-D}}$ =0.064. Additionally, the models with both boundaries active can not be said to represent a cumulative effect of the models where only one is active. Instead, they follow the trend of the convective envelope models at low f_{CBM} values, before hot-bottom burning is quickly suppressed from f_{CBM} =0.016 and above, much earlier than when CBM is only applied to the base of the PDCZ.

5.5 Summary

An investigation was carried out into the buoyancy argument outlined in Lattanzio et al. (2017) which suggests momentum-based overshooting beyond the base of the PDCZ should be severely restricted, which was also seen in the models calculated here. This argument was also then applied to the convective envelope and the corresponding CBM efficiency parameter for both the PDCZ and convective envelope was calculated. Although the value at the PDCZ was an order of magnitude smaller than at the convective envelope, in both cases the value was too small to have any evolutionary impact. However, it was then shown in Sec. 5.2 that the two boundaries can have a similar impact on the third dredge-up when there is such a large disparity between the mixing applied at the respective boundaries, with f_{CE} =0.012 required to have a similar impact as f_{PDD} =0.001. Therefore, it could be suggested from this argument that there can be no momentum-based overshooting at the base of the PDCZ, however, it must then also be taken to be the case for the convective envelope.

It was shown, for a single thermal pulse, that the upper boundary of the PDCZ does not impact upon the third dredge-up, while the base of the PDCZ can have a linearly increasing impact on the third dredge-up efficiency with increased CBM. Meanwhile, the convective envelope was shown to have a limit to its influence on the third dredge-up, with the third-dredge-up efficiency remaining fairly constant above a value of f_{CE} ∼0.016. It was also shown that mixing at the convective envelope can increase the hot-bottom burning of a model, while CBM at the base of PDCZ can suppress the hot-bottom burning.

Chapter 6

Transition to TDU and HBB

Third Dredge-Up (TDU) and Hot-Bottom Burning (HBB) are two hugely important processes in the evolution of TP-AGB stars, and subsequently for the chemical evolution of galaxies (Karakas & Lattanzio, 2007). These processes are far from universal across all TP-AGB stars, with the onset of each primarily determined by the initial mass of the star. This chapter aims to determine the influence on these mechanisms, including whether the masses which experience each, changes due to the treatment of CBM, including during prior evolutionary phases.

Such numerical tests, as were run in the previous chapter, are extremely useful when trying to investigate in more detail a particular phenomenon or parameter. However, to fully understand the outcome and the effect that different convective boundaries can have on the observable properties of stellar evolution models, and the predictions which are a result of them, it is necessary to compute sets of full stellar models which cover a range of masses.

Presented within this chapter are the outcomes of such investigations, where models covering the masses [1.6, 1.8, 2.0, 2.2, 2.4, 2.6, 2.8, 3.0, 3.5, 4.0, 4.5, 5.0, 5.5, 6.0]$M_{\odot}$ were initially calculated and, where it was deemed necessary, additional models were computed covering [1.7, 1.9, 2.1, 2.3]$M_{\odot}$ and [4.8, 5.25, 5.75, 6.25]$M_{\odot}$. The lower mass additions were for clarity regarding which masses experienced third dredge-up for each set of models, while the latter were included to better define the transition to masses which underwent hot-bottom burning.

The models are labelled based on the CBM phases which are included, with the full list given in Appendix A for reference. The boundaries considered are the core hydrogen- and helium-burning phases (CHB and CHeB), the convective envelope (CE) and the PDCZ, which alone indicates mixing upwards (U) and downwards (D) from this region unless an additional letter is included (i.e. PDCZ-D for mixing at

Model	f_{CBM}
CHB	0.0174
CHeB	0.0174
CE	0.0
PDCZ	0.0075

Table 6.1: CBM efficiency parameter for different boundaries.

only the lower boundary).

All models are calculated for metallicity Z=0.02, and evolve from the zero-age main sequence through to the last thermal pulse where possible. The classifications of the models can be seen in section 4.2 and unless otherwise stated, the value of the mixing parameter at the convective boundaries are as follows: where PDCZ refers to upwards and downwards mixing unless otherwise stated.

There are three related, but separate, investigations which are described within this section, the first in section 6.1 is primarily concerned with the influence of additional mixing from convective cores. Following this is a small investigation into the boundaries of the PDCZ in section 6.2, while section 6.3 concludes with an examination on the influence of the base of the convective envelope.

6.1 Convective Cores

There is, of course, no convective core present once a star reaches the AGB phase, however, due to those present in the earlier stages of evolution (during core hydrogen and core helium burning) there exists the possibility that additional mixing from convective cores plays a role during the TP-AGB. Exploring such a possibility is the purpose of this section, with models calculated with different combinations of mixing from the boundary of both the hydrogen and helium burning cores. These are then combined with the same treatment on the TP-AGB, which in this case only involves additional mixing from the PDCZ (both boundaries) and as a further comparison, one set of models were calculated for no additional mixing at any convective boundaries.

Sets of models for the cases 'None', 'CHB-PDCZ', 'CHB-CHeB-PDCZ' and 'PDCZ' were therefore calculated with the intention of covering a range of masses to show the overall effect on the TP-AGB which the prior evolutionary phases can have on the models.

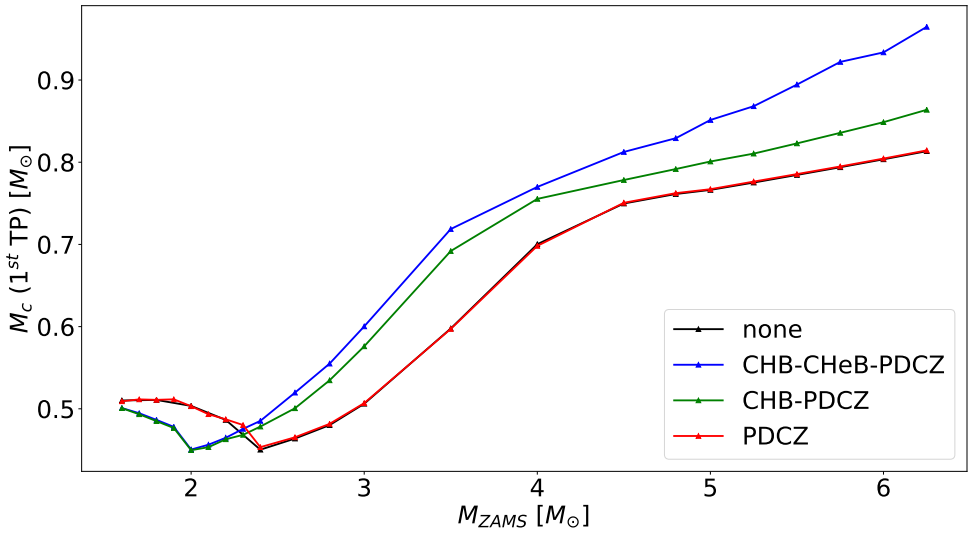

Figure 6.1: The core mass at the first thermal pulse as a function of initial mass for different active convective boundaries.

6.1.1 At the Onset of the TP-AGB

As it is usually good advice to begin at the beginning (in this case of the TP-AGB), the core mass at the first thermal pulse, as shown in Fig. 6.1, provides a good indication of how the mixing beyond the formal boundary of the convective core, during earlier evolutionary phases, influences a key property in determining the behaviour on the TP-AGB. In this plot, the overlap between models for the no additional mixing, and the models with only the PDCZ boundaries active is expected, as neither have any additional mixing from the core in the pre-AGB evolution.

The first difference to note between models without additional mixing and core mixing, is the shift in the minima of the core mass at the onset of the first thermal pulse. This indicates the transition between initial masses at which helium burning commences in a degenerate or non-degenerate core and is influenced by the core mixing on the main-sequence, as shown by the models with and without CHeB boundary having the same minima. Indeed, the set of models which include the CHB boundary have more or less identical core masses at this stage, for models with initial masses less than this transition mass. However, for higher initial mass models, the inclusion, of CHeB begins to influence $M_{\rm c}^{\rm TP1}$, with the CHeB boundary increasing the core masses. This effect becomes even stronger with increasing initial

mass. The effect of including CMB for convective cores, to shift the minimum core mass to a lower initial mass, results in generally less massive cores for the low mass stars.

6.1.2 Third Dredge-Up and Hot-Bottom Burning

Still focusing on the models including CBM during convective core phases, the final surface C/O values can be seen in Fig. 6.2 as a function of initial mass, for the different combinations of boundaries where additional mixing has been applied. Alongside the final C/O value, appears the classification of whether the models undergo third dredge-up, hot-bottom burning or what is here classified as mild hot-bottom burning. This last category arises for models where a reduction in the carbon isotopic ratio, $^{13}C/^{12}C$, is observed although no significant reduction in either the C/O or C/N value occurs.

In the set of models where no additional mixing is applied, there is a lack of dredge-up in all models, although hot-bottom burning still occurs for the higher mass models. In contrast, the models with mixing only applied at the PDCZ experience a significant increase in carbon due to dredge-up, although additional hot-bottom burning is suppressed in comparison to the models with no CBM. This seems to suggest that core size has a significant influence on hot-bottom burning, as the other sets of models have the same treatment on the TP-AGB, with any differences arising from the initial core size as were shown in Fig. 6.1. This can be seen by the fact that the models with the largest cores at higher masses, CHB-CHeB-PDCZ, experience hot-bottom burning at the lowest masses and to the greatest degree, with CHB-PDCZ and then the PDCZ models undergoing progressively less. That the set of models with no additional mixing experience hot-bottom burning to a larger extent than the PDCZ models, despite beginning with the same core size, appears to confirm what was seen in section 5.3. Namely, that the mixing from the PDCZ boundaries inhibits hot-bottom burning, due to the increase in the helium luminosities generated.

Although it has already been seen in Fig. 6.2 which models undergo hot-bottom burning, based on the different core overshooting treatments, that does not necessarily indicate the full differences observed in the models. Fig. 6.3 shows the variation in the carbon to nitrogen ratio, as a function of thermal pulse number, where the colours again indicate the same set of core-overshooting models. Each panel indicates a different initial ZAMS mass, representing (from top to bottom) 5.5, 5.75, 6.0 and 6.25 $M_{\odot}$ models. This figure confirms the overall results which are seen in Fig. 6.2, but also shows that it does not tell the whole story, with the variety in the abundance values clearly not matched by the basic classification of whether hot-bottom burning

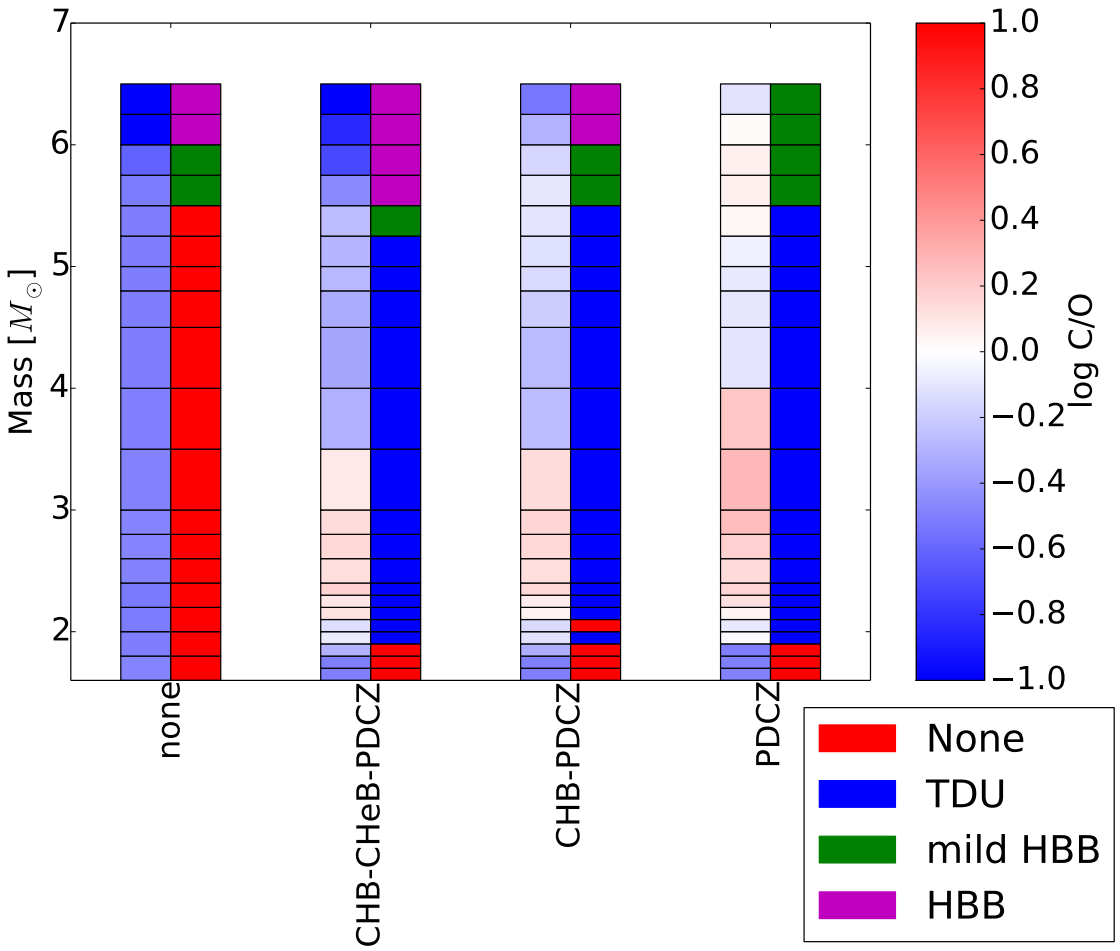

Figure 6.2: Each set of models is represented by two columns, the left of which shows the final surface C/O value (matched to the colourbar at the side) while the right hand column shows the model classification, both of these are plotted in the vertical direction with the models initial mass. The classification is defined as follows; Red - no third dredge-up, blue - third dredge-up, green - mild hot-bottom burning, magenta - hot-bottom burning.

takes place or not.

As for third dredge-up, it can again be seen to alter its behaviour as a result of the treatment of convective core boundaries. The similarity between the CHB-CHeB-PDCZ models and the CHB-PDCZ models for initial masses which have degenerate cores at the onset of Helium burning, begins to diverge above this, with more efficient

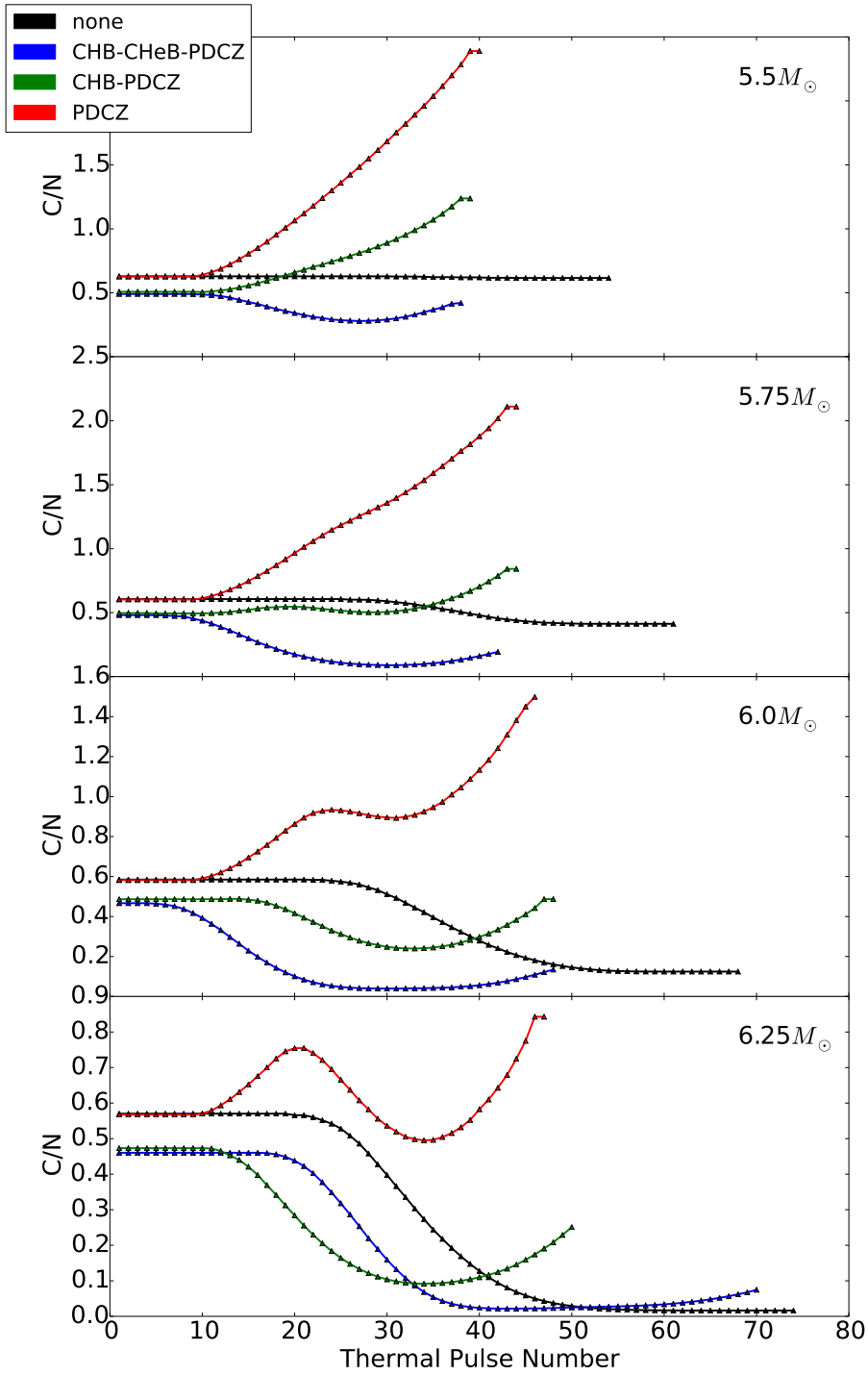

Figure 6.3: Each panel show the C/N value as a function of thermal pulse number for a different mass. From top to bottom, the panels show a $5.5M_\odot$, $5.75M_\odot$, $6M_\odot$ and $6.25M_\odot$ models

dredge-up for the latter indicating the lower core mass results in a final model which is more carbon-rich. This pattern continues when considering the PDCZ only models, which have a lower initial core mass at higher masses (and more efficient dredge-up) but larger cores at lower masses (and less efficient dredge-up). Indeed, combined with the lack of hot-bottom burning in the more massive PDCZ only set of models, it can even be observed that a $5.5M_{\odot}$ model even becomes carbon-rich.

The significantly more carbon-rich nature of the higher mass models with no pre-AGB CBM, but with the PDCZ boundaries active, appears to be partially due to the reduced mass-loss experienced, such that there is more time to reach a peak third dredge-up efficiency. This, in turn, can be related to the reduced core size, such that the PDCZ-only models have lower luminosities and higher effective temperatures, which of course feed into the mass-loss prescriptions.

6.2 Pulse Driven Convective Zone

In the previous section, additional mixing was applied at both the upper and lower boundary of the PDCZ (although not at the convective envelope) during the TP-AGB. To check the individual influence of the two bounds, models were run with one or the other, keeping the same value for f_{PDCZ} as was previously used.

Fig. 6.4 shows the outcome, in comparison with the original models, for the final C/O values as a function of mass, along with whether the models undergo third dredge-up or hot-bottom burning. The models all include the same pre-AGB treatment (with mixing from convective cores), and are instead marked as PDCZ with U/D/both to indicate if upwards or downwards overshooting from the PDCZ is included, and with the models marked as PDCZ-U-D corresponding to those in the previous section which were labelled CHB-CHeB-PDCZ. Clearly seen is that all variation in these models due to the convective boundary treatment is coming from the lower boundary, with the upper bound having no perceivable influence on the outcome. Indeed, this is to be expected as the upper bound is neither connected to the mechanism responsible for third dredge-up as the base of the convective envelope is, nor is it causing the increased helium burning luminosity or the additional chemical mixing from the He-free core, both of which effects the lower PDCZ boundary can alter.

This is of course only for a single choice of f_{PDCZ} , however it seems to be fairly clear from these sets of models that it is additional mixing from the base of the PDCZ which induces the additional third dredge-up seen in the models. This also provides confirmation of the results observed in section 5.2 for models run during a single thermal pulse.

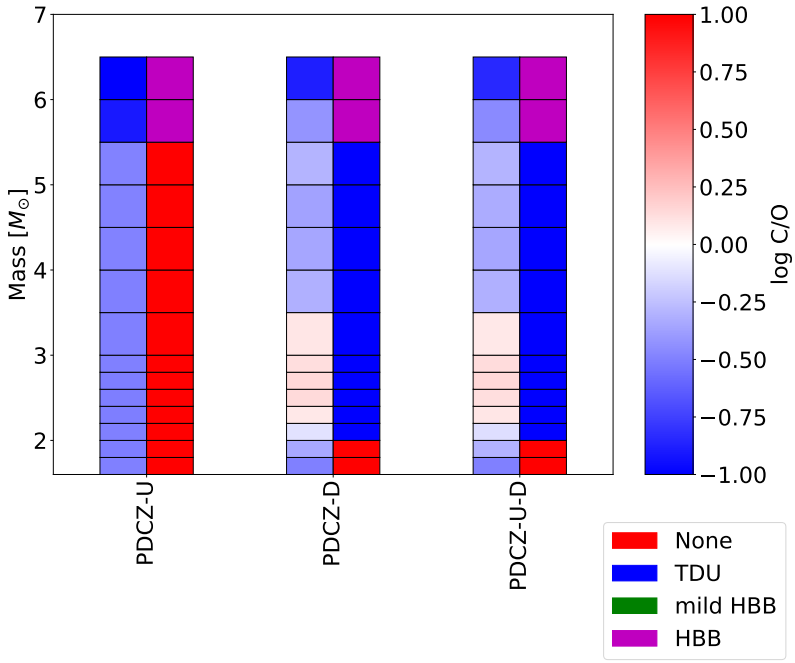

Figure 6.4: Each set of models is represented by two columns, the left of which shows the final C/O value (matched to the colourbar at the side) while the right hand column shows the model classification, both of these are plotted in the vertical direction with the models initial mass. The classification is defined as follows; Red - no third dredge-up, blue - third dredge-up, magenta - hot-bottom burning.

6.3 Convective Envelope

The convective envelope is perhaps the most obvious boundary to consider when it comes to the TP-AGB, given the obvious connection to the third dredge-up, an extremely significant aspect during this stage of evolution, not to mention the formation of the ^{13}C pocket. As such, the models presented here consider the case of including mixing beyond the base of the convective envelope, sometimes in conjunction with mixing from the boundaries of the PDCZ. All models in this section include mixing from both the core hydrogen and core helium burning stages, hence neither is mentioned further in the assignations given hereafter. Otherwise, PDCZ denotes mixing at both convective boundaries of the pulse-driven convection zone, while CE1 and CE2 refer to two different values, $f_{\rm CE}$ =0.0075 and $f_{\rm CE}$ =0.0174, which are applied. These values were chosen as they represent cases where additional mixing should have a small effect for the first, and the second is in the regime of possible maximum

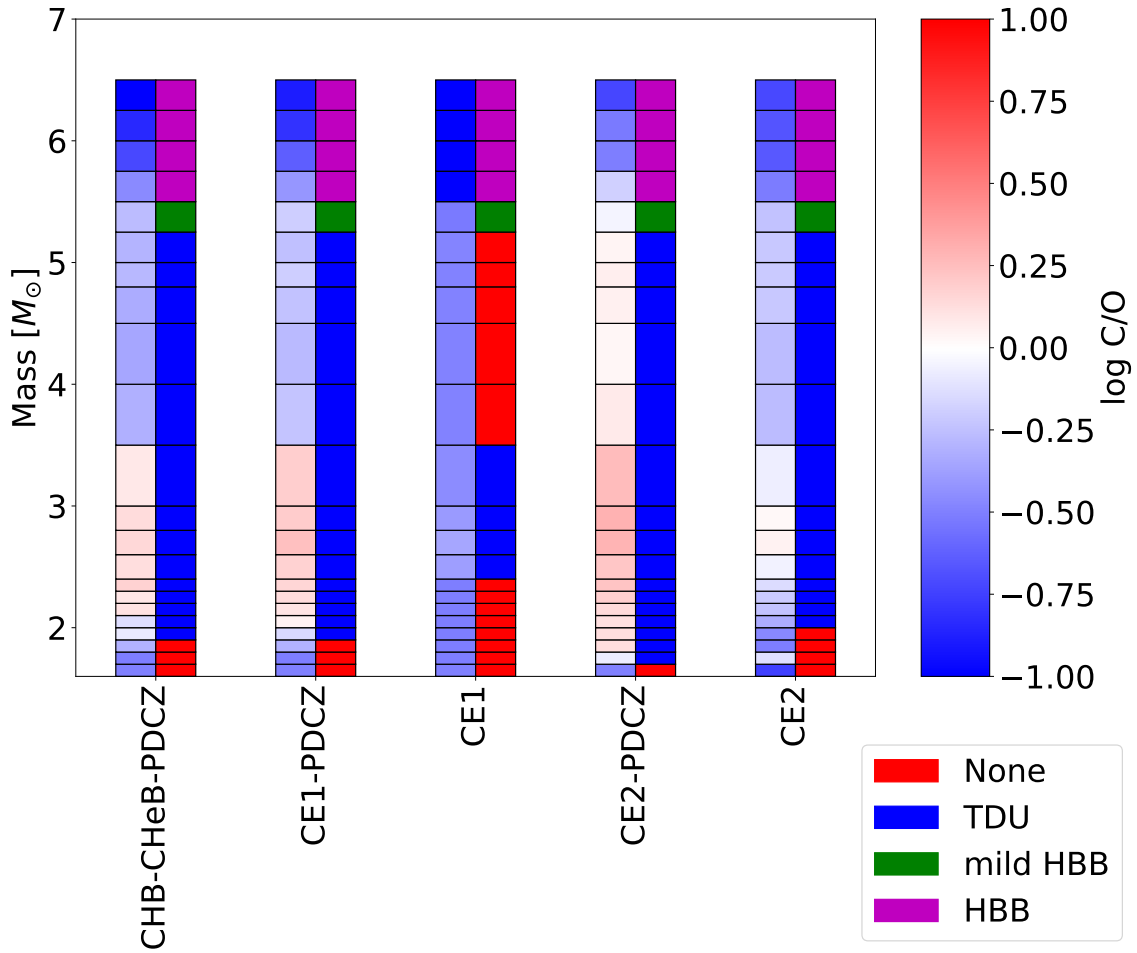

Figure 6.5: Each set of models is represented by two columns, the left of which shows the final C/O value (matched to the colourbar at the side) while the right hand column shows the model classification, both of these are plotted in the vertical direction with the models initial mass. The classification is defined as follows; Red - no third dredge-up, blue - third dredge-up, green - mild hot-bottom burning, magenta - hot-bottom burning

influence, as discussed in section 5.2.

The final C/O values are shown in Fig. 6.5 for the same models, along with their classification of if the model experienced third dredge-up or hot-bottom burning. Looking at the masses in the range of 2.1-3$M_\odot$, the models with PDCZ, CE1-PDCZ and CE2-PDCZ all have comparable final C-rich values, with there only being a

relatively small increase in the C/O value, while above $3.5M_{\odot}$ it is only the models with both PDCZ and the stronger CE2 applied which become slightly carbon rich, a combination which also extends to causing the lower mass stars to experience third dredge-up.

Although models with the weaker CE1 mixing experience a small amount of dredge-up in a limited mass-range, this also seems to confirm the results of section 5.2 that larger values of $f_{\rm CBM}$ are required at the convective envelope in order to have any significant influence.

As far as hot-bottom burning is concerned, this seems to be largely unaffected by the treatments implemented, at least in terms of the masses at which it occurs. In particular, any influence is negligible in comparison to the changes observed due to mixing from convective cores in section 6.1, suggesting that hot-bottom burning is far more sensitive to changes in the core mass of models than the addition of any mixing from convective boundaries during the TP-AGB.

In order to take a closer look at this, the carbon to nitrogen ratios as a function of thermal pulse number are shown in Fig. 6.6 for the higher masses of these sets of models. The picture is not as clearcut as first thought, and the situation is not always the same between the different masses. A principle point of note is that the work of section 5.3 appears to be confirmed, such that mixing from the PDCZ appears to act to suppress hot-bottom burning. The models which do not include additional mixing from this convective region always reach lower values of C/N than the other models.

It also appears to be the case that the stronger mixing included at the convective envelope, CE2, results in the C/N value decreasing earlier than the other models, both when activated with and without the PDCZ boundaries. However, the C/N also begins to increase again in these cases, while the models with CE1 tend to remain flatter, particularly those without the PDCZ activated, reflecting the lack of dredge-up in models with very little boundary mixing during the TP-AGB.

6.4 Discussion

This chapter has focused on two main physical processes present on the TP-AGB, the third dredge-up and hot-bottom burning mechanisms. These aspects were investigated through the calculation of full evolutionary models, applying CBM to different convective boundaries throughout the evolution.

The suppression of hot-bottom burning by mixing from the base of the PDCZ, as was seen in Ch. 5.3, is also clearly seen in the full evolutionary calculations presented in section 6 and it is most notable in the difference between the sets of models where

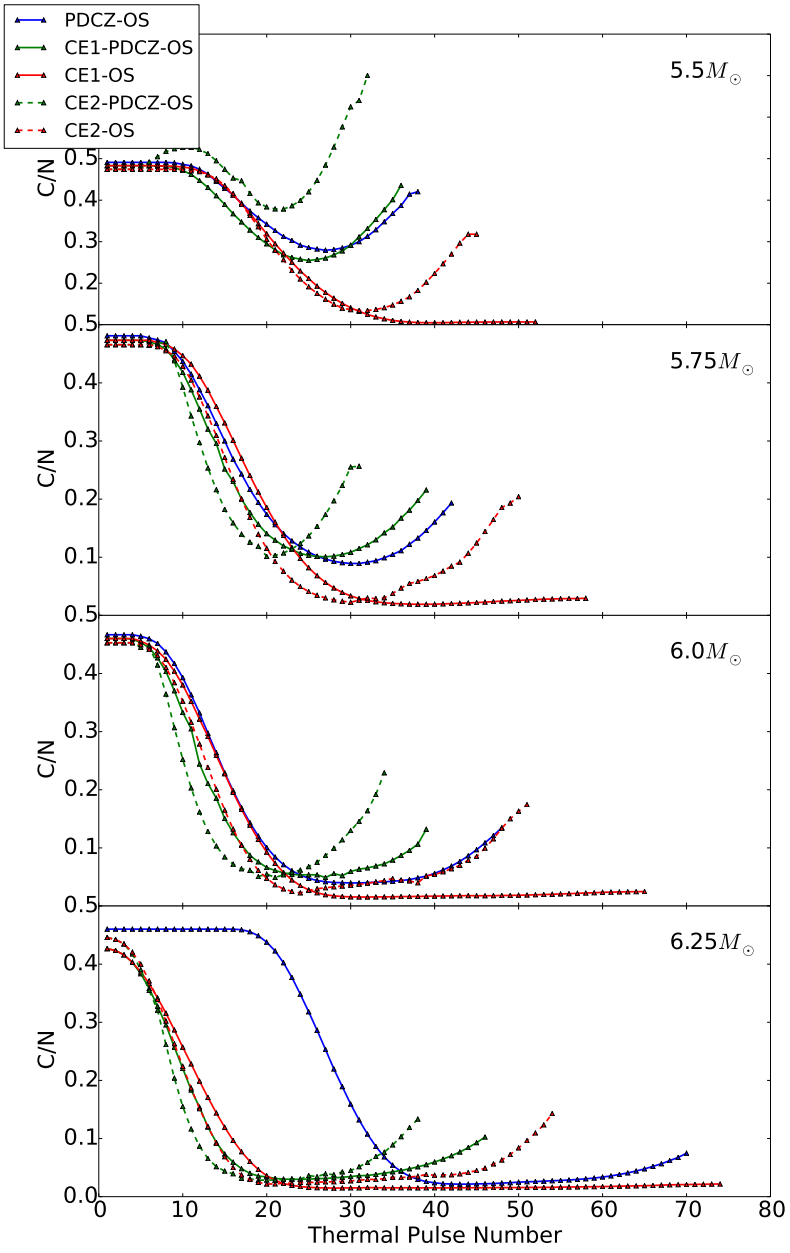

Figure 6.6: Each panel show the C/N value as a function of thermal pulse number for a different mass. From top to bottom, the panels show a $5.5M_\odot$, $5.75M_\odot$, $6M_\odot$ and $6.25M_\odot$ models

no CBM is included in the pre-AGB, and only the PDCZ boundary is then activated in one set during the TP-AGB. This is again seen in the models where the convective envelope becomes active in section 6.3, alongside the confirmation that the convective envelope itself enhances hot-bottom burning, as was also expected from the single thermal pulse investigation.

Another clear message which can be taken from section 6.1 is that, when treating the TP-AGB evolution in an identical way, and only changing the mixing beyond convective cores, there are clear differences in the models. It is sufficiently important, that it even noticeably alters the mass thresholds at which third dredge-up and hot-bottom burning activate, not to mention the alteration to the strength of said phenomena. Obviously what then proceeds to happen during the TP-AGB can counter such results, however, when there is such compelling evidence for mixing beyond the formal convective core it seems unnecessary to neglect to include such a treatment when it unquestionably alters the TP-AGB behaviour in such a substantial manner.

It should be noted, that although the significance of CBM during the core hydrogen burning phase should not be underestimated, it is less clear from the results presented here how significant the boundary of the convective core during helium burning is, as far as the TP-AGB is concerned. For higher mass stars, there is a notable difference in the core mass at the first thermal pulse which manifests itself as a notable change in the behaviour of hot-bottom burning but the change is not as significant as it was for the inclusion of mixing beyond the formal boundary in the hydrogen burning core.

As far as third dredge-up is concerned, the lower core masses at the onset of the thermally pulsing evolution tends to lead to more dredge-up overall through a combination of more time spent on the TP-AGB due to reduced mass-loss and a higher peak dredge-up efficiency being reached. Otherwise, expectations were largely confirmed as far as additional mixing on the TP-AGB were concerned; The inclusion of mixing at the base of the convective envelope and PDCZ increases the amount of material dredged-up, with nothing to suggest that the investigation in section 5.2 of a $3M_{\odot}$ model isn't at least qualitatively correct.

6.5 Summary

The application of CBM during phases prior to the TP-AGB has been shown to influence the evolution during it. Not only does the treatment at the boundaries of convective cores alter the strength of third dredge-up and hot-bottom burning, but also the masses at which they are present. Given the significant empirical evidence

in its favour, it should be taken as a strong recommendation to include some form of mixing beyond the formal convective boundary in the hydrogen burning core. This should be done in all evolutionary models which extend to the TP-AGB phase, whether they are to be used for chemical yields, evolutionary tracks or some other purpose as the outcome demonstrably depends on this prior evolution.

Mixing extending upwards from the PDCZ has again been shown to have negligible effect, while the base of the PDCZ is confirmed to increase third dredge-up and suppress hot-bottom burning. The convective envelope, meanwhile,, has again been seen to require larger values for the CBM mixing efficiency than the base of the PDCZ to influence the third dredge-up, and is confirmed to increase the hot-bottom burning.

Chapter 7

Constraining Mixing on the TP-AGB

The aim of this chapter is to constrain the extent of additional mixing beyond the formal convective boundaries on the TP-AGB, through the use of observations. This is primarily done through the use of carbon star number counts, the semi-empirical initial-final mass relation (IFMR) and the observed abundances of PG 1159 stars.

The previous chapters have laid the foundations for this work, in showing how the treatment of CBM prior to the TP-AGB can have an influence on this later evolutionary phase and investigating in a limited manner the effect of varying the extent of mixing at the boundaries during the TP-AGB. However, this was limited to either specific cases, such as during a single thermal pulse, or to a couple of cases where evolutionary models were run to show the influence.

Presented here is a more thorough investigation of additional mixing at the base of the convective envelope and PDCZ, with a brief discussion of the observables in Sec. 7.1 followed by the results in Sec 7.2.

7.1 Method

This section outlines the basis of the investigation within this chapter, with an initial discussion of the data, which it was felt would provide the best constraints on CBM during the TP-AGB, and then a description of what motivated the selection of the parameters to be used in evolutionary calculations.

7.1.1 Observational Constraints

There is not an excess of data relating the TP-AGB stars, so a few key pieces, which are believed to provide the best constraints on their evolution, formed the basis of this investigation. This also allows for a more focused investigation of parameters, rather than producing a grid for all masses and metallicities for each CBM mixing parameter chosen.

PG 1159 Stars

As was mentioned in Ch. 1, the class of post-AGB stars, known as PG 1159 stars, represent the best method of constraining the chemical composition of the intershell region at the end of the TP-AGB lifetime of a star. The observed oxygen abundances, in particular, cannot be explained without the inclusion of some form of additional mixing at the base of the PDCZ, making this particular observable a good place to start in trying to constrain CBM in TP-AGB stars.

Table 2 in Werner & Herwig (2006) provides the required data about these stars, as it gives a summary of the known PG 1159 stars at the time, taken from various references within, along with the mass abundance ratios (C/He, O/He) and mass of the object. For the purposes of this work, the mass of these objects is considered to be equivalent to the final mass of the TP-AGB models, which is taken to be the mass of the hydrogen free core at the end of the TP-AGB. The uncertainties of the mass and mass fractions are not explicitly given in Werner & Herwig (2006), however the general estimates given are that the mass fractions should be correct within a factor of 2. The final masses are determined from comparison with evolutionary tracks in the $T_{\rm eff}$-log g plane, accurate to 10-15% and 0.5 dex respectively, which leaves quite a large uncertainty for the final mass (see their Fig. 2), although it is not explicitly stated.

The data taken from Werner & Herwig (2006) is shown in Fig. 7.1, although only for objects with both C/He and O/He abundance ratios available. At first, there does not appear to be any obvious trend, with the spread of the data not leading to any clear conclusions. However, two possibilities could be suggested as a way of interpreting the observations. The first is simply that these are anomalous objects, that there is no underlying reason for mixing at the base of the PDCZ but that some object-specific form of mixing (such as rotation) is responsible. This would also provide an explanation for the wide range of abundances which are observed and would mean that little or no additional mixing is required at this convective boundary in general stellar evolution.

To explore the alternative, the oxygen abundances are considered, given these are

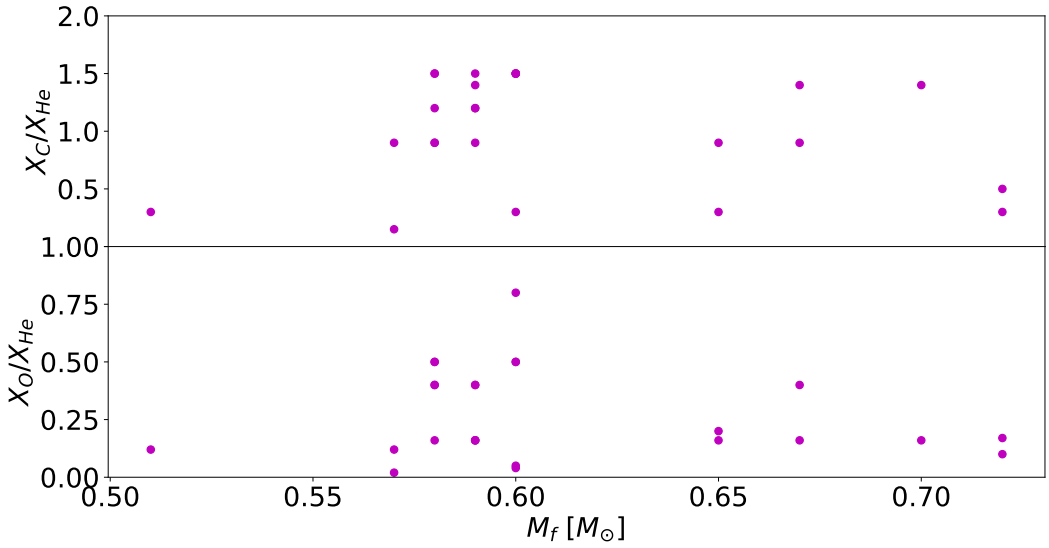

Figure 7.1: Observed mass abundance ratios of PG 1159 stars as a function of final mass, taken from Werner & Herwig (2006), with carbon to helium in the upper panel and oxygen to helium in the lower panel.

the ones which are most difficult to explain without some form of additional mixing at the base of the PDCZ. The O/He abundances are again shown in Fig. 7.2, having been split into two main regions. The objects forming a relatively constant O/He abundance across the range of final masses, at approximately O/He$\sim$ 0.15 covered by the blue ellipse, and the second group with higher values, at O/He $\sim$ 0.5, which are concentrated below a final mass of $M_{\rm f} \lesssim 0.6$ covered by the red. It will be shown later that, potentially, this can be explained by stellar models. The roughly constant relation with final mass covered by the blue region appears to be consistent with stellar models $\gtrsim 2M_\odot$ which produce a fairly constant O/He value with increasing stellar mass for the same CBM treatment. This also helps to negate the importance of the uncertainties in the final masses of these objects. On the other hand, the red region may represent lower mass stars $1.5 - 2M_\odot$, which can have similar final masses, while still resulting in different intershell mass abundances, for the same CBM treatment.

Given the highly evolved nature of these objects, a direct measurement which could imply initial metallicity is impossible. However, it will also be seen that there is not a particularly significant variation in the calculated intershell abundances due

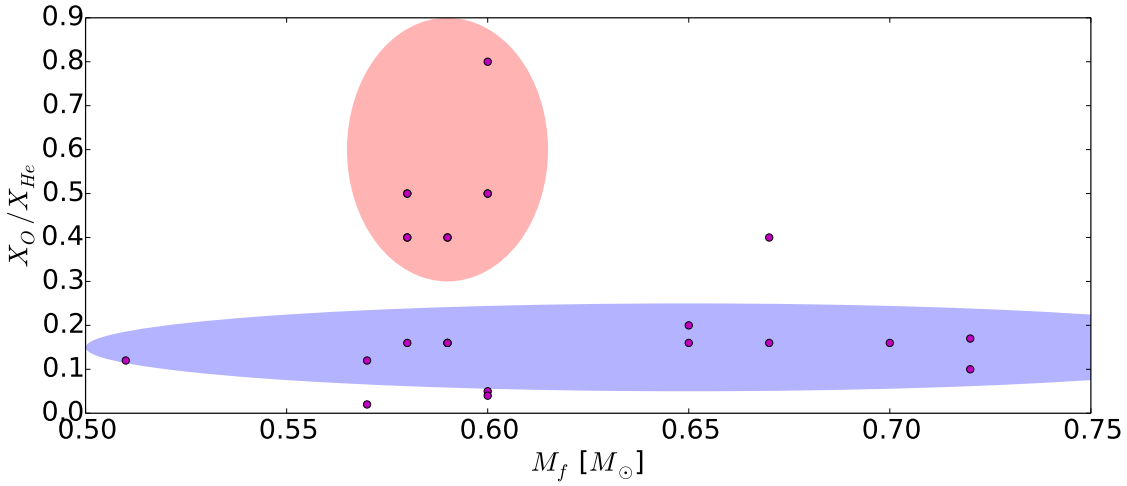

Figure 7.2: Observed mass abundance ratio of oxygen to helium for PG 1159 stars as a function of final mass, taken from Werner & Herwig (2006). See text for discussion of shaded regions.

to metallicity, so it is not considered important which initial composition models are compared to this data set.

Carbon Star Number Counts

As the lifetime of a star during the TP-AGB is so short, there simply aren't sufficient numbers for large statistical samples. This is further complicated by the difficulties determining the properties of the stars which are observed, such as the mass and luminosity of field stars (Lebzelter et al., 2008).

Clusters are a useful tool in studying these stars, as this helps to constrain the age and therefore the mass of the star, and to some extent the luminosity. However, globular clusters in the Milky Way are not particularly helpful in this regard, as the stellar population is too old for the AGB stars in the cluster to be undergoing significant dredge-up (Lederer et al., 2009). On the other hand, the Magellanic Clouds provide a much better sample, given the common distances and intermediate-age (∼1-2Gyr) open clusters present and which are missing in the Milky Way. Girardi & Marigo (2007) gathered information about AGB stars in the clusters of both the Large and Small Magellanic Clouds (LMC and SMC).

Rather than using the M and C-star lifetimes as derived in Girardi & Marigo (2007), it was decided to compare results directly to the number counts of carbon-

$M_{\rm TO}$	$N_{\rm M}$	$N_{\rm C}$
1.66	9	10
2.17	22	32
2.66	4	4

Table 7.1: Turnoff mass ($M_{\rm TO}$) along with the number of M-stars ($N_{\rm M}$) and C-stars ($N_{\rm C}$) taken from Table 2 in Girardi & Marigo (2007) for binned LMC cluster data.

and oxygen-rich stars which had been gathered for the purposes of calculating the lifetimes. This is done to try and remove some of the assumptions which go into the derivation of the lifetimes, relying on stellar isochrones having correct ages for all phases of stellar evolution, for instance. Of course, errors due to the stellar isochrones still enter into determinations of the initial masses of the objects in a cluster.

The clusters in the sample of Girardi & Marigo (2007) were binned according to the turnoff mass of the cluster for the LMC and SMC separately. Although this represents an excellent sample in terms of AGB stars, the numbers are still very small and so the focus presented here is on three of the data bins taken from their Table 2 and which are summarised in Table 7.1. These points are representative of clusters in the LMC, which have the highest numbers of both M and C-stars, and also represent the mass range where carbon stars are expected from the stellar evolution models at this metallicity.

The number counts allow for direct comparison with the stellar evolution models, as it is simple to take the time spent as either oxygen-rich or carbon-rich for any given evolutionary track. There is the additional minimum luminosity cutoff of $L_{\rm cutoff}$=3.336$L_{\odot}$, corresponding to $M_{\rm bol}$=-3.6 which was used as an observational limit for ensuring the stars observed where AGB stars above the tip of the RGB. Thus the fraction of the total number of observed stars which are carbon-rich can be compared to the stellar models. Additionally, to give some indication of how much weight each point should carry, simple upper and lower limits are included in all figures. These limits are taken from considering a Poisson distribution for each number count and taking the maximum and minimum expected number count which would correspond to covering 68% of the distribution. This is further discussed in Appendix B.2.1, however, it should be stressed that this should not be interpreted as a claim of statistical significance, and was done in the interests of indicating the respective importance of each data point.

IFMR

The method of using white dwarfs in open clusters to construct a semi-empirical IFMR is a very useful tool for constraining the TP-AGB evolution. There are two datasets which are used within this work, namely the values taken from models including overshooting in Table 6 of Salaris et al. (2009) and those in Table 1 in Kalirai et al. (2014). In both cases, the data within the tables is a collection of data from different sources, and there are many duplicate objects in both catalogues. This occurs since, in each case, they are making use of the white dwarfs in some of the same clusters, as these are what have been observed. This is not necessarily a negative thing, as the values obtained in each case are not the same, and having the two in place give at least some idea as to the uncertainties involved from the semi-empirical aspect, as well as the observational errors.

7.1.2 Evolutionary Calculations

The evolutionary calculations presented within this chapter follow the same basic principles as in the previous chapter. However, for all models discussed here, additional mixing is included during both core burning phases, such that the mixing efficiency parameters for these boundaries are $f_{\rm CHB}$ =$f_{\rm CHeB}$ =0.0174, where the general $f_{\rm CBM}$ is the parameter entering Eq. 1.11. A variety of values were taken for both $f_{\rm CE}$ and $f_{\rm PDD}$ along with various combinations thereof.

An initial, limited, mass spread of $1.6M_{\odot}$, $2.0M_{\odot}$, $2.4M_{\odot}$ and $2.8M_{\odot}$ was calculated for models with a metal mass fraction of Z=0.008, as a typical value taken for stars in the LMC (which, in reality, of course, has a spread in metallicities). This allows for a rough comparison with the C-star fractions from the LMC, and also for comparison with the intershell abundances which do not vary significantly with metallicity. In some cases, additional masses were inserted between these values, to better resolve the behaviour, and to consider the effects of binning.

The mass range was further extended upwards, to values of $3.0M_{\odot}$, $3.2M_{\odot}$ and $3.5M_{\odot}$, and to a solar-like metallicity of Z=0.02, to better compare with the IFMR relation derived from clusters in the solar neighbourhood.

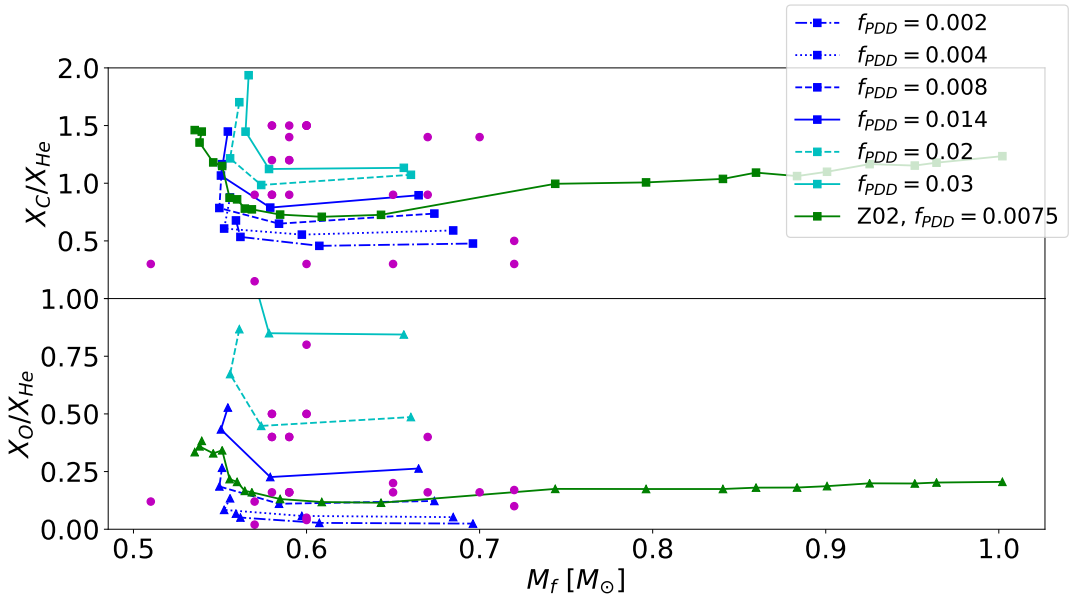

Figure 7.3: Intershell abundances at the end of the TP-AGB given as the ratio of the mass fractions, C/He in the top panel and O/He in the lower panel, as a function of final mass for sets of evolutionary models with the labeled mixing parameter at the base of the PDCZ and Z02 indicating models with initial metal fraction Z=0.02 while all others are calculated for Z=0.008. Additionally, purple circular markers representing observed abundances of PG 1159 stars taken from Werner & Herwig (2006).

7.2 Results

7.2.1 Intershell Abundances

The final intershell abundances of sets of models varying $f_{\rm PDD}$ at the base of the PDCZ are shown in Fig. 7.3 as a function of final mass, along with a set of models taken from calculations in the previous chapter at Z=0.02 (denoted Z02) while all other models are for Z=0.008. For each of the Z=0.008 models, the four initial masses are 1.6, 2.0, 2.4 and 2.8M_{odot}, where the 1.6$M_\odot$ model always has the highest O/He and C/He values and the 2.8$M_\odot$ model always has the highest final mass, with the lines connecting models in the order of initial mass. It can be seen that increasing the value of $f_{\rm PDD}$ certainly changes the intershell abundances, as expected, though the threshold for which this begins to have any notable impact is at a value of $f_{\rm PDD}$

=0.008, in the models considered here.

The models calculated at Z=0.02 with $f_{\rm PDD}$ =0.0075 closely match the Z=0.008 $f_{\rm PDD}$ =0.008 models, therefore having very similar CBM but different metallicity, which shows that the constant value of O/He continues across all higher mass models calculated. This is both reassuring in terms of a comparable behaviour, which has been seen previously (Miller Bertolami, 2016), and that the choice of metallicity for the models here, does not seem to impact on the result of the intershell abundances. The exception to this is, of course, the final mass of the objects observed, something which can equally be influenced by the convective envelope and any additional mixing which may be applied there.

If considering the second interpretation of the data spread discussed in Sec. 7.1.1, then it would have to be said that the models calculated with $f_{\rm PDD}$ =0.004 and $f_{\rm PDD}$ =0.014 seem to encapsulate the observed objects with O/He$\sim$ 0.15 for the $2.4M_{\odot}$ and $2.8M_{\odot}$ models, with a value of $f_{\rm PDD}$ =0.008 perhaps best representing the distribution. Additionally, the $f_{\rm PDD}$ =0.014 $1.6M_{\odot}$ model already reaches the height of the O/He$\sim$ 0.5 objects, albeit at a slightly lower final mass. This does seem to suggest that it is possible to describe the two distinct groups of O/He abundances, as indicated in Fig. 7.2, with a single value of $f_{\rm PDD}$ when the similar final masses, but different O/He values, of the 1.6, 2.0 and $2.4M_{\odot}$ models are considered.

The carbon abundances are perhaps less in favour of any particular set of models, however, none of the sequences calculated could produce anything like the spread of values observed there. This may be more generally attributed to the sensitivity of the carbon abundance, which is far more easily mixed into the intershell region.

Additionally, it was observed that inclusion of CBM at the base of the convective envelope has the potential to alter the intershell abundances, and not in the previously mentioned way of changing the final mass of the object. The intershell abundances as a function of the CBM parameter are explicitly shown in Fig. 7.4, with the panels top to bottom representing masses $1.6M_{\odot}$, $2.0M_{\odot}$, $2.4M_{\odot}$ and $2.8M_{\odot}$ while the solid lines show the helium mass fraction, dashed lines show carbon and dotted oxygen. Included alongside the blue lines, representing models applying the value $f_{\rm CBM}$ at the base of the PDCZ, are the red lines showing models where $f_{\rm CBM}$ is applied at both the base of the PDCZ and convective envelope.

Although the influence of the convective envelope on the intershell abundances is not strong, it does exist in both higher mass models, for $f_{\rm CBM}$ =0.02 and $f_{\rm CBM}$ =0.03. For the case of the PDCZ alone, it appears the oxygen abundance continues to increase linearly with $f_{\rm CBM}$ up until $f_{\rm CBM}$ =0.03, the highest considered here. However, when the convective envelope is also included, it limits this increase in oxygen abundance at such values of $f_{\rm CBM}$.

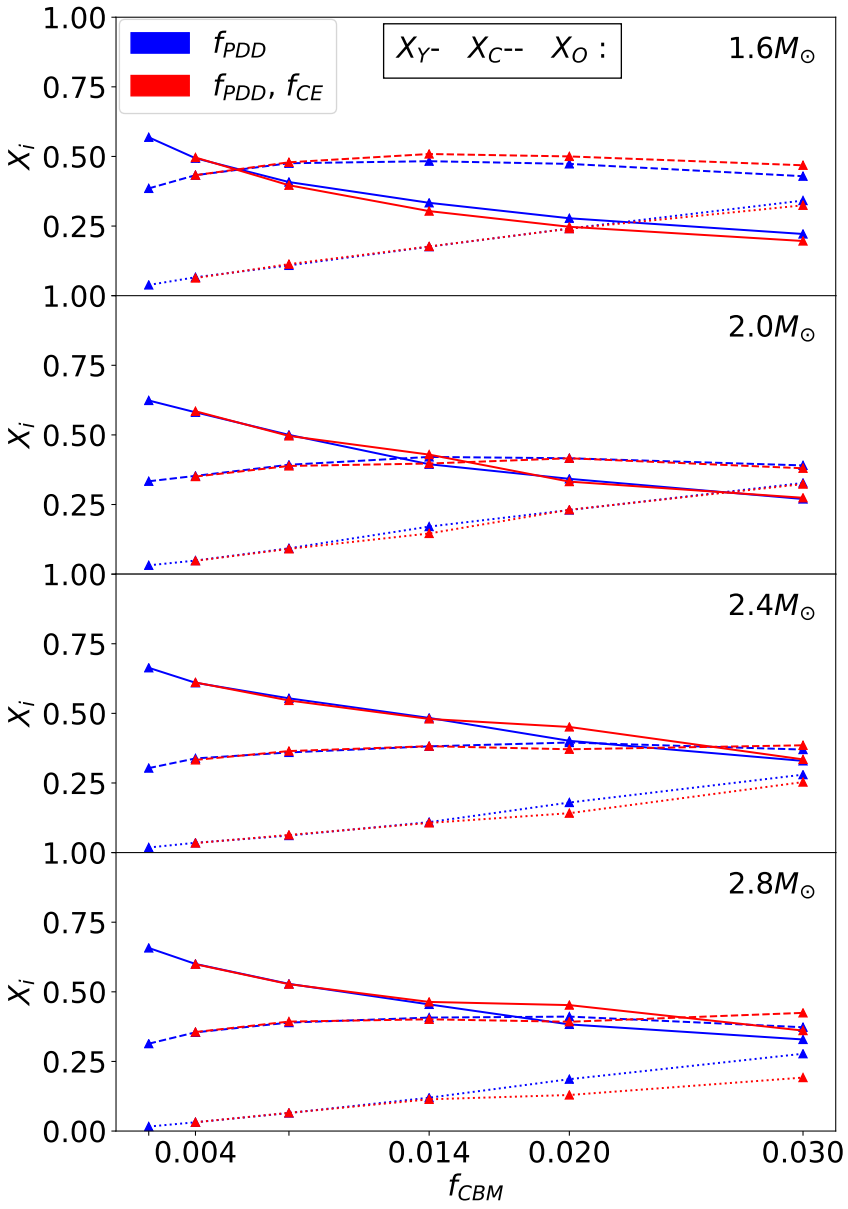

Figure 7.4: Mass fractions in the intershell at the end of the TP-AGB, as a function of $f_{\rm CBM}$, for sets of evolutionary models with the blue lines representing where $f_{\rm CBM}$ has been applied only at the base of the PDCZ, and the red where the same $f_{\rm CBM}$ has also been included at the base of the convective envelope. Each panel represents a different mass model as indicated. Solid lines (-) indicate helium; dashed (–), carbon and dotted (:), oxygen.

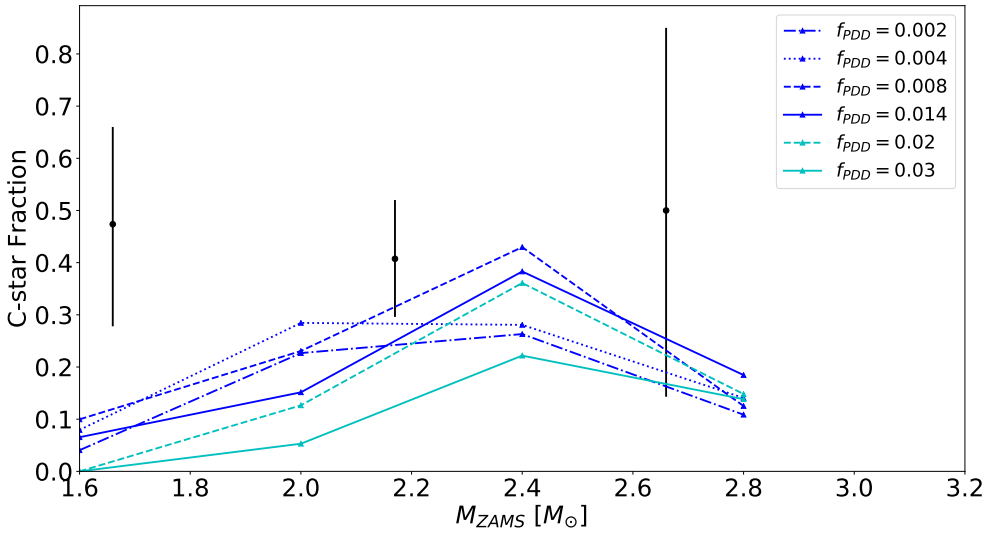

Figure 7.5: Carbon star fractions for models where CBM is applied only at the base of the PDCZ, all calculated at Z=0.008, with data points from Table 2. of Girardi & Marigo (2007) and error bars as discussed in Appendix B.2.1.

In conclusion, it could be claimed that for the models calculated, a value of $f_{\rm PDD}$ in the range 0.004-0.014 appears to be a limit of possible CBM (in agreement with values suggested in Herwig (2005)), with $f_{\rm PDD}$ =0.008 able to explain the observed oxygen abundances of the PG 1159 stars, although it may be that the higher value of $f_{\rm PDD}$ =0.014 is required to simultaneously explain the observed C/He. Surprisingly, it seems CBM at the convective envelope can in fact act to limit the increase of oxygen in the intershell region, though perhaps only at values which are not of interest in any case. It should also be noted, that although the higher values of C/He and O/He can be reproduced, the final mass of the models doing so are perhaps slightly too low (by about $\sim 0.02 M_\odot$).

7.2.2 Star Counts

The models where only the base of the PDCZ is active are now shown in terms of their carbon star fraction, in Fig. 7.5. The range of $f_{\rm PDD}$ covers 0.002-0.03, and the first point to note is that the C-star fraction does not continue to increase with increasing $f_{\rm PDD}$ as may have been expected from the results in Ch. 5.2. This is important

given none of the models shown in Fig. 7.5 appear to satisfactorily reproduce the observed C-star fractions, even accounting for binning and the coarse grid of models calculated. On the whole, the initial impression is that additional mixing at the base of the PDCZ alone is not sufficient to reproduce the observed numbers of carbon stars, for any value of $f_{\rm PDD}$. This presents an initial argument against the values taken by Miller Bertolami (2016), of $f_{\rm PDCZ}$ =0.0075 and $f_{\rm CE}$ =0.0.

The lack of increase in C-star fraction with increasing $f_{\rm PDD}$ is further investigated in Fig. 7.6, showing the final surface C/O value, for a different mass in each panel, as a function of the CBM mixing parameter $f_{\rm CBM}$. Each line colour corresponds to which boundaries this value is applied to, i.e. blue, only the base of the PDCZ is active; red, both the base of the PDCZ and convective envelope and green, only the convective envelope has $f_{\rm CBM}$ applied to it.

The final surface C/O values do not, however, illustrate that the results from the single thermal pulse investigated in Ch. 5.2 cannot be extrapolated to full evolutionary models. Although it was seen in that investigation that increasing the mixing parameter at the base of the PDCZ would lead to a strong, almost linear increase in the dredge-up efficiency, this is not seen in the final C/O values at the surface for the full evolutionary models. However, this is not due to a discrepancy between how the single thermal pulse and full evolutionary models behave. Indeed, when Fig. 7.7 is considered, showing the maximum dredge-up efficiency parameter as a function of initial mass for the models where only the base of the PDCZ is active, the behaviour clearly does follow that expected from the single thermal pulse investigation in Ch. 5.2.

This leaves an open question; Why are both the final surface C/O values, and the carbon star fractions of the models, not increasing with the value of $f_{\rm PDD}$ applied and are, in fact, decreasing beyond a certain value. The answer seems to arise from Fig. 7.3 which was discussed in the previous section. Although higher values for $f_{\rm PDD}$ do indeed lead to more efficient dredge-up, as the single thermal pulse investigation suggested, stronger mixing at the base of the PDCZ also changes the composition of the intershell, something which is primarily determined during the early thermal pulses as the intershell forms, only changing slightly thereafter (this can be seen in Fig. B.2 in Appendix B.1.2).

The means, that although the final C/O value for the $2.4 M_{\odot}$ $f_{\rm PDD}$ =0.03 model is C/O=1.36 compared to a value of C/O=3.51 for the $2.4 M_{\odot}$ $f_{\rm PDD}$ =0.008 model, the final mass fractions of carbon and oxygen at the surface tell a different story. For the $f_{\rm PDD}$ =0.008 model the values are $X_C = 0.017$, $X_O = 0.006$ while for the $f_{\rm PDD}$ =0.03 model, the values are $X_C = 0.014$, $X_O = 0.014$. So the reduced C-star fractions and final C/O values of the models with high $f_{\rm PDD}$ are not due to a reduction in the

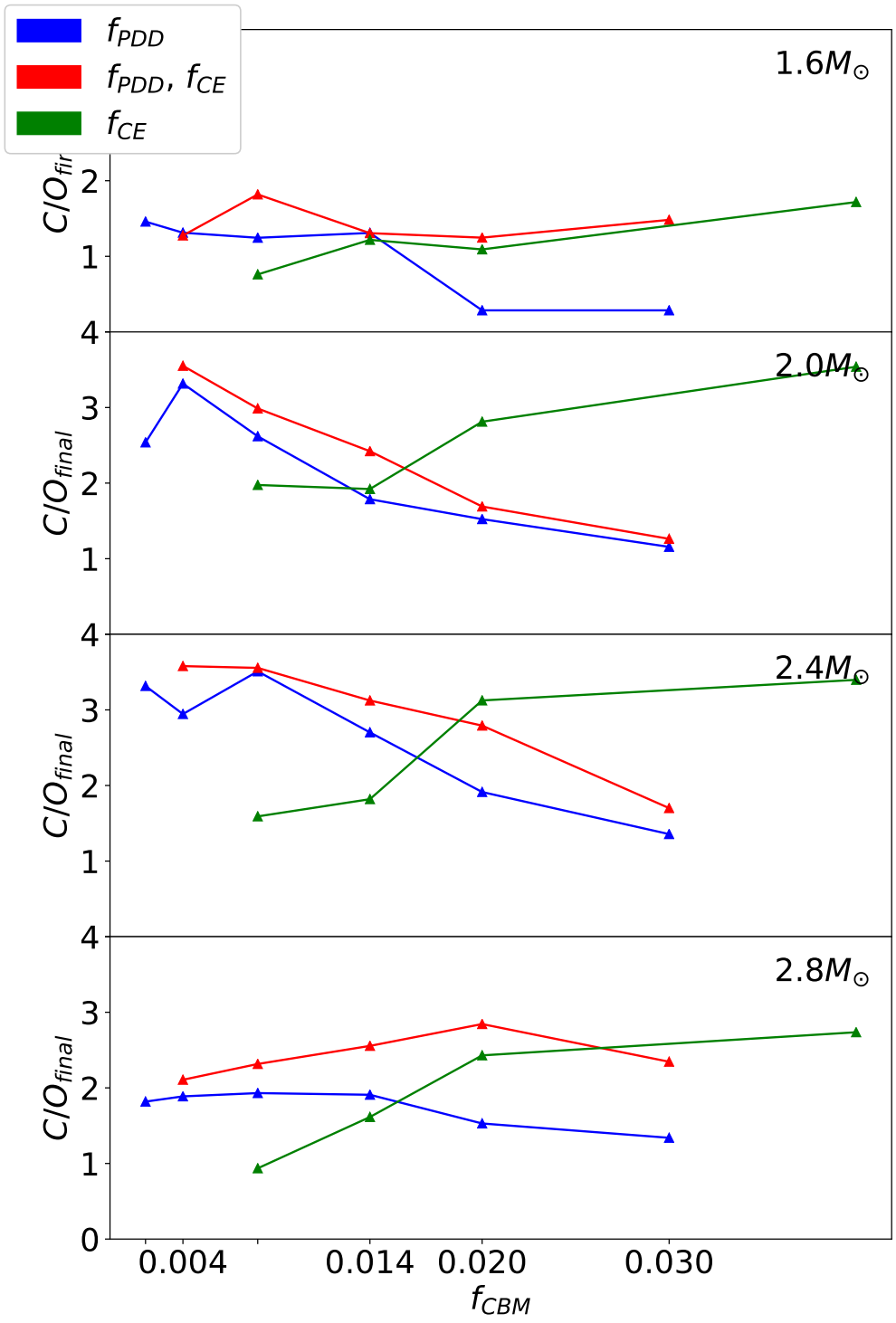

Figure 7.6: Final surface C/O value as a function of CBM efficiency parameter $f_{\rm CBM}$, where each line represent application at different boundaries (base of the PDCZ $f_{\rm PDD}$, base of the convective envelope, $f_{\rm CE}$, or both) with each panel showing a different mass as indicated.

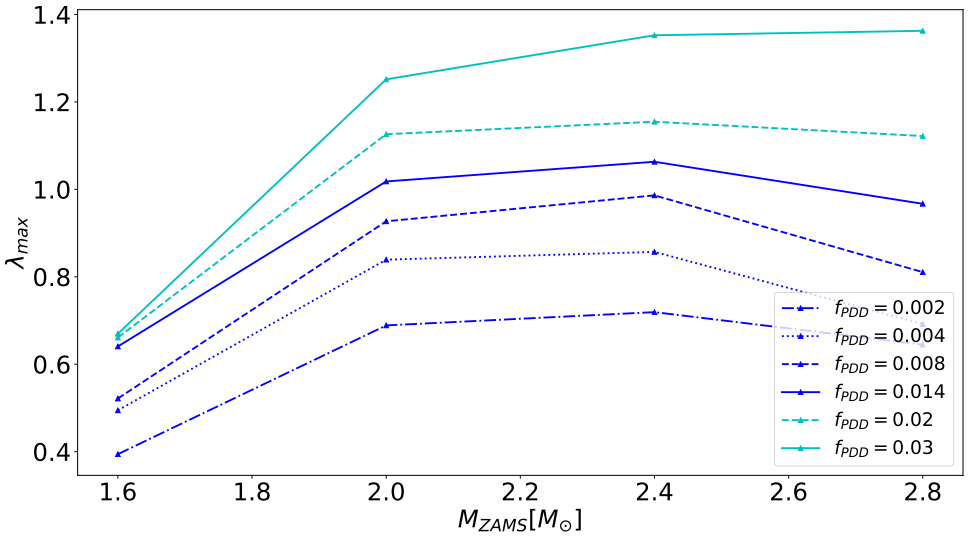

Figure 7.7: The maximum value for the third dredge-up efficiency parameter, λ, experienced by each mass model for the sets calculated with different values of $f_{\rm PDD}$ applied.

dredge-up efficiency, but rather a change in the composition of the material brought to the surface.

Fig. 7.8 shows a similar set of models as Fig. 7.5, this time displaying the C-star fractions for models which vary the mixing at the base of the convective envelope between values $f_{\rm CE}$ =0.008-0.4. In this instance, there is a far more straightforward interpretation, with an increase in $f_{\rm CE}$ producing an increased C-star fraction, in almost all cases. Furthermore, there is more readily acceptable agreement with the observed C-star fractions than was the case for the models including only $f_{\rm PDD}$. The data point at the lowest mass is perhaps still too high, though it is not unreasonable to think the models are sufficiently close when binning and a better-resolved grid of models are taken into account.

Although the C-star fractions increase fairly smoothly at each mass as a function of increasing $f_{\rm CE}$, this is not necessarily the case for the final surface C/O values in Fig. 7.6. At each mass, there is an increase in final C/O value with increasing $f_{\rm CE}$, however, there are also signs that it levels off at higher values, and possibly some indications of the step-like behaviour observed in the single thermal pulse investigation in Ch. 5.2. This is only really seen in the $2.0M_\odot$ and $2.4M_\odot$ cases, but the

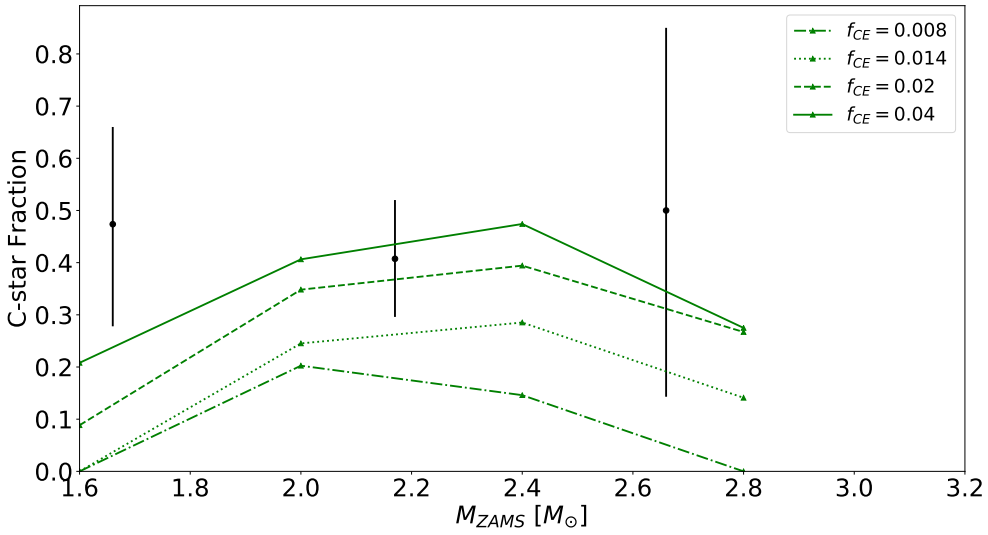

Figure 7.8: Carbon star fractions for models where CBM is applied only at the base of the convective envelope, all calculated at Z=0.008, with data points from Table 2. of Girardi & Marigo (2007) and error bars as discussed in Appendix B.2.1.

upper limit to how enriched a star can become when CBM is applied only to the convective envelope again appears to feature in all cases.

There are two possibilities when including CBM at both the base of the PDCZ and convective envelope. The first is to keep both $f_{\rm PDD}$ and $f_{\rm CE}$ equal at all times, which would limit the number of free parameters which are available when running the code. This implies that there are only two types of convective boundary, outwards and inwards, if hydrogen and helium core burning have the same CBM treatment. Here, the upper boundary of the PDCZ has been neglected, as it was shown in both Ch. 5.2 and Ch. 6.2 that it is not relevant, and that the same CBM could be applied to this boundary as is done for the convective cores without altering the models.

The other option is to apply different CBM at each boundary. A restriction which is applied to this approach is to take account of the maximum allowed distance that would be allowed by the buoyancy argument for momentum-based overshooting, as was investigated in Ch. 5.1. Although the results for both boundaries yielded values for $f_{\rm CBM}$ which were too low ($f_{\rm CE}$ $\sim$0.003, $f_{\rm PDD}$ $\sim$0.0002) to reproduce, even to some approximation, the observables under consideration here, it is the differential between the two which was considered to be of interest. As was previously stated,

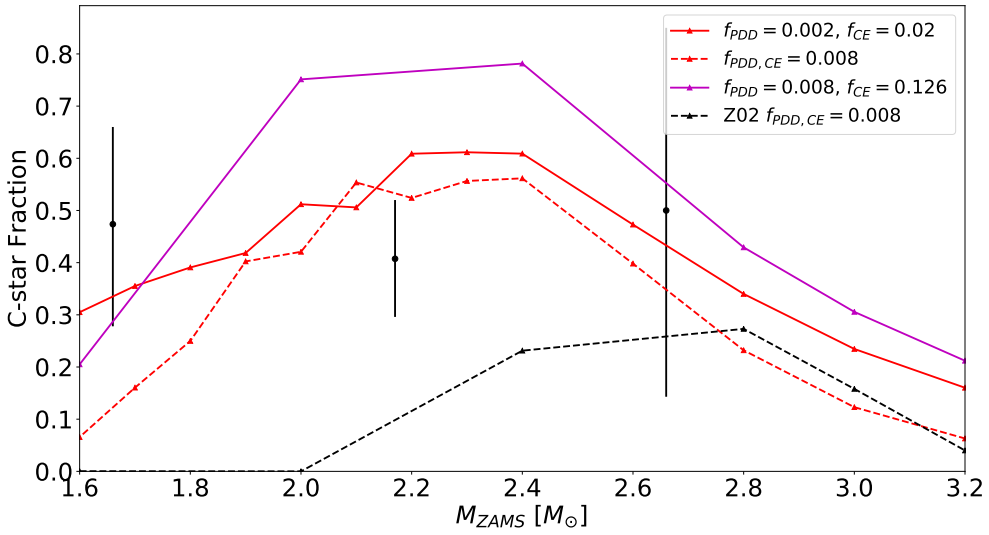

Figure 7.9: Carbon star fractions for models where CBM is applied at both the base of the PDCZ and the convective envelope, all calculated at Z=0.008 except for the black dashed line at Z=0.02, with data points from Table 2 of Girardi & Marigo (2007) and error bars as discussed in Appendix B.2.1.

although the investigation of the maximum allowed distance yielded a value for $f_{\rm PDD}$ up to 20 times smaller than for $f_{\rm CE}$, their respective influence on the third dredge-up has a comparable disparity in values. This was again evident in the full evolutionary calculations, as can be seen in Fig. 7.6 showing that the final surface C/O values for models with $f_{\rm CE}$ =0.02 are comparable to the results for $f_{\rm PDD}$ =0.002.

As such, models for a range of combinations of $f_{\rm PDD}$ and $f_{\rm CE}$ in conjunction were produced, with a focus on models where the two are equal, along with some, where the value of $f_{\rm CE}$ is higher than $f_{\rm PDD}$. Additionally, the preferred value for mixing at the convective envelope, which is derived for the production of the ^{13}C (Herwig et al., 2003), was also considered, namely $f_{\rm CE}$ =0.126, which is higher than would have otherwise been applied. This is sometimes taken alongside a value of $f_{\rm PDD}$ =0.008 (Pignatari et al., 2016; Ritter et al., 2017) for the reproduction PG 1159 star abundances, which agrees with the value found in Sec. 7.2.1.

A selection of models considered to be of interest are presented in Fig. 7.9. The first set of models to note are those represented by the magenta line, which show the models with $f_{\rm PDD}$ =0.008, $f_{\rm CE}$ =0.126 and which produce C-star fractions of close to

80% at both $2.0M_{\odot}$ and $2.4M_{\odot}$. Even with the possible influence of binning on the observed data points, and the fact that these two masses do not represent the peak C-star fraction (as exhibited by the other models), this seems to give a first indication that the values sometimes taken for CBM on the TP-AGB (Pignatari et al., 2016; Ritter et al., 2017) do not necessarily agree with evolutionary observational evidence, even if they are well motivated by other means.

The dashed lines both show models with $f_{\rm PDD}$ =$f_{\rm CE}$ =0.008, with the black line corresponding to models with Z=0.02 to show the difference when the metal fraction of the models is altered. Not only are the C-star fractions significantly lower, in this case, the peak also shifts to higher initial masses, emphasising that composition could play a significant role in how the models relate to the observations.

The other lines shown, for sets of models with $f_{\rm PDD}$ =$f_{\rm CE}$ =0.008 and $f_{\rm PDD}$ =0.002 with $f_{\rm CE}$ =0.02, both show plausible agreement with the observational data, bearing in mind the possible effects of binning on the data and other uncertainties. It is worth noting that the models with the same value for mixing at both boundaries have a more peaked distribution, while the models with the different values suggest more notable C-star fractions beyond the mass range considered. Unfortunately, the mass bins either side of this range, at $M_{\rm TO}$=1.18 and $M_{\rm TO}$=3.17 contain 2 and 1 M-stars respectively, and no carbon stars.

As an additional comparison, the same sets of models as in Fig. 7.9 are shown again in Fig. 7.10, this time showing the C-star lifetimes, in order to directly compare with the data markers derived from the stellar number counts in Girardi & Marigo (2007). Although all the models calculated at Z=0.008 reproduce the basic shape of the observations, the lifetimes are 2-3 times lower than the derived lifetimes, even in the case with $f_{\rm PDD}$ =0.008 and $f_{\rm CE}$ =0.126. Again, the set of models calculated for Z=0.02 show how important the initial composition can be in such comparisons. In fact, none of the models calculated here come close to reproducing the C-star lifetimes. Previously, models calculated with GARSTEC (Kitsikis, 2008; Weiss & Ferguson, 2009) were in better agreement with these observables. However, this was in fact due to the individual models calculated at $2M_{\odot}$ experiencing the phenomenon reported in Ch. 3, which increases the C-star lifetime.

7.2.3 IFMR

The IFMR is shown in Fig. 7.11, where the red lines are models where $f_{\rm PDD}$ =$f_{\rm CE}$ for different values at Z=0.008 while the black lines are their counterparts calculated at Z=0.02. The models with $f_{\rm PDD}$ =0.008, $f_{\rm CE}$ =0.126 calculated at Z=0.008 are also included. The models with $f_{\rm PDD}$ =$f_{\rm CE}$ at Z=0.008 all appear to be in relatively good

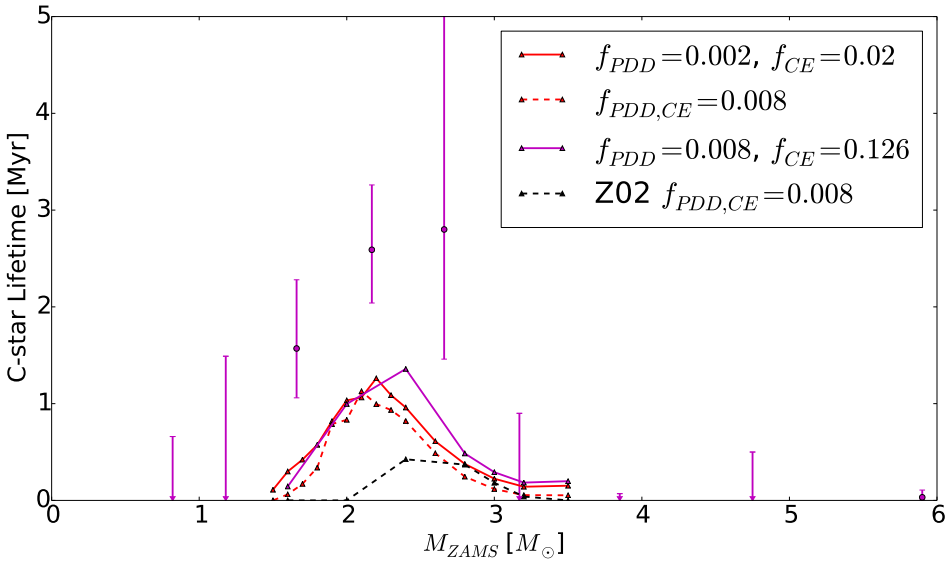

Figure 7.10: Carbon star lifetimes for models where CBM is applied only at both the base of the PDCZ and the convective envelope, all calculated at Z=0.008 except for the black dashed line at Z=0.02, with data points as derived in Girardi & Marigo (2007).

agreement with the main clump of observed objects around $3M_\odot$ and, interestingly, the change arising from the different CBM treatments is significantly less than that arising from the change in initial composition. The models calculated at Z=0.02 were intended to be the 'solar' case for the calculations performed, and hence would allow for reasonable comparison with the IFMR. Although this is likely to be too high a metallicity for solar (see discussion in Ch. 1.2.4), it should still be the closest of the models calculated and it would have to be said that none of these models give particularly good agreement with the $3M_\odot$ observations. This could also be a suggestion that the solar metal fraction suggested by Asplund et al. (2005) (Z=0.012) is more favoured.

Additionally, at the lower mass end ($\lesssim 2M_\odot$) the models are also at the lower boundary of agreement with the final masses observed. This confirms what was seen in Sec. 7.2.1, where the lower mass models, which may provide an explanation for the particularly high oxygen abundances (O/He$\sim$0.5), had final masses which were slightly too low (0.02-0.05$M_\odot$). That all sets of models calculated here roughly agree on the final mass of the stars at the lower mass end suggest something else may be

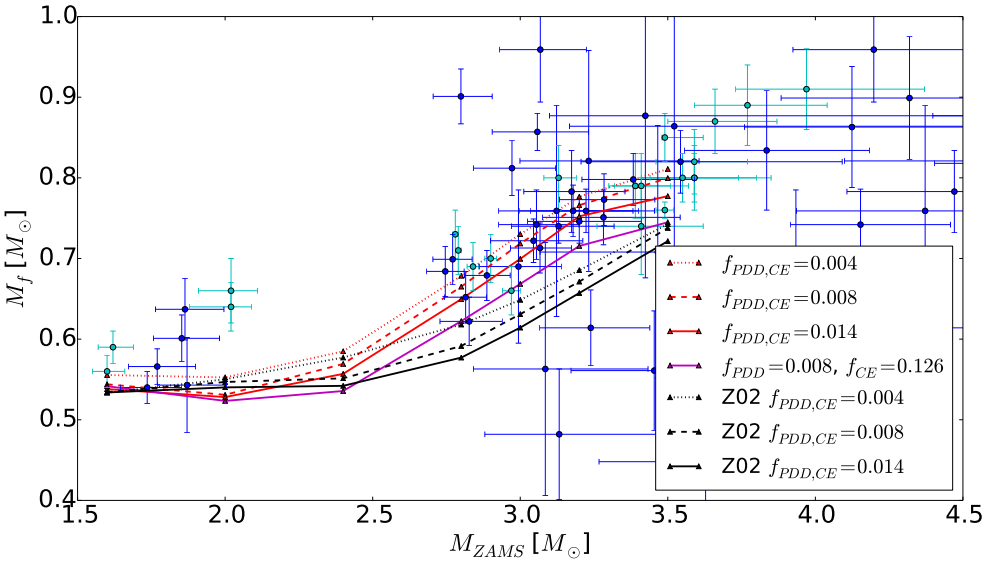

Figure 7.11: Initial-final mass relation for models where CBM has been applied at both boundaries for several values, black lines are all calculated at Z=0.02, all others at Z=0.008. Data markers are from a combination of Salaris et al. (2009) (blue) and Kalirai et al. (2014) (cyan).

the problem, with mass loss being the obvious candidate.

The models calculated for $f_{\rm PDD}$ =0.008, $f_{\rm CE}$ =0.126 are again shown for comparison. They also appear to be in tension with the observations, even though these models are calculated at Z=0.008, so the discrepancy would only get worse if these were also calculated at a higher metallicity of Z=0.02.

For interest, the models from the Ch. 6.1 studying the influence of CBM during phases prior to the TP-AGB are shown in Fig. 7.12. As these models were all calculated with Z=0.02, it is not surprising that they are below the observational markers in the $3M_\odot$ region. The inclusion of core CBM does increase the final masses of the stars, and possibly lead to a functional form which better represents the data, but the final masses still appear to be too low, even though for these models $f_{\rm CE}$ =0 and $f_{\rm PDCZ}$ =0.0075 (apart from the model with no additional mixing).

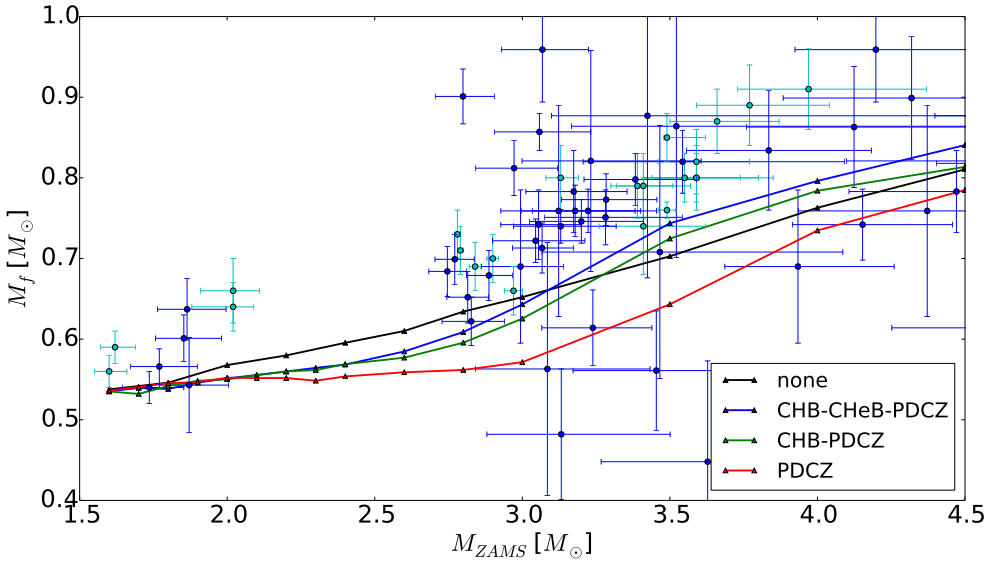

Figure 7.12: Initial-final mass relation for models where CBM has been applied during different convective core stages and at the base of the PDCZ for all except the black line. All are calculated at Z=0.02. Data markers are from a combination of Salaris et al. (2009) (blue) and Kalirai et al. (2014) (cyan).

7.3 Discussion of Observational Comparisons

The results in this chapter have focused on comparison with observations in order to try and constrain the mixing on the TP-AGB. The different observational evidence helps to probe the various aspects of TP-AGB evolution with different approaches, however, it has proven difficult to find satisfactory conclusions about CBM on the TP-AGB which is consistent with the, admittedly limited, observational evidence.

Beginning with the boundary at the base of the PDCZ, it becomes quickly apparent that a value of $f_{\rm PDD}$ =0.008 would be preferable in trying to reproduce the abundances of PG 1159 stars. There is, of course, some flexibility in this value but, of the models calculated, the intershell abundances produced by $f_{\rm PDD}$ =0.004 are too low and those with $f_{\rm PDD}$ =0.014 slightly too high. Although these values perhaps provide suitable limits for the value which $f_{\rm PDD}$ should take and is in agreement with values suggested by Herwig (2005) and used in other evolutionary calculations (Miller Bertolami, 2016; Pignatari et al., 2016; Ritter et al., 2017). A value of $f_{\rm PDD}$ =0.008 is also in agreement with the value suggest by Lugaro et al. (2003) as being possibly

beneficial in s-process nucleosynthesis. Interestingly, there is also some evidence that if CBM is included at both the base of the PDCZ and convective envelope, with the same value, then at higher values of $f_{\rm CBM}$ the increase in oxygen abundance in the intershell is limited compared to models where CBM is active only at the base of the PDCZ. This only occurs at values which are higher than would be suggested here, but it is worth noting that the convective envelope can unexpectedly limit the change in intershell abundances.

When the C-star fractions are considered, it becomes apparent that CBM at the base of the PDCZ alone is probably insufficient, at any strength, to explain the abundance of carbon stars and suggests that setting $f_{\rm CE}$ =0 is perhaps not a good idea, as is done in some cases (Miller Bertolami, 2016). This is due to the fact that, although an increasing value of $f_{\rm PDD}$ leads to an increase in the quantity of material which is dredged-up from the core, it also leads to an increase in the oxygen mass fraction in the intershell region. This limits both the fraction of C-stars as well as the final surface C/O value which is reached, which actually begins to decrease for higher values of $f_{\rm PDD}$. Another argument against $f_{\rm CE}$ =0 is the general requirement for some mixing at this boundary to reproduce s-process abundances (Herwig et al., 2003; Lugaro et al., 2003).

This decrease in final C/O value with increased mixing is in contrast to models which only include mixing at the convective envelope. This follows a more expected trend of increasing the final C/O value with increased mixing, although it does appear to exhibit plateau-like behaviour (as was seen in the single thermal pulse investigation in Ch. 5.2) which means there is a limit to how high $f_{\rm CE}$ can be and still increase the surface C/O value. CBM at the convective envelope alone appears to have a better chance of reproducing the observed C-star abundances, although it may require quite a high value of $f_{\rm CE}$ ∼0.4, however, this would not then account for the abundances of PG 1159 stars.

The apparent requirement of additional mixing at the PDCZ for the intershell abundances, and seeming inability to reproduce C-star fractions with mixing only at the base of the PDCZ, led to multiple combinations of $f_{\rm PDD}$ and $f_{\rm CE}$ to determine if the ranges of these values could be constrained. Primarily this was done with the principle that a limited number of free parameters is probably a good thing and that as both boundaries are mixing inwards into the star there is a basic argument for keeping the parameters the same. As such, many cases investigated were carried out with $f_{\rm PDD}$ =$f_{\rm CE}$ also limiting the combinations.

However, there was also an argument, based on the investigation of the maximum allowed distance for momentum-based overshooting in Ch. 5.1, which suggested that the conditions at the base of the PDCZ are less favourable for such mixing as

compared to the base of the convective envelope. This must be considered alongside the fact that the base of the PDCZ can influence the evolution for far smaller values of $f_{\rm CBM}$, which was seen in both the single thermal pulse investigation in Ch. 5.2 and also in the full evolutionary models in this chapter, from the third dredge-up observed. In particular, for the final C/O values reached by the evolutionary models presented in 7.2.2, models with $f_{\rm PDD}$ =0.002 produced comparable values to $f_{\rm CE}$ =0.02. This is a similar disparity in the values obtained from the maximum distance investigation, with an order of magnitude difference between the two parameters, although for both boundaries these values are an order of magnitude higher than the results in Ch. 5.1 suggested.

Reasonable agreement with the observed C-star fractions was obtained, both for models with $f_{\rm CE}$ =$f_{\rm PDD}$ =0.008 and when $f_{\rm PDD}$ =0.002, $f_{\rm CE}$ =0.02, bearing in mind the uncertainties in the observations due to the low number statistics, uncertainty in initial mass and effects of binning the clusters. These two sets of models provide a reasonable agreement, with different motivations for the relation between the values of $f_{\rm PDD}$ and $f_{\rm CE}$. Keeping the same large differential between the two parameters, as was suggested by the investigation in Ch. 5.1, while simultaneously increasing the value mixing at the base of the PDCZ to a value of $f_{\rm PDD}$ =0.008 to reproduce the abundances of PG 1159 stars would make agreement with the C-star observations difficult. If instead, the mixing for both boundaries is kept the same, then it is perhaps in better agreement with observations but may suggest that the mechanism behind the additional mixing is not momentum based overshooting, at which point there is again a question of why they should take the same value.

The models which were calculated at Z=0.008 are in reasonable agreement when compared with the IFMR, particularly in the clump of stars around $3M_{\odot}$, although also within the lower edge of agreement with the stars below $2M_{\odot}$. However, this semi-empirical relation is for solar-like metallicities and when models for the same parameters are also calculated for Z=0.02 the result is a significant drop ($\sim$0.08$M_{\odot}$) in the final mass of the stars, raising tensions with the observations and demonstrating that within the parameter range, the initial composition can be more influential than the CBM treatment. Although a value of Z=0.02 is perhaps too high to be considered solar (see Ch. 1.2.4 for a discussion), it is nonetheless expected to be closer than the Z=0.008 models.

Additionally, it was investigated what the effects of taking a value for mixing at the convective envelope of $f_{\rm CE}$ =0.126 would be. This is motivated by the production of the ^{13}C pocket (Herwig et al., 2003), which is sometimes taken as justification for its use in evolutionary calculations (Pignatari et al., 2016; Ritter et al., 2017), normally alongside a value of $f_{\rm PDD}$ =0.008 to reproduce PG 1159 star abundances.

Although individually well motivated, the results of the models calculated here suggest a C-star fraction which seems substantially too high and an IFMR which even at Z=0.008 is in tension with the observations making the parameters seem unlikely to be suitable for evolutionary calculations.

In several instances, there appears to be tension of the final masses of the models with the observational data. Not only for the Z=0.02 models with the final masses for initial mass models in the region of $3M_{\odot}$, but also for all models with $M \lesssim 2M_{\odot}$. However, it should be noted that far better agreement in the region of $3M_{\odot}$ was obtained for models calculated at Z=0.008, perhaps favouring the lower solar abundances suggested by Asplund et al. (2005) (Z=0.012) in particular but also Asplund et al. (2009) (Z=0.014), which were discussed in Ch. 1.2.4. This would have a smaller influence on the models with $M \lesssim 2M_{\odot}$ but would also act in a way to increase the final masses slightly, easing tension with observations.

Although the final masses of the lower mass models cannot explicitly be said to be too low given the spread of data, it is again observed when comparing with the abundances of PG 1159 stars. In this case, the lower mass models, which may be responsible for the higher oxygen abundances (O/He$\sim$0.5), have a final mass which is also $\sim$0.02-0.05$M_{\odot}$ too low, although the uncertainties in the observational masses prevent any strong conclusion when taken in isolation. Coupled with the discrepancy with the derived C-star lifetimes of Girardi & Marigo (2007), this may be an indication that the mass loss is too strong, although the constraints are not tight enough to be sure. If a lower mass loss were taken, this may also impact on which CBM parameters would best agree with observations, although this does not so significantly impact on the IFMR.

Alternatively, the phenomenon which was observed in Ch. 3 would be another way of significantly increasing the C-star lifetimes and core masses, for a very limited range of models. The latter would even result in far too high C-star lifetimes, however, as it would only occur (if at all) in a very limited mass range, then the effect of binning may smooth this effect out increasing the overall observed C-star lifetimes.

7.4 Summary

The work presented in this chapter has attempted to constrain the efficiency of any additional mixing which may be required beyond the formal convective boundaries during the TP-AGB evolution. The two boundaries which were considered to be of interest were the base of the PDCZ and the base of the convective envelope, while the upper boundary of the PDCZ was neglected as it was demonstrated in Ch. 5

and Ch. 6 to be irrelevant.

It has been shown that mixing with a value $f_{\rm PDD}$ =0.008 at the base of the PDCZ is a good choice for the reproduction of PG 1559 star oxygen abundances, with models at $f_{\rm PDD}$ =0.014 and $f_{\rm PDD}$ =0.004 providing upper and lower limits, in agreement with those suggested in Herwig (2005). It has also been demonstrated that while some mixing at the base of the convective envelope is required, as no value of $f_{\rm PDD}$ appears to suitably explain the C-star abundances, a value of $f_{\rm CE}$ =0.126 as taken from nucleosynthesis arguments (Herwig et al., 2003; Pignatari et al., 2016; Ritter et al., 2017) is too high to be used in evolutionary models given the high C-star fractions and low final masses.

Both the final masses of the PG 1159 stars and the semi-empirical IFMR suggest that for low mass initial models ($\lesssim 2M_{\odot}$) the final masses obtained in all cases were possibly slightly too low ($\sim$0.02$M_{\odot}$). More of an issue are the models at Z=0.02, with mixing which could reproduce the C-star fractions, have final masses which are in tension with the objects observed $\sim 3M_{\odot}$, again on the low side. Coupled with the inability to reproduce the derived C-star lifetimes of Girardi & Marigo (2007), this potentially suggests that the mass loss rates of these models are too high. If the mass loss rates were lowered, this would have a knock-on effect on the CBM, as less efficient mixing could still result in sufficient carbon stars if given more time.

On the balance of the evidence presented here, it seems quite clear that mixing at the base of the PDCZ should be included, with $f_{\rm PDD}$ =0.008 appearing to be a good choice. There also appears to be a good argument for including mixing at the convective envelope, and since a significantly higher value than $f_{\rm CE}$ =0.008 can also safely be ruled out for evolutionary calculations it seems to be reasonable to suggest keeping the two values equal, i.e. $f_{\rm PDD}$ =$f_{\rm CE}$ =0.008. Although it must also be noted that this investigation has only considered one method for including additional mixing.

Chapter 8

Conclusion

This thesis has primarily explored two aspects governing the evolution of Thermally Pulsing Asymptotic Giant Branch (TP-AGB) stars. The first, the atmospheric boundary condition, was an aspect where the typical assumptions made by stellar evolution codes were known to be questionable when it came to the TP-AGB evolution. The second, mixing at convective boundaries is a known problem within 1-dimensional evolution codes but not one with a known solution and where implementations are chosen for a variety of reasons. Additionally, behaviour which is believed to be previously unseen in TP-AGB models was observed and further investigated.

Improvements and alterations were made to the code to explore the effects of both the atmospheric and convective boundaries within the stellar evolution code. Throughout the investigations reported in this thesis, it has been abundantly clear that the TP-AGB evolution is incredibly complex, with the processes during this phase being inextricably linked and intertwined in such a way that isolating direct cause and effect relations becomes almost impossible.

Initially, the fundamental justifications, which are typically used in determining the outer boundary condition for the interior stellar evolution code, were considered. This was done through changing the geometry to take account of the geometric extent of the TP-AGB atmosphere by replacing the plane-parallel approximation with a spherically symmetric implementation. The influence of the opacities was also considered, as the standard Rosseland mean values usually taken are not strictly valid in the outermost layers of a star. This was done through the inclusion of Planck mean opacities in the outer layers of the atmospheric calculation. A grid of radiative transfer models was also implemented as a way of providing the outer boundary condition for the interior model, although, unfortunately, this grid did not extend to

sufficiently low surface gravities to follow the full TP-AGB evolution to its conclusion.

Through a combination of these different atmospheric implementations, it was shown that the grey opacity treatment is hugely relevant to the effective temperature, showing the importance of a radiative transfer approach. The geometry, at least as implemented through analytic relations, did not significantly alter the evolution of the stellar models. By comparing with the implemented grid of radiative transfer models, an approach which transitioned from Planck mean opacities at $\tau = 0$ to Rosseland mean at $\tau = 2/3$ was taken to approximate the effects of using radiative transfer models for the full evolution and explore the extent to which this outer boundary can alter full TP-AGB evolutionary calculations.

The results of this investigation suggested that the influence of the outer boundary condition on the evolution is primarily limited to a change in the mass-loss, due to a change in the effective temperature. However, any changes to the internal behaviour of the star appears to be limited to a small change in the depth to which the convective envelope penetrates, while the influence on observable quantities of TP-AGB stars is negligible. It can be said that due to the changes in the mass-loss, the yields from these stars may change as the surface composition varies during the TP-AGB. However, most mass is lost at the final thermal pulse and the number of thermal pulses is not significantly altered. Furthermore, any changes arising from a different treatment of the outer boundary condition could also be achieved through changes to the mass-loss prescription or even the mixing length parameter, which also directly influences the effective temperature. Therefore, given the other uncertainties which exist in TP-AGB modelling, it must be said that the atmospheric boundary condition is not a priority, especially given the lack of a suitable alternative which covers the full evolution. A physically motivated alternative would be preferable, if it were available, as although the effects can be largely reproduced through other means, a better atmospheric treatment would help to remove an uncertainty in the models which does have at least some influence.

A curious point which arose during the investigation of the outer boundary condition was the anomalous behaviour discussed in Ch. 3. Under specific conditions, of a low core mass at the first thermal pulse and strong CBM leading to third dredge-up which decreases the size of the core on the TP-AGB, thermal pulses are suppressed and the star briefly resumes stable double shell burning in what has been referred to here as the quiescent phase. This appears to have been the first time such behaviour has been observed in TP-AGB models and does appear to arise from physical, rather than numerical, conditions. However, the conditions which lead to such behaviour are quite particular and so it is not expected to be widely occurring, if at all. There is the possibility such behaviour could be present in a star, especially if the mechanism

behind CBM in TP-AGB stars is something which can is more specific to individual objects, such as rotation. In the case that this would occur in a star, then it drastically changes key observable properties in terms of the final mass of the object and the carbon-star lifetime, both of which are significantly increased by the anomalous behaviour observed.

A deeper understanding of the potential influence of the mixing at different convective boundaries has also been achieved, through a combination of detailed numerical experiments which explore the parameter space in more depth, and full evolutionary calculations. The different methods have proven to be complementary to one another and together have helped to provide insight into the importance of the different convective boundaries considered. Although additional mixing beyond the formal convective region, at the various boundaries during the TP-AGB, has proven difficult to constrain and isolate, it has been shown that those boundaries which exist prior to this phase are also capable of having a profound impact on the outcome.

Investigating the effect of CBM in phases prior to the TP-AGB was, at least partially, motivated by the fact that some TP-AGB models produced, do not include core CBM (Karakas & Lattanzio, 2007; Cristallo et al., 2009). Given the clear impact on the TP-AGB evolution seen here, including changing the thresholds at which third dredge-up and hot-bottom burning take place, there is a strong argument for the inclusion of such CBM considering the observational evidence in its favour.

Mixing extending upwards from the PDCZ has been shown to have a negligible effect, from both exploratory investigations of a single thermal pulse, where the strength of the mixing was varied and through evolutionary calculations across a range of masses, where only one mixing parameter was explored.

Following the claim in Lattanzio et al. (2017) that momentum-based overshooting could not be responsible for any additional mixing beyond the base of the PDCZ, an investigation was carried out to test the consistency of this argument. By applying the buoyancy argument outlined in Lattanzio et al. (2017) to calculate the maximum distance which any mixing could extend beyond the base of the PDCZ. It was indeed found to be severely limited, however, when the same method was applied to the convective envelope, the values for the mixing efficiency parameter which would correspond to these distances at the two boundaries were perhaps an order of magnitude apart. For both boundaries these values were too low to be of significance, however, the disparity between the values at each boundary is not as significant as it first sounds. This is due to the fact that it was also shown in the single thermal pulse investigations, and later confirmed by evolutionary calculations at various masses, that mixing at the base of the PDCZ begins to influence the evolution and the third dredge-up to an extent comparable with the convective envelope, when the

value of the mixing parameter is an order of magnitude lower. Therefore it has to be taken to be the case that if the argument presented in Lattanzio et al. (2017) is considered valid, then it rules out momentum-based overshooting as the mechanism at both boundaries. However, no mixing at these boundaries would not consistent with observations of PG 1159 stars or C-star fractions.

The mixing from the boundaries during the TP-AGB, i.e. the convective envelope and the base of the PDCZ, were thoroughly explored through both investigations of a single thermal pulse (at two different masses) and through evolutionary models at a range of masses. The effect of the convective envelope on the third dredge-up efficiency displayed a similar upper limit as was observed in Herwig (2000), although it was not quite the on/off switch seen there. This trend was also seen in the evolutionary calculations, although not necessarily the same at all masses, as was the increased hot-bottom burning which was observed in both cases.

The base of the PDCZ was seen to increase the third dredge-up, seemingly without limit, while suppressing hot-bottom burning. It also appears to cumulatively act to increase the third dredge-up if mixing is applied in conjunction with the convective envelope. However, when attempts were made to constrain the mixing on the TP-AGB using observational data, it became apparent that there was a limit to the fraction of stars which could be carbon-rich when only the base of the PDCZ is active. This is not a result of some limit to the third dredge-up but rather a consequence of an altered intershell abundance changing the composition of material brought to the surface.

It was already known that to reproduce the abundances of PG 1159 stars, oxygen, in particular, requires mixing at the base of the PDCZ (Herwig, 2000). The values obtained here to constrain this boundary require $f_{\rm PDD} \sim 0.004 - 0.014$, in agreement with Herwig (2005), with the best agreement for the models at $f_{\rm PDD}$ =0.008 and was a result which appears to be metallicity independent, apart from the possible influence on final masses. This seems to be a very sound argument for the inclusion of additional mixing at the base of the PDCZ, however, it was seen that there was a limit to the carbon-star fraction when mixing is only included at this boundary which was possibly in tension with the observations, requiring the inclusion of mixing at the convective envelope at the same time.

Given the findings from considering the maximum distance that momentum-based overshooting could extend, in particular, the disparity between the mixing values at the two boundaries, then it may be reasonable to consider a significantly higher value for mixing at the convective envelope. Additionally, there is a nucleosynthesis argument (Herwig et al., 2003; Lugaro et al., 2003) for a value of $f_{\rm CE}$ =0.126 to reproduce the ^{13}C pocket. When such a value is taken alongside $f_{\rm PDD}$ =0.008, there

is significant tension between the models produced here and the observations, both in terms of carbon-star fractions and final masses. The final masses of the models was also to some extent a problem in other cases, although not as severe and may point to a problem in the mass loss or in the previous evolution, both of which could alter the required mixing to reproduce carbon-star fractions. The tension can also be alleviated by a reduction in the 'solar' metal mass fraction, such that there was far better agreement with the IFMR for the Z=0.008 models than the Z=0.02 models, possibly indicating a preference for the lower solar abundance given in Asplund et al. (2005).

Based on the evidence from PG1159 stars, a value at the base of the PDCZ of $f_{\rm PDD}$ =0.008 seems to be reasonably well justified. Additionally, it seems necessary to include some mixing from the base of the convective envelope and despite the disparity found in the allowed values from the buoyancy argument outlined in Lattanzio et al. (2017), it seems that the value for $f_{\rm CE}$ must remain fairly close to $f_{\rm CE}$ =0.008. If $f_{\rm CE}$ is significantly higher than this, there is tension with the observations and given the more basic consideration of limiting the number of free parameters, it would seem reasonable to apply $f_{\rm PDD}$ =$f_{\rm CE}$ =0.008 during TP-AGB evolutionary calculations.

Although there is still significant work left to fully understand these stars, it is nonetheless remarkable how successful stellar evolution models have been in reproducing, at least qualitatively, the behaviour of TP-AGB stars. Accurate mass-loss rates and further studies of mixing at the convective boundaries are required, as these remain the main sources of uncertainty within the models. Although synthetic TP-AGB models allow for wider population studies and the nucleosynthesis and yields from these objects is an important contribution to the wider community, the physical evolution remains an important aspect which requires continued development, as it contributes to both.

In conclusion, the work in this thesis has thoroughly explored the effects and suitability of the outer boundary condition along with mixing at convective boundaries. Primarily this has focused on the influence on the TP-AGB evolutionary phase, while during the course of the investigation new, previously unseen, behaviour has been observed in the models. There are still many uncertainties when modelling the TP-AGB but this thesis has constrained certain aspects and should help to inform future calculations.

Appendices

Appendix A

Acronyms and Model Labels

A.1 General Acronyms

- C-Star: Star with C/O>1
- CBM: Convective Boundary Mixing
- CE: Convective Envelope
- CHB: Core Hydrogen Burning
- CHeB: Core Helium Burning
- E-AGB: Early Asymptotic Giant Branch
- HB: Horizontal Branch
- HBB: Hot-Bottom Burning
- M-Star: Star with C/O<1
- MLT: Mixing Length Theory
- MS: Main Sequence
- PDCZ: Pulse-Driven Convection Zone
- PM: Planck Mean
- RGB: Red Giant Branch
- RM: Rosseland Mean
- RT: Radiative Transfer
- TDU: Third Dredge-Up
- TP-AGB: Thermally-Pulsing Asymptotic Giant Branch

A.2 Atmospheric Model Labels

For the models calculated in Ch. 2, model labels refer to the following:

- pp: Plane-parallel
- ss: Spherically symmetric
- RM: Rosseland mean opacities
- PM: Planck mean opacities
- RM-CO: Rosseland mean opacities interpolated in C/O value
- RT: interpolation within MARCS (pre-1st TP) and COMARCS (TP-AGB) grid of atmospheres
- ms: model evolved from the main sequence with stated atmospheric boundary

A.3 Convective Boundary Model Labels

Certain terms are used throughout Part II to refer to the inclusion of mixing at certain boundaries in models and also as a subscript in the CBM efficiency parameter, $f_{\rm CBM}$, to specify the strength of mixing at particular boundaries. The acronyms used have the following meanings:

- CBM: Convective Boundary Mixing
- CHB: Core Hydrogen Burning
- CHeB: Core Helium Burning
- CE: Convective Envelope
- PDCZ: Pulse-Driven Convective Zone
  - PDCZ-D or PDD: Downwards
  - PDCZ-U or PDU: Upwards

Appendix B

Technical Details

This appendix contains additional technical details pertaining to the stellar evolution code GARSTEC and some of the relevant parameters/methods for the work in this thesis, with sections covering the stellar evolution code, observations and numerical details.

B.1 Stellar Evolution Code

B.1.1 Identifying Convective Bundaries

The convective zones within GARSTEC are identified as follows:

- **Convective Core**: If the lower bound of the convective zone is at the centre of the star, then it is considered to be a convective core. Further categorisation is then achieved through checking whether energy generation is taking place, such that:
  - $\epsilon_H(r = 0) > 10^{-5} \implies$ Core Hydrogen Burning (CHB) convective zone.
  - $\epsilon_{He}(r = 0) > 10^{-5} \implies$ Core Helium Burning (CHeB) convective zone.

  where ϵ_i is the local energy generation (erg/s) due to nuclear burning of element i, considered here at the centre of the star.
  - During the initial stages of an evolutionary sequence ($< 1Myr$ after leaving the ZAMS), the convective core manifests as a series of small convective zones (up to 50). This appears to arise from evolving the star from

the ZAMS, and not all grid points are immediately convective. If core CBM is specified, it is in principle applied to each zone, although with or without additional mixing the zones quickly merge into a single convective zone at the core.

- **Convective Envelope (CE)**: If the lower boundary of the convective zone is above the mass shell where ϵ_H peaks and the upper bound satisfies $M(r)/M_* > 0.95$ then the convective zone is taken to be the convective envelope.

  – During testing, it became apparent that additional criteria were required, as, during the TP-cycle, the lower bound of the CE can dip below the peak Hydrogen burning shell during the quiescent Hydrogen burning stage. As such, a convective zone is also considered to be the convective envelope under the circumstances that all of the following criteria are satisfied:

    * max value of $\epsilon_H < 10^{-3}$
    * at the lower bound of the convective zone $\epsilon_{He} < 10^{-5}$
    * Over 90% of the mass in the convective zone is above the shell with peak H-burning

- **Pulse-Driven Convective Zone (PDCZ)**: If $\epsilon_{He} > 10^{-5}$ at lower boundary and the shell with maximum Helium burning is above 0.05 mass shell, then the convective zone is considered to be the PDCZ.

B.1.2 Intershell Abundances

The intershell abundances at the end of the TP-AGB phase of evolution are interesting as it is believed to be the same composition as is observed at the surface of PG 1159 stars. This represents a unique opportunity to gain insight into the internal workings of TP-AGB stars.

Ideally, the composition at the top of the intershell would be stored after each thermal pulse, when the PDCZ has disappeared. Unfortunately, this is not done in GARSTEC, and so the intershell abundances within this thesis are instead taken from the full stellar structure which is stored periodically, typically every 2500 evolutionary timesteps. This presents a problem, as the full structure which is committed to output can fall during a different stage of the thermal pulse cycle, leading to some variability in the values. To determine the values, the abundance within the mass shell halfway between the peak hydrogen and helium burning shells was taken, however, certain caveats were then applied to ensure reasonable results.

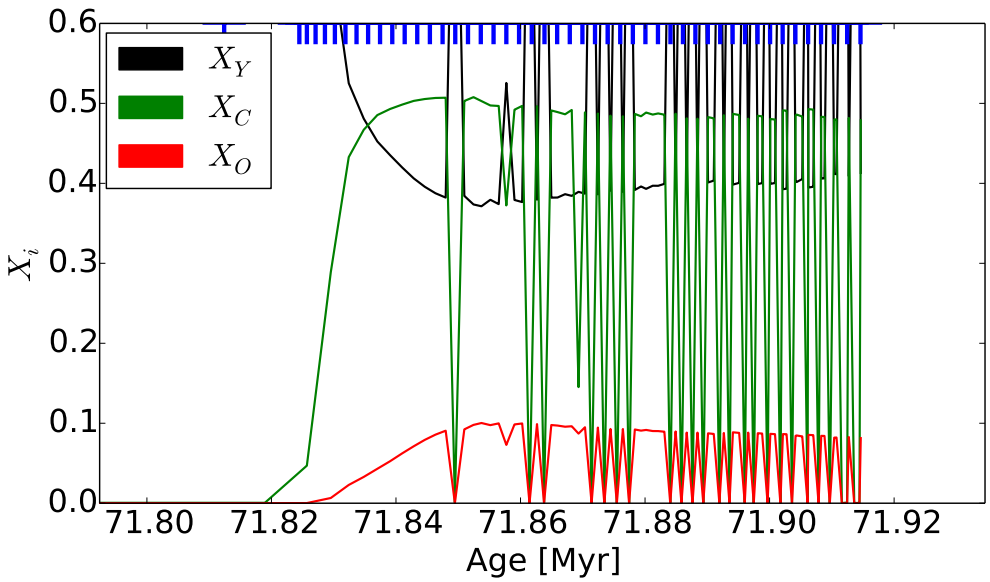

Figure B.1: Mass fractions (X_Y-black, X_C-green, X_O-red) in the intershell region for a $6M_\odot$ model, with $f_{\rm PDCZ}$ =0.0075. Blue markers indicate the time of a thermal pulse.

To illustrate what is obtained if the value between the two nuclear burning shells is taken for every full structure model available, Fig. B.1 shows the intershell abundances for a $6M_\odot$ evolutionary model, where core CBM was applied during both hydrogen and helium burning, and a value of $f_{\rm PDCZ}$ =0.0075 was taken. Each line shows a different mass fraction (X_Y-black, X_C-green, X_O-red) as a function of age, with the blue markers along the top indicating when a thermal pulse occurs.

Clearly, there is significant noise in the values presented in Fig. B.1; The most common cause of this, is the build-up of helium below the hydrogen burning shell during the interpulse phase, and which is then incorporated into the intershell composition during the subsequent thermal pulse. Rather than trying to avoid this build-up, and essentially search for where the composition is in line with expectations, models where the returned helium value exceeds $X_Y = 0.9$ were excluded. Additionally, models were also excluded if they were stored during the thermal pulse, where the helium luminosity was high, or during the quiescent hydrogen-burning phase, where the position of maximum hydrogen burning is not well defined.

The intershell abundances obtained as a result of these modifications are shown in Fig. B.2, for the same model as was shown in Fig. B.1. The result is a far

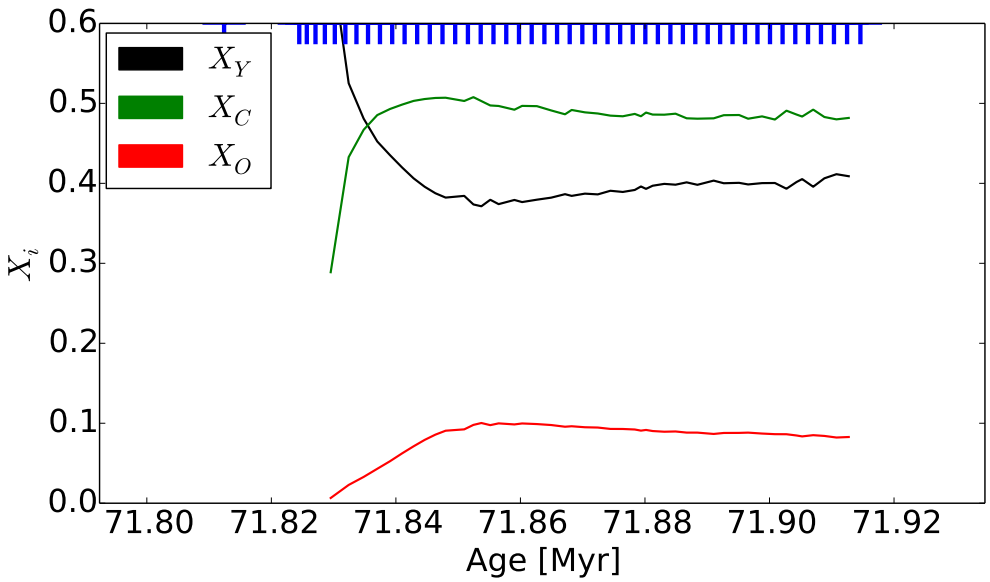

Figure B.2: Mass fractions (X_Y-black, X_C-green, X_O-red) in the intershell region for a $6M_\odot$ model, with $f_{\rm PDCZ}$ =0.0075 where certain models have been excluded from the calculation of the intershell abundance for reasons discussed in the text. Blue markers indicate the time of a thermal pulse.

more consistent representation of the intershell abundances, with the initial build up of carbon and oxygen during the early thermal pulses, before the burning shells start progressing outwards and the helium begins to gradually increase with each successive thermal pulse.

B.1.3 Convergence and Consistency

As much as possible is done to enforce consistency among the sets models which are compared here, however it is an unfortunate reality that not all, in particular at higher masses, reach the end of the TP-AGB evolution due to convergence problems. Fig. B.3 shows the mass ratio, between the core and total mass, at the final thermal pulse as a function of initial mass for sets of models taken from Ch. 6.1. This illustrates that there can be some differences amongst the models, but that there does not appear to be any systematic effects which fundamentally alter any of the observed results which are otherwise discussed.

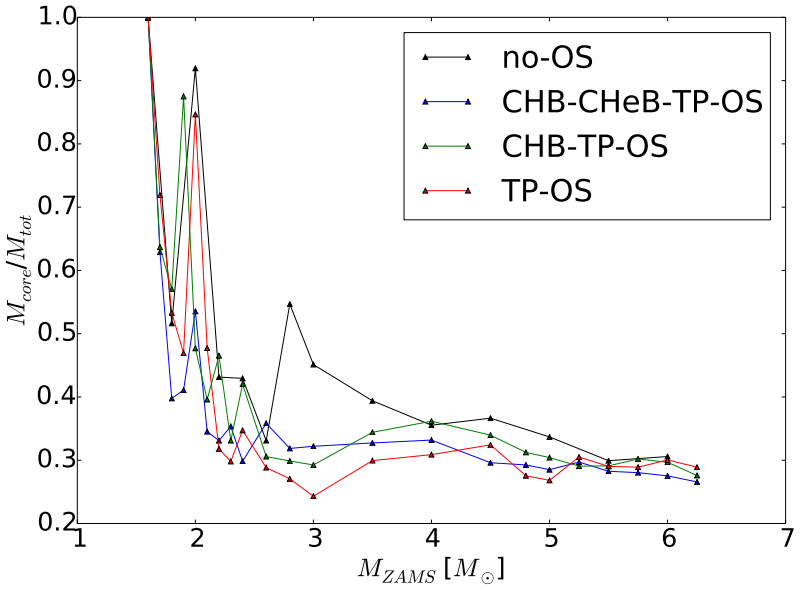

Figure B.3: The ratio between the core mass and the total mass at the last thermal pulse calculated as a function of initial mass for different active convective boundaries.

B.2 Observations

B.2.1 Star Counts

The way the observational constraint is implemented within this work is to consider the fraction of all stars at a given mass which are carbon-rich, taken as $N_{\rm C}/(N_{\rm C}+N_{\rm M})$, where N_C denotes the number of stars where the surface C/O>1 and N_M is the number of M-stars, where C/O<1. The total number of stars in each of the three bins being considered are [19, 54, 8], so it is desirable to have some indication of how much weight each should be given in any investigation.

As a simple indication of importance, a cumulative Poisson distribution of each number count was taken and interpolated such that the region around the initial count which covers 68% of the total distribution is covered. This is shown in Fig. B.4 for N=32, with the vertical dotted lines indicating the limits. In this case, the corresponding limits are 25.87 and 37.12 which are then rounded down or up respectively.

For a given data point, there is both an M-star and C-star number count, so if the

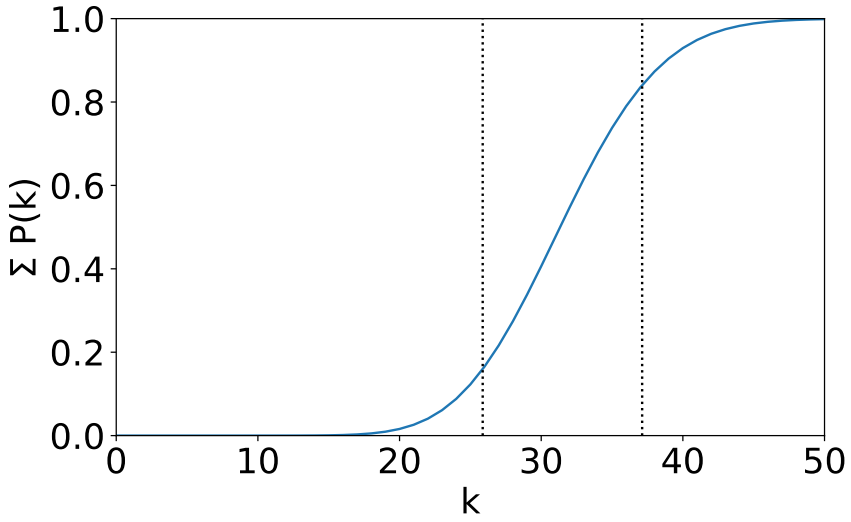

Figure B.4: Cumulative Poisson distribution for N=32, with vertical dashed lines marking the points enclosing 68% of the distribution centered on 32.

minimum M-star count possible (within this very wide tolerance) and maximum C-star count are taken, this should give the maximum observed C-star fraction possible within these limitations, i.e. the maximum C-star fraction is given by

$$\frac{N_{\mathrm{C}}^{\mathrm{max}}}{N_{\mathrm{C}}^{\mathrm{max}} + N_{\mathrm{M}}^{\mathrm{min}}}. \tag{B.1}$$

Equally, the minimum C-star fraction can be obtained by taking the maximum value N_M^{max} and the minimum value N_C^{min}. The minimum and maximum values for the number counts taken were as listed in Table B.1.

B.3 Numerics

B.3.1 Diffusive Cutoff

The form taken within GARSTEC for any additional mixing beyond the formal convective boundary takes the form outlined in Eq. 1.11. However, what is not always stated is the value of the numerical cutoff implemented along with this description. In GARSTEC, this cutoff value is typically taken to be $D_{\mathrm{cutoff}} = 10^{-20} D_0$, where D_0 is the value of the diffusion constant at the boundary of the convective region,

N	$N^{\min}$	$N^{\max}$
4	1	6
9	5	12
10	6	13
22	16	27
32	25	38

Table B.1: The minimum and maximum values taken for a given observation of N objects, calculated as discussed in the text.

and which enters into Eq. 1.11. The cutoff value is the lowest value of the diffusion constant calculated which is applied, i.e. no mixing is included for grid points where $D(z) < D_{\text{cutoff}}$. Given the nature of the work in Part. II into convective boundary mixing it was deemed worthwhile to take a moment to consider the importance of this numerical cutoff, D_{cutoff} .

Additionally, there is the option within GARSTEC of treating the mixing within the formal convective region diffusively, rather than instantaneously as is done in the standard case. In the region where additional mixing is applied, it is always treated diffusively. This treatment is governed within the code using Key 23 and was investigated alongside the treatment of D_{cutoff} to determine whether it was necessary or not. Throughout this section, the labels given to models are as follows

- DCa: gives the value of D_{cutoff} given by 10^{-a}, e.g. $10^{-10} \rightarrow$ DC10.
- K23: signifies the inclusion of Key 23.

Fig. B.5 shows the evolution of the core mass for a $1.8M_{\odot}$ star in the lower panel, and a $3M_{\odot}$ star in the upper panel, showing the size of the hydrogen free region. Black lines are with $D_{\text{cutoff}} = 10^{-20}D_0$, blue with $D_{\text{cutoff}} = 10^{-10}D_0$, red shows $D_{\text{cutoff}} = 10^{-20}D_0$ also using Key 23 and green $D_{\text{cutoff}} = 10^{-10}D_0$ also with Key 23.

There appears to be an offset in the age, but not significant differences in the outcomes of the models. The exception to this is perhaps the combination of $D_{\text{cutoff}} = 10^{-10}D_0$ with Key 23 in the $3M_{\odot}$ case, where a difference can be seen to the case without Key 23 during the RGB phase.

The lack of any significant differences in the models, other than the ages at which the progress through evolutionary stages, is further illustrated in Table B.2, which shows the age, total mass and core mass of the models at the first thermal pulse. It

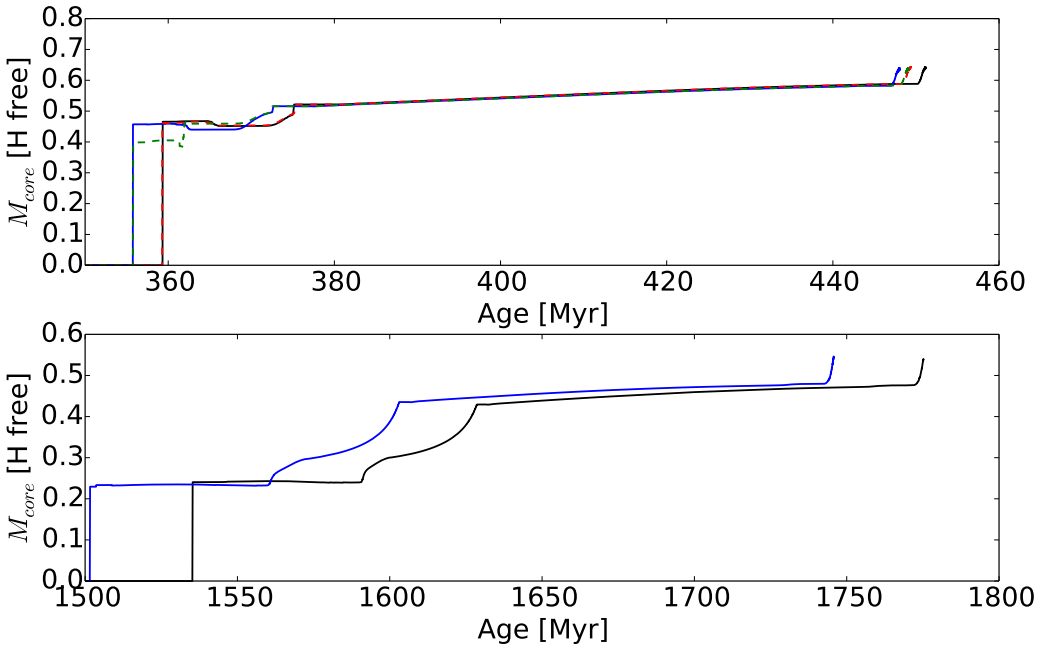

Figure B.5: The core Mass for a $3M_{\odot}$ (top panel) and $1.8M_{\odot}$ (lower panel) model, taken as the size of the hydrogen free region. The models shown are black, DC20; blue, DC10; red (dashed), DC20-K23; greed (dashed), DC10-K23. Only the first two models are shown in the $1.8M_{\odot}$ case.

can be seen that the maximum difference in core mass which is achieved in the $3M_{\odot}$ case is $0.008M_{\odot}$, while the difference in core mass between the $1.8M_{\odot}$ models is $0.003M_{\odot}$. It should also be noted that the reason core CBM results in a lower core mass for the $1.8M_{\odot}$ model is due to the effect on which cores undergo degenerate He-ignition.

In order to try and understand the significance of these values, and put them into context, the core masses at the first thermal pulse based on different core CBM, taken from models calculated in Part. II, are shown in Table B.3. The different models cover the case with no mixing beyond the formal convective boundary (labelled 'None'), models with CBM included during core hydrogen burning (CHB) only and finally models with core CBM during both the core hydrogen and core helium burning (CHB, CHeB) phases.

Additionally Fig. B.6 shows models which have been evolved from the same

a $[D_{co} = 10^{-a} D_0]$	t^{1TP} [Myr]	M^{1TP}_{tot} $[M_\odot]$	M^{1TP}_{core} $[M_\odot]$
	$1.8 M_\odot$		
10	1744.0	1.601	0.4895
20	1773.5	1.615	0.4865
	$3 M_\odot$		
10	447.3	2.898	0.595
20	450.5	2.897	0.600
10 Key(23)	448.3	2.907	0.592
20 Key(23)	448.7	2.897	0.599

Table B.2: The age at the first thermal pulse (t^{1TP}) along with the total (M^{1TP}_{tot}) and core masses (M^{1TP}_{core}) at the first thermal pulse, for models altering the CBM cutoff limit and the treatment of convective mixing as discussed in the text.

Core CBM	M^{TP1}_{core} $[M_\odot]$	
	$1.8 M_\odot$	$3 M_\odot$
None	0.511	0.506
CHB	0.485	0.576
CHB, CHeB	0.487	0.6

Table B.3: Core masses at the first thermal pulse for $1.8 M_\odot$ and $3 M_\odot$ models with different treatments of CBM during convective core phases, taken from Part. II.

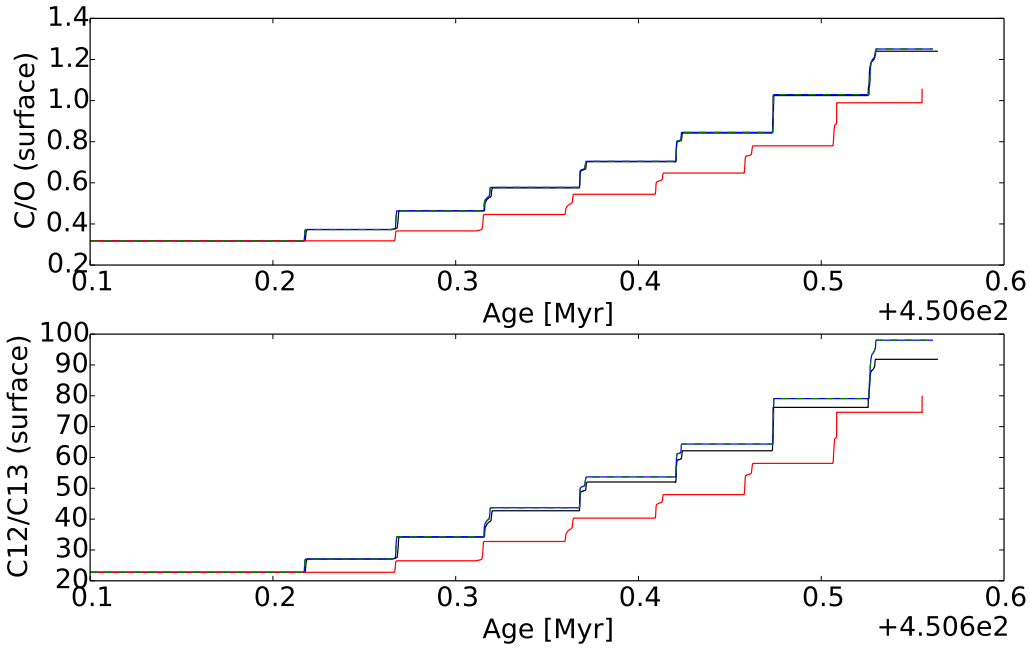

Figure B.6: Surface C/O ratio (top panel) and $^{12}C/^{13}C$ (lower panel) for a $3M_{\odot}$ star, where black, DC20; blue, DC10; red, DC5 and green, DC10-K23.

initial $3M_{\odot}$ star, taken prior to the first thermal pulse. This time there is also a red line included to show a model with $D_{\rm cutoff} = 10^{-5}D_0$, while the two models with $D_{\rm cutoff} = 10^{-10}D_0$, but where the green uses Key 23, overlap so exactly that one has been changed to a dashed line. This seems to indicate that between the $D_{\rm cutoff}$ $=10^{-10}$ and $D_{\rm cutoff}$ $=10^{-20}$ models, there is effectively no difference, apart from a small change in the carbon isotopic ratio. While the case where $D_{\rm cutoff}$ $=10^{-5}$ clearly has a limiting influence on the third dredge-up efficiency.

Overall this seems to indicate that the choice of the numerical cutoff for the calculated diffusive constant is important in influencing models prior to the TP-AGB, although the changes are not huge and are only a fraction of the change induced by including CBM during the convective core phases. However, the fact that a change is observed between models when the entire convective region is treated diffusively, but only between the models using the higher cutoff limit of $D_{\rm cutoff}$ $=10^{-10}$, along with the lack of effect on models on the TP-AGB suggests that the difference between $D_{\rm cutoff}$ $=10^{-10}$ and $D_{\rm cutoff}$ $=10^{-20}$ is only of importance over longer timescales. This also suggests that on instantaneous timescales they are equivalent, and mixing beyond a limit of $D_{\rm cutoff}$ $=10^{-10}$ is happening diffusively as had been suggested by Miller Bertolami (private communication).

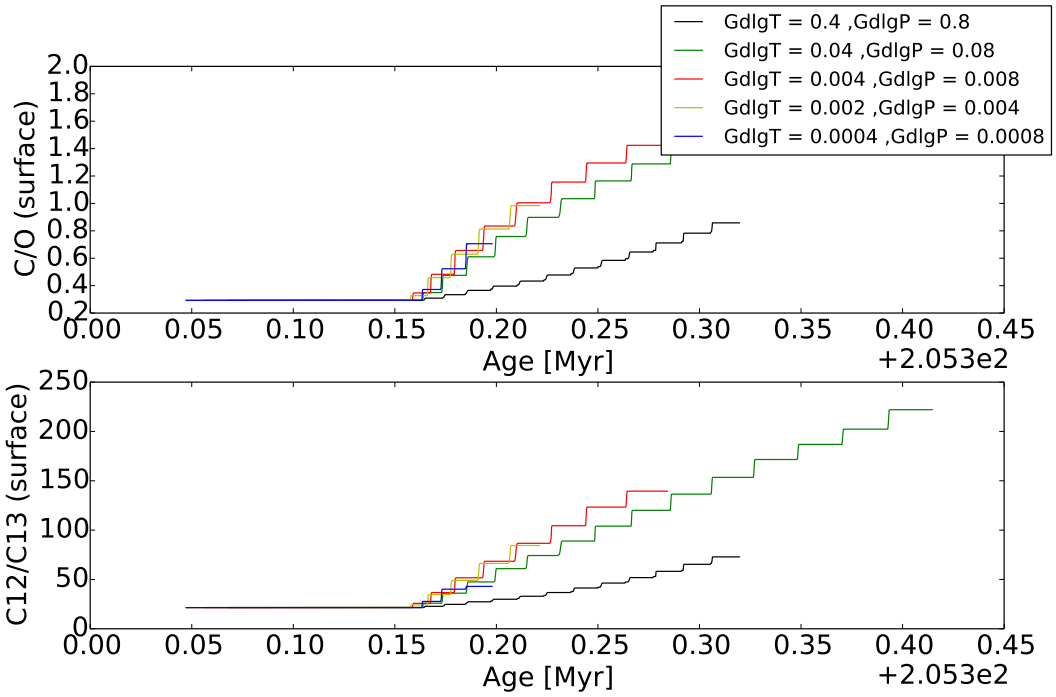

Figure B.7: Surface C/O ratio (top panel) and $^{12}C/^{13}C$ (lower panel) for a $4M_{\odot}$ star, with the lines representing models varying certain numerical parameters as indicated, where GdlgT limits time-steps based on changes in the temperature, and GdlgP does the same for pressure.

Given the above, the value for the numerical cutoff was kept at $D_{\rm cutoff}$ $=10^{-20}$ within GARSTEC for the models calculated for this thesis, however when translating the maximum allowed distance for momentum-based overshooting into a mixing efficiency parameter $f_{\rm CBM}$ in Ch. 5.1, a value of $D_{\rm cutoff}$ $=10^{-10}$ was taken, as during the TP-AGB values smaller than this don't appear to play a role in the evolution. If a value of $D_{\rm cutoff}$ $=10^{-20}$ was used to calculate $f_{\rm CBM}$ in this way, the value of $f_{\rm CBM}$ would halve. However, since there is little difference between models calculated with the two values of $D_{\rm cutoff}$ the higher value is used to calculate $f_{\rm CBM}$ as it is taken to represent the maximum distance influenced by the mixing.

B.3.2 Time-Step Control

There are different methods of controlling the time-step between successive structure models during an evolutionary sequence, both explicitly limiting the size of the time-

step and through limiting changes in certain physical quantities. The latter is in many ways preferable, as it allows the code to choose when it is necessary to resolve an evolutionary phase more closely temporally, and when it is possible to save on computational time without worsening the treatment of the physics.

Two such parameters in GARSTEC are GdlgT and GdlgP, which limit the changes between successive evolutionary structure models in temperature and pressure respectively. These typically take the values of 0.04 and 0.08, though it became apparent during the course of this thesis that certain physical effects, such as the third dredge-up, could be strongly influenced by changing these values. Smaller values for these parameters place stronger limitations on the allowed changes between models, leading to smaller timesteps.

To demonstrate this effect, evolutionary calculations were performed for a $4M_{\odot}$ star, all taken from the same starting model just prior to the first thermal pulse, and evolved with different values for GdlgT and GdlgP. The resulting surface C/O ratio (top panel) and $^{12}C/^{13}C$ ratio (lower panel) of these models are shown in Fig. B.7, with the range of parameters covering GdlgT=[0.0004, 0.4] and GdlgP=[0.0008,0.8] as indicated.

Clearly, changing these parameters can have a substantial impact on the outcome of these evolutionary models, however, it must be said that only the lowest resolution case completely diverges from the other models. The case with the standard values, GdlgT=0.04 and GdlgP=0.08, also perhaps experiences slightly less efficient dredge-up than all the other models, although it must be said that it appears to have converged to similar solutions to the other cases. This is particularly true when the fluctuation between the higher resolution cases is considered, with the highest resolution runs also indicating why the standard values are chosen such as they are. Namely, the computational time required to run the highest resolution models is substantially larger than the standard case, and as such their evolution has been cut short.

On the whole, the standard choice of these particular parameters seems to be reasonable, especially when balanced with the additional computational time required to run higher resolution models, however, it is worth bearing in mind that lowering the resolution could have quite significant consequences for the third dredge-up mechanism in particular.

B.3.3 Atmospheric Grid Interpolation

In order to implement a grid of radiative transfer, model atmospheres as the atmospheric boundary condition for the stellar evolution code, it was necessary to

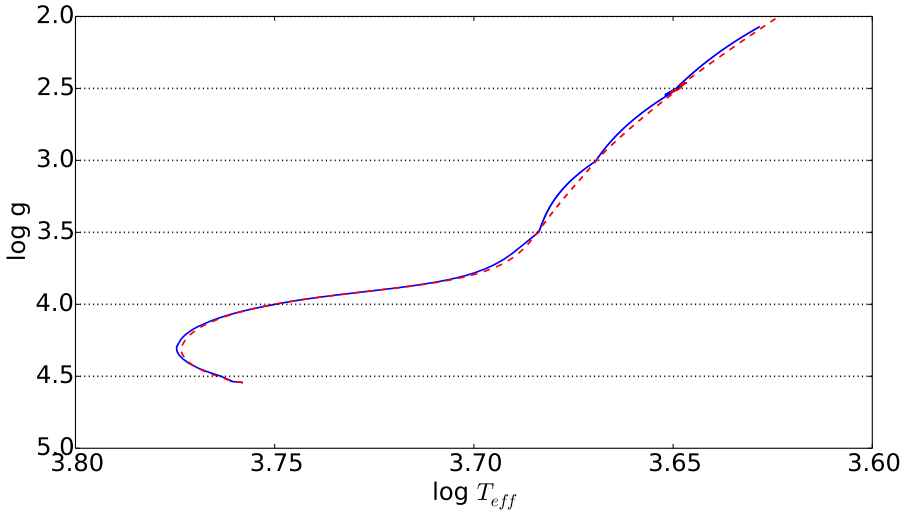

Figure B.8: Kiel diagram for a $1M_{\odot}$ model, evolved with a linearly interpolated MARCS grid (blue line) or a higher order interpolation (red, dashed line). The dotted black lines indicated the locations in surface gravity where MARCS models exist.

interpolate within the grid parameters, [log g, $T_{\rm eff}$, Z]. Initially, this led to problems in terms of interpolation and was the reason for then implementing a higher order interpolation scheme to try and better constrain the models.

As an example, Fig. B.8 shows the evolutionary tracks of a $1M_{\odot}$ model in a Kiel diagram ($T_{\rm eff}$, log g), with the blue track evolved using the MARCS grid, interpolated linearly, while the red dashed line shows the interpolation 4th order polynomial method used in this thesis. The dotted black lines indicate the locations in log g where MARCS models exist and illustrate the susceptibility of the evolution on the RGB to the interpolation method. This also shows how difficult it would be to see such effect on the main sequence. That the higher order interpolation results in a smooth evolutionary track, which reproduces the same values as the linear case close to the log g values of the grid, suggests the method is giving at least reasonable results.

A further example that the log g parameter is of more concern in this case than the effective temperature is shown in Fig. B.9, plotting the difference between the two interpolation schemes across a range of effective temperatures and log g values. The left panel shows the logarithmic change in the pressure value at a fitting depth of $\tau = 1$, while the right shows the same for the change in structural temperature.

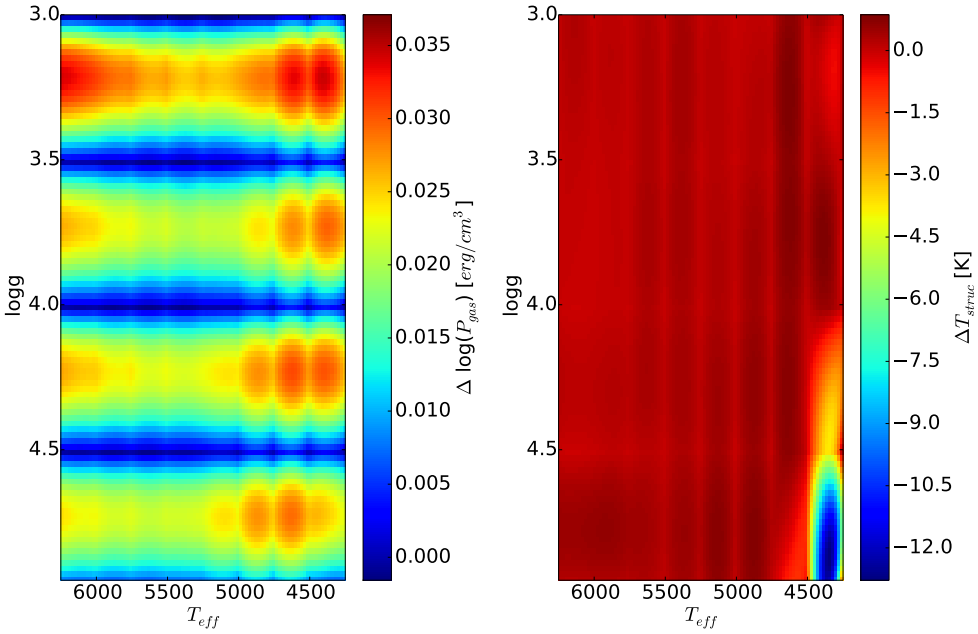

Figure B.9: The difference at $\tau = 1$ in pressure (left panel, log P) and temperature (right panel) across the $T_{\rm eff}$-log g parameter space between the linear and higher order interpolation schemes.

It seems that the sensitivity is entering the pressure interpolation, and is clearly far more sensitive to the log g parameter than the effective temperature.

Appendix C

Physical Information

Additional physical information about the models is provided within this appendix, in the form of a table entry summarising each evolutionary model for certain sets of parameters. The Tables follow in the order of the thesis, with the set of models using the standard RM-pp atmosphere, Z=0.012 and a value of $f_{\rm CBM}$ =0.016 at all boundaries in Table C.1.

Then follow the models calculated to explore the effect of core CMB on the TP-AGB, with Z=0.02 starting with no CBM in Table C.2, followed by no core CBM but during the TP-AGB in Table C.3, then models including core CBM during hydrogen core burning as well in Table C.4 and finally models with core CBM during both core burning phases and on the TP-AGB in Table C.5.

Lastly come models which try to constrain mixing on the TP-AGB, where core CBM is included during both core burning phases and varying the values on the TP-AGB of $f_{\rm CE}$ and $f_{\rm PDD}$ with Table C.6 showing Z=0.008 models where $f_{\rm CE}$ =$f_{\rm PDD}$ followed by models where $f_{\rm CE} \neq f_{\rm PDD}$ in Table C.7 and finally models with $f_{\rm CE}$ =$f_{\rm PDD}$ at Z=0.02 in Table C.8.

The table columns display the following information:

- M_i [$M_\odot$]: The ZAMS mass of the star.
- $M_c^{\rm TP1}$ [$M_\odot$]: The hydrogen free core mass at the first thermal pulse.
- M_f [$M_\odot$]: The final mass of the star, taken to be the mass of the hydrogen free core at the final thermal pulse.
- $t^{\rm TP1}$ [Myr]: The age of the star at the first thermal pulse.
- $\tau^M_{\rm TP-AGB}$ [Myr]: The M-star lifetime of the star, i.e. the length of time it is oxygen rich above a luminosity of $L = 3.336 L_\odot$.

- $\tau^{C}_{\mathrm{TP-AGB}}$ [Myr]: The C-star lifetime of the star, i.e. the length of time it is carbon rich
- TPs [N]: The number of thermal pulses undergone.
- TDU [TP_i, TP_f]: The initial (TP_i) and final (TP_f) thermal pulse number the star experienced third dredge-up (TDU)
- HBB [TP_i, TP_f]: As above but for hot-bottom burning (HBB)
- C/O: The final surface C/O value.
- X_Y: Mass fraction of helium in the intershell region at the final thermal pulse.
- X_C: As above for carbon.
- X_O: As above for oxygen.

$M_{\rm i}$	M_c^{TP1}	$M_{\rm f}$	t^{TP1}	$\tau^{M}_{\rm TP-AGB}$	$\tau^{C}_{\rm TP-AGB}$	TPs	TDU	HBB	C/O	X_Y	X_C	X_O
$[M_\odot]$	$[M_\odot]$	$[M_\odot]$	[Myr]	[Myr]	[Myr]	N	[$TP_{\rm i}$, $TP_{\rm f}$]		-	Mass Fractions		
Z=0.012												
$f_{\rm CHB}$ = 0.016, $f_{\rm CHeB}$ = 0.016, $f_{\rm CE}$ =0.016, $f_{\rm PDCZ}$ =0.016												
1.6	0.508	0.518	2381.92	0.343	0.424	5	[4, 5]	-	2.47	0.357	0.482	0.143
1.8	0.495	0.504	1710.73	0.291	0.832	6	[4, 6]	-	2.60	0.384	0.439	0.150
2.0	0.477	0.472	1327.21	0.350	2.288	10	[5, 9]	-	2.68	0.468	0.357	0.132
2.1	0.451	0.526	1263.54	0.001	9.184	20	[3, 20]	-	1.91	0.225	0.446	0.276
2.2	0.459	0.513	1112.52	0.010	10.025	20	[4, 17]	-	2.24	0.214	0.466	0.239
2.3	0.469	0.521	977.55	0.000	12.508	16	[3, 6]	-	2.46	0.229	0.491	0.202
2.4	0.485	0.479	870.65	0.550	3.317	13	[5, 13]	-	3.05	0.538	0.304	0.096
2.6	0.516	0.508	688.90	0.399	2.437	11	[4, 11]	-	3.33	0.562	0.302	0.084
2.8	0.558	0.549	555.86	0.358	1.342	10	[3, 10]	-	3.31	0.559	0.316	0.081
3.0	0.606	0.593	456.06	0.234	0.720	10	[3, 9]	-	2.89	0.535	0.347	0.088
3.5	0.734	0.725	294.13	0.082	0.179	11	[3, 10]	-	1.99	0.414	0.440	0.123
4.0	0.772	0.759	205.46	0.185	0.183	15	[3, 14]	-	1.97	0.451	0.403	0.118
5.0	0.835	0.815	117.56	0.165	0.193	27	[3, 26]	-	1.95	0.437	0.399	0.138
6.0	0.935	0.931	76.98	0.155	0.000	32	[3, 32]	[4, 10]	0.39	0.427	0.447	0.101

Table C.1: See C for details about the columns.

$M_{\rm i}$	M_c^{TP1}	$M_{\rm f}$	t^{TP1}	$\tau^M_{\rm TP-AGB}$	$\tau^C_{\rm TP-AGB}$	TPs	TDU	HBB	C/O	X_Y	X_C	X_O
$[M_\odot]$	$[M_\odot]$	$[M_\odot]$	[Myr]	[Myr]	[Myr]	N	[$TP_{\rm i}$, $TP_{\rm f}$]		-	Mass Fractions		
Z=0.02												
$f_{\rm CHB}$ = 0.0, $f_{\rm CHeB}$ = 0.0, $f_{\rm CE}$ =0.0, $f_{\rm PDCZ}$ =0.0												
1.6	0.510	0.538	2546.18	1.041	0.000	6	-	-	0.33	0.743	0.232	0.006
1.8	0.511	0.546	1738.80	1.203	0.000	7	-	-	0.32	0.724	0.250	0.007
2.0	0.504	0.568	1254.13	1.230	0.000	11	-	-	0.31	0.733	0.242	0.006
2.2	0.486	0.580	973.31	1.799	0.000	15	-	-	0.30	0.742	0.233	0.006
2.4	0.450	0.595	875.52	2.369	0.000	25	-	-	0.32	0.750	0.226	0.005
2.6	0.464	0.610	691.12	2.403	0.000	24	-	-	0.33	0.751	0.225	0.004
2.8	0.480	0.634	548.54	2.400	0.000	25	-	-	0.33	0.756	0.221	0.004
3.0	0.506	0.652	440.58	2.114	0.000	24	-	-	0.33	0.756	0.221	0.004
3.5	0.598	0.703	270.74	1.421	0.000	23	-	-	0.32	0.750	0.228	0.003
4.0	0.700	0.763	183.42	1.019	0.000	22	-	-	0.31	0.740	0.238	0.003
4.5	0.750	0.810	133.35	0.990	0.000	28	-	-	0.32	0.722	0.255	0.004
4.8	0.761	0.829	112.57	1.021	0.000	34	-	-	0.32	0.722	0.254	0.004
5.0	0.766	0.844	101.31	1.055	0.000	41	-	-	0.31	0.729	0.248	0.004
5.25	0.775	0.857	89.49	1.085	0.000	47	-	-	0.31	0.717	0.259	0.004
5.5	0.785	0.871	79.72	1.122	0.000	54	-	-	0.31	0.717	0.259	0.004
5.75	0.794	0.884	71.56	1.161	0.000	61	[30, 50]	-	0.24	0.707	0.269	0.005
6.0	0.804	0.897	64.59	2.144	0.000	68	[28, 56]	[30, 49]	0.09	0.716	0.260	0.004
6.25	0.813	0.908	58.64	3.059	0.000	74	[27, 52]	[26, 47]	0.01	0.696	0.280	0.006

Table C.2: See C for details about the columns.

$M_{\rm i}$	M_c^{TP1}	$M_{\rm f}$	t^{TP1}	$\tau^{M}_{\rm TP-AGB}$	$\tau^{C}_{\rm TP-AGB}$	TPs	TDU	HBB	C/O	X_Y	X_C	X_O
$[M_\odot]$	$[M_\odot]$	$[M_\odot]$	[Myr]	[Myr]	[Myr]	N	[$TP_{\rm i}$, $TP_{\rm f}$]		-	Mass Fractions		
Z=0.02												
$f_{\rm CHB}$ = 0.0, $f_{\rm CHeB}$ = 0.0, $f_{\rm CE}$ =0.0, $f_{\rm PDCZ}$ =0.0075												
1.6	0.509	0.536	2317.16	1.026	0.000	7	-	-	0.32	0.358	0.519	0.104
1.7	0.511	0.541	1891.46	1.059	0.000	7	-	-	0.32	0.375	0.513	0.093
1.8	0.511	0.545	1570.74	1.215	0.000	8	-	-	0.31	0.365	0.498	0.118
1.9	0.512	0.547	1324.38	1.170	0.000	8	[7, 8]	-	0.96	0.388	0.480	0.109
2.0	0.503	0.552	1137.20	1.120	0.000	11	[9, 10]	-	0.82	0.393	0.467	0.117
2.1	0.493	0.552	999.45	1.275	0.149	13	[10, 12]	-	1.10	0.435	0.433	0.109
2.2	0.487	0.552	904.71	1.389	0.268	14	[11, 14]	-	1.32	0.476	0.404	0.096
2.3	0.480	0.548	813.16	1.543	0.291	14	[11, 14]	-	1.47	0.497	0.389	0.086
2.4	0.453	0.554	823.73	1.949	0.309	21	[16, 20]	-	1.40	0.507	0.379	0.085
2.6	0.465	0.559	671.20	1.868	0.444	20	[14, 19]	-	1.52	0.503	0.389	0.075
2.8	0.482	0.562	527.47	1.781	0.582	19	[11, 18]	-	1.84	0.560	0.347	0.056
3.0	0.507	0.571	426.47	1.497	0.657	18	[9, 17]	-	1.90	0.573	0.340	0.051
3.5	0.597	0.643	267.09	1.124	0.365	18	[6, 17]	-	1.68	0.567	0.353	0.048
4.0	0.698	0.735	183.07	0.983	0.000	17	[8, 16]	-	0.79	0.512	0.401	0.060
4.5	0.751	0.785	133.90	0.951	0.000	21	[9, 20]	-	0.80	0.482	0.421	0.072
4.8	0.762	0.797	113.48	0.974	0.000	24	[9, 23]	-	0.81	0.443	0.447	0.086
5.0	0.767	0.806	102.16	1.003	0.000	28	[11, 27]	-	0.87	0.435	0.457	0.084
5.25	0.776	0.819	90.48	1.053	0.020	35	[10, 34]	-	1.08	0.484	0.420	0.069
5.5	0.786	0.829	80.63	1.077	0.035	40	[10, 39]	-	1.15	0.479	0.423	0.070
5.75	0.795	0.838	72.47	1.119	0.032	44	[11, 43]	-	1.15	0.465	0.439	0.067
6.0	0.804	0.847	65.47	2.085	0.007	46	[11, 46]	-	1.05	0.476	0.428	0.067
6.25	0.814	0.855	59.49	3.002	0.000	47	[12, 46]	-	0.76	0.362	0.498	0.108

Table C.3: See C for details about the columns.

$M_{\rm i}$	M_c^{TP1}	$M_{\rm f}$	t^{TP1}	$\tau^{M}_{\rm TP-AGB}$	$\tau^{C}_{\rm TP-AGB}$	TPs	TDU	HBB	C/O	X_Y	X_C	X_O
$[M_\odot]$	$[M_\odot]$	$[M_\odot]$	[Myr]	[Myr]	[Myr]	N	[$\rm TP_i$, $\rm TP_f$]		-	Mass Fractions		
Z=0.02												
$f_{\rm CHB}$ = 0.0174, $f_{\rm CHeB}$ = 0.0, $f_{\rm CE}$ =0.0, $f_{\rm PDCZ}$ =0.0075												
1.6	0.501	0.535	2476.46	0.782	0.000	8	-	-	0.32	0.354	0.512	0.115
1.7	0.493	0.532	2061.10	0.949	0.000	9	-	-	0.32	0.348	0.501	0.132
1.8	0.485	0.542	1761.50	1.189	0.000	11	-	-	0.48	0.322	0.516	0.142
1.9	0.477	0.548	1540.19	1.513	0.000	14	[12, 13]	-	0.76	0.385	0.462	0.131
2.0	0.450	0.550	1454.17	1.747	0.000	18	[17, 17]	-	0.72	0.389	0.452	0.136
2.1	0.453	0.555	1260.83	1.839	0.083	19	[17, 19]	-	1.12	0.439	0.424	0.113
2.2	0.463	0.560	1114.19	1.893	0.128	20	[17, 19]	-	1.19	0.463	0.411	0.101
2.3	0.468	0.562	953.66	1.828	0.190	19	[16, 19]	-	1.42	0.492	0.393	0.087
2.4	0.478	0.569	856.93	1.779	0.235	19	[14, 18]	-	1.35	0.501	0.390	0.082
2.6	0.501	0.577	664.02	1.542	0.216	18	[12, 17]	-	1.41	0.518	0.383	0.072
2.8	0.535	0.596	532.53	1.214	0.267	16	[9, 15]	-	1.46	0.535	0.372	0.062
3.0	0.576	0.625	434.02	1.037	0.195	15	[7, 14]	-	1.38	0.538	0.376	0.058
3.5	0.692	0.725	278.62	0.882	0.000	13	[10, 12]	-	0.54	0.467	0.436	0.074
4.0	0.755	0.784	193.74	0.866	0.000	15	[12, 15]	-	0.53	0.461	0.441	0.073
4.5	0.778	0.814	142.47	0.946	0.000	22	[13, 22]	-	0.64	0.458	0.449	0.071
4.8	0.792	0.829	120.93	0.996	0.000	27	[13, 26]	-	0.71	0.443	0.457	0.077
5.0	0.801	0.839	109.20	1.671	0.000	30	[12, 29]	-	0.76	0.402	0.489	0.085
5.25	0.810	0.851	96.82	2.694	0.000	34	[12, 33]	-	0.79	0.428	0.474	0.074
5.5	0.823	0.865	86.53	3.290	0.000	39	[13, 38]	-	0.81	0.437	0.463	0.075
5.75	0.836	0.879	77.86	4.100	0.000	44	[14, 43]	-	0.69	0.386	0.495	0.092
6.0	0.849	0.891	70.46	8.743	0.000	48	[13, 47]	[18, 28]	0.50	0.358	0.493	0.119
6.25	0.864	0.905	64.20	17.020	0.000	50	[12, 50]	[13, 30]	0.30	0.422	0.475	0.077

Table C.4: See C for details about the columns.

$M_{\rm i}$	M_c^{TP1}	$M_{\rm f}$	t^{TP1}	$\tau^{M}_{\rm TP-AGB}$	$\tau^{C}_{\rm TP-AGB}$	TPs	TDU	HBB	C/O	X_Y	X_C	X_O
$[M_\odot]$	$[M_\odot]$	$[M_\odot]$	[Myr]	[Myr]	[Myr]	N	[$TP_{\rm i}$, $TP_{\rm f}$]		-	Mass Fractions		
Z=0.02												
$f_{\rm CHB}$ = 0.0174, $f_{\rm CHeB}$ = 0.0174, $f_{\rm CE}$ =0.0, $f_{\rm PDCZ}$ =0.0075												
1.6	0.501	0.535	2490.64	0.735	0.000	8	-	-	0.32	0.351	0.513	0.117
1.7	0.495	0.539	2087.14	0.940	0.000	10	-	-	0.31	0.346	0.502	0.133
1.8	0.487	0.538	1773.49	1.143	0.000	10	[10, 10]	-	0.50	0.362	0.489	0.130
1.9	0.478	0.546	1549.02	1.507	0.000	13	[12, 13]	-	0.84	0.390	0.460	0.128
2.0	0.450	0.551	1462.18	1.774	0.000	18	[16, 17]	-	0.74	0.392	0.451	0.134
2.1	0.456	0.556	1280.16	1.900	0.081	19	[17, 19]	-	1.30	0.465	0.406	0.101
2.2	0.465	0.560	1113.84	1.915	0.098	19	[16, 19]	-	1.26	0.472	0.406	0.097
2.3	0.476	0.564	983.06	1.798	0.156	18	[14, 18]	-	1.50	0.497	0.388	0.083
2.4	0.485	0.568	866.67	1.677	0.225	17	[13, 17]	-	1.36	0.501	0.387	0.080
2.6	0.520	0.585	687.85	1.351	0.199	16	[10, 15]	-	1.42	0.523	0.381	0.068
2.8	0.555	0.609	553.29	1.157	0.154	15	[9, 14]	-	1.36	0.530	0.376	0.063
3.0	0.600	0.643	450.50	1.046	0.090	13	[7, 13]	-	1.24	0.527	0.383	0.061
3.5	0.719	0.744	287.67	0.794	0.000	11	[10, 11]	-	0.49	0.452	0.450	0.079
4.0	0.770	0.796	198.33	0.792	0.000	15	[11, 14]	-	0.45	0.445	0.449	0.078
4.5	0.812	0.841	146.13	0.722	0.000	20	[15, 20]	-	0.48	0.442	0.459	0.077
4.8	0.829	0.860	123.54	0.753	0.000	24	[16, 24]	-	0.53	0.430	0.470	0.078
5.0	0.851	0.883	111.81	1.295	0.000	28	[19, 28]	-	0.51	0.436	0.463	0.079
5.25	0.868	0.901	98.95	2.251	0.000	34	[15, 33]	-	0.55	0.427	0.470	0.080
5.5	0.894	0.925	88.44	6.388	0.000	38	[12, 37]	[13, 24]	0.35	0.412	0.481	0.082
5.75	0.922	0.951	79.59	7.227	0.000	42	[6, 42]	[9, 26]	0.19	0.414	0.477	0.082
6.0	0.934	0.964	71.81	10.551	0.000	48	[9, 48]	[8, 24]	0.15	0.409	0.482	0.083
6.25	0.965	1.002	65.41	18.193	0.000	70	[21, 70]	[20, 38]	0.08	0.397	0.490	0.081

Table C.5: See C for details about the columns.

$M_{\rm i}$	M_c^{TP1}	$M_{\rm f}$	t^{TP1}	$\tau^{M}_{\rm TP-AGB}$	$\tau^{C}_{\rm TP-AGB}$	TPs	TDU	HBB	C/O	X_Y	X_C	X_O
$[M_\odot]$	$[M_\odot]$	$[M_\odot]$	[Myr]	[Myr]	[Myr]	N	[TP_i, TP_f]		-	Mass Fractions		
Z=0.008												
$f_{\rm CHB}$ = 0.0174, $f_{\rm CHeB}$ = 0.0174, $f_{\rm CE}$ =0.004, $f_{\rm PDD}$ =0.004												
1.6	0.508	0.555	1920.49	1.108	0.098	8	[8, 8]	-	1.28	0.496	0.433	0.063
2.0	0.467	0.553	1138.88	1.505	0.565	16	[12, 16]	-	3.55	0.585	0.350	0.048
2.4	0.535	0.585	681.46	0.812	0.696	12	[5, 12]	-	3.58	0.611	0.333	0.034
2.8	0.637	0.679	440.34	0.939	0.173	14	[6, 13]	-	2.11	0.599	0.356	0.032
3.0	0.692	0.730	361.70	0.902	0.101	16	[7, 16]	-	1.87	0.592	0.362	0.031
3.2	0.745	0.777	303.41	0.860	0.017	17	[9, 16]	-	1.18	0.567	0.386	0.034
3.5	0.777	0.811	240.45	0.842	0.024	22	[10, 21]	-	1.33	0.537	0.413	0.039
$f_{\rm CHB}$ = 0.0174, $f_{\rm CHeB}$ = 0.0174, $f_{\rm CE}$ =0.008, $f_{\rm PDD}$ =0.008												
1.6	0.505	0.544	1921.50	0.883	0.062	8	[7, 8]	-	1.82	0.397	0.479	0.113
2.0	0.472	0.531	1141.18	1.147	0.833	13	[7, 12]	-	2.99	0.496	0.389	0.091
2.4	0.534	0.569	684.03	0.640	0.820	12	[3, 11]	-	3.56	0.546	0.365	0.063
2.8	0.637	0.665	441.14	0.813	0.246	12	[3, 11]	-	2.32	0.527	0.393	0.065
3.0	0.691	0.719	362.18	0.839	0.118	14	[3, 13]	-	1.94	0.514	0.403	0.066
3.2	0.742	0.766	303.77	0.811	0.055	15	[4, 14]	-	1.41	0.490	0.425	0.072
3.5	0.774	0.800	240.64	0.795	0.053	19	[5, 18]	-	1.55	0.473	0.437	0.072
$f_{\rm CHB}$ = 0.0174, $f_{\rm CHeB}$ = 0.0174, $f_{\rm CE}$ =0.014, $f_{\rm PDD}$ =0.014												
1.6	0.505	0.538	1915.65	0.713	0.159	8	[6, 8]	-	1.31	0.304	0.509	0.177
2.0	0.468	0.528	1141.45	1.088	0.891	14	[8, 14]	-	2.42	0.429	0.397	0.146
2.4	0.537	0.557	686.78	0.570	0.889	10	[3, 10]	-	3.12	0.480	0.382	0.107
2.8	0.637	0.650	442.90	0.728	0.323	10	[3, 10]	-	2.56	0.464	0.401	0.114
3.0	0.690	0.700	362.79	0.708	0.165	10	[3, 9]	-	1.84	0.419	0.430	0.133
3.2	0.742	0.752	305.11	0.717	0.124	12	[3, 12]	-	1.82	0.423	0.428	0.131
3.5	0.766	0.777	240.89	0.747	0.097	15	[3, 14]	-	1.72	0.420	0.431	0.130

Table C.6: See C for details about the columns.

$M_{\rm i}$	M_c^{TP1}	$M_{\rm f}$	t^{TP1}	$\tau^{M}_{\rm TP-AGB}$	$\tau^{C}_{\rm TP-AGB}$	TPs	TDU	HBB	C/O	X_Y	X_C	X_O
$[M_\odot]$	$[M_\odot]$	$[M_\odot]$	[Myr]	[Myr]	[Myr]	N	[$\rm TP_i$, $\rm TP_f$]		-	Mass Fractions		
Z=0.008												
$f_{\rm CHB}$ = 0.0174, $f_{\rm CHeB}$ = 0.0174, $f_{\rm CE}$ =0.002, $f_{\rm PDD}$ =0.02												
1.6	0.509	0.539	1914.94	0.681	0.299	6	[4, 6]	-	2.39	0.569	0.381	0.037
2.0	0.465	0.539	1142.43	0.986	1.034	15	[9, 14]	-	3.65	0.626	0.319	0.032
2.4	0.534	0.571	684.72	0.616	0.960	11	[3, 11]	-	4.88	0.686	0.270	0.016
2.8	0.634	0.650	442.21	0.731	0.377	11	[3, 10]	-	3.34	0.694	0.277	0.014
3.0	0.688	0.700	363.11	0.732	0.224	12	[3, 11]	-	2.79	0.681	0.291	0.013
3.2	0.739	0.748	304.55	0.741	0.141	14	[4, 13]	-	2.45	0.132	0.739	0.115
3.5	0.763	0.771	240.93	0.741	0.152	16	[3, 16]	-	2.77	0.652	0.319	0.015
$f_{\rm CHB}$ = 0.0174, $f_{\rm CHeB}$ = 0.0174, $f_{\rm CE}$ =0.008, $f_{\rm PDD}$ =0.014												
1.6	0.509	0.534	1915.80	0.611	0.175	6	[4, 5]	-	1.37	0.403	0.494	0.092
2.0	0.466	0.529	1141.33	1.120	0.852	14	[8, 13]	-	2.85	0.492	0.389	0.097
2.4	0.537	0.567	686.78	0.578	0.886	11	[3, 11]	-	4.10	0.556	0.357	0.059
2.8	0.637	0.657	442.90	0.725	0.348	11	[3, 11]	-	3.00	0.537	0.379	0.061
3.0	0.690	0.707	362.79	0.733	0.190	12	[3, 11]	-	2.19	0.513	0.405	0.068
3.2	0.742	0.760	305.11	0.745	0.115	14	[3, 14]	-	1.90	0.499	0.409	0.069
3.5	0.766	0.786	240.89	0.768	0.103	18	[3, 17]	-	1.93	0.500	0.415	0.067
$f_{\rm CHB}$ = 0.0174, $f_{\rm CHeB}$ = 0.0174, $f_{\rm CE}$ =0.008, $f_{\rm PDD}$ =0.126												
1.6	0.524	0.542	1953.21	0.558	0.144	5	[4, 4]	-	1.17	0.434	0.488	0.070
2.0	0.506	0.523	1079.88	0.330	0.996	8	[3, 8]	-	4.38	0.551	0.353	0.070
2.4	0.524	0.536	711.75	0.380	1.359	10	[4, 10]	[10, 10]	4.86	0.614	0.297	0.049
2.8	0.620	0.622	457.58	0.645	0.485	9	[3, 9]	-	3.67	0.593	0.327	0.059
3.0	0.672	0.668	374.88	0.662	0.292	10	[3, 9]	-	3.15	0.570	0.345	0.066
3.2	0.723	0.716	313.55	0.684	0.184	10	[3, 9]	-	2.83	0.550	0.355	0.074
3.5	0.753	0.745	247.81	0.650	0.199	12	[3, 12]	-	2.91	0.526	0.376	0.078

Table C.7: See C for details about the columns.

$M_{\rm i}$	M_c^{TP1}	$M_{\rm f}$	t^{TP1}	$\tau^{M}_{\rm TP-AGB}$	$\tau^{C}_{\rm TP-AGB}$	TPs	TDU	HBB	C/O	X_Y	X_C	X_O
$[M_\odot]$	$[M_\odot]$	$[M_\odot]$	[Myr]	[Myr]	[Myr]	N	[$TP_{\rm i}$, $TP_{\rm f}$]		-	Mass Fractions		
Z=0.02												
$f_{\rm CHB}$ = 0.0174, $f_{\rm CHeB}$ = 0.0174, $f_{\rm CE}$ =0.004, $f_{\rm PDD}$ =0.004												
1.6	0.503	0.534	2489.57	0.723	0.000	7	-	-	0.32	0.393	0.509	0.079
2.0	0.451	0.550	1458.96	1.849	0.000	19	[18, 19]	-	0.68	0.466	0.427	0.086
2.4	0.487	0.577	867.68	1.687	0.212	18	[12, 17]	-	1.30	0.563	0.361	0.047
2.8	0.555	0.618	549.64	1.205	0.205	16	[8, 15]	-	1.35	0.592	0.346	0.034
3.0	0.599	0.649	450.19	1.132	0.000	14	[7, 14]	-	1.05	0.574	0.364	0.036
3.2	0.643	0.685	373.93	0.978	0.000	14	[8, 13]	-	0.71	0.558	0.377	0.038
3.5	0.715	0.743	287.16	0.820	0.000	12	[10, 12]	-	0.45	0.520	0.417	0.044
$f_{\rm CHB}$ = 0.0174, $f_{\rm CHeB}$ = 0.0174, $f_{\rm CE}$ =0.008, $f_{\rm PDD}$ =0.008												
1.6	0.501	0.534	2489.63	0.725	0.000	8	-	-	0.32	0.344	0.506	0.131
2.0	0.453	0.547	1458.22	1.759	0.000	18	[15, 17]	-	0.86	0.387	0.447	0.143
2.4	0.486	0.551	869.86	1.412	0.425	16	[9, 15]	-	1.60	0.492	0.386	0.086
2.8	0.555	0.591	550.04	0.984	0.370	13	[4, 12]	-	1.69	0.527	0.373	0.064
3.0	0.598	0.631	450.63	0.971	0.182	13	[4, 12]	-	1.42	0.524	0.382	0.063
3.2	0.640	0.671	371.29	0.963	0.040	13	[4, 12]	-	1.08	0.491	0.410	0.072
3.5	0.714	0.738	288.11	0.809	0.000	12	[6, 11]	-	0.62	0.450	0.440	0.083
$f_{\rm CHB}$ = 0.0174, $f_{\rm CHeB}$ = 0.0174, $f_{\rm CE}$ =0.014, $f_{\rm PDD}$ =0.014												
1.6	0.501	0.534	2490.66	0.717	0.000	8	-	-	0.32	0.265	0.525	0.191
2.0	0.469	0.540	1390.98	1.556	0.136	15	[12, 15]	-	1.12	0.340	0.433	0.198
2.4	0.486	0.542	871.07	1.462	0.410	15	[8, 15]	-	1.58	0.427	0.397	0.138
2.8	0.557	0.577	555.99	0.825	0.510	11	[3, 11]	-	1.78	0.464	0.390	0.108
3.0	0.596	0.614	451.00	0.879	0.265	11	[3, 11]	-	1.62	0.463	0.392	0.109
3.2	0.640	0.657	373.96	0.867	0.185	13	[3, 12]	-	1.40	0.450	0.402	0.115
3.5	0.712	0.721	287.87	0.803	0.000	10	[3, 9]	-	0.90	0.383	0.444	0.145

Table C.8: See C for details about the columns.

Bibliography

Abate C., Stancliffe R. J., Liu Z.-W., 2016, A&A, 587, A50

Abia C., Domínguez I., Gallino R., Busso M., Straniero O., de Laverny P., Wallerstein G., 2003, Publ. Astron. Soc. Australia, 20, 314

Anders E., Grevesse N., 1989, Geochimica Cosmochimica Acta, 53, 197

Andrews J. J., Agüeros M. A., Gianninas A., Kilic M., Dhital S., Anderson S. F., 2015, ApJ, 815, 63

Aringer B., Girardi L., Nowotny W., Marigo P., Lederer M. T., 2009, A&A, 503, 913

Aringer B., Girardi L., Nowotny W., Marigo P., Bressan A., 2016, MNRAS, 457, 3611

Arlandini C., Käppeler F., Wisshak K., Gallino R., Lugaro M., Busso M., Straniero O., 1999, ApJ, 525, 886

Arnett W. D., Meakin C., Viallet M., Campbell S. W., Lattanzio J. C., Mocák M., 2015, ApJ, 809, 30

Asplund M., Grevesse N., Sauval A. J., 2005, in Barnes III T. G., Bash F. N., eds, Astronomical Society of the Pacific Conference Series Vol. 336, Cosmic Abundances as Records of Stellar Evolution and Nucleosynthesis. p. 25

Asplund M., Grevesse N., Sauval A. J., Scott P., 2009, ARA&A, 47, 481

Baraffe I., Pratt J., Goffrey T., Constantino T., Folini D., Popov M. V., Walder R., Viallet M., 2017, ApJ, 845, L6

Basu S., Antia H. M., 2008, Phys. Rep., 457, 217

Bloecker T., 1995, A&A, 297, 727

Buonanno R., Corsi C. E., Buzzoni A., Cacciari C., Ferraro F. R., Fusi Pecci F., 1994, A&A, 290, 69

Caffau E., Ludwig H.-G., Steffen M., Freytag B., Bonifacio P., 2011, Sol. Phys., 268, 255

Cannon R. D., 1970, MNRAS, 150, 111

Caputo F., Castellani V., Wood P. R., 1978, MNRAS, 184, 377

Cassisi S., Salaris M., Irwin A. W., 2003, ApJ, 588, 862

Castellani V., Chieffi A., Tornambe A., Pulone L., 1985, ApJ, 296, 204

Claret A., 2007, A&A, 475, 1019

Constantino T., Campbell S., Gil-Pons P., Lattanzio J., 2014, ApJ, 784, 56

Constantino T., Campbell S. W., Christensen-Dalsgaard J., Lattanzio J. C., Stello D., 2015, MNRAS, 452, 123

Constantino T., Campbell S. W., Lattanzio J. C., van Duijneveldt A., 2016, MNRAS, 456, 3866

Cox J. P., 1967, in Thomas R. N., ed., IAU Symposium Vol. 28, Aerodynamic Phenomena in Stellar Atmospheres. p. 3

Cristallo S., Straniero O., Lederer M. T., Aringer B., 2007, ApJ, 667, 489

Cristallo S., Straniero O., Gallino R., Piersanti L., Domínguez I., Lederer M. T., 2009, ApJ, 696, 797

Cristallo S., et al., 2011, ApJS, 197, 17

Cruz M. A., Serenelli A., Weiss A., 2013, A&A, 559, A4

Denissenkov P. A., Tout C. A., 2003, MNRAS, 340, 722

Doherty C. L., Gil-Pons P., Siess L., Lattanzio J. C., Lau H. H. B., 2015, MNRAS, 446, 2599

Dreizler S., Heber U., 1998, A&A, 334, 618

Eddington A. S., 1922, MNRAS, 83, 32

Eddington A. S., 1959, The internal constitution of the stars

Eggleton P. P., Faulkner J., Flannery B. P., 1973, A&A, 23, 325

Ekström S., et al., 2012, A&A, 537, A146

Ferguson J. W., Alexander D. R., Allard F., Barman T., Bodnarik J. G., Hauschildt P. H., Heffner-Wong A., Tamanai A., 2005, ApJ, 623, 585

Freytag B., Ludwig H.-G., Steffen M., 1996, A&A, 313, 497

Frogel J. A., Mould J., Blanco V. M., 1990, ApJ, 352, 96

Frost C. A., Lattanzio J. C., 1996, ApJ, 473, 383

Gallart C., 1998, ApJ, 495, L43

Girardi L., Marigo P., 2007, A&A, 462, 237

Goldman S. R., et al., 2017, MNRAS, 465, 403

Gratton R. G., Carretta E., Bragaglia A., 2012, A&ARv, 20, 50

Grevesse N., Noels A., 1993, in Prantzos N., Vangioni-Flam E., Casse M., eds, Origin and Evolution of the Elements. pp 15–25

Grevesse N., Sauval A. J., 1994, in Jorgensen U. G., ed., Lecture Notes in Physics, Berlin Springer Verlag Vol. 428, IAU Colloq. 146: Molecules in the Stellar Environment. p. 196, doi:10.1007/3-540-57747-5˙44

Grevesse N., Sauval A. J., 1998, Space Sci. Rev., 85, 161

Grevesse N., Asplund M., Sauval A. J., 2007, Space Sci. Rev., 130, 105

Grevesse N., Asplund M., Sauval J., Scott P., 2013, in European Physical Journal Web of Conferences. p. 01004, doi:10.1051/epjconf/20134301004

Gustafsson B., Edvardsson B., Eriksson K., Jørgensen U. G., Nordlund Å., Plez B., 2008, A&A, 486, 951

Hayashi C., 1961, PASJ, 13

Henyey L. G., Forbes J. E., Gould N. L., 1964, ApJ, 139, 306

Henyey L., Vardya M. S., Bodenheimer P., 1965, ApJ, 142, 841

Herwig F., 2000, A&A, 360, 952

Herwig F., 2005, ARA&A, 43, 435

Herwig F., Bloecker T., Schoenberner D., El Eid M., 1997, A&A, 324, L81

Herwig F., Blöcker T., Langer N., Driebe T., 1999, A&A, 349, L5

Herwig F., Langer N., Lugaro M., 2003, ApJ, 593, 1056

Herwig F., Freytag B., Fuchs T., Hansen J. P., Hueckstaedt R. M., Porter D. H., Timmes F. X., Woodward P. R., 2007, in Kerschbaum F., Charbonnel C., Wing R. F., eds, Astronomical Society of the Pacific Conference Series Vol. 378, Why Galaxies Care About AGB Stars: Their Importance as Actors and Probes. p. 43 (arXiv:0709.0197)

Higl J., Weiss A., 2017, A&A, 608, A62

Höfner S., 2015, in Kerschbaum F., Wing R. F., Hron J., eds, Astronomical Society of the Pacific Conference Series Vol. 497, Why Galaxies Care about AGB Stars III: A Closer Look in Space and Time. p. 333 (arXiv:1505.07425)

Hubeny I., Mihalas D., 2014, Theory of Stellar Atmospheres

Hurlburt N. E., Toomre J., Massaguer J. M., Zahn J.-P., 1994, ApJ, 421, 245

Iben I., 1968, Nature, 220, 143

Iglesias C. A., Rogers F. J., 1996, ApJ, 464, 943

Izzard R. G., Tout C. A., Karakas A. I., Pols O. R., 2004, MNRAS, 350, 407

Izzard R. G., Dray L. M., Karakas A. I., Lugaro M., Tout C. A., 2006, A&A, 460, 565

Jones S., Ritter C., Herwig F., Fryer C., Pignatari M., Bertolli M. G., Paxton B., 2016, MNRAS, 455, 3848

Kalirai J. S., Marigo P., Tremblay P.-E., 2014, ApJ, 782, 17

Karakas A., 2003, PhD thesis, Monash University, Melbourne, Australia

Karakas A., Lattanzio J. C., 2007, Publ. Astron. Soc. Australia, 24, 103

Kippenhahn R., Weigert A., 1990, Stellar Structure and Evolution

Kippenhahn R., Weigert A., Hofmeister E., 1967, Methods in Computational Physics, 7, 129

Kippenhahn R., Weigert A., Weiss A., 2012, Stellar Structure and Evolution, doi:10.1007/978-3-642-30304-3.

Kitsikis A., 2008, PhD thesis, Ludwig-Maximilians-Universität München

Knapp G., Pourbaix D., Jorissen A., 2001, A&A, 371, 222

Kobayashi C., Karakas A. I., Umeda H., 2011, MNRAS, 414, 3231

Koesterke L., Hamann W.-R., 1997, A&A, 320, 91

Krishna Swamy K. S., 1966, ApJ, 145, 174

Langer N., Heger A., Wellstein S., Herwig F., 1999, A&A, 346, L37

Lattanzio J. C., 1986, ApJ, 311, 708

Lattanzio J. C., Tout C. A., Neumerzhitckii E. V., Karakas A. I., Lesaffre P., 2017, preprint, (arXiv:1706.07615)

Lau H. H. B., Gil-Pons P., Doherty C., Lattanzio J., 2012, A&A, 542, A1

Lebzelter T., Lederer M. T., Cristallo S., Hinkle K. H., Straniero O., Aringer B., 2008, A&A, 486, 511

Lederer M. T., Lebzelter T., Cristallo S., Straniero O., Hinkle K. H., Aringer B., 2009, A&A, 502, 913

Ledoux P., 1958, Handbuch der Physik, 51, 605

Lodders K., Palme H., Gail H.-P., 2009, Landolt Börnstein,

Lucy L. B., 1976, ApJ, 205, 482

Lugaro M., Herwig F., Lattanzio J. C., Gallino R., Straniero O., 2003, ApJ, 586, 1305

Maeder A., Meynet G., 1991, A&AS, 89, 451

Marigo P., 2002, A&A, 387, 507

Marigo P., Aringer B., 2009, A&A, 508, 1539

Marigo P., Bressan A., Chiosi C., 1998, A&A, 331, 564

Marigo P., Bressan A., Nanni A., Girardi L., Pumo M. L., 2013, MNRAS, 434, 488

Meakin C. A., Arnett D., 2007, ApJ, 667, 448

Miller Bertolami M. M., 2016, A&A, 588, A25

Mocák M., Müller E., Weiss A., Kifonidis K., 2008, A&A, 490, 265

Mocák M., Müller E., Weiss A., Kifonidis K., 2009, A&A, 501, 659

Ostlie D. A., Cox A. N., 1986, ApJ, 311, 864

Paczynski B., 1975, ApJ, 202, 558

Piersanti L., Cristallo S., Straniero O., 2013, ApJ, 774, 98

Pignatari M., et al., 2016, ApJS, 225, 24

Pratt J., Baraffe I., Goffrey T., Constantino T., Viallet M., Popov M. V., Walder R., Folini D., 2017, A&A, 604, A125

Refsdal S., Weigert A., 1970, A&A, 6, 426

Reimers D., 1975, Memoires of the Societe Royale des Sciences de Liege, 8, 369

Ritter C., Herwig F., Jones S., Pignatari M., Fryer C., Hirschi R., 2017, preprint, (arXiv:1709.08677)

Rogers F. J., Swenson F. J., Iglesias C. A., 1996, ApJ, 456, 902

Rosseland S., 1924, MNRAS, 84, 525

Roxburgh I. W., 1978, A&A, 65, 281

Roxburgh I. W., 1989, A&A, 211, 361

Salaris M., Serenelli A., Weiss A., Miller Bertolami M., 2009, ApJ, 692, 1013

Schroder K.-P., Pols O. R., Eggleton P. P., 1997, MNRAS, 285, 696

Schwarzschild K., 1906, Nachrichten von der Königlichen Gesellschaft der Wissenschaften zu Göttingen. Math.-phys. Klasse, 195, p. 41-53, 195, 41

Serenelli A. M., Basu S., Ferguson J. W., Asplund M., 2009, ApJ, 705, L123

Spruit H. C., 2015, A&A, 582, L2

Stancliffe R. J., Fossati L., Passy J.-C., Schneider F. R. N., 2015, A&A, 575, A117

Stothers R. B., Chin C.-W., 1992, ApJ, 390, 136

Thomas H.-C., 1967, Z. Astrophys., 67, 420

VandenBerg D. A., Bergbusch P. A., Dowler P. D., 2006, ApJS, 162, 375

VandenBerg D. A., Edvardsson B., Eriksson K., Gustafsson B., 2008, ApJ, 675, 746

Vassiliadis E., Wood P. R., 1993, ApJ, 413, 641

Ventura P., Zeppieri A., Mazzitelli I., D'Antona F., 1998, A&A, 334, 953

Viallet M., Meakin C., Prat V., Arnett D., 2015, A&A, 580, A61

Wachter A., Schröder K.-P., Winters J. M., Arndt T. U., Sedlmayr E., 2002, A&A, 384, 452

Wagenhuber J., Groenewegen M. A. T., 1998, A&A, 340, 183

Wagenhuber J., Weiss A., 1994, A&A, 286, 121

Weiss A., Ferguson J. W., 2009, A&A, 508, 1343

Weiss A., Schlattl H., 2008, Ap&SS, 316, 99

Werner K., Herwig F., 2006, PASP, 118, 183

Wood P. R., Faulkner D. J., 1986, ApJ, 307, 659

Wood P. R., Whiteoak J. B., Hughes S. M. G., Bessell M. S., Gardner F. F., Hyland A. R., 1992, ApJ, 397, 552

van Loon J. T., Cioni M.-R. L., Zijlstra A. A., Loup C., 2005, A&A, 438, 273

Acknowledgements

I would first like to thank my supervisor, Achim Weiss, for the opportunity to come to MPA and for his guidance and support throughout. Also for allowing me to pursue different avenues of research, and for the many possibilities to collaborate with others. There are many people whom I would like to thank for their support during my PhD, Simon Campbell, who deserves particular thanks for helpful discussions and support over a prolonged period; Marcelo Miller Bertolami, for many useful discussions about AGB stars; John Lattanzio, Amanda Karakas and others at Monash University for making me feel welcome; Gregory Feiden and others at Uppsala University, for helping me to understand stellar atmospheres; George Angelou, for helpful discussions and all the others whom I have encountered along the way.

Additional thanks must be given to those who have made life bearable, the friendly secretaries at MPA, Maria Depner and Gabi Kratschmann, who made living in Munich and dealing with German bureaucracy manageable and Andi Weiss for always being willing to help with computational support. I'd also like to thank the various PhD students and postdocs that have distracted me from work during lunch and outside of work. Finally, I would of course like to thank the Alps, as without the ability to escape the city so easily, I doubt I would have made it this far.